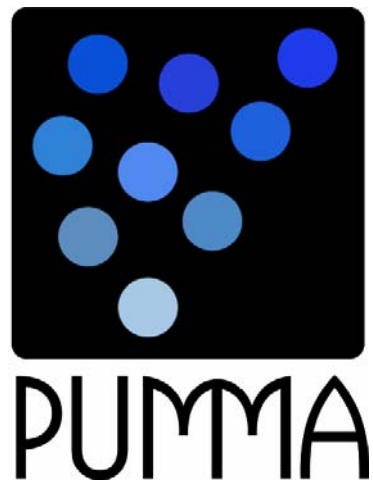# Modelling and Measurement of Bubbles in Decompression Sickness

Michael Chappell

St. Hugh's and Linacre Colleges

Submitted in partial fulfilment of the requirements for the
degree of Doctor of Philosophy
University of Oxford

Trinity Term 2006

Supervised by Dr. Stephen Payne

Modelling and Measurement of Bubbles in Decompression Sickness

Michael Chappell

St. Hugh's and Linacre Colleges

Submitted in partial fulfilment of the requirements for the degree of Doctor of Philosophy

Trinity term 2006

Abstract

Decompression Sickness (DCS), also known as 'the bends', is a recognised problem for SCUBA divers and is a danger for anyone undertaking decompression. The condition arises because gas which has collected in solution in the body is released in the form of bubbles when the ambient pressure falls. Bubbles can form throughout the body, causing a wide range of symptoms, and have been observed both stationary in various body tissues and moving in the blood. Although bubbles are known to be the cause of DCS, their production and behaviour is still not well understood.

In this work the problem of bubble formation is examined in two complementary ways: firstly by automating the predominant method for the measurement of bubbles in the blood. A bubble detection algorithm is derived which offers quantitative information about the occurrence of individual bubbles in the blood based on Doppler ultrasonic measurements. However, since only limited information about bubbles can be extracted by such a technique, mathematical modelling is then used to describe the formation of bubbles in the body. A model is presented for the growth of bubbles in the vasculature from crevice shaped nuclei. Since the precise form of vasculature nuclei is not known, the effect of nucleus geometry on bubble behaviour is explored. The behaviour of a bubble which breaks away from the nucleation site is also examined and finally the relationship between bubbles forming in the blood and those forming stationary in the tissue is modelled.

The combination of quantitative measurements and physiological models as presented in this work offers a complete approach to the investigation of bubble formation in the body. Ultimately it offers a novel approach to the understanding and prevention of DCS.

Dedicated to

Leslie Charles Chappell

1919-2004

'Grampi'

You see, at just the right time, when we were still powerless, Christ

died for the ungodly. Very rarely will anyone die for a righteous

man, though for a good man someone might possibly dare to die.

But God demonstrates his own love for us in this: While we were

still sinners, Christ died for us. Romans 5 v6-8

Acknowledgements

Give thanks to the LORD, for he is good; his love endures forever. Psalm 118 v1.

Of all the (many) pages of this work this is probably one of the hardest but one of the most satisfying: here finally I can give credit to all those without whom the last 3 years would not have been possible.

I am eternally indebted to my wife, Becca, for a great deal of love, support and patience. I have far too much to thank her for than I could possibly fit here.

I am also greatly indebted to Stephen Payne, who has guided me carefully and efficiently through this whole process. I have learnt a great deal from him both at undergraduate and post-graduate level, for which I am very thankful. I hope that, as his first student, I might have taught him one or two things about supervising post-graduates for the benefit of all who follow after me.

I cannot omit to thank my parents who have been exceptionally supportive, always very excited about the next adventure I was about to embark upon and very understanding with my lack of a 'real' job. Alongside them there is a much wider family who have all had their effect on who I am today and what under, God's sovereignty, I have achieved. This includes, in more recent times, Andrew and Sandra, who have the great honour of being Becca's parents (hence I have much to thank them for).

I must also thank Steve Collins, who when confronted with a reply to the question "are you considering doing a doctorate next year" of "only if someone pays for me to go diving", took me seriously and helped me find a topic (although no-one ever did pay for my diving). I am also very grateful to Steve Daniels who provided very useful insight into the subject of bubbles in the body and a pile of literature I would never have found elsewhere. I am also thankful to the many people I have met at the UHMS and EUBS meeting who have been very welcoming and helpful including Alf Brubakk, Ron Nishi, Hugh Van Liew, David Doolette and Johnny Conkin.

And finally thanks to all those around me day-by-day who provided much needed diversions and conversation. Alongside a large number of students from Univ. and Corpus to whom, perhaps, I have passed on some knowledge.

Contents

1. Introduction

Decompression Sickness[*] (DCS), more popularly known as 'the bends', is a recognised risk for all 'deep-sea' divers, from the growing population of SCUBA divers through to commercial and military diving operations. Since DCS is associated with decompression, its influence also extends to aviators and astronauts undertaking 'space-walks', DCS describing the range of symptoms that arise from the formation of bubbles in the body during and after decompression. Gases may transfer into and out of the body from the inhaled atmosphere through the lungs into the blood, from where it transfers in solution between the blood and the body tissues. This process proceeds to achieve equilibrium between the inhaled gases and their concentration in solution in the body, i.e. over time the tissues become saturated with gas. Whilst underwater, and thus breathing gases at a raised pressure, a diver accumulates gases in solution in his or her body tissues, Figure 1-1a, the final concentration being determined by the rate of gas transfer and the length of time spent at depth. At the end of the dive he or she returns to the surface and the pressure acting upon him or her is released: decompression. The concentration of gases in his or her body exceeds those in the breathed atmosphere, so the tissues are now super-saturated, thus gas transfer will proceed in the opposite direction to remove the gases from the body, Figure 1-1b. However, gases may also

---

[*] In this work the term DCS will be adopted to describe "conditions resulting from the evolution of gas phase within the body from a supersaturated state" in keeping with the mechanistic classification employed in the 5th edition of Bennett and Elliott's Physiology and Medicine of Diving, Brubakk, A.O. & Neuman, T.O. eds, Saunders, 2003.

escape from solution by the formation of bubbles in the tissue, Figure 1-1c, if the difference in concentrations between body tissue and atmosphere is sufficient.
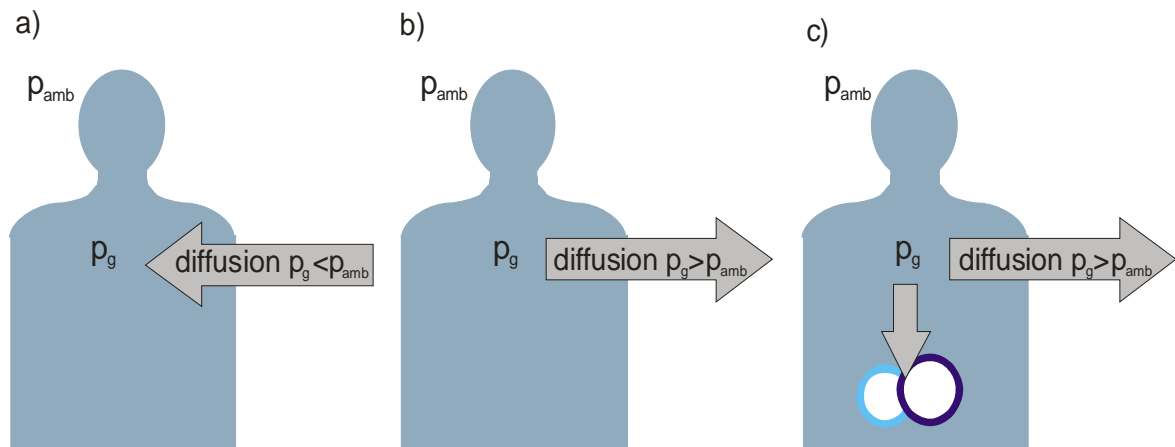
Figure 1-1: (a) Under compression atmospheric pressure, p_{amb}, is greater than the tension (concentration measured in units of pressure) of gas in the body, p_g, hence gas diffuses into the body; (b) under decompression the pressure difference is reversed and so is the direction of the diffusion; (c) if the decompression is sufficient bubbles will also form from the dissolved gas in the body, potentially resulting in the symptoms of DCS.

A common analogy for this process is that of a carbonated drink: at the factory carbon dioxide gas is dissolved in the drink and sealed at high pressure. Upon the release of the seal the gas escapes from the drink both by diffusion (through the liquid surface) and by the formation of bubbles. It is known that production of bubbles in the carbonated drink can be reduced by opening the seal gradually, providing a slow release of pressure in the container. A similar principle is employed by all divers who control their decompression in a manner designed to avoid, or limit, bubble formation.

The first observation of the formation of bubbles under decompression is ascribed to Boyle (1670). However, their role in DCS was not recognised until the work of Bert in 1878, Elliott *et al.* (2003). A description of the dynamics of the dissolved gases had to wait for Haldane, Boycott *et al.* (1908), upon whose work most decompression schemes for the avoidance of DCS have been based. These have historically been based on the principle of critical gas saturations: the decompression is staged in such a manner to avoid gas concentrations in body tissues (typically modelled more generally by non-specific 'compartments') exceeding empirically established limits. Characteristically these 'tables' bring the diver as close to the surface as possible to speed the rate of gas transfer out of the body. It has not been until more recently that the mechanics of bubble formation have been

considered in decompression schemes, leading to the concept of 'deep-stops': early stages in the decompression performed at deeper depths than previously recommended, to suppress bubble formation.

Despite almost 100 years having passed since Haldane's work, the risks of DCS are far from being eliminated and the role of bubbles in DCS is still not thoroughly understood. Although in the commercial diving industry humans are being replaced in many situations by remote-operated-vehicles, the need for a comprehensive description of DCS is no less important, especially in the face of a growing community of 'technical' divers who are taking recreational diving to greater depths where far less research has been performed and so the risks of DCS are currently greater.

It has long been recognised that bubbles form under decompression and are associated with DCS, not least because of the improvement in DCS symptoms observed under recompression. It is possible to observe bubbles in the body using ultrasonic techniques, Rubissow *et al.* (1971), Daniels *et al.* (1980), Daniels (1984), both stationary in tissues and the vasculature as well as moving with the blood flow. Moving bubbles are most commonly observed in DCS studies using a Doppler ultrasound device, Nishi *et al.* (2003), typically in the blood flow around the heart. However, it is unclear how these measurements may relate to the risk and symptoms of DCS. One of the difficulties is that the measurements must be graded manually allowing only semi-quantitative measures to be obtained. Additionally, it is not clear how the bubbles observed in the blood are related to the bubbles that form in various parts of the body, especially the ones that remain stationary in the tissues. Hence this work addresses the two issues of accurate blood bubble measurement and the interpretation of these measurements using physiological models, as illustrated in Figure 1-2. This figure illustrates the limits imposed by using a Doppler ultrasonic method for observing bubbles: even if quantitative information can be extracted it still only provides information about the moving, blood-borne bubbles. Despite this limitation Doppler is the most practical method to use for bubble detection on a large scale. Hence, as illustrated in the figure, mathematical models are needed to describe the formation of both types of bubbles and their interaction, such that quantitative measurements of moving bubbles can be interpreted in relation to the bubble production in the whole body. This work is thus a combination of mathematical modelling and signal processing, where the two techniques are being employed to make the most of

the available information about decompression bubbles forming in the body and the interpretation of this information in the understanding and prevention of DCS.
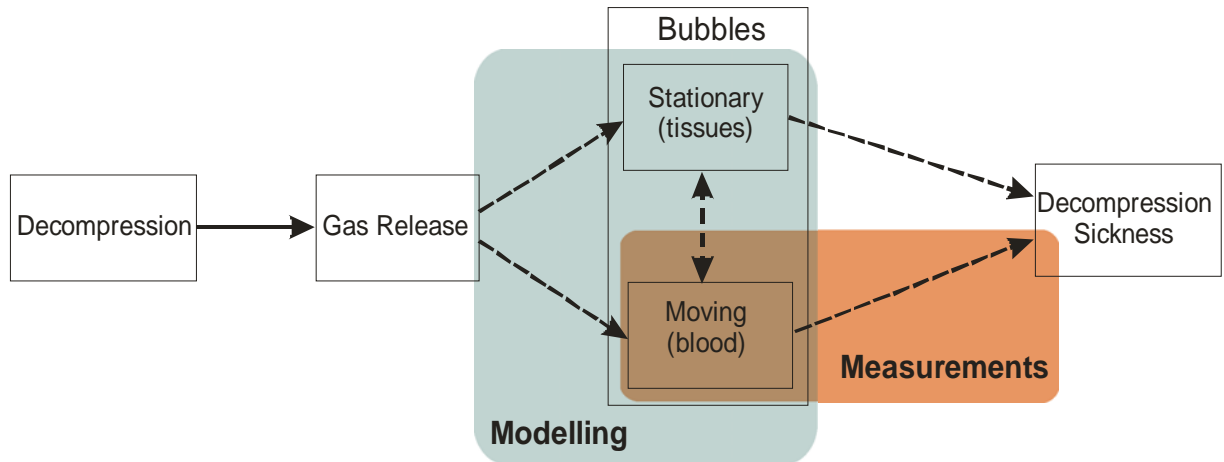
Figure 1-2: Since it is only possible using Doppler ultrasonic equipment to measure moving bubbles, it is necessary to use mathematical models to interpret measurements in terms of bubble production in the whole body.

In chapter 2 the literature is thus reviewed in relation to both the measurement of bubbles in the body using ultrasound and the mathematical modelling of these bubbles under decompression. In chapter 3 an algorithm is described based on non-stationary signal processing techniques for the automated detection of bubbles in the blood, some preliminary results are presented and the difficulties in validating this algorithm against available expertly labelled data are examined. In chapter 4 a model for the formation of bubbles in the blood from crevice shaped nucleation sites in the walls of blood vessels, due to dissolved gases in the tissues, is derived. Chapter 5 presents the results from simulations of this model to examine the behaviour of crevice nuclei under both compression and decompression. Since the model is derived in chapter 4 for a nucleation site with a simple conical geometry, the effects of variations in this geometry in relation to potential nucleation sites in the body is examined in chapter 6. Chapter 7 examines in greater detail the detachment of bubbles from the nucleation sites as a consequence of the blood flow and the subsequent growth of such bubbles in blood vessels. Chapter 8 addresses the relationship between the formation of bubbles in the blood, using the model of chapter 4, and those that form in the tissues. Finally conclusions are drawn in chapter 9 and future directions of this work are discussed.

2. Literature review
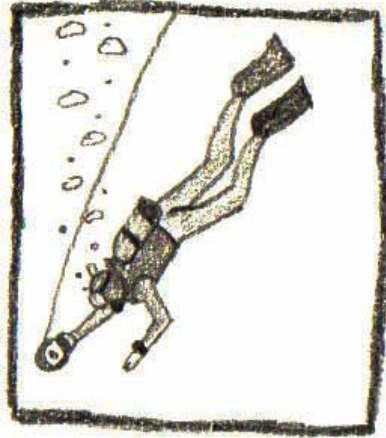
2.1 Introduction

In this chapter the literature relating to the role of bubbles in DCS is examined, specifically addressing two areas: firstly, the main ultrasonic techniques which can be used to detect bubbles in the body and the extent to which accurate information can automatically be extracted from them are described. Secondly, the current theories for the sources of bubbles in the body and the current state of physiologically based mathematical models of bubble formation are also explored.

2.2 Bubble detection

This section examines the current state of ultrasonic techniques in bubble detection for the study of DCS. The two techniques of Doppler and imaging ultrasound will be examined, including the current methods by which the data is interpreted and the progress that has been made on automated bubble detectors. The use of ultrasound for detection of post-operative emboli will also be examined to consider the applicability of the technology developed in that field for DCS study.

2.2.1 Principles of Ultrasonic bubble detection

Ultrasound is a widely used medical diagnostic tool, which has also found use in the study of decompression induced bubbles. It operates by transmitting sound waves from a transducer into the body; information may then be obtained from the returning echoes. The waves are generated in the transducer by a piezoelectric crystal, which produces an ultrasound pulse in response to an

electrical driving signal. A second transducer, also employing a piezoelectric crystal, can be used to convert echoes from the body into electrical signals: such a system is known as continuous wave (CW). Alternatively a single transducer may be employed both to transmit and to receive; a burst of ultrasound is transmitted by the transducer, the reflected ultrasound being collected by the same transducer after a delay: a Pulse-Echo system often refereed to as Pulsed Wave (PW) in the DCS field. The advantage of a PW system is that depth information may also be inferred from the echo return time; the deeper the feature from which the echo originates, the greater the time delay.

Both CW and PW systems may be used for Doppler monitoring of intra-vascular bubbles. PW allows the depth of interest to be set, so that signals from other depths are discarded. In theory this should increase the signal to noise ratio, as Doppler shifts from the movement of features outside the blood vessel can be excluded. "In practice, however, such systems may not be as advantageous as good CW systems", Nishi *et al.* (2003), since the PW system requires more complex electronics than a CW system and needs to be adjusted for depth individually for every subject. Additionally both types of system may be focused to a particular depth using an array of transducers, but once again the focus would need to be adjusted on a subject-by-subject basis.

Ultrasonic echoes occur at interfaces between media with different acoustic properties. Tissues often have inhomogeneous acoustic properties: at interfaces between these inhomogenities some of the incident ultrasound energy is reflected. For a plane wave, incident at right angles to a plane interface, the ratio between the reflected (E_r) and incident (E_i) energy is given by:

$$R = \frac{E_r}{E_i} = \left(\frac{Z_2 - Z_1}{Z_2 + Z_1} \right)^2 , \tag{2.1}$$

where Z_1 and Z_2 are the acoustic impedances of the two media. The impedance is related to the density and speed of sound in the tissues. Large differences in acoustic impedance yield high-energy echoes: since the acoustic impedance of tissues and blood is typically 3000 - 4000 times higher than that of air, Nishi (1975), a tissue-air will reflect almost all of an incident ultrasound wave, i.e. $R \approx 1$.

Typical ultrasound frequencies used for the detection of decompression-induced bubbles lie in the 1-10 MHz range, with the choice of frequency based on the desired penetration depth and. Lower frequencies, 2-4 MHz, are required to survey deep structures such as the heart, as higher frequencies are attenuated more rapidly within the body. Higher frequencies permit a narrower ultrasound beam to be generated and greater spatial resolution to be achieved, but are only suitable for peripheral sites.

The cyclic pressure amplitude of an ultrasound wave will also produce forced vibration of the gas inside a bubble, this effect is maximal for bubbles of a resonant size. Typically ultrasound systems which operate in the MHz range are not sufficiently sensitive to detect bubbles of resonant size *in vivo*, for example the resonant size for a bubble at 5 MHz is 1 μm, Nishi (1975). For a gas bubble larger than the resonant size, the amplitude of the ultrasound echo is proportional to its radius, which should permit bubble size to be determined. However, in practice variable attenuation of the ultrasound signal throughout the sample volume makes accurate estimation of bubble size difficult, Nishi *et al.* (2003).

The use of the higher harmonics of the reflected signal has been proposed for their use in bubble detection, for example Didenkulov *et al.* (1999), Shankar *et al.* (1999), Palanchon *et al.* (2001), Palanchon *et al.* (2003). However, it is unclear to what extent these methods, which have thus far been primarily developed *in vitro* or in animal models, might transfer to the *in vivo* detection of decompression bubbles, especially with the need for monitoring in the pre-cordial area as discussed below. This review will concentrate on the technologies which have a more proven track record for their use in bubble detection: Doppler ultrasonography and ultrasonic imaging.

2.2.2   Doppler ultrasonography

2.2.2.1 *Principles of Doppler ultrasound*

This is the most common method for decompression monitoring, because the instrumentation is cheap, compact and simple to operate. Doppler ultrasound systems exploit the Doppler Effect, which describes how sound from a moving source as observed by a stationary receiver is shifted in frequency according to the speed of sound in the transmitting media and the velocity of the object:

$$f = f_0\left(\frac{c}{c - v_s}\right), \tag{2.2}$$

where f_0 is the frequency of the ultrasound probe, c is the speed of sound in the medium and v_s is the velocity of the source. Since ultrasonic diagnostic tools are used to measure reflections from acoustic interfaces in the body the equation for a moving reflector is required:

$$f = f_0\left(\frac{c + v}{c - v}\right), \tag{2.3}$$

where the reflector is moving toward the source with a velocity v. In a Doppler ultrasound system the electronic signal generated by the echoes is demodulated to remove the ultrasound signal, leaving only the Doppler shifted frequency, which (assuming that v is much smaller than c) is approximately $2vf_0/c$. Since the range of Doppler frequencies observed lies within the audible range, the output from a Doppler system is typically an audio signal.

2.2.2.2 Doppler ultrasonic detection of bubbles

Only moving bubbles, i.e. intra-vascular bubbles, may be detected by this method. In practice, bubbles are only monitored in the venous system, as few are expected in the arterial system, Francis *et al.* (2003). Doppler shift signals will also arise from other moving objects in the collection volume of the ultrasound probe, including blood cells, heart valves, Nishi *et al.* (2003), and other tissue movements, for example muscle contraction. The acoustic impedances of blood and soft tissue are very similar, Evans *et al.* (2000): however, the combined signal from the moving blood cells at peak flow, during the systole phase of the heart beat, can also create significant audible signals. Typically the audio output of a Doppler system is high-pass filtered to remove the effects of slow tissue movements. However, differentiation between bubble generated sounds and background sounds due to blood cell movement can be difficult, Nishi *et al.* (2003).

Generally, bubble monitoring is performed in the precordium (the area around the heart) the preferred location being the pulmonary artery, Nishi *et al.* (2003). Theoretically, this allows an estimate to be made for the rate of bubble production in the entire venous system, as all the returning blood from the body must flow through here. However, in practice small bubbles may not be detectable above the background signals from the blood cells, and signals from slow moving bubbles may be attenuated by high-pass filtering. Additionally, the assumption is made that all the

bubbles persist long enough to reach this point, and that the sample volume of the probe covers the full cross sectional area of the vessel, Nishi *et al.* (2003). Peripheral sites may also be monitored, for example the subclavian veins, femoral veins or inferior vena cava, Nishi *et al.* (2003), although these will only give information regarding the bubble production in one part of the body.

2.2.2.3 Characteristics of Doppler bubble signals

The Doppler signal may be subdivided into bubble events and a background signal. The latter signal arises from reflections of moving blood cells, movement of the blood vessel wall and moving extra-vascular tissues. Analysis of the spectra of Doppler signals by Kisman (1977) has shown that the background signal typically has minimal magnitude for frequencies above 1 kHz, whereas bubble transients introduce frequencies above 1 kHz. The background signal may be classified as a non-stationary but almost periodic process, whereas the bubble events are transient non-stationary random processes. A non-stationary process is one whose statistical properties (e.g. mean frequency) vary over time, for example the blood cell motion sounds are periodic but the period varies because the heart rate is not constant. The non-stationary nature of the Doppler audio signal means that conventional stationary spectral analysis using the Fourier transform is inappropriate, as it does not permit localisation in time; consequently, joint time-frequency representations (TFR) are required, such as the Short-Time Fourier Transform (STFT), also known as the windowed Fourier transform, the squared magnitude of which is referred to as the spectrogram.

A number of authors, for example Evans *et al.* (1999), consider the STFT to be limited for Doppler audio analysis, since to achieve high frequency resolution a lower time resolution has to be used and vice versa, preferring to use the Wigner-Ville Spectrum (WVS) or Smoothed-Pseudo WVS (SPWVS), which is not subject to this limitation. However, other authors have found the spectrogram to be preferable, for example Roy *et al.* (2000), a great advantage being its lower computational cost and, unlike the WVS which is quadratic, the absence of cross-component terms.

Belcher (1980) assumed that Doppler bubble events occupy a very narrow bandwidth about a centre frequency, which may be of the order of kHz. This means that a bubble sound would have a high $Q = \Delta\omega/\omega_0$, where $\Delta\omega$ is the bandwidth at half power and ω_0 is the centre frequency.

16

However, subsequently bubble events have been regarded as having chirp-like characteristics, Evans *et al.* (1999), Krongold *et al.* (1999), i.e. the frequency varies during the event. Under this assumption the frequency associated with the bubble event should still be narrowband, but varying with time. Some authors have observed wide distributions in frequency, for example Kisman (1977), although this may be a result of saturation in the audio amplifier, Smith *et al.* (1994), which will distort the sinusoidal wave shape. This illustrates the limitation of a Fourier based approach which assumes a sinusoidal basis set.

2.2.2.4 Doppler audio grading

The detection of bubbles is typically done from the Doppler audio signal by trained observers. They listen to the Doppler shift signal to detect the characteristic bubble sounds, which have been described as pops, clicks, or chirps, see for example Kisman (1977), El-Brawany *et al.* (2002). These must be discerned against the sounds arising from blood cell movement and heart valve motion, which give a regular swishing sound, Strong *et al.* (1997). It is generally not possible to quantify bubbles individually by this method. Consequently a number of standard grading procedures exist, which permit comparison of results between different researchers.

The two main schemes in current use are the Spencer scale and the Kisman-Masurel (KM) code. The Spencer scale assigns a grade from 0 to IV according to the definitions given in Table 2-1. Roman numerals are used for the grades to make it clear that the grades cannot be treated as numerical values; in fact the relationship between Spencer grades and the number of bubbles is believed to be highly non-linear, Nishi *et al.* (2003). The KM code is based on three parameters, Table 2-2:

- Frequency (*f*): The number of bubbles per cardiac period.
- Rest percentage (*p*): The number of cardiac periods containing bubbles with subject at rest.
- Amplitude (*A*): A comparison of the audible amplitude of bubble to heart cycle sounds.

The code is converted to a grade using the left-hand side of Table 2-3. The KM code also makes allowance for a measurement after a prescribed movement, since it has been found that after the subject has performed some form of muscle contraction, for example a deep-knee bend, a shower of bubbles is observed. To grade these signals the same method is used except that the Percentage

parameter is replaced with the Duration parameter, which measures the number of heart cycles for which elevated bubble sounds are heard after movement, Table 2-4. The three-digit code produced from this analysis is converted to a KM bubble grade using the right-hand side of Table 2-3. Although the KM code is more complex than the Spencer code, it is believed to be much easier to learn and to use in practice, Nishi *et al.* (1989), possibly because it proceeds in a systematic step-by-step manner, Nishi *et al.* (2003). In principle it is possible to convert a KM score to an equivalent Spencer grade using Table 2-5.

2.2.2.5 Doppler audio monitoring

It has often been observed that the peak number of bubbles observed in the precordium does not occur immediately after the end of decompression, i.e. surfacing for a recreational diver. In fact bubbles may not even be detected until an hour after decompression, although generally bubbles start to appear earlier than this, peaking after 1 hour, Nishi *et al.* (2003). Detection of bubbles may continue for some time after exposure: in severe cases bubbles have been detected more than 6 hours after decompression, Nishi *et al.* (1989).

Table 2-1: The Spencer Scale, Nishi *et al.* (2003)

Grade	Spencer code
0	A complete lack of bubble signals.
I	An occasional bubble signal discernable with the cardiac motion signal with the great majority of cardiac periods free of bubbles.
II	Many, but fewer than half, of the cardiac periods contain bubbles, singly or in groups.
III	Most of the periods contain showers of single-bubble signals, but not dominating or over-riding the cardiac motion signals.
IV	The maximum detectable bubble signal sounding continuously throughout systole and diastole of every cardiac period, and over-riding the amplitude of normal cardiac signals.

Table 2-2: The KM code, composed of three parameters, Nishi *et al.* (2003)

Code	Frequency (f)	Rest Percentage (p)	Amplitude (A)
0	0	0	No bubbles discernable
1	1 – 2	1 – 10	Barely perceptible, $A(b) \ll A(c)$
2	Several, 3 – 8	10 – 50	Moderate amplitude, $A(b) < A(c)$
3	Rolling drumbeat, ≥ 9	50 – 99	Loud, $A(b) \approx A(c)$
4	Continuous sound	100	Maximal, $A(b) > A(c)$

Table 2-3: Table to convert KM code to KM grade for the rest condition (left), and the movement condition (right), Nishi *et al.* (2003). Codes in grey are improbable or unlikely. BG = bubble grade.

Precordial at rest								Precordial after movement							
fpA	BG	fpA	BG	fpA	BG	fpA	BG	fdA	BG	fdA	BG	fdA	BG	fdA	BG
111	I-	211	I-	311	I	411	II-	111	I-	211	I-	311	I	411	II-
112	I	212	I	312	II-	412	II	112	I	212	I	312	II-	412	II
113	I	213	I+	313	II	413	II+	113	I	213	I+	313	II	413	II+
114	I	214	II-	314	II	414	III-	114	I	214	II-	314	II	414	III-
121	I+	221	II-	321	II	421	III-	121	I+	221	II-	321	II	421	III-
122	II	222	II	322	II+	422	III	122	II	222	II	322	II+	422	III
123	II	223	II+	323	III-	423	III	123	II	223	II+	323	III-	423	III
124	II	224	II+	324	III	424	III+	124	II	224	II+	324	III	424	III+
131	II	231	II	331	III-	431	III	131	II	231	II	331	III-	431	III
132	II	232	III-	332	III	432	III+	132	II	232	III-	332	III	432	III+
133	III-	233	III	333	III	433	IV-	133	III-	233	III	333	III	433	IV-
134	III-	234	III	334	III+	434	IV	134	III-	234	III	334	III+	434	IV
141	II	241	III-	341	III	441	III+	141	II	241	III-	341	III	441	III+
142	III-	242	III	342	III+	442	IV	142	III-	242	III	342	III+	442	IV
143	III	243	III	343	III+	443	IV	143	III	243	III	343	III+	443	IV
144	III	244	III+	344	IV-	444	IV	144	III	244	III+	344	IV-	444	IV

Table 2-4: KM duration parameter (replaces percentage parameter for the movement condition), Nishi *et al.* (2003).

Code	Duration cardiac periods (d)
0	0
1	1-2
2	3-5
3	6-10
4	>10

Table 2-5: Conversion from KM code (or grade) to Spencer scale, Nishi *et al.* (2003).

Spencer Grade	KM code (bubble grade)
0	000
I	111 (I-), 112 (I), 113 (I), 211 (I-), 212 (I), 213 (I+)
II	212 (I+), 122 (II), 123 (II), 221 (II-), 222 (II), 223 (II+)
III	232 (III-), 233(III), 242 (III), 243 (III), 332 (III), 333 (III), 342 (III+), 343 (III+)
IV	444 (IV)

Despite the data collection regime proposed by Nishi *et al.* (1989), there is still incomplete standardisation of Doppler signal collection between different groups, especially with regard to the number of readings. This lack of standardisation has made it difficult to compare data from different research programmes. Where only one reading is available it is impossible to tell whether

it represents the peak bubble grade from that exposure. It is also unclear with what frequency data should be collected.

2.2.2.6   Inter-rater agreement for Doppler bubble grades

Sawatzky *et al.* (1991) analysed the agreement between different observers in grading Doppler signals using the KM system to investigate the problems associated with the subjectivity of the grading schemes. Variation between observers has been tackled in various ways in the past, for example by observers working in pairs and re-grading by the same observers two weeks later. However, none of these procedures allow for the quantitative assessment of the agreement between different observers. The authors recommended a method via which inter-rater agreement could be assessed to ensure that grades from different observers could be combined. The first step is to produce a 'contingency table', which plots the gradings for a set of data of two observers against each other. Complete agreement is signified by all the values lying on the diagonal. The data can then be analysed using non-parametric statistics, which must be used for Doppler data as the grades are ranked (ordinal) data, Sawatzky *et al.* (1991), rather than being continuously distributed. Both the subjectivity of the Doppler audio grading method and the likelihood of disagreement between different operators is a significant problem in decompression bubble monitoring.

2.2.2.7   Automatic bubble detection

A number of attempts have been made to develop automatic bubble counting systems based on Doppler ultrasound. The majority of these have been based on detecting events where the reflected energy exceeds a threshold based on the background signal either in time, see Nishi *et al.* (2003), or based on comparing the energy spectra with and without bubbles, Nishi *et al.* (1989). Such methods are limited because it is difficult to set a threshold which excludes all false positives, such as the peak power of blood cell movement, without excluding smaller bubbles. Success has been found where other sources of Doppler ultrasound can be excluded, for example where the transducer is implanted around a blood vessel or in some peripheral locations, Nishi *et al.* (2003). Consequently automatic bubble detection has been possible in animal studies, but has performed poorly in humans, where monitoring of the venous return, which is essential for decompression studies, is complicated by reflections from other moving structures.

Belcher (1980) developed a system to quantify bubbles from Doppler ultrasound signals for animal use, and later developed the technique for use on human precordial signals. The system was based around a comb filter which divided the signal into 16 channels, each with the same Q value, essentially an early implementation of wavelet decomposition. The system generated estimates of the signal due to blood movements in a particular channel using the other channels apart from the neighbouring ones. If the error between the signal estimate in each channel and the actual signal at the output of the detector exceeded a manually set threshold, a bubble was counted. The estimation process typically took 5 minutes to stabilise, and the weights in the estimator were adjusted to reach four or five false counts per minute. A 6 dB improvement in the SNR was reported by adding the adaptive algorithm to the comb-filtered signal, Belcher (1980). However, the need for 5 minutes of settling time and the dependence on a manually set threshold according to an acceptable false alarm rate limits the applicability of this system.

Both gaseous and solid emboli may be introduced into the circulation during some operative procedures, Gibby (1993). Doppler ultrasonography is also used to detect these, requiring the anaesthetist continuously to monitor the Doppler audio signal for passing emboli. Gibby and colleagues developed a system for clinical emboli detection using precordial Doppler signals, Gibby *et al.* (1988), Gibby (1993). However, a human expert was still required to verify that an embolus had been detected. The later system showed good sensitivity, comparable to a human observer, in a limited trial on dogs for large emboli, but performed poorly for small emboli. Strong *et al.* (1997) used a Neural Network (NN) on the FFT spectra of precordial Doppler ultrasound signals to determine air embolism infusion rates in dogs. Although the results were promising, the trial was limited to only four animals. Chan *et al.* (1997) developed a system to detect heartbeat cycles that contained the passing of an embolus in signals from a precordial location. This used the Wavelet Transform (WT) to analyse the signals on different scales, essentially to look for the higher frequency components observed in embolic heart cycles. The system was successful and a correlation was found between the calculated power and embolus size for trials performed in dogs. Although both Gibby and Chan have found success in detecting single emboli in dogs, it is likely that the precordial signal in humans will be corrupted by complex artefacts which look like bubble transients and have similar spectra, Nishi *et al.* (1989).

A number of different commercial systems have been developed for the detection of post-operative emboli in peripheral blood vessels, for example Markus *et al.* (1993), Siebler *et al.* (1994), Van Zuilen *et al.* (1996), Markus *et al.* (1999), Fan *et al.* (2001). However, these systems operate on Transcranial Doppler (TCD) signals, with a sample collection volume in the base of the skull, which is not subject to as many background sources as precordial locations. Hence these detection systems do not lend themselves to the detection of decompression related gas bubbles. Since there are few sources of noise in the peripheral locations, most work for the detection of operative and post-operative bubbles has been concentrated here, with few studies addressing the precordial site.

Krongold *et al.* (1999) appears to be the most recent study to address post-operative bubbles. They considered the use of wavelets for the detection of emboli in the blood. The motivation for that work was the inverse relationship between the Doppler frequency of a passing emboli and its transit time through the sample region, both of which are related to its velocity, which "suggests a time-scale-based, or wavelet-based, detector might yield an optimal matched filter". These systems were compared to a STFT based system on data where the SNR has been degraded by the addition of white Gaussian noise. However, the improvement in the SNR when using the WT over the STFT was only 1 dB, which does not justify the extra computational expense of the WT. The use of white Gaussian noise source is also severely limiting, as it does not truly represent Doppler signals from ultrasound reflections of blood components or other body tissue structures, as these are largely non-stationary.

Nishi *et al.* (1989) have previously concluded that "advanced signal processing involving pattern recognition and artificial intelligence techniques would be required to be able to discriminate between sources of signal that occur on a regular basis (such as valve action and heart wall motion) and signals which result from bubbles". More recent advances in signal processing technology has led Nishi *et al.* (2003) to suggest that with "high computing power available now at relatively low cost, fully automatic bubble detection systems may become more practical". They cite Sutherland (1999), who reported the development of a bubble detection system for precordial Doppler signals on the KM scale using Holographic/Quantum Neural Technology. The prototype system was designed to operate in real time on CW Doppler ultrasound signals and the development illustrated "the complexity and difficulty in identifying and classifying bubbles in the high noise environment

of the precordium", Nishi *et al.* (2003). Unfortunately, no further details or performance measures for this system have been made available.

2.2.3   Ultrasound imaging

2.2.3.1   Principles of ultrasonic imaging

Imaging systems are based on PW technology, and utilise the ability to gather the depths of reflecting objects from the time delay between transmission and reception of ultrasound bursts. There are a number of ways to display the signals in ultrasound imaging; the most widely used in medical applications is B-mode scanning ultrasound, where a number of ultrasound beams are scanned through a section of the patient, the resulting echoes being built up into a 2D image. Bubbles, being highly reflective, appear as bright points on the B-mode image. To be detectable, the magnitude of the reflection must exceed the background signals from the body tissues. As for Doppler systems, estimation of bubble size can be difficult, since the spatial resolution may be insufficient and there is variable attenuation through the collection volume.

2.2.3.2   Ultrasonic monitoring for bubbles

As for Doppler systems, it is advantageous to monitor bubbles around the heart, looking for all the bubbles returning from the body. However, the movement of the heart walls makes the counting of bubbles more difficult in this location. Consequently, this has not been widely used outside animal trials. Most work with ultrasonic imaging has been done in monitoring peripheral sites. Daniels and colleagues developed the work of Rubissow *et al.* (1971) in the study of bubble formation in the hind legs of guinea pigs, Daniels *et al.* (1979), Daniels *et al.* (1980), the instrument subsequently being developed for human use, Daniels (1984).

This device used mechanical scanning to produce a B-mode image of a cross section through the leg. Originally these images were examined visually by comparing them with a reference image to discount any artefacts that visually appear similar to bubbles. A new frame was recorded every 2 seconds from 1 minute to 30 minutes after compression. Subsequently an electronic method, based on an integrator, was developed which was better suited to extensive studies, Daniels (1984). This method was limited by the presence of moving artefacts, for example reflections due to the deformation of structures in the leg with movement. Although accurate bubble size could not be

extracted from the magnitude of the bubble reflection, Daniels *et al.* (1979), a semi-quantitative approach to bubble sizing was possible, bubbles being grouped into three ranges: <100 μm, 100-500 μm, >500 μm, Daniels *et al.* (1980).

A scanning system was also developed for human use, Daniels (1984). Bubbles were observed in subjects without any symptoms and with only mild symptoms of DCS, for example skin itching, in a few cases. Occurrences of mild symptoms were only present in divers who also had bubbles within the collection volume. Very few serious DCS incidents were monitored, because the decompressions were within safe limits, so the utility of an integrator output for DCS prediction could not be thoroughly assessed. However, for recompression the quantity of bubbles in the observation volume, and hence the integrator output, was seen to reduce dramatically. However, the system does not appear to have been developed further subsequently.

2.2.3.3 Bubble grading for ultrasonic images

As with Doppler techniques, grading schemes have been established to make the evaluation of images easier by an observer. It has been found that accurate assessments of ultrasound images can be made using grading schemes, even by relatively untrained personnel, Eftedal *et al.* (1997), unlike Doppler audio signals. Table 2-6 illustrates the scoring system of Eftedal *et al.* (1997), termed the EB Grade: as with the Doppler schemes only non-parametric statistics may be used.

Table 2-6: EB scale for grading ultrasonic images, Eftedal *et al.* (1997).

Grade	Description
0	No bubbles.
1	Occasional bubbles.
2	At least one bubble every 4th cycle.
3	At least one bubble per cycle.
4	Continuous bubbling, at least one bubble/cm^2 in all frames.
5	'White-out', individual bubbles cannot be seen.

2.2.3.4 Automated bubble quantification

Eftedal *et al.* (1993) have developed a system automatically to count bubbles in an ultrasound image. The routine assesses both the quantity and a relative size measure of bubbles within an area either defined on the image manually or generated semi-automatically by edge detection. The system searches the image to identify the high intensity spots that correspond to bubbles. The

bubble count is only incremented if a potential bubble site fulfils set criteria of size and intensity above the background level. The output of the process is the number of bubbles per cm^2. The system is found to have good agreement with manual bubble counts on the same image. The method is better suited for imaging the heart than peripheral locations, because the number of detections is averaged over the detection area, and in the heart this area is larger. The intensity of the bubble reflection is used to give a measure of bubble size: in a series of in-vitro trials with bubbles of known size, a linear correlation between bubble size and measured amplitude of the reflection was confirmed. For use *in vivo*, exact bubble size is not calculated, as this would require complex calibration, so only a histogram of relative sizes can produced.

This system has allowed the relationship between bubble numbers and the EB grade to be investigated over several hundred experiments, along with the correspondence between the EB grade and the KM grade as shown in Table 2-7. This correlation potentially allows bubble grades to be converted onto a linear scale amenable to parametric statistics.

Table 2-7: Conversion between KM grade, EB grade and bubble counts, Nishi *et al.* (2003)

KM grade	EB grade	Bubble count (bubbles/cm^2)
0	0	0
I-	1	0.01
I	1	0.05
I+	1	0.1
II-	2	0.15
II	2	0.2
II+	2	0.3
III-	3	0.5
III	3	1
III+	4	2
IV-	4	5
IV	5	10

2.2.4   Application of bubble grades for DCS assessment

Both Doppler and imaging ultrasound have been used to study decompression in humans. Since the Doppler device is cheap and easy to use, especially in the field, it has been widely used; problems arise, however, in the interpretation of the data. The simplest measure is simply to consider the peak bubble grade, which allows a simple comparison to be made between different decompression

profiles. However, it is difficult to do further analysis because bubble grade are ranked data, i.e. the intervals between the grades are non-uniform. Therefore common statistical measures cannot be used. Parametric statistical measures exist, and a wide range was considered by Sawatzky *et al.* (1991): however, many of these are of limited practical use for the study of decompression. Additionally the peak bubble grade may be misleading, as it does not indicate the time duration of the maximum bubble grade or any further information about the total distribution of bubbles post-decompression. Daniels (1984) has already noted that the speed with which peak bubble counts are attained may be correlated with the severity of the decompression profile and the resulting symptoms. A number of authors have considered integrating the amount of bubbles detected in an individual over time until they disappear, Nishi *et al.* (2003). The result of this is an index of severity named the Kisman Integrated Severity Score (KISS), Jankowski *et al.* (1997), Nishi *et al.* (2003). The KISS attempts to linearise the data, converting it into a form that can be used with normal parametric statistics. However, this method is nowhere near as quantitative as having a continuous measure of individual bubble occurrence.

A number of studies have examined the use of Doppler data for the prediction and assessment of DCS. However, no simple correlation between bubble grade and symptoms has been found. Variation has been observed from subject to subject after the same pressure profile and some people may exhibit high bubble grades and yet show no symptoms of DCS. In general bubble grade is a poor predictor of symptoms, although a high bubble grade does indicate a greater probability of symptoms, and there is no substantial evidence of DCS symptoms presenting without some bubbles being detectable. For example, Conkin *et al.* (1996) found in aviation studies that "it is likely, but not certain, that an individual will report a [DCS] symptom if bubbles are detected early in the altitude exposure…". They later found that "the absence of bubbles is highly correlated with the absence of a DCS symptom", but presence of bubbles could not be used to predict that symptoms would occur. This supports the conclusion of Kumar *et al.* (1997) that "the Doppler test was of greater utility in excluding DCS than confirming its presence".

A difficulty with Doppler measurement is that it only detects moving bubbles, which means that stationary bubbles go undetected. Although scanning systems can identify stationary emboli they only provide information on a small proportion of the body. It is not clear whether DCS symptoms

arise from emboli that are blood borne, stationary or both. It has been suggested, for example, that joint pains are consistent with the growth of bubbles in the joints, although there has been the suggestion that growth of bubbles in bone marrow may be the cause, Walder (1991). It has been established that the lung is a good filter of gas emboli as long as it does not become overloaded, Butler *et al.* (1979). Consequently, it has been suggested that bubbles are actually a good method via which gas can be expelled from the body, Lightfoot *et al.* (1978). However, the calculations of Daniels *et al.* (1980) would tend to refute this. Generally, high bubble grades are regarded as a negative sign for any decompression profile, and it is presumed that, over a wide range of subjects, the profile that produces lower bubble grades is safer.

Widespread use has been made of Doppler bubble grades to evaluate dive and decompression procedures known, as 'dive tables', Nishi *et al.* (2003). Bubble grades offer an alternative criterion for testing decompression schedules than occurrence of DCS, if not for the simple reason that it is more ethically sound. For example recent work by Divers Alert Network (DAN) Europe as part of their Diving Safety laboratory (DSL) has been to look at the addition of 'deep-stops', i.e. decompression stops undertaken at depths below those commonly employed by recreational diving agencies, using Doppler ultrasound on recreational divers in the field, Marroni *et al.* (2004). Bubble detection has also allowed studies to be undertaken into the effect of exercise, age, weight and body fat percentage on DCS. For example, Jankowski *et al.* (1997) found that exercise during the decompression phase of a dive reduced the amount of Doppler-detectable bubble after diving, using the KISS score to analyse the data. Wisløff and colleagues have found that rats who undergo a bout of exercise 20 hours before a 'dive' in a hyperbaric chamber exhibit fewer bubbles when detected using an imaging system, Wisløff *et al.* (2001), Wisløff *et al.* (2003), Wisløff *et al.* (2004). However, exercise earlier or later than 20 hours before the dive does not have the same effect. Further trials have suggested that the results may be applicable to humans, Dujić *et al.* (2004). There is also the suggestion that the temperature of the diver during the dive and also during decompression can make a significant difference to the incidence of bubbles, Marroni *et al.* (2001), Ruterbusch *et al.* (2004).

2.2.5 Bubble detection conclusions

Detection of gaseous emboli using ultrasound has been an area of active research for over 30 years. The automated detection of occasional large post-operative emboli is now feasible and the performance of such systems is approaching that of the experts. However, these techniques are of only limited applicability to the study of DCS. Imaging ultrasound has enabled the study of decompression-induced emboli in various parts of the body and the creation of an automated system for bubble counting. However, imaging ultrasound is still impractical for anything besides laboratory studies. Although bubbles may only represent part of the liberated gas that accumulates during decompression, they are recognised as an important feature of DCS study. Consequently Doppler ultrasound is widely used to study DCS and evaluate diving safety. However, the techniques for quantification of bubble rely on grading schemes operated by human observers, which is time consuming and has been shown to be subjective. Progress toward automated Doppler grading has been made, but no satisfactory solution has yet been produced. Despite this, recent advances in post-operative emboli detection and in signal processing techniques, together with the "high computing power available now at relatively low cost, [mean that] fully automatic bubble detection systems may become more practical", Nishi *et al.* (2003).

2.3   Bubble modelling

One of the major limitations of the bubble measurement methods outlined in the previous section is the restricted information that they can provide. Bubbles can only be measured at a limited number of body sites and typically at only a few sample occasions post-decompression. At best, therefore, both imaging and Doppler methods can only provide an estimate of the bubble production in one part of the body. However, no clear, simple correlation has been found between such measurements and the occurrence of DCS symptoms. It is not even clear how measurements relate to the actual rate and quantity of bubbles produced in the whole body. For example, precordial assessments of bubbles do not take into account those vascular bubbles which remain at fixed sites in the vasculature. There is clearly a need for a comprehensive theoretical understanding of bubble formation in various regions of the body. Potentially the mathematical models arising from theory can then be used as a tool for interpreting bubble measurements. For the interpretation of Doppler it is clearly important to be able to describe the formation of bubbles in the blood, although it will

also be necessary to understand how these bubbles relate to those forming fixed within the body tissues. In this section the literature relating to the theory of bubble growth in the body will thus be examined.

2.3.1   Gas exchange modelling

Bubbles grow from the gas held in solution in the tissues; hence all models of bubble formation have to include a description of the gas exchange process. The modelling of gas exchange in DCS has a much longer history than that of bubbles, as the concentration of gas in tissue was (and to some extents still is) used to control decompression for the avoidance of DCS. This subject can be traced back to the pioneering work of Boycott *et al.* (1908), although it is not the intention of this section to give a comprehensive history of the subject.

There is a continuous equilibration of gas content between the atmosphere and the body tissues. This occurs firstly through gas exchange between the blood and the atmosphere in the lungs, and then gas exchange between the blood and the tissues. The kinetics of this gas exchange process determines how quickly the gas concentration within each tissue responds to perturbations to this equilibrium, for example due to an atmospheric pressure change. Under decompression the kinetics will thus determine the degree and duration of the super-saturation found in the tissues.

Typically it is assumed that there is almost perfect equilibrium between the partial pressure of gases in the atmosphere and the gas concentration of those gases in pulmonary, and hence arterial, blood. This should be a reasonable assumption given that the gases are sparingly soluble in the blood and that there is a long exposure time for the pulmonary blood to the atmosphere, Hills (1977). Small discrepancies between alveolar and arterial gas pressure do occur, Tikuisis *et al.* (2003), although these are normally ignored in DCS models.

The most general expression for the rate of change of gas concentration at any point in a tissue for a particular gas is given by the combined Fick-Fourier diffusion rate equation Wienke (1989), Tikuisis *et al.* (2003):

$$\frac{\partial c_t}{\partial t} = \nabla \left(D \cdot \nabla c_t \right) + \dot{Q} \left(c_a - c_v \right) - Z_{met} - Z_b \,, \tag{2.1}$$

where the first term on the right refers to the diffusion of the gas throughout the tissue, the second term is the result of blood perfusion and $\dot{Q}$ is the blood perfusion rate, V_t the tissue volume, c_t, c_a and c_v the tissue, arterial blood and venous blood concentrations of the gas respectively and Z_{met} and Z_b are the rates of consumption of the gas by metabolism and bubble growth.

2.3.1.1 Henry's law

The major diving gases, i.e. nitrogen and helium, are not metabolised by the body, hence for these the Z_{met} term in equation (2.1) disappears. Additionally these gases do not bind to sites in the body or combine chemically with any species to any great extent, and thus are considered 'inert'. The concentration of these gases in solution can be written in terms of their gas tension according to Henry's law, which can be expressed as:

$$c_x = \frac{L_x}{\Re T} p_x,$$ (2.2)

where $\Re$ is the universal gas constant, T the temperature, c_x is the concentration ($\mathrm{mol\ m^{-3}}$) and p_x ($\mathrm{Nm^{-2}}$) is the gas tension of an 'inert' gas in the medium x, which has an Ostwald co-efficient of solubility L_x, which is defined as the "gas volume, measured at ambient temperature and at 1 atm partial pressure, which dissolves in a unit volume of fluid", Lango *et al.* (1996). Henry's law is useful because it permits dissolved gas concentrations to be described in terms of gas tensions, which are the equivalent in a liquid to the concept of a partial pressure in a gas mixture. Hence for equilibrium between a tissue and the atmosphere the partial pressures of gases in the atmosphere should equal the gas tensions in the tissue.

2.3.1.2 Perfusion-limited model

It is usual in decompression theory to treat the tissue as well stirred and thus to ignore diffusion, so that the kinetics of the tissue are assumed to be dominated by perfusion. Hence for an 'inert' gas, incorporating Henry's law, equation (2.1) becomes:

$$\frac{\mathrm{d}p_t}{\mathrm{d}t} = \frac{\dot{Q}L_b}{L_t}\left(p_a - p_v\right) - Z_b,$$ (2.3)

where p_t is the gas tension and L_t and L_b are the coefficients of solubility in the tissue and blood respectively. If there is no diffusion, and hence no concentration gradients, then the tissue gas

tension must equal the venous blood gas tension, $p_t = p_v$. Hence, neglecting loss of gas into any growing bubbles, equation (2.3) becomes:
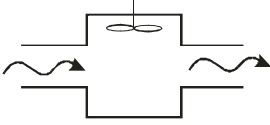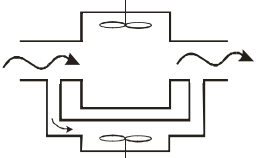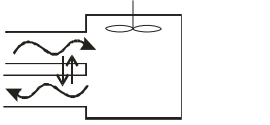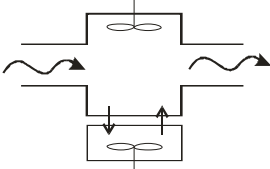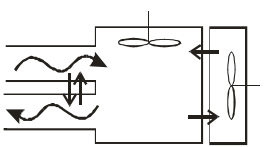
$$\frac{\mathrm{d}p_t}{\mathrm{d}t} = \frac{p_a - p_t}{\tau},$$ (2.4)

where τ is the gas exchange time-constant:
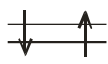
$$\tau = \frac{L_t}{\dot{Q}L_b},$$ (2.5)

more often given as the corresponding half-time value: $t_{1/2} = \tau \ln 2$. The perfusion-limited model can be represented graphically as in Table 2-8a. Tissues are often described as 'fast' or 'slow' based on their half-time value. In general, fast tissues have high blood perfusion and are primarily aqueous in their content, giving them a relatively low solubility. A slow tissue tends to have higher fat levels, as fat has a much higher solubility.

Table 2-8: Common tissue gas-exchange models after Doolette *et al.* (2005a), 2005b).

	Gas exchange model	Graphical representation
a)	Perfusion-limited	
b)	Perfusion-limited: two parallel compartments	
c)	Perfusion-limited counter-current diffusion	
d)	Perfusion-diffusion	
e)	Perfusion-diffusion counter-current diffusion	

Key to graphical representation

Well stirred compartment	Gas transfer by perfusion (blood flow)	Gas transfer by diffusion

Gas exchange in the whole body is typically treated as a collection of parallel compartments, a strategy pioneered by Boycott *et al.* (1908). Often these compartments are not identified with specific tissues, but may represent general groupings of tissues (or parts of tissues) with similar gas kinetics: compartments. Parameter values for the compartments are chosen to cover a reasonable range; for example Bühlmann (1984) used 16 compartments with half-times ranging from 2.65 to 635 minutes for nitrogen in man. Generally the 'fast' compartments are associated with the Central Nervous System, skin and muscles, whereas 'slow' compartments tend to be associated with the joints or bones, Bühlmann (1984).

2.3.1.3   Other gas exchange models

The perfusion-limited model of gas exchange of equation (2.4) leads to a single-exponential response of a tissue (or compartment) to a step change in breathing gas composition. However, this has not been found to be a perfect fit to experimental results, Homer *et al.* (1990). One possible explanation is the presence in the tissue of regions of high and low blood flow, which could be modelled with a mixture of exponential models in parallel, as illustrated in Table 2-8b. Alternatively the complexity of gas exchange may be explained by counter-current blood flow, Homer *et al.* (1990). Counter-current flow in the body results in the 'direct' transfer of gas, in solution, between the arterial and venous blood before the blood passes through the tissue region. This process was included in the bubble evolution model of Himm *et al.* (1999). A more complete perfusion-limited counter-current model, where the tissue itself is described by the standard perfusion-limited equation, but counter-current gas exchange is also included, was given by Doolette *et al.* (2005a) and is illustrated graphically in Table 2-8c.

Diffusion of gas from the blood vessel into the tissues may be important in the gas exchange process, especially in a poorly perfused tissue or where the inter-capillary distances are large, Tikuisis *et al.* (2003). It is possible to derive entirely diffusion-limited gas exchange models, akin to the perfusion-limited models, where the perfusion term in the Fick-Fourier equation is neglected. The diffusion equation may then be solved with a planar geometry or a cylindrical geometry, also known as the Krough geometry, Tikuisis *et al.* (2003), which is intended to represent the tissue surrounding cylindrical blood vessels. It is more common, if diffusion is considered important, to combine both perfusion and diffusion. For example the Kidd-Stubbs model, Tikuisis *et al.* (2003),

treats a tissue as a series arrangement of four compartments. However, a full model that accounts for perfusion of the tissue and diffusion of gas through the tissue is infeasible given the complex geometry of vessels in a typical tissue. A simple combined diffusion-perfusion model is a well-perfused compartment connected, via diffusion, to a second compartment, as illustrated in Table 2-8d, Doolette *et al.* (2005a). It is possible to create more complex models, for example combining a perfusion-diffusion model with a counter-current exchange process, Table 2-8e, although clearly the more complex the model the more physiological parameters are needed to describe it.

2.3.1.4 Experimental gas kinetics

Experimental results for the gas exchange kinetics for body tissues with gases that are important in DCS research, i.e. nitrogen and helium, appear to be scarce. This is presumably because of the great difficulty of performing such experiments. Doolette *et al.* (2005a) examined the helium kinetics for sheep cerebral tissue, and calculated the fit of the experimental results to a number of common models, including those shown in Table 2-8. For helium the results favoured the full perfusion-diffusion counter-current model, although not significantly more so than any other model besides the simple perfusion-limited model. The single exponential of the perfusion-limited model was found to over-predict the exchange rates for a state of low blood flow, which is consistent with the conclusions of Homer *et al.* (1990). In skeletal muscle in sheep, Doolette *et al.* (2005a) also found that a simple perfusion-limited model gave the poorest fit and that all the other models in Table 2-8 provided a better, but similar, fit. It was argued, based on the comparison of the parameter estimates to the physiology, that a perfusion-limited counter-current model is most realistic. Similar conclusions have been reported for nitrous oxide, Doolette *et al.* (1998), in the brain and nitrogen in the skeletal muscle, Doolette *et al.* (2005b).

2.3.1.5 Metabolic gases

The kinetics of the metabolic gases, oxygen and carbon dioxide, are more complex than that of the inert gases. Firstly the solubility in blood no longer follows the linear relationship of Henry's law, which in the case of oxygen is due to the binding of oxygen molecules to haemoglobin, making oxygen far more soluble in blood than would be suggested by its solubility in plasma alone. Additionally, these gases participate in metabolism in the tissues and hence the Z_{met} term in equation (2.3) has to be specified. Although it is possible to describe mathematically the non-linear

solubility in blood and contribution due to metabolism of the metabolic gases, Burkard *et al.* (1994), Himm *et al.* (1999), Tikuisis *et al.* (2003), this is often unnecessary for the physiological modelling of decompression. Instead, the presence of the metabolic gases is typically considered as a fixed gas tension in the tissue. Under aerobic metabolism oxygen is converted practically mole-for-mole into carbon dioxide and carbon dioxide is more soluble, thus the total contribution to gas tension in the tissue is smaller than in the atmosphere. This leads to the concept of the 'oxygen window', Benkhe (1951), Van Liew *et al.* (1993b), Tikuisis *et al.* (2003), where a tissue can experience a small decompression without super-saturation occurring and hence without the risk of bubble formation, because the tissue is inherently under-saturated with respect to the atmosphere. Although the metabolic gases in tissue are often taken to be a fixed component, in practice the value will vary both with the applied atmospheric pressure and with breathing gas content.

2.3.1.6 Tissue model conclusions

The majority of decompression models have taken the perfusion-limited approach, using multiple compartments to describe gas exchange in the whole body. Generally in decompression models for bubble formation (discussed below) the perfusion-limited tissue assumption is also taken. The main advantage of this approach is that only a single parameter, the tissue half-time, is required to describe the gas exchange kinetics. This is particularly important given the scarcity of measured parameter values for the diving gases. The experimental evidence suggests that gas-exchange is more complex and that a better fit to real data may be obtained using more complex models. However, comprehensive experimental analysis of this problem has only become available relatively recently in the work of Doolette and colleagues. Despite this it seems likely for the time being that the perfusion-limited model will continue to be used, as there is not enough data to estimate the parameters, for example the counter-current co-efficient, for many tissue types. Similarly, although more complex models exist for the metabolic gases, the simple assumption that they form a fixed component in the tissue is most commonly accepted.

2.3.2   The Laplace equation

The equilibrium of a bubble can be examined by considering the balance of normal stresses across the bubble interface, which is expressed by the Laplace equation[*]:

$$p_i + p_v = p_{amb} + \frac{2\sigma}{R},$$
(2.6)

where the terms on the left-hand side act to cause the bubble to expand and those on the right-hand side act to collapse the bubble. p_i is the pressure of gases in the bubble, p_v is the vapour pressure of the liquid in which the bubble is suspended, p_{amb} is the ambient pressure acting on the bubble through the liquid, σ is the surface tension and R is the radius of curvature of the gas-liquid interface. For decompression bubble modelling bubbles are formed in aqueous tissues, thus the value for p_v is taken to be the vapour pressure of water at 37°C: 6.3 kPa.

For a free spherical bubble the radius of curvature of the interface will always be positive, hence, for a spherical bubble to be stable, the total pressure of gases and vapour in the bubble must be greater than the atmospheric pressure by the pressure contributed by the surface tension, this value getting progressively larger as the size of bubble reduces. Since there is a transfer of gas between the bubble and the surrounding fluid this condition can be achieved in a super-saturated liquid, i.e. where the gas tension in the liquid is greater than that in the atmosphere. This effect accounts for the production of bubbles in carbonated beverages, in the body causing DCS and in flows causing cavitation; in all cases super-saturation is attained due to a reduction in the pressure.

2.3.2.1   The critical radius

The equilibrium solution of the Laplace equation for R is termed the critical radius:

$$R_c = \frac{2\sigma}{(p_i + p_v) - p_{amb}}.$$
(2.7)

It can be shown that this equilibrium is unstable Tikuisis *et al.* (2003); hence all bubbles larger than the critical radius will grow, whilst those smaller will decay. However, equation (2.7) only holds

---

[*] The Laplace equation is the steady state solution of the full Rayleigh-Plesset equation. The time dependent terms are negligible for decompression bubble growth. As shown in in:
Chappell, M. A. and S. J. Payne (2006a). "A Physiological Model of Gas Pockets in Crevices and Their Behavior under Compression." Respiration Physiology & Neurobiology **152**: 100-114.

true if p_i is not a function of R. If, for example, gas transfer between the bubble and the liquid is not permitted, p_i becomes a function of volume following Boyle's law (assuming ideal gas). Under these conditions there may be more than one physically realistic (real and positive) solution to the Laplace equation, of which only one is expected to be a stable equilibrium. If a second solution exists it will be unstable and be at a larger value of radius, thus it would correspond with the critical radius defined above. Bubbles smaller than the critical radius would not collapse entirely but settle to the stable equilibrium.

It should be noted that Atchley *et al.* (1989) considered this case, but defined the critical radius as "the largest possible [stable] radius that a bubble containing *n* moles of gas at a temperature *T* can have at equilibrium", which differs from the definition conventionally adopted in the DCS field. Tikuisis *et al.* (1983b) considered the stability of a bubble in a closed volume of liquid and likewise found that more than one equilibrium radius was possible, again if two states existed one would be stable and one unstable. In reality there will be gas transfer between the liquid and the bubble, and the system containing the bubble will not be closed. Unless the gases involved can be treated as being in continuous equilibrium, i.e. they have an infinite diffusivity, it cannot be assumed that p_i is independent of R and hence that expansion of the gas in the bubble is insignificant. In practice this effect will only become important once the bubble has grown significantly from its initial size. Therefore, the critical radius can be treated as a threshold for the initiation of growth of appropriately sized bubbles, for example once decompression has occurred it can be established whether a bubble of a given size would grow. The growth itself is unlikely to be unstable, as it will be controlled by gas transfer as discussed below.

2.3.2.2   Multiple gases

The Laplace equation can be extended to the case where the bubble contains multiple gases, as would be expected in bubbles that arise from decompression in the body. Typically two 'types' of gas are identified: those with a significantly higher diffusion constant are separated from the 'diffusible gases', because they equilibrate more rapidly between the liquid and the bubble. To a first approximation these can be assumed to equilibrate instantaneously and are thus considered to be 'infinitely diffusible'. The Laplace equation then becomes, Srinivasan *et al.* (1999):

$$\sum_{m=1}^{M} p_{i,m} + \sum_{n=M+1}^{N} p_{i,n} + p_v = p_{amb} + \frac{2\sigma}{R}, \qquad (2.8)$$

where there are M diffusible gases, $p_{i,m}$ and N-M infinitely diffusible gases, $p_{i,n}$. For decompression modelling it is the metabolic gases which are treated as infinitely diffusible i.e. $p_{i,n} = p_{i,O_2}$ or p_{i,CO_2}. Thus the metabolic gases are often treated as contributing a fixed partial pressure, in the same manner to their contribution to the tissue gas tension, outlined in Section 2.3.1.5. Table 2-9 gives some values from the decompression modelling literature for the values used for the metabolic gases. There is a general agreement for a value of approximately 17 kPa for the contribution of all the 'infinitely diffusible' gases and water vapour.

Table 2-9: Typical values for the fixed component used to model the contribution of the metabolic gases in body tissues.

Source	p_{O_2} (kPa)	p_{CO_2} (kPa)	$\sum p_{i,n} + p_v$ (kPa)
Gürmen *et al.* (2001)	-	-	17.73
Nikolaev (2000)	-	-	17
Van Liew *et al.* (1993a)	5.3	6.0	17.6
Kislyakov *et al.* (1988)	2.7	6.7	16.3

2.3.3 Nucleation

Nucleation can be defined as the formation of a new phase due to the local aggregation of molecules, for example the formation of a gas phase from the molecules held in solution in a body tissue. It is clear from the Laplace equation that, if diffusion of gas occurs across the bubble surface, spherical bubbles are not expected to remain in a liquid for any great length of time. Hence bubbles growing under decompression either must be formed spontaneously under decompression or have already been present in the liquid, but stabilised by some mechanism which prevented their collapse.

2.3.3.1 Homogeneous nucleation

In principle it is possible for bubbles to be formed spontaneously in the bulk of a liquid under decompression. The formation of a gas-liquid interface homogenously in the liquid requires the cohesive strength of the liquid to be overcome. The energy must be sufficient for a bubble of critical size to be formed, as any smaller bubble would collapse back into solution. Ultimately the probability of homogenous nucleation in liquids at the gas super-saturation typically encountered in

DCS is negligible, Tikuisis *et al.* (2003). It is theoretically possible that homogenous nucleation could be the source of bubble formation in DCS if the surface tensions of physiological fluids are sufficiently low, for example due to the action of surfactants. However, work performed by Hemmingsen (Tikuisis *et al.* (2003)) on the effects of surfactants on bubble nucleation in water suggests that they do not have sufficient time during nucleation to accumulate to an extent that the surface tension would be sufficiently reduced.

Jones *et al.* (1999) designates this type of nucleation as Type I. They also identify a variation on this mode of nucleation called Type II, which is essentially the same mechanism for bubble formation, but where bubble formation is catalysed by the presence of some solid, for example in a cavity where less energy is needed to create the gas-liquid interface. However, Type II nucleation does not require substantially lower super-saturation. There is extensive experimental support for the requirement of very high super-saturations for homogenous nucleation, for example Hemmingsen (1989), Jones *et al.* (1999). In practice the large super-saturations associated with homogenous nucleation are not encountered and hence this mechanism is not associated with the formation of bubbles associated with DCS.

2.3.3.2   *Heterogeneous nucleation*

In general, decompression bubbles are assumed to grow from pre-existing nuclei, which are stabilised against collapse, due to the surface tension forces, by some mechanism. Jones *et al.* (1999) subdivided homogeneous nucleation into two types. Both involve the growth of a pre-existing gas pocket, but in Type III the decompression is insufficient to cause spontaneous growth of the nucleus, for example the radius of curvature of the bubble is less than the critical value, and growth is initiated due to local fluctuations in super-saturation. In Type IV nucleation there is no energy barrier to overcome, as the decompression is sufficient to promote the nucleus to grow. It is most common in DCS modelling to ignore Type III nucleation and only to consider nucleation sites that will be recruited to Type IV nucleation. Heterogeneous nucleation is not strictly nucleation according to the definition given above, as the nucleus already exists, i.e. it might be considered that 'nucleation' has already occurred during the creation of the stable gas pocket. However, as in practice the formation of bubbles from nuclei is referred to as a nucleation event, this more general

definition will be adopted here. Two main mechanisms for the stabilisation of gas nuclei have been proposed.

2.3.3.3 Surface stabilisation

In this mechanism it is presumed that surface-active materials adsorb to the gas-liquid interface and that it is this 'skin' of molecules that permits the bubble to resist a compressoin, Fox *et al.* (1954), Yount (1979). A number of mechanisms have been proposed, differing in the effects of the adsorbed layer on gas permeability and how the mechanical properties of this layer vary with the size of the nucleus. Van Liew and colleagues introduce a further pressure term on the right-hand side of the Laplace equation to describe the effect of mechanical stabilisers, which must take a negative value if it is to prevent the collapsing forces due to applied pressure and surface tension, Van Liew *et al.* (1995), Van Liew *et al.* (1997).

2.3.3.4 Geometric stabilisation

Alternatively it has been proposed that gas nuclei may be stabilised within hydrophobic crevices in the surfaces of materials in contact with the liquid, Harvey *et al.* (1944), Harvey (1951). A crevice nucleus is able to withstand collapse as the radius of curvature of the bubble interface may take a negative value, Figure 2-1, when the centre of this radius lies outside the bubble. Hence the surface tension pressure term in the Laplace equation may take a negative value. Thus a crevice nucleus can resist the application of increased atmospheric pressure (or lowered gas partial pressure) by penetrating deeper within the crevice.
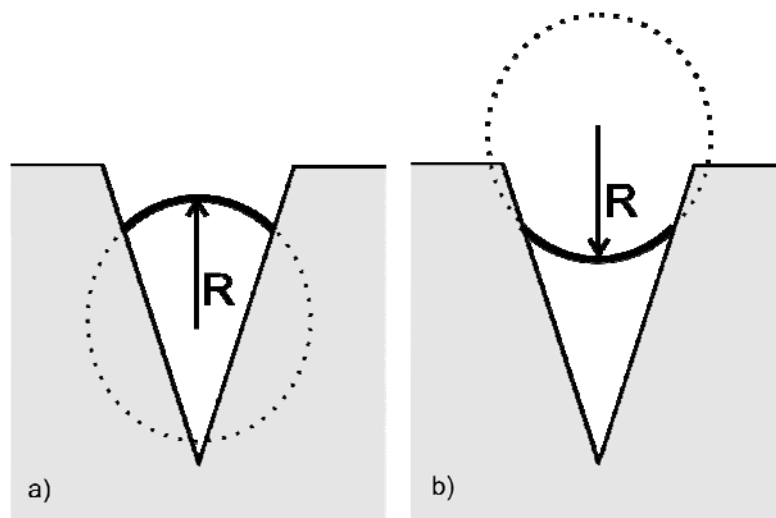
Figure 2-1: A crevice bubble with a) positive or b) negative radius of curvature.

The ability of a crevice nucleus to resist the applied pressure is primarily determined by the largest negative radius of curvature the interface can take. This sets the largest negative value of the pressure term in the Laplace equation. This will be determined by what angle the interface can make with the crevice surface: this angle, measured through the liquid, is called the contact angle, Figure 2-2a. If a drop of a liquid is placed on a surface the angle that the liquid makes with the surface at the three-phase line of contact is the contact angle, Figure 2-2b. It is generally found that the contact angle may take a range of values depending upon whether the line of contact is advancing or receding along the surface, hence, Atchley *et al.* (1989):

$$\alpha_r \leq \alpha \leq \alpha_a . \tag{2.9}$$

In a crevice the limiting values of contact angle establish the limits for the radius of curvature of the interface. Note that the definitions of advancing and receding are counter intuitive as used here, as the collapse of the nucleus is associated with the advance of the liquid, hence it is the advancing contact angle that is associated with the stability of the nucleus under applied compression. Likewise growth of the nucleus, nucleation, is associated with the receding contact angle.
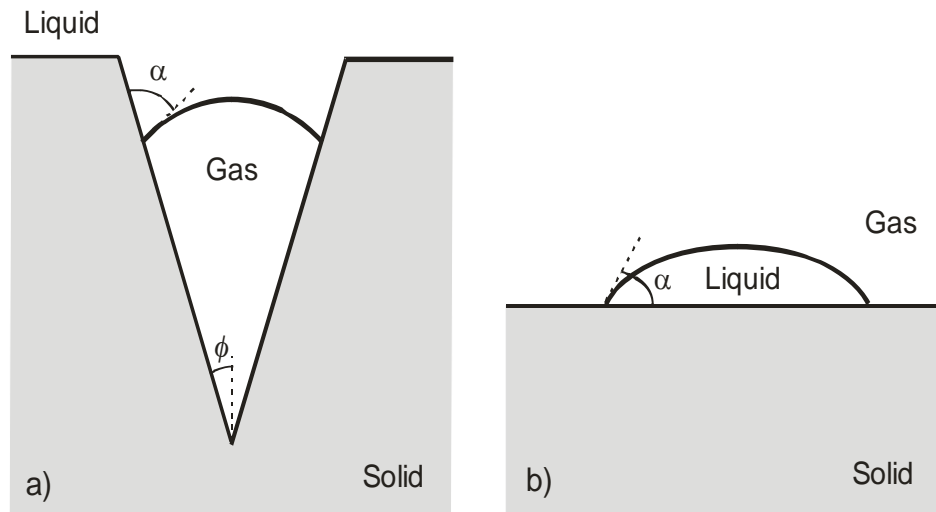
Figure 2-2: The definition of the contact angle, α a) in a crevice nucleus and b) for a drop of liquid on a surface.

The contact angle that water makes with various surfaces allows them to be classified as hydrophilic (low contact angles around 20°) or hydrophobic (contact angles around 80°). For a negative radius of curvature, and hence for the nucleus to resist compression, the advancing contact angle limit must exceed $\pi/2 + \phi$, where ϕ is the crevice half-angle as illustrated in Figure 2-2. For crevice nuclei in the blood the liquid in which the bubbles are formed is primarily aqueous,

hence the crevice surface will need to be hydrophobic, and more strongly so the larger the crevice angle.

2.3.4 Spherical bubble models

It has already been noted that once a bubble is larger than the critical size it will grow and that this process is likely to be governed by gas transfer. It is thus necessary to develop a dynamic model to describe the growth of bubbles in response to decompression. Such models in the literature have focused on the growth of spherical bubbles in tissues; these can be treated in a manner which is a close analogue of the behaviour of a bubble in a liquid. For both cases the basic equations are:

- The Laplace equation (2.6).

- The diffusion equation, which describes the diffusion of the gas through the tissue:

$$\frac{\partial c}{\partial t} = D\nabla^2 c , \qquad (2.10)$$

  where c is the concentration and D the bulk diffusion constant of the gas dissolved in the tissue. This equation neglects convection due to movement of the bubble and sources or sinks of gas within the tissue.

- The Fick equation, which describes the rate of change of the gas content of the bubble due to transfer through the bubble surface:

$$\frac{1}{\Re T}\frac{\mathrm{d}}{\mathrm{d}t}(P_i V_i) = A_i D \left.\frac{\partial c}{\partial r}\right|_{r=r_i} \qquad (2.11)$$

  where A_i is the surface area and V_i the volume of the bubble.

- One further equation is required to describe the variation in the gas content of the tissue as discussed in section 2.3.1.

2.3.4.1 Two-region models

Epstein *et al.* (1950) considered the dissolution of a gas bubble in a liquid of infinite extent. They solved the diffusion equation in polar co-ordinates with spherical symmetry, with a fixed concentration at infinity. In that work, mass flow of gas between bubble and liquid was described for a stationary bubble boundary, this process was modelled by Tao (1978) using the more familiar Fick equation described above.

The application of the Epstein *et al.* type model to bubbles in tissues results in what Srinivasan *et al.* (1999) term a 'two-region' model, where the bubble is one region and the tissue is the other. A good example of this type of model is that proposed by Van Liew *et al.* (1969), where the tissue concentration is not solved explicitly, instead the perfusion term from the Fick-Fourier equation is included in the diffusion equation. This term takes the form of a sink (or source) of gas, which assumes the region around the bubble is uniformly perfused. The equation is solved by employing the quasi-static approximation (discussed further below), neglecting surface tensions and changes in hydrostatic pressure. Subsequently the quasi-static assumption was relaxed by Hlastala *et al.* (1975). The model has subsequently been employed by Van Liew *et al.* (1993a), Burkard *et al.* (1994): in the latter case the model was modified to include multiple diffusing gases. Other examples of the use of this type of model exist: for example Kislyakov *et al.* (1988), although their model neglects the effect of perfusion and they assume instantaneous decompression, Burkard *et al.* (1994). Kunkle *et al.* (1983) elaborate Epstein & Plesset's model to consider the dissolution of bubbles in the treatment of DCS.A major limitation of the two-region model is that it assumes that the tissue has infinite extent and therefore is only applicable where the tissue volume is much larger than the bubble volume.

2.3.4.2 Three-region models

In a 'three-region' model the assumption that the tissue has infinite extent is removed by solving the diffusion equation with the boundary condition that the gas concentration is fixed at a set distance from the bubble interface. Thus the concentration gradient is limited to a specified boundary layer around the bubble. Tikuisis and colleagues have used this approach to model the evolution of a gas bubble in a finite volume of liquid closed to gas transport, Tikuisis (1982), Tikuisis *et al.* (1983b). The original development of a such a model specifically for the growth of decompression bubbles appears to be due to Gernhardt, Tikuisis *et al.* (2003). More recently Srinivasan *et al.* (1999) have developed a three-region model and compared it with its two-region counterparts. In this model the diffusion equation was solved assuming spherical symmetry and the quasi-static approximation (discussed below). The bubble was considered to be covered by an unstirred layer of constant and uniform thickness: the boundary layer. The Fick equation was used to describe the transfer of gas into the bubble and the Laplace equation is used to express p_i in terms of the bubble radius. The resulting equation for bubble radius was:

$$\frac{\mathrm{d}r_i}{\mathrm{d}t} = \frac{L_t D_b \left(\dfrac{1}{h} + \dfrac{1}{r_i} \right) (p_t - p_i) - \dfrac{r_i}{3} \dfrac{\mathrm{d}p_{amb}}{\mathrm{d}t}}{p_{amb} + \dfrac{4\sigma}{3r_i}}, \tag{2.12}$$

where D_b is the diffusion constant for the boundary layer, which may differ from that of the bulk diffusion constant in the tissue, but was taken to be equal to the latter in simulation. This result was very similar to the models derived by Tikuisis *et al.* (1983b) and Gernhart, only deviating in the term for $(p_t - p_i)$, which arose from the assumption that $r_i \gg h$, Tikuisis *et al.* (2003). Srinivasan *et al.* (1999) showed that this model is structurally similar to the two-region model, and for tissues of large volume, with suitable transformation of parameters, the two can be made the same. However, in practice the more physically explicit formation of the 'three-region' model seems preferable.

Srinivasan *et al.* (2000) found that a constant boundary layer thickness would not obey Henry's law and modified the model accordingly. The resulting equation for the rate of change of bubble radius was unaltered, expect that D_b in equation (2.12) was replaced with D_s, the diffusivity at the bubble surface. The value for h was no longer fixed, but found as a solution of an equation which ensured that the boundary layer satisfied Henry's law. Critically, the model required that the bubble surface has its own specified diffusivity and thus practically forms a 'fourth' region to the model. Tikuisis (1982) also solved his three-region model with a variable boundary region thickness although in this case the function that defined the thickness was defined *a priori*.

In a more recent work Srinivasan *et al.* (2002) generalised the 'two-region' model of Van Liew and Hlastala to incorporate a finite tissue volume by incorporating deviations to the uniform sink pressure. This permits the diffusion gradient to be zero at a finite distance from the bubble, hence replicating a finite tissue volume. Thus this model was also constituted by three regions, but the 'boundary layer' is now not defined *a priori*. These variations in the uniform sink pressure of Van Liew and Hlastala represent, in a mathematically tractable form, the effect of uneven perfusion due to the distribution of capillaries in the tissue. The resultant equation for the rate of change of bubble radius is structurally similar to that in their original model but with the $1/h$ term being replaced by

a constant that represents the effects of uneven perfusion. Under this model the 'boundary layer' can now, unlike the earlier derivation, incorporate the effects of perfusion, i.e. capillaries may now be present within this region. However, similarly to the earlier model, there is no way of determining the value of this parameter from the physiology of the problem and it no longer explicitly represents a specific length scale. In their most recent work, Srinivasan *et al.* (2003), this model is used in the interaction between multiple bubbles within one tissue space and compared with the results of similar analysis performed using a two-region model, Van Liew *et al.* (1993a).

2.3.4.3   Equilibrium at the phase boundary

It is typically assumed that there is local equilibrium between gas and liquid at the gas-liquid interface. However, this need not be the case, as strictly there are two transport processes involved Tikuisis (1982), Ward *et al.* (1982b): transport of gas molecules from gaseous phase to surface phase and transport from the surface phase to the liquid phase. It has been found that the latter is the rate-limiting process, Tikuisis (1982), Ward *et al.* (1982a). In work on the stability of gas bubbles in a finite volume of liquid, Tikuisis and colleagues took into account the non-equilibrium at the phase boundary, Tikuisis (1982), Tikuisis *et al.* (1983b), using statistical rate theory, Ward (1977), Ward *et al.* (1982a).

2.3.4.4   Quasi-static approximation

It is common in decompression bubble monitoring to use the quasi-static approximation, Van Liew *et al.* (1969), Himm *et al.* (1999), Srinivasan *et al.* (1999), Srinivasan *et al.* (2000), Srinivasan *et al.* (2002), which assumes that $\partial c/\partial t = 0$ in the diffusion equation. This assumption applies that "the concentration of gas in the liquid at the phase boundary can be assumed constant during small time intervals", Tikuisis (1982). Epstein *et al.* (1950) showed that in their model the quasi-static approximation was reasonable and that it resulted in an acceptably small error. It has subsequently been shown that for bubble dissolution that it is a reasonable assumption expect for the final stage of complete bubble dissolution, Subramanian *et al.* (1980), and was accepted by Tikuisis (1982). In decompression bubble modelling variations in tissue concentration do not occur solely via gas entering and leaving the bubble. Hence the application of the quasi-static approximation also assumes that "changes in tissue gas concentration are … slow compared to the rate of equilibration between bubble and surrounding tissue," Srinivasan *et al.* (2002), which is reasonable as the tissue

time constant is typically much larger than the equivalent time for transfer of gas between bubble and tissue.

2.3.5 Crevice bubble models

Unlike spherical bubbles growing under decompression, there are no dynamic models for the growth of bubbles in crevices in the body, although the nucleation of bubbles has been analysed in terms of stability of the interface under specific conditions. Forest (1982) used a free energy approach to investigate the stability of pre-existing nuclei trapped in solid surface cavities of arbitrary, but axisymmetric, geometry. He presented results specifically for a conical crevice, although for one which had a smooth transition from the inside to the outside of the cavity. In this work it was assumed that the contact angle took a single equilibrium value. The primary conclusion from this work was that bubble growth occurs once the radius of curvature liquid-gas interface reaches a minimum value.

In an attempt to predict the conditions under which bubbles might nucleate in an osteoclast (bone cell) during decompression, Ward *et al.* (1983) analysed a conical crevice. In this case the crevice nucleus was assumed to be contained within a gas-liquid system of constant mass and volume. They considered the stability of the nucleus in the crevice using a similar energy approach to Forest (1982). Four equilibrium radii of curvature were found, two of which were unstable, one metastable and one stable. The smallest radius of curvature was unstable and hence represented a threshold for nucleation in the system: a nucleus greater than this size would grow to either the metastable or the stable equilibrium. They examined the rate at which an equilibrium-sized nucleus would form for homogenous nucleation. In this work this whole process was identified as heterogeneous nucleation, however according to the definitions of Jones *et al.* (1999), this would be classed as a Type II process. Tikuisis *et al.* (1983a) considered a Type II nucleation in crevices in the body under decompression.

Atchley *et al.* (1989) have provided a very extensive analysis of the nucleation of pre-existing gas pockets, i.e. a Type IV process, in conical crevices under decompression based on the Laplace equation assuming that the mass of gas in the bubble remains constant. They identify four phases to the nucleation process:

1. Growth of the nucleus by a reduction in the radius of curvature of the interface, reduction in the contact angle, until the receding contact angle is reached.

2. Once the receding contact angle has been reached, the nucleus may continue to grow by movement of the interface up the walls of the crevice until it reaches the mouth of the crevice.

3. At the mouth of the crevice the contact angle should now be measured with respect to the surface into which the crevice is embedded, thus further growth will proceed by reduction in that contact angle, with a further reduction in the radius of curvature.

4. Once again the third phase can only proceed until the receding contact angle is reached with the external surface, whereupon the nucleus can grow by movement of the line of contact along the external surface, i.e. a lateral expansion of the bubble.

Atchley *et al.* (1989) addressed the problem of nucleation from a crevice gas pocket by defining nucleation as having occurred once the growth of the nucleus has become unstable, i.e. it will continue to grow even if the decompression stops. They determine two thresholds for unstable growth:

1. The first cavitation threshold. This is associated with the unstable growth of the nucleus inside the crevice, due to the pressure reduction required to cause the interface to reach the receding contact angle, unless the interface has yet to reach the critical radius. In the latter case the threshold will be associated with the interface reaching the critical radius during the second phase of growth.

2. The second cavitation threshold. This is similar to the first cavitation threshold, but for the growth of the nucleus outside the crevice. Hence it is associated with reaching the receding contact angle with the external surface, unless the critical radius has not been reached, in which case the threshold will occur during the fourth phase of growth.

Whichever of these two thresholds occurs at a lower pressure is critical for nucleation. Atchley *et al.* (1989) analyse theoretically these thresholds for a variety of crevice half angles. Like Forest (1982) these thresholds are associated with minima in the radius of curvature of the liquid-gas interface. One of the conclusions of this analysis was that "the picture that emerges … is unfortunately quite complex" and so they proceeded with a numerical analysis. The presented results tend to suggest that the nucleation threshold will be associated with the receding contact angle either inside or outside the crevice and not the critical radius. Wide crevices tend to be

associated with nucleation at the 'first cavitation threshold', whereas narrow crevices are associated with the 'second cavitation threshold'. The main limitation of this study for application to DCS nucleation analysis is that it was only performed for nuclei without gas transfer, which would not be expected of nuclei in the body. Hence their results were aimed primarily at acoustic cavitation, where the time for gas transfer is small. Despite this limitation the analysis establishes the basic framework in which both the stability under compression and growth of crevice nuclei under decompression can be analysed in terms of the pressure balance in the Laplace equation.

2.3.6 Nucleation sites in the body

Experimental evidence, for example Vann *et al.* (1980), suggests that there is an ever present population of gas nuclei in the body. In such experiments, an animal is subjected to a brief treatment of very high pressure prior to a more normal compression-decompression profile. Such pre-treatment would be expected to destroy at least some of the pre-existing gas nuclei and is found to reduce DCS incidence in such studies, thus suggesting that nuclei are responsible for decompression bubbles.

In general most tissue bubble decompression models assume a population of spherical gas nuclei are present, although these have not been observed directly in man or any other animal. It has been proposed that crevices may be found in a number of sites in the body, particularly on intercellular components and points of cellular contact, Tikuisis *et al.* (1983a), for example the membrane of mitochondria or osteoclasts found in bone, Ward *et al.* (1983). Alternatively the clefts between cells in the endothelium may also present a geometrically similar nucleation site, Tikuisis *et al.* (1983a), and these may be responsible for the formation of bubbles seen in the blood. Tikuisis (1986) has proposed a modification on the standard conical crevice, making the walls elliptical, Figure 2-3, which it is proposed would make it easier for the interface to emerge outside the crevice and may be more similar to the smooth transitions that might be expected of crevices in the body.

Intra-vascular bubbles are unlikely to be formed within the body of the blood itself. Not only are there no obvious sources for bubble nuclei in the blood, but decompression experiments on blood have shown that it has a significant resistance to bubble formation, like other liquids, Lee *et al.* (1993). Most recently Brubakk (2004) has proposed that caveolae, spherical or flask shaped

invaginations on the surface of endothelial cells, Rothberg *et al.* (1992), may be responsible for the nucleation of bubbles in the vasculature. These sites are likely to have the required properties of hydrophobicity because of their high lipid content. Their shape differs somewhat from that of the standard crevice and they are more closely related to cavities of the 'reservoir type' recognised in boiling studies.
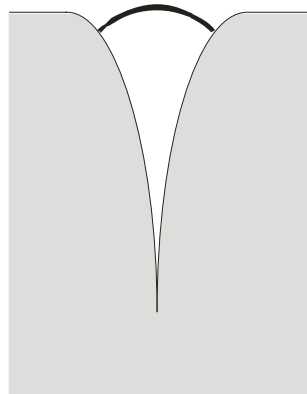
Figure 2-3: Cross section of an elliptical crevice as proposed by Tikuisis (1986).

2.3.7 Bubble theory conclusions

The models for the growth of bubbles in body tissues during decompression, assuming pre-existing spherical bubbles, are fairly advanced. The 'three-region' model has been extensively developed, although some of the physiological parameters values are not well known. However, the source of bubbles in the blood is less well established. It seems probable that intra-vascular bubbles are due to the growth of pre-existing gas nuclei like those in the tissue, but it is more likely in this case that these nuclei are housed in some cavity present on the vessels walls. The conical crevice is generally accepted as a simple representation of a gas nucleation site and has been analysed theoretically to a limited extent. However, most of the analysis of nucleation from crevices has been concerned with the stability of the gas-liquid interface under a range of conditions such as constant mass, Atchley *et al.* (1989), or contained in a larger closed system, Ward *et al.* (1983). Unlike the tissue bubbles there is no equivalent dynamic model for the growth of bubbles. This is a significant gap in the theory of bubble formation and the understanding of the production of bubbles under decompression. Unlike acoustic caviation, decompression bubble growth includes a significant contribution from gas transfer, which is not represented well in stability analysis. Importantly the analysis of bubbles in crevices has always assumed that no gas transfers through the solid wall of

the cavity. However, for blood bubble nuclei these cavities are embedded in the vessel surface, through which gas is continuously diffusing between blood and tissue. Hence gas transfer though the wall is likely to be important.

2.4   Conclusions

Doppler ultrasound is the predominant method for the detection of bubbles in the body, but is significantly limited both by the subjective, semi-quantitative expert labelling method and by the limited correlation between observed bubble grades and symptoms of DCS. However, the method is cheap and easy to operate. An automated bubble detection algorithm would remove the issues of subjectivity and potentially improve upon the accuracy of the expert grades. However, to date no attempt has been sufficiently successful to create a robust and reliable replacement to the expert labelling.

There is convincing evidence for the formation of decompression bubbles from pre-existing gas nuclei. On this basis the growth of tissue bubbles has been well modelled, incorporating the kinetics of gas transfer between the blood and body tissues and from the tissue to the bubbles. However, a similar approach has not been taken to explain the appearance of bubbles in the vasculature under decompression. It is these bubbles that are detected using the Doppler ultrasound technique and hence, if such measurements are to be interpreted for their relevance to DCS, a mathematical description will be required of these bubbles. It seems likely that blood bubbles are formed from nuclei present on the walls of blood vessels. The conical crevice is the generally adopted model for this process: however, unlike the tissue bubbles, a dynamic mathematical model of crevice bubbles under decompression has not been provided. It would appear timely, therefore, to derive such a model based on the existing theory for spherical bubbles. It would then be feasible to join the two models together to examine the interaction of the two forms of bubble and hence to begin to interpret what measurements of blood bubbles can indicate about all the bubbles in the body.

3. An algorithm for the detection of bubbles[*]

3.1 Introduction

In this chapter the automated detection of bubbles in the blood will be addressed. A method will be presented that can extract the characteristic appearances of bubbles from Doppler ultrasound recordings made at the precordial site. Data from the pulmonary artery is addressed specifically because of its importance to the estimation of total bubble production in the body. This site typically gives rise to the greatest quantity of artefact signals, e.g. blood flow and heart value movements, which makes aural grading difficult, giving rise to particular issues of the subjectivity of the manual system and the need for an objective automated technique. However, these factors also increase the complexity of automated bubble detection; hence a novel approach will be taken based on non-stationary signal analysis. The aim of this automated system will be to provide quantitative information about individual bubble occurrence in the data, unlike the semi-quantitative information available from manual grading. The gradings produced by the aural method are the current 'gold standard' and the only information available against which validation

---

[*] The work presented in this chapter (sections 3.1-3.5) has appeared as:
Chappell, M. A. and S. J. Payne (2005). "A Method for the Automated Detection of Venous Gas Bubbles in Humans Using Empirical Mode Decomposition." Annals of Biomedical Engineering **33**: 1362-1372.

can be performed. However, this raises significant issues for the validation of an algorithm that produces more quantitative information than a single grade for each individual signal. This particular issue is addressed in greater depth in section 3.6.

3.2 Doppler ultrasound data

The data used was provided by the Diving Safety Laboratory (DSL) which is part of Divers Alert Network (DAN) Europe. The full database contains recordings of Doppler data collected from recreational SCUBA divers, in the field, post-decompression. Originally the data was collected as part of Project SAFE DIVE involving collection of data from typical recreation diving profiles, Marroni *et al.* (1995). More recently, special projects have been undertaken using Doppler detected bubbles to compare different decompression schemes, for example the introduction of a 'deep-stop', Marroni *et al.* (2004). Doppler ultrasound recordings were collected by specially trained members of the diving group using an Oxford Instruments 3.5 MHz probe with a custom assembled digital recorder sampling at 8 kHz.

Each recording is approximately 70 seconds long, comprising two active sections, each of at least 30 seconds length, separated by a 'silent' section. The first section represents the measurement made during rest, during the 'silent' phase a specified movement is performed and the final section is the post-movement measurement. The data used here were taken first after the completion of a dive to 25 m for 25 minutes. A further dive was then completed after a 3.5 hour surface interval to a depth of 25 m for 20 minutes. Each subject was monitored every 15 minutes after both dives for up to 90 minutes. Since these profiles are designed for use in recreational diving, it is expected that primarily low quantities of bubbles would be observed in these recordings. Variability in the audible amplitude of the signal occurs as a result of movement of the probe, and consequential movement of the collection volume.

It has already been noted that Doppler ultrasound signals from blood vessels also contain components due to the reflection of moving blood cells. The velocity of blood in the major blood vessels varies with time according to the pumping action of the heart. This is clearly seen in signals obtained from the pulmonary artery, at the exit to the heart. Consequently the Doppler audio signal exhibits cyclic features associated with the heartbeat: the main feature being a high-energy pulse

during systole, when the heart empties and a large blood movement occurs. This can be seen in Figure 3-1, which shows the smoothed energy in a section of Doppler audio: the peak systole can be clearly identified. The data obtained from the pulmonary artery also exhibits further cyclic features, for example the smoothed energy plot of Figure 3-1 also shows an increase in energy during diastole. The spectrogram (i.e. the squared magnitude of the Short-Time Fourier Transform) shows that these are primarily due to the appearance of short duration features with a wide frequency spread. These features do not seem to be due to bubbles, because they appear regularly at the same point in each heart cycle and can be seen in data that have been graded as containing no bubbles. It is likely that these features relate to movement of the heart valves, Nishi *et al.* (2003), because of the proximity of the ultrasound collection volume to the heart. Thus the bubble detection algorithm needs to be able to discriminate between these regular events and transient bubbles.
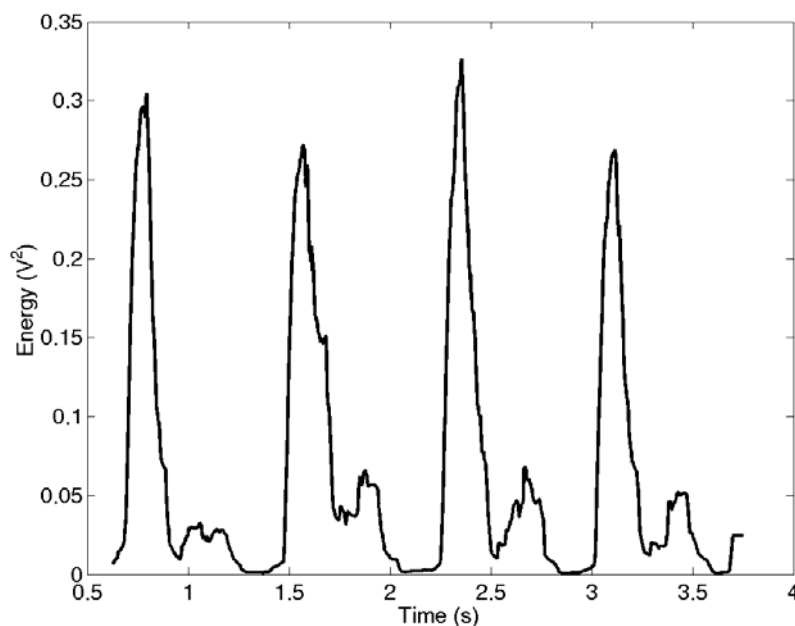
Figure 3-1: Lightly smoothed (moving average with a 100 ms window) energy of a typical Doppler signal from the pulmonary artery. High-energy peaks correspond to the systole phase of the heartbeat.

3.3 Bubble detection algorithm

3.3.1 Empirical Mode Decomposition

The non-stationary nature of the signals means that traditional stationary signal processing techniques are not appropriate. Thus a new method for the analysis of non-stationary signals proposed by Huang *et al.* (1998) was considered. This technique is based on the decomposition of

the signal into a series of non-stationary components, called Intrinsic Mode Functions (IMF), whose shape is not pre-defined: hence the basis set derives purely from the signal. The process is termed Empirical Mode Decomposition (EMD) and theoretically the components represent the effects of the different physical processes that generate the signal. In principle, therefore, EMD may be able to separate the contributions of bubble movement from other sources of sounds in the signal.

To ensure that an IMF represents a single oscillatory mode of the data the following two conditions need to be satisfied, Huang *et al.* (1998):

1. The number of extrema and number of zero crossings must either be equal or differ by one.

2. At any point the ensemble mean value of the envelope defined by the local maxima and the envelope defined by the local minima is zero.

Ideally the second condition should be that the local mean of the IMF is zero. However, this would involve the definition of a local time scale which is impossible, Huang *et al.* (1998).

EMD was performed on the data here using the Hilbert-Huang Transform Digital Processing Software (HHT-DPS), provided by NASA. Firstly, the extrema of the data are identified and then the envelopes of maxima and minima are created using cubic spline fitting. The ensemble mean of the two envelopes is designated m_1 and the difference between the data, x, and m_1 is the first component h_1:

$$h_1(t) = x(t) - m_1(t). \tag{3.1}$$

Ideally h_1 should be an IMF by the definition given earlier. However, in practice this will not necessarily be the case, Huang *et al.* (1998), Huang *et al.* (2003). Consequently the sifting process described above is repeated: in the second sifting h_1 is treated as the data so that:

$$h_{11}(t) = h_1(t) - m_{11}(t). \tag{3.2}$$

This procedure is repeated k times, until h_{1k} is an IMF:

$$h_{1k}(t) = h_{1(k-1)}(t) - m_{1k}(t), \tag{3.3}$$

which is then designated as $c_1(t)$. If the sifting process was continued ad-infinitum, eventually the component h_{1k} would become a pure frequency modulated signal of constant amplitude and the

physically meaningful amplitude fluctuations would be obliterated, Huang *et al.* (1998). To avoid this, the sifting process is stopped once the number of zero crossings and extrema remains the same for S successive sifting steps. Over sifting can have a detrimental effect on the results and it has been found that a value of $3 < S < 5$ is a successful default stopping criteria, Huang *et al.* (2003). The default value applied by the HHT-DPS is $S = 3$ and this has been used in this study. We have not extensively analysed the effect of this parameter on the algorithm's performance for reasons described below.

c_1 should contain the finest scale, i.e. the shortest periods, in the data and is subtracted from the signal to give a residue, r_1, which contains information about longer period components. It is thus treated as new data and subjected to the same sifting process described above. This procedure is repeated until a predetermined criterion is met: either no more IMF can be extracted because the residue is monotonic, or the residue is so small that it is insignificant. The final result is thus:

$$x(t) = \sum_{i=1}^{n} c_i(t) + r_n(t), \tag{3.4}$$

where the signal has been decomposed into n empirical modes and a residue, which is either a mean trend or constant.

The number of IMF generated varies with the length of signal, since longer signals contain longer time scale components and hence more IMF. These extra components will typically represent slow variations over time in the signal and are likely to be negligible compared to the shorter time scale IMF. For a typical Doppler signal used here with duration of approximately 70 seconds, in the region of 20 IMF are produced. An example of some of the IMF produced from one Doppler signal is given in Figure 3-2.

In theory EMD can separate different physical components. However, in practice the approach doesn't guarantee to extract the information exactly as required. For the Doppler signals used here there is not a perfect separation of blood cell movement and bubble movement sounds into the different IMF. Although this means that bubbles cannot be reliably detected using one IMF alone, a selection procedure can be used to provide a robust detection method. Essentially by focusing on

certain IMF an improved signal-to-noise ratio is achieved over the original signal. Since EMD decomposes the signal into a series of time scale bands it acts like a filter bank. Consequently, characteristics corresponding to blood cell movements will be represented across the spread of IMF in a different manner to those of bubbles. Support for the filter bank interpretation of EMD comes from Wu *et al.* (2004), and Flandrin *et al.* (2004) who have established that for fractional Gaussian noise, EMD can be regarded as a dyadic filter bank resembling those used in wavelet decompositions, Flandrin *et al.* (2004).
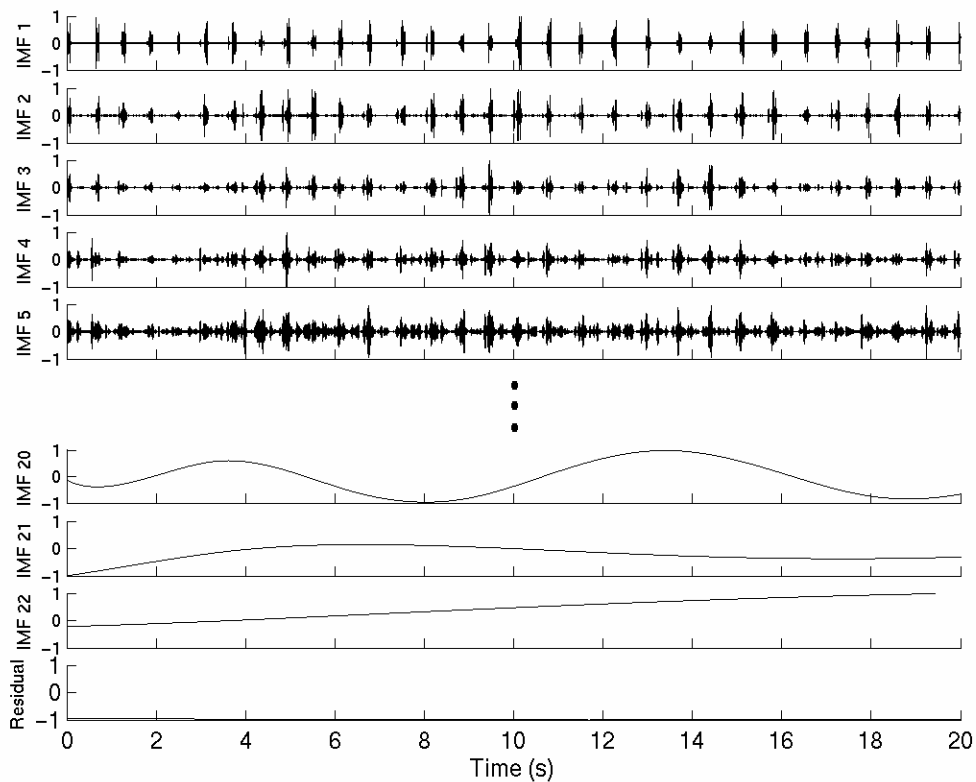
Figure 3-2: A selection of IMF produced from a Doppler audio signal, showing the first 20 seconds (arbitrary units throughout).

3.3.2 Peak detection

The method for detection of bubbles relies upon the determination of individual cycles of the heartbeat; this requires the location of peak systole. Hamilton *et al.* (1986) proposed a robust method for the detection of peaks, primarily to improve the accuracy detection of the QRS complex in ECG signals. Although their signals are derived in an entirely different manner to the signal used here, the method was found to be applicable. Firstly, the signals are band-pass filtered, which for the Doppler signals has already been performed in hardware, and then processed as follows:

- Differentiation, which emphasises the changes from the baseline.

- Squaring, which emphasises higher frequencies into which interesting features such as bubbles are expected and which ensures the signal is positive for the later stages of analysis.

- Time averaging, which gives a measure of how the energy is distributed in the signal. For the Doppler signals a window size of 67.5 ms is chosen: this is done to achieve greater smoothing, allowing the large systole peaks to be detected whilst smoothing out other peaks that are due to bubbles and heart valve motion.

The process applied to a section of a signal is shown in Figure 3-3.
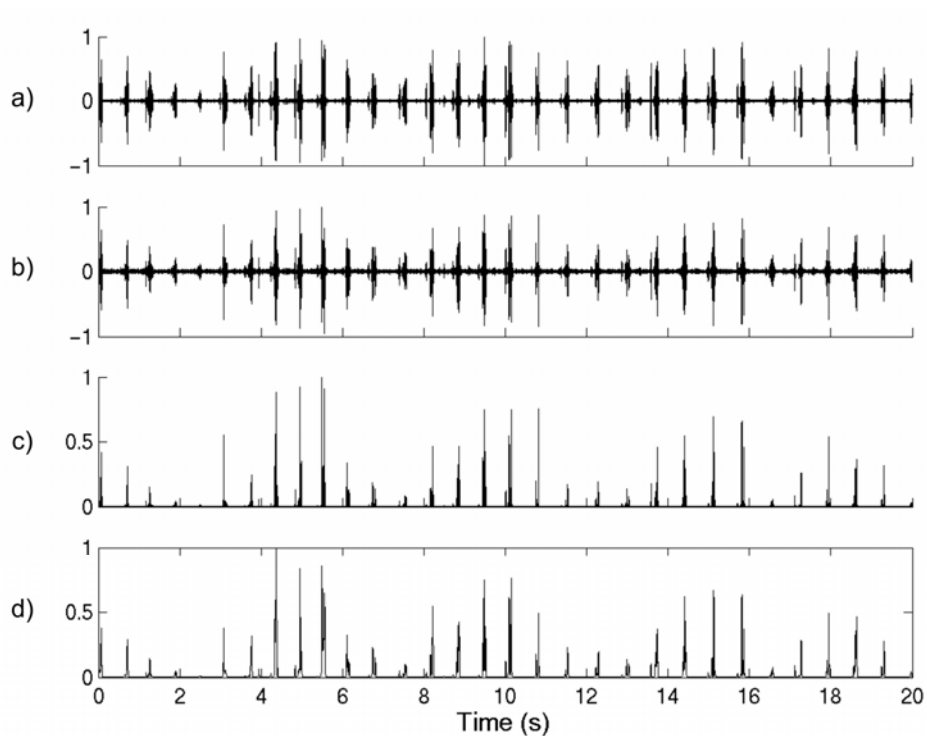
Figure 3-3: Pre-processing applied to a section of a signal (arbitrary units throughout), showing (a) the original signal, (b) after differentiation, (c) followed by squaring, (d) and time averaging.

Peak detection is then performed using a modification of Hamilton & Tompkins original method (based on a modification used by Clifford (2002)): a peak is defined as the maximum in a region that begins where the waveform exceeds twice the moving average and ends where the waveform falls below the moving average. For the moving average a window size of 1.25 seconds is chosen, which, being longer than a single heart cycle, is insensitive to variation of the signal over the heart cycle, but which still permits the variations in signal intensity between individual cycles to be followed. This essentially ensures that each detected peak is separated by a distinct trough, so that local ripples in the signal are excluded. The use of twice the moving average has been empirically determined to improve the detection of systole peaks whilst excluding other repeating features such as heart valve motion.

3.3.3 Detection of heart beats

In principle the above method should pick out the peak systole from each heartbeat reliably. However, in practice the quality of the signal and the occurrence of other repeating features, such as the motion of the heart valves, complicate the problem. The following procedure has thus been developed to detect heartbeats robustly from variable quality Doppler audio signals. After the pre-processing described above, a pseudo heart-rate is generated using the times between each peak and the two peaks following it. This procedure is necessary because in some signals other repeating features, such as heart valve motion, are identified by peak detection. These extra features typically appear approximately mid-way through the period; consequently it is necessary to use the following two peaks if the pseudo heart-rate is to approximate the real heart-rate and not half the correct value. For example if synthetic data is considered with repeating features which appear in half the cycles a histogram for pseudo heart-rate is produced as shown in Figure 3-4a. The histogram has a mode at the true heart rate, and contributions at 50%, 150% and 200% of this value. Figure 3-4b shows the histogram of pseudo heart-rates from a typical signal, which clearly shows the expected features, although there is some spreading due to natural variations in the heart rate. The Estimated Heart Rate (EHR) is calculated as the centre of the modal bin of the histogram of pseudo heart-rate.

The Estimated Heart Period (EHP) is then calculated as the inverse of the EHR. This allows a comparison of the timings of peaks to be made to those expected given the EHR. The determination of which peaks refer to systole requires a starting point of some 'known' heartbeats. Here 'reference' heartbeats are identified: peaks whose neighbours both lie at a time between 70% and 130% of the EHP, i.e. that are physiologically compatible with the heart rate. Subsequently other heartbeats are identified in the gaps between the reference heartbeats. Firstly, the peaks not labelled as reference heart beats are examined to see if their proximity to the reference heartbeats is compatible with the EHP, i.e. whether the peak lies within 25% of the EHP either side of the position where a heartbeat would be expected given the EHP. Secondly, in any gaps in the list of heartbeats greater than 160% of the EHP, a more thorough search is performed using a locally estimated heart period, using the preceding five heartbeats. It is assumed that the heart rate will not vary by more than 20% from beat to beat. Therefore, the local heart period estimate is used to

generate expected timings for heartbeats and the processed signal is examined for the presence of a peak within 20% of the estimated heart period either side of these times, with a signal magnitude at least 10% of the median of the preceding 5 heartbeats. The heart beat detection process applied to a typical signal is shown in Figure 3-5; in this case the heart beat detection is found to be robust even where the signal strength varies widely from beat to beat.
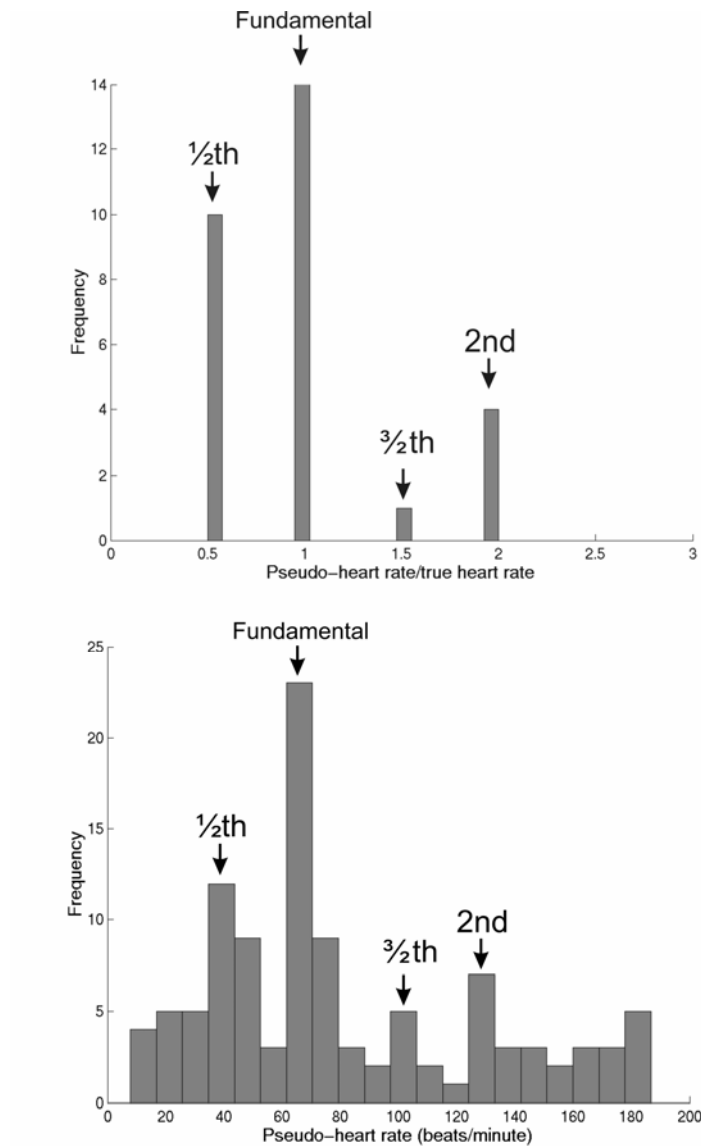
Figure 3-4: a) The histogram of pseudo-heart rate for a theoretical signal, wherein half the heart cycles contain a distinct repeating feature; b) The histogram of pseudo-heart rate for a typical signal.
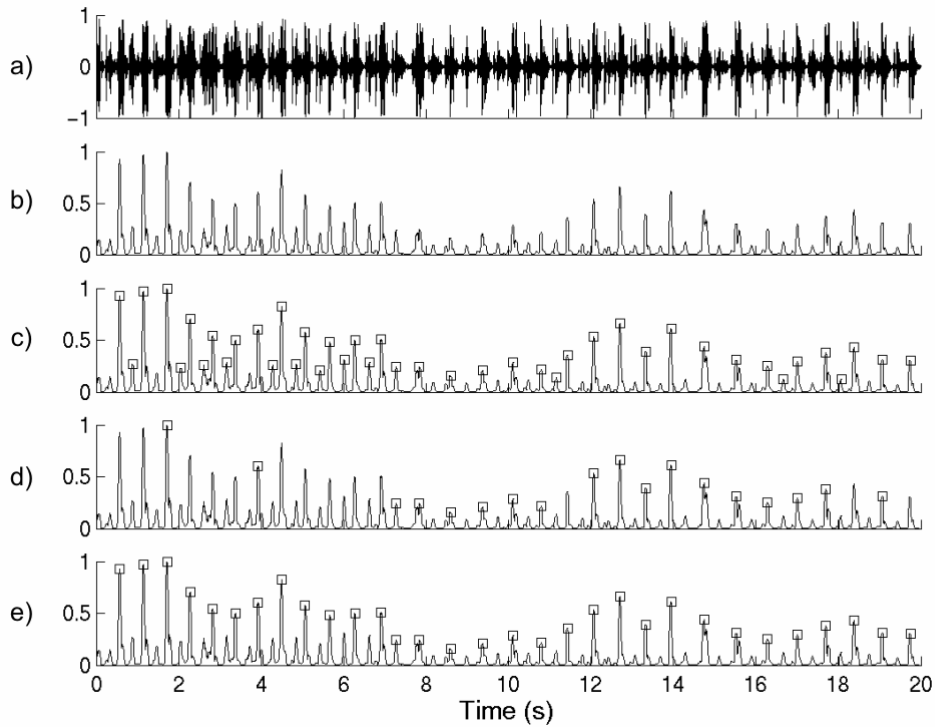
Figure 3-5: Robust heart beat detection routine applied to a 20 second section of a typical signal (arbitrary values throughout), a) original signal, b) pre-processed signal, c) pre-processed signal with peaks detected, d) peaks identified as 'reference peaks', e) peaks identified as referring to peak systole.

3.3.4   Detection of features

The transit time for a bubble through the ultrasound collection volume is of the order of 10 ms, Nishi *et al.* (2003). Since IMF corresponding to time scales longer than this will not provide any useful information about the position of bubbles, they are discarded. This typically leaves 7 IMF which are pre-processed using the method described in Section 3.3.2 with a smaller time-average window size of 12.5 ms; which, being of similar order to the transit time of a bubble, means that smoothing is performed without losing the appearances of individual bubbles. Bubbles are expected to pass through the ultrasound field during the systole phase of the heart cycle which typically lasts 270 ms, Schneck (2000). Therefore, sections of the pre-processed IMF are extracted, $\text{pIMF}_{n,k}$ for the *n*th IMF and *k*th heartbeat, corresponding to 50 ms before and 300 ms after peak systole as illustrated in Figure 3-6.
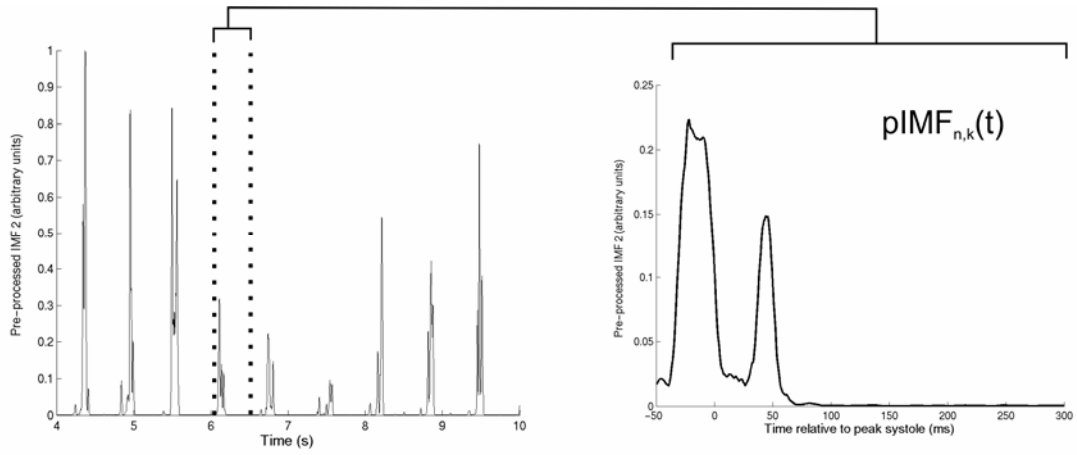
Figure 3-6: Sections of the pre-processed IMF are extracted over the time from 50ms before to 300ms after peak systole. In this case a section of the second IMF of Figure 2 is shown.

In each pIMF sections are generated for every heart beat and then ensemble averaged:

$$\mu_n\left(\tau\right) = \frac{1}{K}\sum_{k=1}^{K}\mathrm{pIMF}_{n,k}\left(\tau\right),\tag{3.5}$$

where -50 ms $< \tau <$ 300 ms and K is the total number of heart cycles found in the signal. Similarly the ensemble standard deviation for each pIMF, $\sigma_n\left(\tau\right)$, is also calculated over the different heart beats at each point in the heart cycle.

Each individual heart cycle section of the pIMF is then compared to the ensemble mean by calculation of the normalised IMF:

$$\mathrm{nIMF}_{n,k} = \frac{\mathrm{pIMF}_{n,k}\left(\tau\right) - \mu_n\left(\tau\right)}{\sigma_n\left(\tau\right)}.\tag{3.6}$$

Each heartbeat is considered in turn by examining the nIMF for that beat. Firstly, search regions are defined within which it is suspected that a feature of interest may lie. These search regions are derived by considering all the IMF and are located wherever at least one of the nIMF exceeds 1.5 standard deviations; this value is chosen empirically and has been selected to be relatively low so that the search regions for a feature will tend to be quite wide, permitting better location of features at a later stage. Within each of these regions a search is performed for the peak magnitude in each of the pIMF in turn, ensuring that a distinct peak is identified, rather than a simple maximum which might occur at one edge of the region.

For each of these locations the values in the corresponding nIMF are extracted, which gives a measure of how novel that peak is, i.e. if nIMF is high at that location, then the peak probably refers to a feature of interest rather than noise. The values are sorted in ascending order, weighted and summed to give a measure of likelihood of a feature being present. Bubbles are expected to appear significantly, i.e. have large nIMF values at the peak in the pIMF, in only two or three IMF. This is consistent with an observation made by Belcher that bubbles have a narrow frequency band Belcher (1980). It is unlikely that a bubble would appear significantly in one IMF alone. Hence the (normalised) weighting is chosen to take the values 0.42, 0.33, 0.25 for the three largest nIMF values in descending order, thereafter the values are ignored. A number of different weighting schemes have been considered but this appears to provide the best sensitivity. Although further validation is clearly required, the difficulties involved in this will be discussed below. If the level of support exceeds a threshold of two then a feature has been found in the search region, a higher threshold being chosen here than is used for the identification of search regions to achieve a better separation of bubbles and other spurious features.

The features detected by this method will primarily be the transient bubble events, since in principle cyclic events, i.e. those corresponding to blood cell and heart valve motion, should be excluded by the ensemble averaging process. However, these events may still be picked out by the above method where the magnitude or position within the cycle deviates significantly from the mean. Occasionally, features are detected that are not clearly related either to a cyclic event or to a bubble. The significant difference here is the lack of total energy in the signal that may be associated with a bubble reflection. Consequently, a final classification stage is used to remove spurious non-bubble features.

3.3.5 Classification of features

Two measures are used to remove features not associated with bubble reflections as illustrated in Figure 3-7. Firstly features appearing in the IMF which have no significant energy contribution in the original signal are discarded. The pre-processed signal is used as an estimate of local energy; it is sectioned into individual heartbeats, as outlined above, and the ensemble average calculated. Values greater than two standard deviations from the mean are excluded from the ensemble, so that transient bubble events are not incorporated in the average. The value of energy for each feature is

then compared to the ensemble average at the corresponding point within the cycle. Although the repeating cyclic features have high energy levels, this process still removes a quantity of these features that are detected by the above method, where they have produced large deviations within the IMF but do not appear as significant when they are examined using the estimate of local energy content of the original signal.

Feature

Does the feature have greater than average energy in the original signal — No → Discard

Yes

Does the feature lie where repeating non-bubble features are expected — Yes → Discard

No
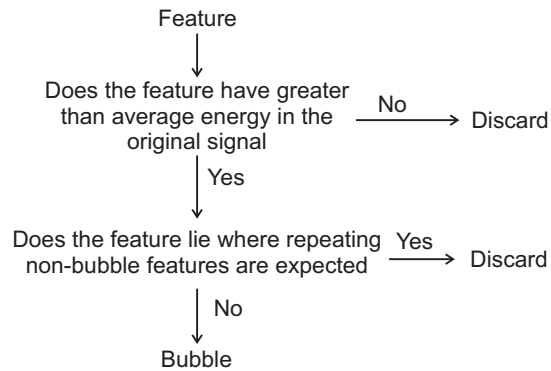
Bubble

Figure 3-7: Classification of features.

Secondly it is necessary to remove spurious peaks that arise from the repeating non-bubble events e.g. peak systole, heart valve motion. Periods within the heart cycle section are identified where high-energy cyclic events regularly occur: i.e. where the ensemble average of the energy estimate exceeds the mean value taken over the whole cycle. Consequently, any features detected within these regions most likely refer to these cyclic events and not bubbles.

3.4 Results

The current state of the art in bubble detection is aural grading by trained experts. It is not generally possible by this method to identify the occurrences of individual bubbles, unlike the automated method presented here. Instead a number of standard scales exist which assign a grade to the signal. The grade implies that a certain quantity of bubbles is present in the whole signal. However, the correspondence between different grades and bubble quantities is poorly understood and believed to be highly non-linear, Nishi *et al.* (2003). These limitations, coupled with the subjectivity of aural assessment, make the verification of the method presented here against expert labels very complex. In particular it is the lack of bubble occurrence information for each signal that makes the validation of this method very difficult. It is recognised that the empirical nature of a number of parameters in the method will require much wider validation to ensure that the method is generally applicable to Doppler ultrasound data from the precordium and is not limited to the database which

has been examined here. It will be shown in section 3.6 that to validate this (or any other) method fully, of order 1000 signals with expert labels would need to be considered. Given the large scale of such analysis this is not pursued further here. Instead some preliminary results will be presented based on a method of visual inspection of the performance of the algorithm.

Some information about the occurrence of bubbles in Doppler ultrasound signals can be obtained from inspection of the spectrogram and it has been used in this study to provide some form of verification of the features extracted by this method. From the spectrogram it is possible to identify the repeating features associated with the heart cycle, such as the peak systole and Doppler shifts arising from the movement of heart valves. If the algorithm identifies one of these features as a bubble then it is presumed to have made an incorrect classification. Additionally, it is possible to identify features in the spectrogram that have short time duration and a wide frequency band and that do not appear to correspond with the repeating features of the heart cycle. These have the correct characteristics to be bubbles and hence if identified by the algorithm as bubbles it is presumed a correct classification has been made. Finally where the algorithm identifies a bubble occurrence which corresponds with no obvious feature in the time-frequency plot then this is assumed to be a misclassification.

Two signals are considered here to demonstrate the typical performance of the new method. The spectrogram will be used to illustrate the time-frequency characteristics of the features detected. In all cases the spectrogram is generated with a Hanning window of length 8 ms, each window overlapping the previous by 4 ms. The first signal to be considered has been expertly graded as containing "1-2 sporadic bubble signals over the 1 minute recording", Marroni *et al.* (2004). A section of the signal's spectrogram, with heartbeats and bubbles as identified by the algorithm marked, is shown in Figure 3-8. The algorithm identifies 20 features as bubbles, of which the majority are found by inspection of the spectrogram (not illustrated) to be repeating features associated with the systole. The section of the spectrogram in Figure 3-8 shows the likely location of a bubble, which has been detected by the algorithm. Since this signal has a low strength, the bubble that has been detected appears as only a very small feature and cannot be seen without close inspection. The main limitation for signals of very poor strength is accurate heart beat detection, as the peak energy during systole is not distinct from other events such as heart valve motion.

Figure 3-8: The spectrogram of a section of a signal which has been graded 0.5 on the ESS (arbitrary units). Heart beats (-), identified at peak systole, and the location of detected bubbles (- -) are shown.

The second example has been graded as containing "continuous bubble signals over the 1 minute recording, with numerous bubble showers", Marroni *et al.* (2004). Over 95% of the heartbeats are detected despite the high number of bubbles and 64 bubble features found. A section of the signal's spectrogram is shown in Figure 3-9. In the first heart cycle shown, two bubbles have been identified which appear to be correct, as the features correspond to transient short-duration wide-frequency events. In the second heart cycle a further two bubbles are detected, although it is possible that the first is associated with the peak energy of the systole phase. In the fourth cycle a single bubble is identified, although it is possible that it should have also identified one before this.

Qualitative analysis of a larger number of signals shows that the algorithm appears to exhibit good sensitivity: visual examination of the spectrogram identifies few bubble candidates that are not identified as features by the bubble detector. However, the specificity of the method is not yet as high as would be desired: typically the algorithm detects more bubbles than are expected according to the expert grading.
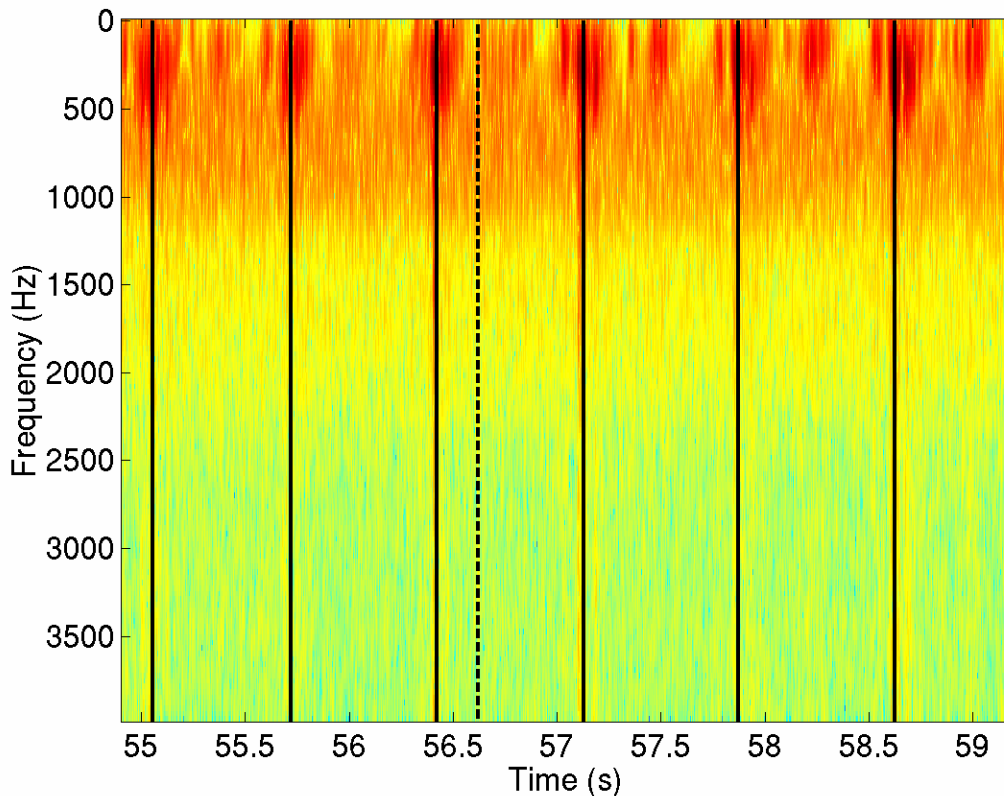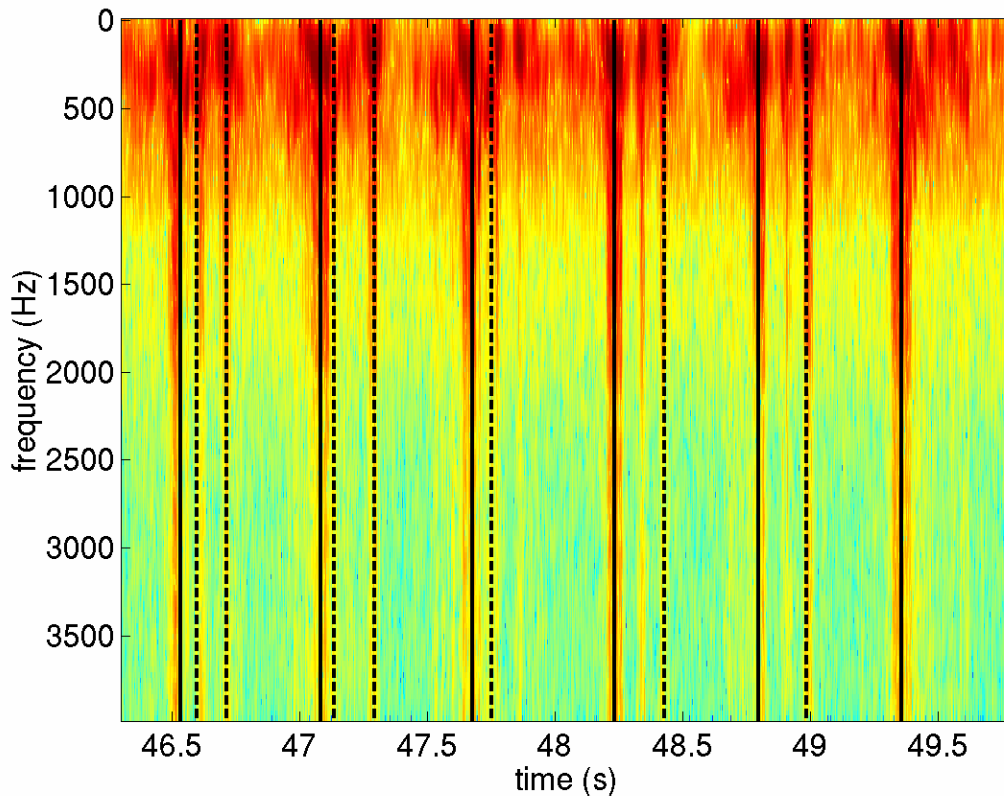
Figure 3-9: The spectrogram of a section of a signal which has been graded 3.5 on the ESS (arbitrary units). Heart beats (-), identified at peak systole, and the location of detected bubbles (- -) are shown.

Two areas have been identified in which errors arise in bubble detection:

- Noise sources: There are specific high energy wide frequency noise features observed in some signals, possibly due to probe movement or the connection between probe and recording device. These are erroneously classified as bubbles by the algorithm and may also confuse heart beat detection.

- Erroneous detection of repeating features as bubbles: Although the algorithm reduces this source of error, some incorrect classifications are still made.

The nature of the algorithm, employing an ensemble average, makes it ill suited to very high bubble grades. If too many bubbles are present then they may be incorrectly classed as repeating features, although this has not been found to have a significant impact of the performance with the signals available for this study. High grades are not observed regularly in practice and can easily be detected aurally.

3.5   Discussion

This method potentially offers a significant improvement over the current aural assessment technique for the detection of bubbles associated with DCS by removing the subjectivity that arises through human evaluation and by provision of bubble occurrences rather than grading on a semi-quantitative scale. As has already been noted, the link between the standard scales and bubble number is not well understood. This makes it difficult directly to compare this method to the manual approach. However, the subjectivity of the manual technique is widely recognised and lengthy procedures are required to account for it. The most recent attempt at bubble detection by Sutherland was, in principle, able to avoid subjectivity, but was still restricted to assessment on the standard scales. Hence, again, it is difficult to compare this to the method presented here, especially in the absence of performance data for Sutherland's system, although it appears that Sutherland's method was unable to supplant the performance of the manual method, Nishi *et al.* (2003).

The method presented here is an off-line algorithm. Aural assessment of signals can be performed in real time, although often evaluation is performed offline to blind the expert to the decompression profile under test and to permit independent evaluation. However, the algorithm could be modified for online application, allowing for continuous monitoring. An online system would require an initial training period to generate an appropriate mean heart cycle. The offline system is able to operate with sections of signal of 1-minute duration as used in this study and it has been found that it can operate with even shorter sections, which suggest the necessary training time would be less than 1 minute.

At present the algorithm is not yet a full bubble detection solution. However, in its current form it could already be used as a first step for an expert labeller, in which the algorithm identifies regions of interest or particular recordings which the expert can then examine. The detection of bubbles is a very difficult problem due to the nature and quality of the available data, and the algorithm presented here gives a first attempt, which will require further refinement.

3.6   Validation considerations[†]

As has already been noted the validation of the automated bubble detection algorithm is particularly difficult because the expert labels are based not sufficiently quantitative. These only provide an aggregate grade for the whole recording, unlike the algorithm presented here which provides individual bubble occurrences. Since the expert label is essentially only a measure of the average number of bubbles per heartbeat, it is impossible to tell from a single recording whether the algorithm correctly identifies all bubbles and artefacts or fractions of both such that the total number of events identified as bubbles is correct. Both would replicate the expert score, but only the former would actually correctly identify the bubbles. In theory it should be possible to use multiple recordings, with varying numbers of bubbles and artefacts, to learn whether the algorithm is correctly identifying all the bubbles or mislabelling some artefacts as bubbles. In principle the extra information provided by the multiple recordings should enable more information about the likelihood of correct classification of bubbles to be learnt. This section deals with a statistical analysis of this validation problem by considering simulated data and assessing whether this data can be used to estimate the classification probabilities.

Artificial data is generated assuming that there are three types of event that can occur in a recording: heartbeats (HB), bubbles (B), artefacts (A). The ratio of B to HB determines the bubble grade, G, and hence is assumed to vary over a range $0 < \Pr(B)/\Pr(HB) < G$. G does not correspond to any particular grading scheme, but is a representative number to enable labelling of the artificial recordings to be performed. Artefacts are typically associated with blood movement and heartbeats hence their probability is assumed to be related to that of the HB by a factor k:

$$\Pr(A) = k \Pr(HB). \tag{3.7}$$

Hence the probability of HB lies in the range:

$$\frac{1}{1+G+k} < \Pr(HB) < \frac{1}{1+k}, \tag{3.8}$$

and the probability of a bubble can then be determined as:

[†] This section summarises work that has appeared as:
Payne, S. J. and M. A. Chappell (2005a). "Automated Determination of Bubble Grades from Doppler Ultrasound Recordings." Aviation Space and Environmental Medicine **76**: 771-777.
Payne, S. J. and M. A. Chappell (2005b). "The Effects of Expert Error on the Accuracy of Automated Bubble Classifiers." International Conference on Diving and Hyperbaric Medicine, Barcelona, EUBS.

$$\Pr(B) = 1 - \Pr(HB) - \Pr(A).$$ (3.9)

Artificial data is generated comprising a sequence of HB, B and A, by sampling a random number in the range 0-1 for each event and assigning it to one of the three events using the relevant probabilities. Each set of artificial data is simply a sequence of events and makes no assumptions about their relative timings. The lack of timings is not important, since the presence of an event is determined by whether it is detected by the algorithm. Whether it is labelled as a bubble or an artefact depends on the labelling probabilities, discussed below. It is assumed here that the sequences contain 60 HB, corresponding to approximately 1 minute of recorded data like those sequences analysed in this chapter. The pseudo-expert label for each event sequence is determined from the fraction of B to HB, rounded up to the nearest integer fraction. For example a sequence containing 3 B and 60 HB gives a score of 0.5 on a half-integer scale, which would correspond with a scheme like the ESS. In comparison the KM scale corresponds to a third-integer grading. Like the standard grading procedures the maximum score is limited to 4, although in practice higher scores are rare. This procedure produces graded artificial data which is biased toward lower values, which is consistent with those observed in diving practice, although the generated artificial data is not specifically designed to represent any particular data set.

The algorithm that labels the traces is based on a matrix of probabilities. Since there are three types of events, and hence three possible labels, there are nine probabilities to be considered, for example the probability that a HB label is assigned to a B is denoted by $\Pr(HBL|B)$, with the L denoting the label. The probability matrix is shown in Table 3-1 and has 6 degrees of freedom. By sampling from a uniform distribution over the range 0 to 1 for every event in the sequence, a label can be assigned to the event, based on the distribution of probabilities and the actual label. Every event sequence is labelled in this way and the predicted bubble grade score calculated. Over a number of event sequences this gives rise to a contingency table, Sawatzky *et al.* (1991), determining the predicted class labels against the actual class labels, an example of which is shown in Table 3-2 for 1000 recordings and a half-integer scale, with perfect HB labelling and some confusion between B and A. Note that the majority of examples lie on the diagonal, i.e. they are correctly labelled.

Table 3-1: Matrix of classification probabilities

		Actual		
		HB	B	A
Label	HB	Pr(HBL|HB)	Pr(HBL|B)	Pr(HBL|A)
	B	Pr(BL|HB)	Pr(BL|B)	Pr(BL|A)
	A	Pr(AL|HB)	Pr(AL|B)	Pr(AL|A)

Table 3-2: Contingency table for 1000 simulated recordings on a half-integer scale with perfect HB labelling and some confusion between B and A.

Actual labels	Predicted labels								
	0	0.5	1	1.5	2	2.5	3	3.5	4
0	462	107							
0.5	1	204	18						
1		11	91	2					
1.5			16	21					
2				20	13				
2.5					2	5			
3						3			
3.5								1	
4									

The key question is whether the matrix of probabilities can be estimated from the contingency table and, if so, how many event sequences are required to determine accurately these probabilities to a given accuracy. The problem is slightly simplified here by assuming that the heartbeat detector is robust. This is a reasonable simplification given the success with heartbeat detection found above; additionally, it is important that the HB detector is highly robust as poor accuracy of the detection of HB is likely to have a significantly deleterious effect on the overall performance. For a robust HB detector, the matrix of probabilities reduces to 2 degrees of freedom, as shown in Table 3-3. For simplicity the probabilities of correctly labelling B and A events are denoted by α and β, respectively. The determination of these two parameters is thus the next step. Initially it is also assumed that the expert labelling is correct for every recording, although this is unlikely to be the case, especially since it has been shown that there are inter-rater differences in bubble grades, Sawatzky *et al.* (1991), which will be examined later.

Table 3-3: Assumed matrix of probabilities.			
	Actual		
	HB	B	A
Label HB	1	0	0
B	0	α	1-α
A	0	1-β	β

A number, *M*, of event sequences are generated, corresponding to the number of available recordings. They are labelled according to the above procedure for chosen baseline values of $\bar{\alpha}$ and $\bar{\beta}$ to yield a contingency table. Values of α and β are then independently sampled and a second contingency table generated. A measure of the error between the two contingency tables is then calculated as the sum of the differences between their elements over all the elements. The optimum values of α and β are then estimated by minimization of the error. Since it is not clear what the underlying functional form of the error is, the method chosen here was to use discrete values of β and to sample over α as this was found to simplify the analysis. Five values of β were chosen, (0, 0.25, 0.5, 0.75, 1) and 100 samples of α taken at each of these five values. Although more samples would give a more accurate underlying fit, this was found to be sufficient for the purposes here. The error was found to fit well the functional form:

$$E = a\mathrm{e}^{-\frac{(\alpha-\hat{\alpha})^2}{2b}} + c, \tag{3.10}$$

with different values of the coefficients, *a*, *b*, *c*, $\hat{\alpha}$ for each value of β. The error function has a minimum at $\alpha = \hat{\alpha}$ with a value of $E_{\min} = a + c$. Since these two parameters are functions of β, the optimal values of α and β can then be calculated by interpolation. The variance of the two parameters is estimated using Bayes' theorem, assuming a flat prior over both parameters, since there is no reason to expect any particular range of values. To calculate the required probability values, the error values are assumed to be normally distributed about the functional form of equation (3.10).

The mean and standard deviations for both α and β are dependent upon a number of parameters: the chosen baseline values of α and β, the number of HB in a recording, the number of event sequences, *M*, and the value of *k*. In practice, the value of *k* has a negligible effect on the results as

long as it is not very small. For small values of k the accuracy of β is unimportant: since there are so few artefacts, the accuracy of artefact detection has only a small impact on the accuracy of the classifier. The performance of the algorithm is relatively insensitive to the precise number of HB, within reasonable limits. The key parameter is the number of event sequences, M, which would correspond to the number of recordings that would have to be processed to validate an algorithm.

The first condition considered is $\alpha = \beta = 0.6$ with a score with 9 levels, i.e. half-integers. The resulting means and standard deviations for both α and β are shown in Figure 3-10. Note that there is some scatter on the estimates for the means and standard deviations: this is due to the intrinsically statistical nature of the process used to generate the results. However, this scatter is relatively small and decreases monotonically with the number of event sequences. The estimates of the means show that there is some bias in the estimates, which is largely invariant of the number of event sequences. It is not clear what is causing this bias, although it is relatively small. The standard deviations monotonically decrease with the number of event sequences and show similar behaviour for both α and β. For 100 event sequences, the standard deviations for α and β are 0.0826 and 0.0664, respectively, decreasing to 0.0314 and 0.0308 for 1000 event sequences. There is, as might be expected, a significant decrease in the variance of the estimates of α and β as the number of event sequences increases.

Using $\alpha = 0.8$, $\beta = 0.6$, again with a half-integer scoring system, very similar results to those for $\alpha = \beta = 0.6$ are obtained. The biases are of similar magnitude although slightly smaller, which is unsurprising since as the baseline values approach 1 the possible bias decreases. The variances are also similar: the standard deviations are 0.0752 and 0.0830 for 100 event sequences and 0.0323 and 0.0297 for 1000 event sequences.
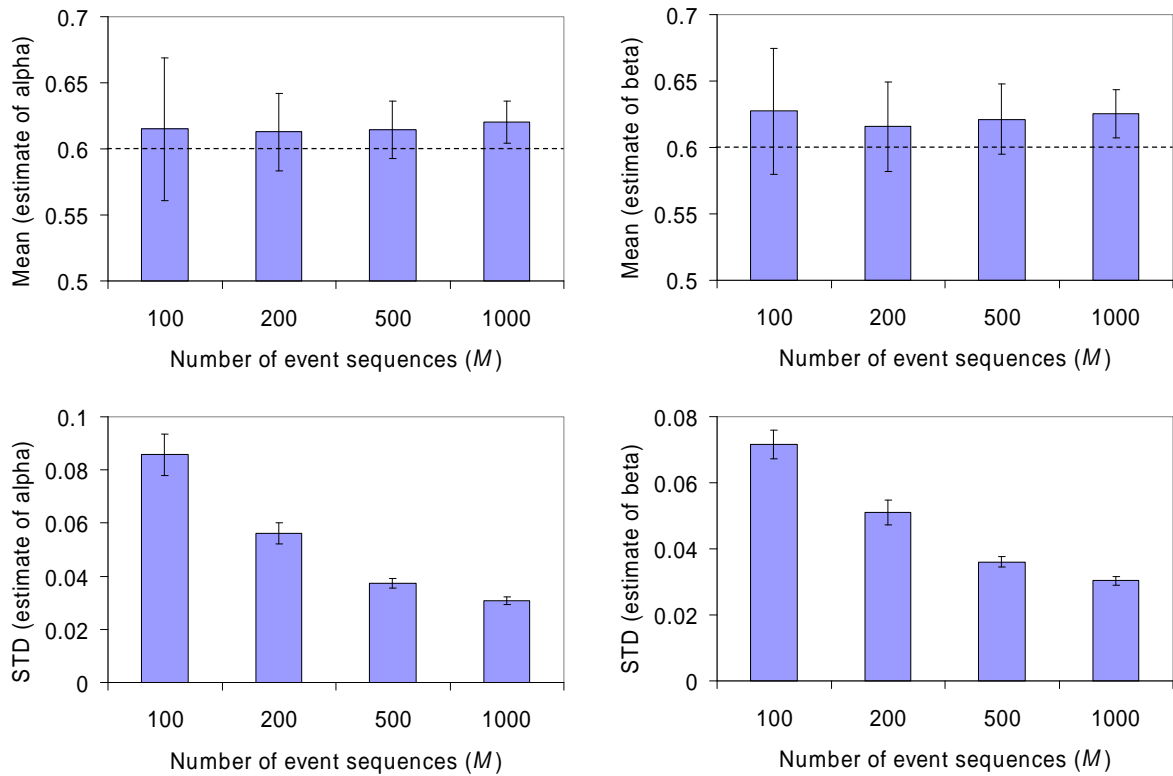
Figure 3-10: Estimates for the mean and standard deviation of α and β against number of event sequences.

Thus far the classification probabilities have been estimated when a half-integer scoring system was used: the effects of using an integer scoring system (c.f. the Spencer scale) and a third-integer scoring system (c.f. KM grades) are also thus examined. The estimates of the means and standard deviations for both α and β are shown in Figure 3-11 and Figure 3-12, respectively, for the three scoring systems and $\bar{\alpha} = \bar{\beta} = 0.6$. The choice of scoring system appears to have no significant effect on the estimate of the mean for α; however, the large scatter on the estimates means that it is difficult to draw firm conclusions. The bias on the estimate of the mean of β does appear to reduce with the number of grades available in the scoring system. The integer scoring system produces a large bias, which is unlikely to be acceptable, whereas the half- and third-integer scoring systems reduce this bias substantially to a more acceptable level, comparable to the bias on the estimate of the mean of α.
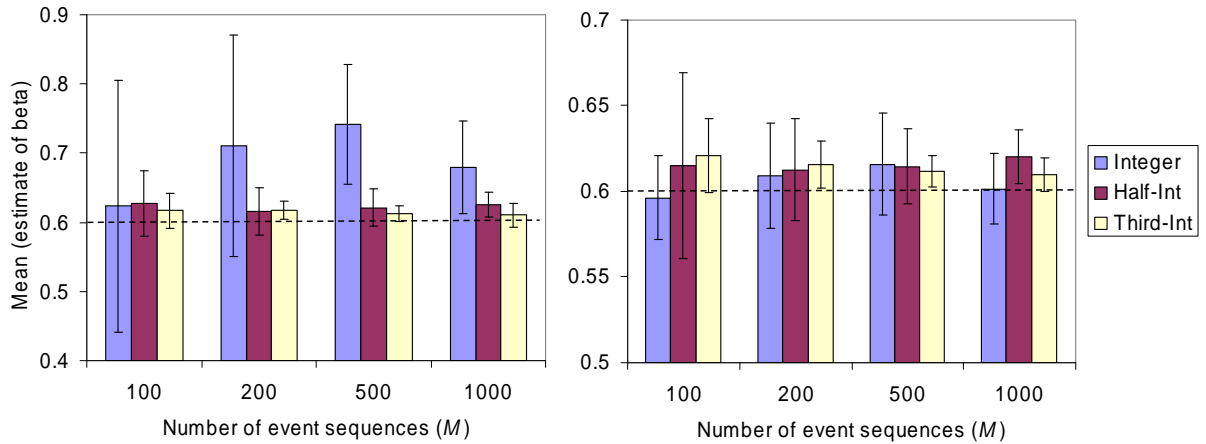
Figure 3-11: Mean estimates for α and β against the number of event sequences for integer and half-integer and third-integer scales.
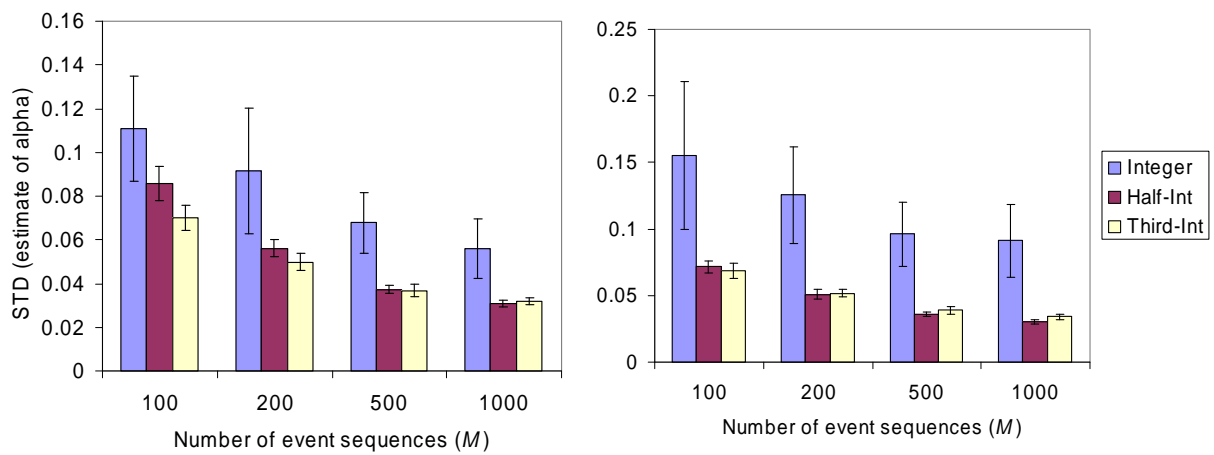

Figure 3-12: Standard deviation estimates for α and β against the number of event sequences for integer and half-integer and third-integer scales.

The estimates of the standard deviations of both α and β are significantly lower for both the half- and third-integer scoring systems than for the integer scoring system. However, there is no significant reduction in the estimates of the standard deviations of both α and β when the third-integer scoring system is used in preference to the half-integer scoring system. This occurs because the available scores are both averaged over the length of each recording before being converted into a discrete score; thus, there are two sources for a loss of information. The similarity in the estimates of the standard deviations of both α and β between the half- and third-integer scoring systems seems to show that once a half-integer scoring system is used, there is no further improvement available in the estimates of α and β by using a more detailed scale. The limitation is thus due to the aggregate nature of the labelling, rather than the discretization of the scores. Despite there being no significant improvement found when using a third-integer scoring system

this does not imply that these results advocate the ESS over the KM scale for Doppler recording scoring. Although it indicates that the finer gradation of the KM is not advantageous for validation of bubble detection algorithms, the choice of grading scheme is based on the ease and accuracy with it can be applied. Alongside there being a limit to the standard deviation with the gradation of the scoring scheme it also seems to tail off as M increases, i.e., there appears to be only limited improvement as M increases past 1000. The aggregate nature of the expert labels thus appears to put a fundamental limit on the accuracy of determinations of the classification probabilities.

One of the main aims of calculating the variance in the estimated values of α and β is to check whether changes in the estimates of these parameters as the bubble detection algorithm is optimized are statistically significant. Without an estimate of the likely variance, this is not possible. For 1000 event sequences, the standard deviation is approximately 3 %, so changes in the values of either α and β of less than this will clearly be statistically insignificant. Even with a large number of event sequences, it is thus difficult to obtain changes in either α and β that are significant. This provides a limit on the optimization of algorithms to detect individual bubble events based purely on the aggregate labels of event sequences. However, the fact that the parameters can be estimated with a relatively small standard deviation enables some information about the performance of bubble detection algorithms to be obtained from aggregate labels.

There is likely to be error in the expert labels arising from the subjectivity of the expert grading procedure and this has previously been observed by Sawatzky *et al.* (1991). Consequently it is important that the effect of such errors on the validation of bubble detection algorithms is considered. This can be incorporated in the above method replacing the actual label for each recording with an expert label which is derived in the same manner as the algorithm label above, but with an expert matrix of probabilities as shown in Table 3-4. It is unlikely that values for expert accuracy from real data can be reliably obtained, although in many organisations careful procedures are used to counter the subjectivity of the procedure and keep accuracy high, Nishi *et al.* (1989), Sawatzky *et al.* (1991). Hence it is likely that expert accuracy will approach 100%.

Table 3-4: Matrix of probabilities for the expert label, with 90 % expert accuracy.

		Actual		
		HB	B	A
Label	HB	1	0	0
	B	0	0.9	0.1
	A	0	0.1	0.9

Figure 3-13 and Figure 3-14 show estimates for the means and standard deviations for α and β, for both integer and half-integer scoring systems where expert accuracy may be 90% or 100%, baseline values of $\alpha = \beta = 0.6$ again being used. The inclusion of expert inaccuracy is found not to have a significant impact on the estimate of standard deviation for α and β. However, it does increase the bias on the estimate of the mean bubble (although not artefact) classification probability.
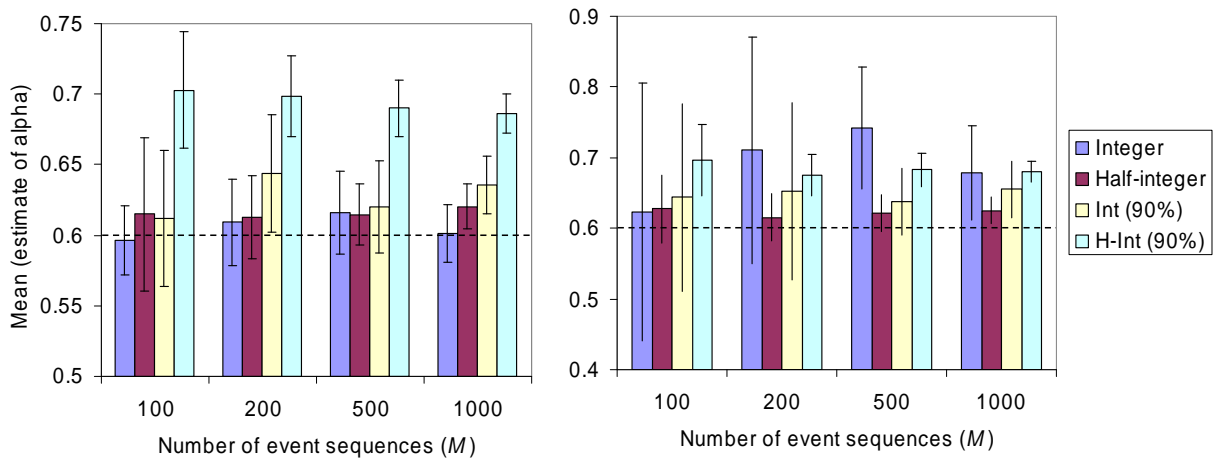

Figure 3-13: Mean estimates for α and β against the number of event sequences for integer and half-integer scales, with 90% and 100% expert label accuracy.
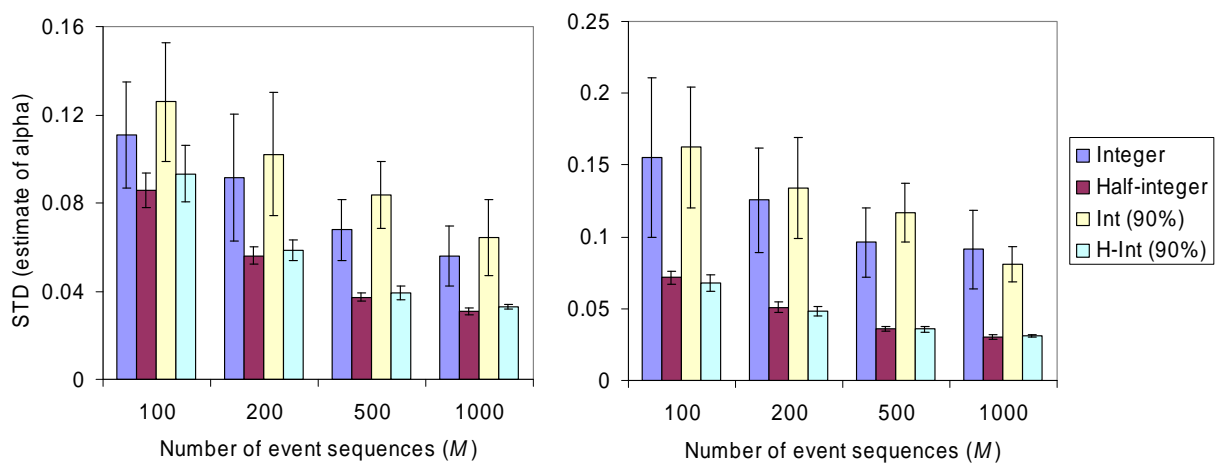

Figure 3-14: Standard deviation estimates for α and β against the number of event sequences for integer and half-integer scales, with 90% and 100% expert label accuracy.

These results indicate that it is possible using multiple recordings to estimate the classification probabilities from a bubble detection algorithm, implying that such an algorithm can be validated. The classification probabilities can be learnt with a bias of approximately 1% and a standard deviation that drops from 7.5% for 100 sequences to 3% for 1000 sequences, using 60 HB sequences (an approximately 60 s recording) and a half-integer scoring system. There appears to little advantage to using more than 1000 sequences and a finer gradation than half-integer scoring as the standard deviation on the estimates for both the bubble and artefact classification probabilities converges toward approximately 3%. This may make it difficult to show that one algorithm is superior to another or to fine-tune the parameters in an algorithm to a high degree of statistical significance.

3.7   Summary and Conclusions

The Empirical Mode Decomposition method offers a means by which Doppler ultrasound signals from the pulmonary artery can be analysed for the presence of bubbles within the venous system of humans. A method is presented here based on EMD which detects the occurrence of bubbles in such signals. EMD is used to decompose the signal into a series of components, termed IMF. Individual heart cycles within the signal are determined using a robust peak detection based on the technique devised by Hamilton and Tompkins. Features are then detected in each heart cycle from the IMF by looking for deviations from the ensemble average. From these features bubbles are detected as features that appear in a number of IMF that have the correct energy characteristics. The method appears to be robust to variability in the signal strength, although heart beat detection is prone to failure if the signal strength is particularly low. The method has been applied to a subset of a large data set and appears to detect bubbles with good sensitivity. However, some spurious features, such as noise artefacts, are misclassified as bubbles, which reduce the specificity. The method offers the ability to provide an automatic grading of Doppler audio signals, avoiding the subjectivity of the manual alternatives. It is also more quantitative than using a grading scheme alone, because it can provide information about the presence of individual bubbles. However, validation is still required to verify the performance of the algorithm and to determine final values for the various empirical parameters.

4. Crevice model theory[*]

4.1 Introduction

In this chapter a model for the formation of bubbles in the blood will be presented. This model is based on the assumption that bubbles form in blood vessels from pre-existing gas nuclei housed in cavities on the vessel wall. The aim of this chapter is to provide a dynamic model for bubble growth in blood vessels to complement those for bubble formation in the tissue and thus to describe the formation of the bubbles that are observed in the blood using ultrasonic techniques. The mathematical model is derived for the growth of a bubble in a spherically symmetric crevice, as illustrated in cross-section in Figure 4-1. This geometry is chosen in keeping with the literature on the nucleation of bubbles in cavities, Forest (1982), Tikuisis *et al.* (1983a), Atchley *et al.* (1989), where the conical crevice has been adopted for its relatively simple geometry. Although the true nucleation sites in the body may take a more complex form, it is considered to be a reasonable representative form to adopt here. This assumption will be re-examined in chapter 6.

It is assumed that the crevice is embedded in a blood vessel wall and that the nearby tissue is the primary source of gas for the bubble, diffusion occurring through the crevice wall. For simplicity,

---

[*] This chapter expands upon the theory that appears as:
Chappell, M. A. and S. J. Payne (2006a). "A Physiological Model of Gas Pockets in Crevices and Their Behavior under Compression." Respiration Physiology & Neurobiology **152**: 100-114.
Chappell, M. A. and S. J. Payne (2006b). "A Physiological Model of the Release of Gas Bubbles from Crevices under Decompression." Respiration Physiology & Neurobiology **153**: 166-180.

diffusion of gas across the interface between the bubble and the blood is ignored: the validity of this assumption will be examined in chapter 5. A similar approach will be taken to that used for the model of the growth of a spherical bubble in a tissue presented by Srinivasan *et al.* (1999). Although the model will be presented here in a form suitable for a single inert gas, a more comprehensive model that incorporates multiple inert gases is given in Appendix A.
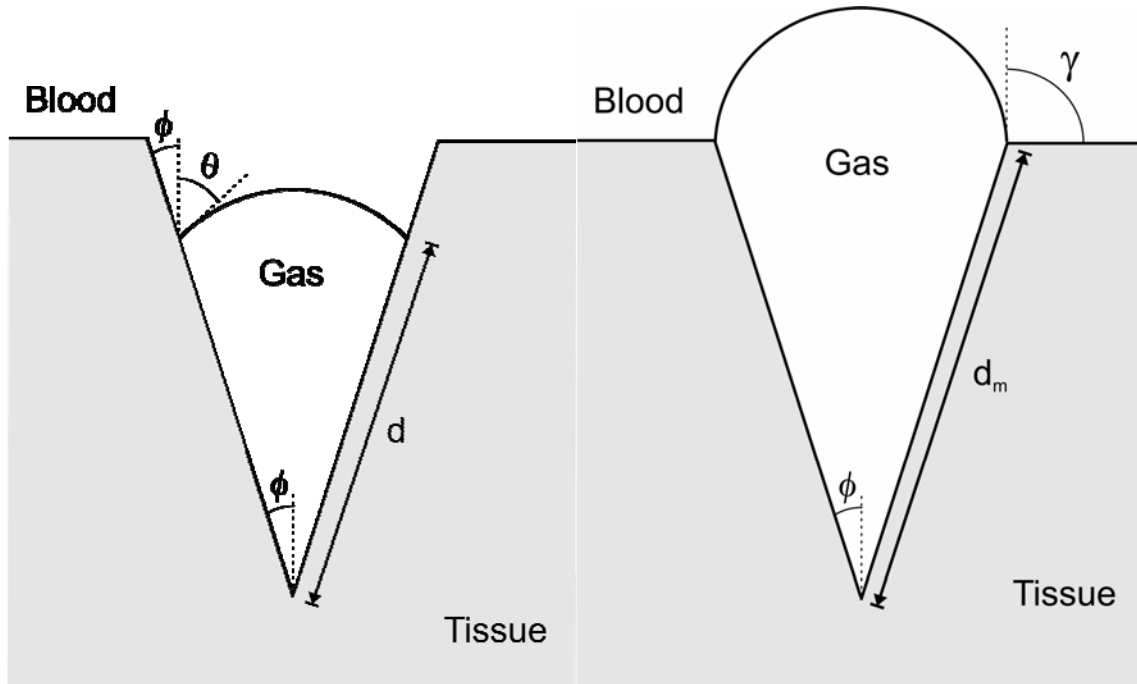
Figure 4-1: Cross sectional view of the conical crevice with a half-angle ϕ and a length d_m : a) the gas pocket inside the crevice has a length d and interface angle θ, b) the gas pocket when it emerges outside the crevice has a new contact angle γ.

4.2 Crevice geometry

4.2.1 Inside the cavity

The geometry of the gas pocket when inside the crevice is completely defined by the bubble length, d, the interface angle, θ, and the half-angle of the crevice, ϕ, where these parameters are defined in Figure 4-1. The contact angle between the interface and the cavity wall is thus the sum of the two angles:

$$\alpha = \theta + \phi .$$ (4.1)

The radius of curvature is found by treating the interface as the spherical cap of a sphere with radius:

$$R = \frac{d \sin \phi}{\cos \theta} .$$ (4.2)

Likewise the volume is composed of the volume of the spherical cap and the volume of the cavity below the three-phase contact line, Atchley *et al.* (1989):

$$V_i = \frac{1}{3}\pi d^3 \left(\cot\phi + \eta\right)\sin^3\phi,$$ (4.3)

where:

$$\eta = \frac{2 - \left[2 + \cos^2\theta\right]\sin\theta}{\cos^3\theta}.$$ (4.4)

4.2.2 Outside the cavity

The gas pocket interface once it is outside the crevice is described by the contact angle between the interface and the external surface, γ, as shown in Figure 4-1b. Hence the radius of curvature becomes:

$$R = \frac{d_m \sin\phi}{\sin\gamma}.$$ (4.5)

The volume of the bubble is given by, Atchley *et al.* (1989):

$$V_i = \frac{1}{3}\pi d_m^3 \left(\cot\phi + \zeta\right)\sin^3\phi,$$ (4.6)

where:

$$\zeta = \frac{2 + \left(2 + \sin^2\gamma\right)\cos\gamma}{\sin^3\gamma}.$$ (4.7)

4.3 Gas transfer

Gas transfer to and from the bubble may occur both via the crevice wall between the bubble and the surrounding tissue, as well as through the interface between the bubble and the blood. It is often assumed that crevices suitable for nucleation sites are narrow, i.e. have a small half-angle, Tikuisis *et al.* (1983a), Tikuisis (1986), because this enhances the ability of the nuclei to resist dissolution under compression. Thus the surface area of the gas-blood interface will be significantly smaller than the gas-tissue interface. Hence it is expected that gas transfer by the latter route will be more significant. It will thus be assumed here that gas transfer through the bubble-blood interface can be neglected, although this will be discussed further in section 5.4.3.

4.3.1 Within the crevice

Diffusion of a gas within the tissue is described by the diffusion equation:

$$\frac{\partial c(x,t)}{\partial t} = D_t \nabla^2 c(x,t), \tag{4.8}$$

where c (mol m^{-3}) is the concentration and D_t (m^{2}s^{-1}) is the bulk diffusion constant of the gas in the tissue. For simplicity the diffusion is approximated as being 1-dimensional, which is reasonable if the depth of the crevice is significantly less than the inter-capillary distance. Additionally, changes in ambient pressure are assumed not to be very rapid so that a quasi-static approximation can be made, Srinivasan *et al.* (1999), i.e. $\partial c/\partial t \approx 0$, so that the diffusion equation becomes:

$$\frac{d^2 c}{dx^2} \approx 0. \tag{4.9}$$

If the origin for x (m) is at the crevice wall and it is assumed that the diffusion occurs over some representative length scale, λ (m), then the boundary conditions are given by:

$$c(0,t) = c_i(t), \tag{4.10}$$

$$c(\lambda,t) = c_t(t), \tag{4.11}$$

where c_i and c_t are the concentrations of gas in the bubble and tissue respectively (mol m^{-3}). The resulting solution for concentration in the tissue is thus:

$$c(x,t) = \frac{c_t(t) - c_i(t)}{\lambda} x + c_i(t). \tag{4.12}$$

4.3.2 Between the bubble and the tissue

The rate of change of mass of gas in the bubble is equal to the flux of gas through the bubble boundary:

$$\frac{1}{\Re T} \frac{d}{dt}(p_i V_i) = A_i D_t \frac{dc}{dx}\bigg|_{x=0}, \tag{4.13}$$

where V_i is the volume (m^3), A_i the surface area of the crevice bubble (m^2) and temperature is presumed to remain constant. As it is assumed that the dominant gas flux is through the crevice wall, when the bubble is inside the crevice: $A_i = \pi d^2 \sin\phi$, the surface area of the crevice within the bubble. Incorporating the solution to the diffusion equation from equation (4.12) and using Henry's law, equation (2.2), to express concentration in terms of gas tension gives:

$$\frac{d}{dt}(p_i V_i) = L_t D_t \pi d^2 \sin\phi \frac{p_t - p_i}{\lambda}. \tag{4.14}$$

When the bubble has emerged outside the cavity the surface area of the bubble (ignoring the gas-liquid interface surface) is constant because the line of contact is at the crevice mouth, hence equation (4.14) becomes:

$$\frac{d}{dt}(p_i V_i) = L_t D_t \pi d_m{}^2 \sin\phi \frac{p_t - p_i}{\lambda} \,. \tag{4.15}$$

4.3.3 Between the tissue and the blood

As in Srinivasan *et al.* (1999), the transfer of gas between the blood and the tissue is assumed to be perfusion-limited as described in section 2.3.1. The tissue tension of each gas is thus assumed to obey and equation of the form of (2.4):

$$\frac{dp_t}{dt} = \frac{p_a - p_t}{\tau} \,. \tag{4.16}$$

For a single inert gas the arterial pressure in the blood, p_a, is equal to the ambient pressure, p_{amb}.

4.4 Bubble growth phases

The crevice bubble model is described by three different phases of growth, which reflect three of the four phases identified by Atchley *et al.* (1989):

1. Bubble interface curvature varies inside crevice (variation in θ).

2. Bubble interface moves up or down the crevice (variation in d).

3. Bubble is at the mouth of the crevice and the interface curvature is varying (variation in γ).

The conditions for transition between phases are given in Figure 4-2. As an example, if the bubble starts with a flat interface and inside the crevice, then any variation in the bubble size will start with variation in θ, as it is between the two limits imposed by the receding and advancing contact angles. If the bubble is growing, firstly the interface will become more convex, i.e. 'swell' upward: a reduction in θ. When θ reaches the receding contact angle variation in θ stops and the bubble may continue to grow by variation in the bubble length, d. The bubble will continue to grow until the bubble reaches the mouth of the crevice whereupon growth may continue by variation in the contact angle between the bubble interface and the vessel wall. If the bubble growth halts in the γ varying case and then the bubble starts to shrink, the interface will become gradually more convex, γ increasing until the advancing contact angle between the interface and the vessel wall is reached, whereupon the interface can move down the crevice by reduction in d. Alternatively if the bubble

continues to grow then once $\gamma = \gamma_s$ a free bubble is released and the interface returns to the advancing contact angle, where γ_s is defined as the critical value of contact angle for bubble detachment.
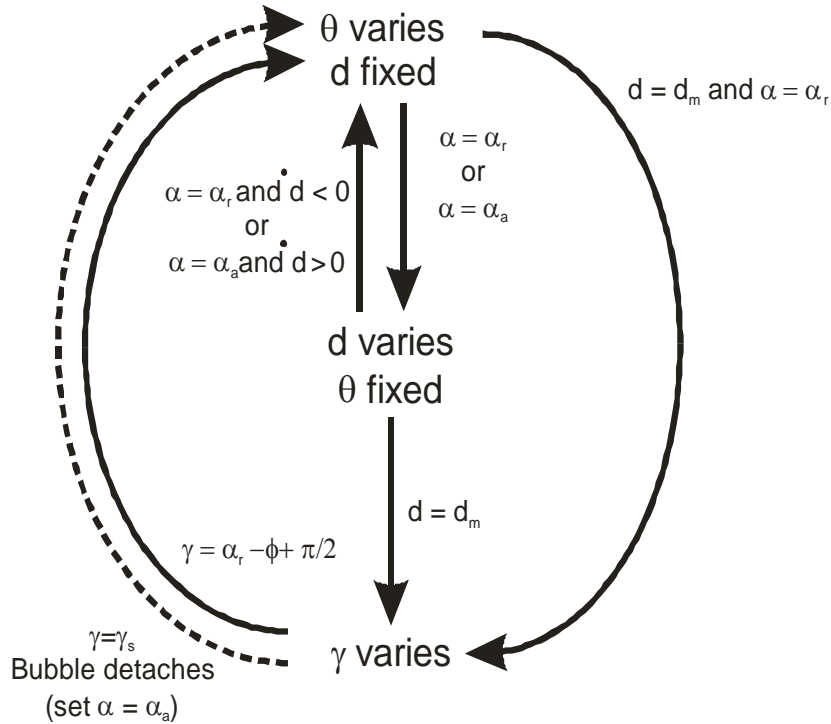
Figure 4-2: The case transition diagram, illustrating the conditions for transition between the three cases of bubble size variation in the crevice bubble model.

4.5   Crevice model

For a single inert gas it is possible to solve equation (4.14) for the rate of change of θ with d constant or vice versa to describe the first two phases of growth, with p_i being given by the Laplace equation. Likewise equation (4.15) is solved for γ to describe the third phase, once again the Laplace equation being used to calculate p_i. Thus the full model can be described in the three phases described above:

4.5.1   Phase one

During phase one only the interface angle changes, the bubble length being fixed. During this phase the interface angle is between the two limiting values of the receding and advancing contact angles:

$$\alpha_r < \phi + \theta < \alpha_a. \tag{4.17}$$

Equation (4.14) is solved for the rate of change of θ with $\mathrm{d}d/\mathrm{d}t = 0$ to give:

$$\frac{\mathrm{d}\theta}{\mathrm{d}t} = \frac{\frac{3 L_t D_t}{\lambda}(p_i - p_t) + d\varepsilon \frac{\mathrm{d}p_{amb}}{\mathrm{d}t} \sin^2 \phi}{\frac{3}{4} d p_{amb} \sin^2 \phi + 2\sigma \left\{ \varepsilon \sin\theta + \frac{3}{4} \cos\theta \right\} \sin\phi} , \tag{4.18}$$

where:

$$\varepsilon = \cot\phi - \frac{3}{4}\left(\theta - \frac{\pi}{2}\right). \tag{4.19}$$

and p_i is given by equation (2.6), with R (for the interface inside the crevice) given by equation (4.2):

$$p_i = p_{amb} + \frac{2\sigma \cos\theta}{d \sin\phi}. \tag{4.20}$$

4.5.2 Phase two

If the advancing or receding contact angles are reached during phase one then the bubble length may change. The contact angle will now be set at either the receding or advancing contact angle dependent upon whether the bubble is growing or collapsing:

$$\begin{aligned} \text{growing:} \quad & \phi + \theta = \alpha_r \\ \text{collapsing:} \quad & \phi + \theta = \alpha_a \end{aligned} \tag{4.21}$$

Equation (4.14) is now solved for the rate of change of d with $\mathrm{d}\theta/\mathrm{d}t = 0$ to give:

$$\frac{\mathrm{d}d}{\mathrm{d}t} = -\frac{\frac{3 L_t D_t}{\lambda}(p_i - p_t) + d^2 \varepsilon \frac{\mathrm{d}p_{amb}}{\mathrm{d}t} \sin^2 \phi}{\left(4\sigma \cos\theta + 3 d p_{amb} \sin\phi\right)\varepsilon \sin\phi} , \tag{4.22}$$

and p_i is again given by the Laplace equation given in equation (4.20).

4.5.3 Phase three

Outside the crevice, i.e. if the bubble interface reaches the mouth of the crevice, the bubble is governed by the interface angle with the external surface, the bubble length now being fixed at the length of the crevice:

$$d = d_m. \tag{4.23}$$

As the interface is now outside the crevice equation (4.15) is solved for the rate of change of γ :

$$\frac{\mathrm{d}\gamma}{\mathrm{d}t} = \frac{\frac{3L_t D_t}{\lambda}(p_i - p_t)\sin^3\left(\frac{\gamma}{2}\right) + d_m \sin\phi \frac{\mathrm{d}p_{amb}}{\mathrm{d}t}\xi_1}{3d_m p_{amb}\sin^2\phi\csc\left(\frac{\gamma}{2}\right) + 2\sigma\xi_2},$$ (4.24)

where:

$$\xi_1 = 3\sin(\phi + \gamma/2) - \sin(\phi + 3\gamma/2),$$ (4.25)

$$\xi_2 = 6\sin\phi\cos(\gamma/2) - \xi_1\cos\gamma,$$ (4.26)

and p_i is given by the Laplace equation, with R given (for the interface outside the crevice) by equation (4.5):

$$p_i = p_{amb} + \frac{2\sigma\sin\gamma}{d_m\sin\phi}.$$ (4.27)

4.6 Bubble release

It is possible that if γ reaches the receding contact angle for the interface with the vessel wall, then the bubble could grow laterally by spreading along the vessel wall, Atchley *et al.* (1989). Alternatively at some point a proportion of the gas in the bubble may detach from the crevice due to the forces exerted by the blood flowing past. It will be assumed that the latter occurs first, because experimental evidence suggests that it is more likely that the bubble will detach before growing laterally along the vessel wall surface, Bai *et al.* (2001).

The exact condition under which a bubble detaches from the crevice mouth under the forces exerted by flowing blood is a complex problem and will be dealt with more fully in chapter 7. For simplicity it will initially be assumed that a proportion of the gas detaches once a threshold value of γ, γ_s, is reached. Once a free bubble has been released a pocket of gas remains in the crevice and it is necessary to define where the interface of the remaining gas pocket lies in the crevice. Since a free bubble will be released by the bubble interface detaching around the crevice mouth it is assumed that for the remaining gas pocket $d = d_m$, i.e. it is at the mouth of the crevice. In the first instance it is assumed that the gas pocket that remains will be concave into the crevice and hence the value of θ is set to the advancing contact angle, i.e. the interface is at its concave limit. The state of the crevice bubble after a free bubble has been released is illustrated in Figure 4-3.
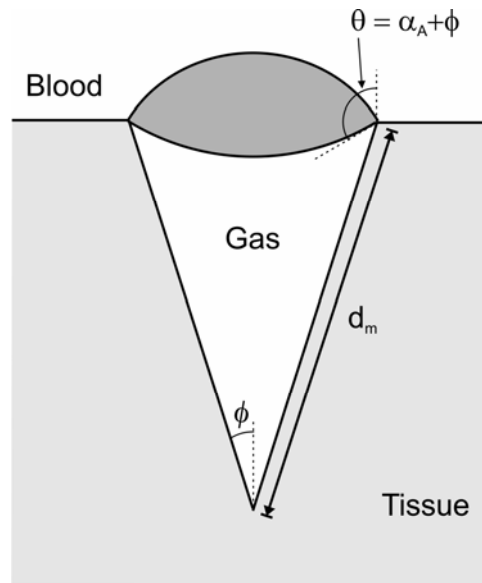
Figure 4-3: Crevice bubble on the point of release of a free bubble, where it is assumed that the interface of the gas pocket returns to the advancing contact angle and so the shaded section of gas is released as a free bubble in the blood.

4.7 Model Parameterization

For numerical solutions of the bubble model equations, the equations were firstly recast into a pseudo non-dimensional form where only the time dimension is retained. This was necessary to reduce the possibility of errors in the numerical solver, as there are 11 orders of magnitude difference between the pressure in the bubble and the bubble length. Additionally it is possible to assess from the pseudo non-dimensional form how many parameters are needed to describe the model. The parameters $\bar{p}$ (1 bar) and $\bar{r}$ (1 μm) are introduced as a characteristic pressure and length respectively, so that the equations can be re-written in terms of non-dimensional bubble length and pressures. In the pseudo non-dimensional form it is possible to identify 8 parameters which govern the dynamics of the crevice bubble for a single gas and these are given in Table 4-1. The pseudo non-dimensional version of the model equations are given in Appendix B.

Table 4-1: The pseudo non-dimensional parameters which fully describe the crevice model.

Governing Parameter	Dimensions	Description
Bubble interface		
$\sigma' = \dfrac{\sigma}{\bar{P}\bar{r}}$	[-]	Non-dimensional surface tension
α_r	[-]	Receding contact angle
α_a	[-]	Advancing contact angle
γ_s	[-]	Bubble detachment contact angle
Tissue		
τ	[T]	Tissue time constant
$\tau_D = \dfrac{\lambda \bar{r}^2}{L_t D_t}$	[T]	Gas diffusion time constant
Crevice		
$d'_m = \dfrac{d_m}{\bar{r}}$	[-]	Non-dimensional crevice length
ϕ	[-]	Crevice half angle

Many of the physiological parameter values needed for the crevice bubble model are not well established and their influence will thus be explored in the next chapter. Baseline values that will be used in the numerical simulations are given in Table 4-2, where the inert gas is assumed to be nitrogen. Values for surface tension, diffusion constant and solubility were chosen to be the same as those that have been used previously in tissue bubble models, Srinivasan *et al.* (1999). A 'fast' tissue half time of 600 seconds (10 minutes), giving a tissue time constant of 2000 seconds, has been chosen as the default value. Using these values the tissue gas constant is approximately two orders of magnitude greater than the gas diffusion time constant, which implies that the rate of transfer of gas into the bubble from the tissue is much faster than the transfer of gas between tissue and blood.

Tikuisis *et al.* (1983a) has previously concluded that crevices for DCS related bubbles should have a small half angle, of less than 5°, hence a value of 2° has initially been chosen. The length scale for diffusion has been chosen to be 1μm, which is of a similar order to the boundary layer for diffusion used in tissue bubble models, Srinivasan *et al.* (1999). There is a notable scarcity of values for the

receding and advancing contact angles for cellular membranes, Tikuisis *et al.* (1983a). It is expected that the crevice will have to be hydrophobic to support a gas pocket under compression, hence a value for receding contact angle of 80˚ will be used here. It is clear from the Laplace equation that the contact angle range must include the case where θ = 90˚, as it is only for this value of interface angle that the surface tension term is zero, assuming that the pressure of the metabolic gases is negligible. If a flat interface is not possible there will always be a pressure difference between the bubble and the atmosphere driving gas in or out of the bubble. Thus it would be impossible, with a single gas, for the bubble to attain equilibrium. A default value of receding contact angle of 100˚ will be assumed because it is symmetrical with the advancing contact angle about 90˚. The bubble is assumed to be initially in equilibrium, i.e. θ = 90˚, with internal pressure equal to ambient pressure.

Table 4-2: Baseline values for the physiological parameters for the crevice model.

Parameter	Value
Bubble interface	
σ	0.03 N/m Srinivasan *et al.* (1999)
σ'	0.3
α_r	80°
α_a	100°
γ_s	90°
Tissue	
L_t	0.0125 ml gas/ml tissue, Srinivasan *et al.* (1999)
D_t	$2.2 \times 10^{-12} \, \text{m}^2/\text{s}$, Srinivasan *et al.* (1999)
τ	2000 seconds
λ	1 μm
τ_D	36.4 seconds
Crevice	
d_m	2 μm
d'_m	2
ϕ	2°

As a specific physiological site has not been identified for bubble growth, no value is available for d_m. Given that these nucleation sites are presumed to exist on the wall of capillaries, lengths of the order of micrometres are expected, hence a value of 2 μm will initially be assumed for d_m and a range of values explored below. An initial bubble length of 1 μm is similarly assumed. Further analysis will be required to establish the appropriate value of γ_s, as the conditions for bubble release have not previously been explored: its effects will thus be examined in detail. An initial default value of 90° is chosen because at this contact angle the direction of the surface tension force is perpendicular to the wall and thus the bubble would, in principle, be easy to detach from the crevice mouth by flow along the wall. The choice of the physiological parameters used in the model will be considered further in chapter 5 once their effect on the behaviour of the bubble has been explored.

4.8   Summary & Conclusions

In this chapter a model has been presented that allows the phase of bubble growth and emergence from a crevice. The model represents a nucleation site for bubbles that might be expected to be present on the lining of blood vessels, giving rise to vascular bubbles in humans under decompression. Although a number of simplifications have been made to make the model mathematically tractable, in the form presented here the model will allow the general behaviour of a crevice stabilised bubble to be examined both for its ability to resist compression and for the growth of the bubble under decompression, which is the topic of the next chapter .

5. Crevice model results[*]

5.1 Introduction

In this chapter results from the crevice model for the formation of bubbles in blood vessels described in chapter 4 are presented. These results are then discussed to consider the effects of variations in the physiological model parameters and comparisons with experimental values for these parameters from the literature are made. In this chapter results are presented from simulations assuming only a single inert gas without the presence of the metabolic gases and water vapour. The inclusion of these will then be discussed via the inclusion of a fixed factor in the Laplace equation as discussed in section 2.3.2.2.

5.2 Compression behaviour

Firstly the behaviour of a crevice bubble is examined for a typical compression profile. The profile starts at 1 bar and consists of a compression, at a rate of 0.0167 bar s^{-1} (1 bar min^{-1}) to 4 bar, approximately equivalent to 40 m of sea-water. The evolution of bubbles with different values of advancing contact angles is shown in Figure 5-1. Three different outcomes are observed: the bubble length doesn't change, the bubble shrinks to a smaller length or the bubble collapses. The

---

[*] This chapter expands upon the results which appear as:

Chappell, M. A. and S. J. Payne (2006a). "A Physiological Model of Gas Pockets in Crevices and Their Behavior under Compression." Respiration Physiology & Neurobiology **152**: 100-114.

Chappell, M. A. and S. J. Payne (2006b). "A Physiological Model of the Release of Gas Bubbles from Crevices under Decompression." Respiration Physiology & Neurobiology **153**: 166-180.

bubble doesn't change in length if the advancing contact angle is relatively large as illustrated in Figure 5-1a. As the pressure increases, the bubble interface curves into the crevice, hence the bubble reduces in volume. However, the compression is not sufficient for the interface to reach the advancing contact angle, so the bubble length does not change. As the gas tension in the tissue starts to approach the ambient pressure by perfusion, the bubble interface returns to the equilibrium state ($\theta = 90°$) due to diffusion of gas into the bubble from the tissue.

For certain values of advancing contact angle the bubble shrinks to a new stable size, as illustrated in Figure 5-1b. Initially the interface angle increases as the bubble interface becomes concave into the crevice. After 109 seconds the advancing contact angle is reached and the bubble length decreases as blood advances into the crevice. The bubble stabilizes at 0.8 μm once the diffusion of gas into the bubble from the tissue into the bubble is sufficient to prevent further reduction in bubble volume. As the tissue reaches equilibrium with the atmosphere and the bubble does likewise with the tissue, the interface returns to the equilibrium state. For advancing contact angles near 90° the bubble collapses, Figure 5-1c. Initially the interface angle increases until the advancing contact angle is reached and so the bubble length reduces. However, the bubble does not stabilize to a new bubble length; instead it collapses, because there is insufficient diffusion of gas into the bubble from the tissue.

The final value that d reaches can be used to examine the behaviour of the bubble under various conditions; Figure 5-2 shows the final value of bubble length for a range of advancing contact angles and different magnitudes of compression, on each occasion the compression proceeding at 0.0167 bar s^{-1}. From this figure it is possible to identify the ranges of advancing contact angles over which the bubble will stay the same length, shrink or collapse. The effect of larger compression magnitude is to shift these ranges further away from 90°. Hence the greater the compression that the crevice bubble must resist, the higher the advancing contact angle needed. This arises because the larger the compression magnitude the faster is the bubble's initial shrinkage and hence the less time there is for gas tension to increase and for sufficient gas diffusion between tissue and bubble to be established to prevent complete bubble collapse.
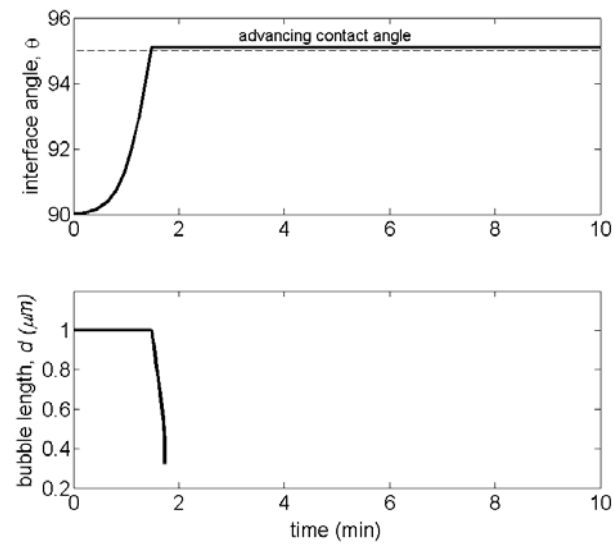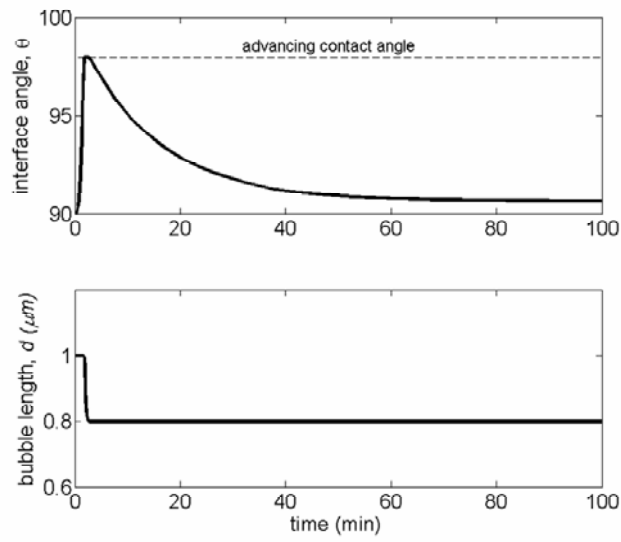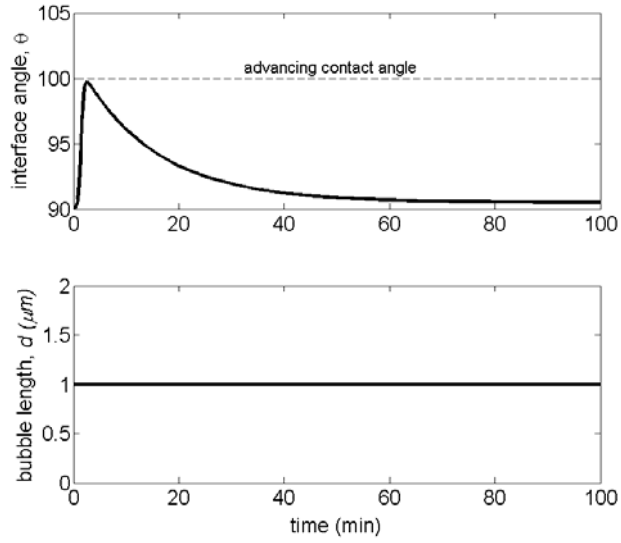
Figure 5-1: Evolution of crevice bubble under 4 bar compression where the receding contact angle is a) 100°, b) 98°, c) 95°.
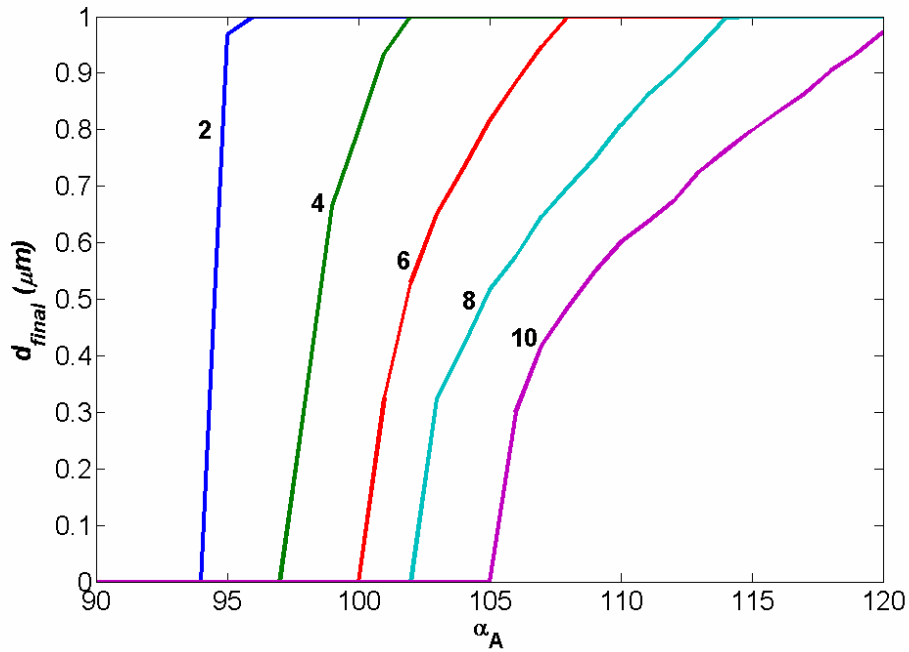
Figure 5-2: Final value of bubble size for a range of advancing contact angle and compression pressures (bar).

The effects of uncertainty in the values of the underlying physiological parameters will now be examined by considering variations in the appropriate non-dimensional parameters in the model. Variation in the advancing contact angle has already been considered and is critical to the behaviour of a crevice bubble under compression. For a bubble under compression it is unnecessary to specify the receding contact angle, as this will not be reached. The behaviour of the bubble under compression for variations in the remaining 4 pseudo non-dimensional parameters given in Table 4-1 will now be examined.

An important parameter for the crevice bubble is the crevice half angle, ϕ, as this is the main parameter that defines the geometry of the bubble. Figure 5-3 shows the results for a 4 bar compression, on a crevice bubble for a range of crevice half angles. A wider crevice has lower ability to sustain a bubble against compression, i.e. the advancing contact angle required to avoid bubble collapse increases with an increase in ϕ. This is consistent with the Laplace equation as the pressure difference, between the bubble and ambient pressures, that can be supported by curvature of the bubble interface is inversely proportional to the cosine of the crevice half angle.
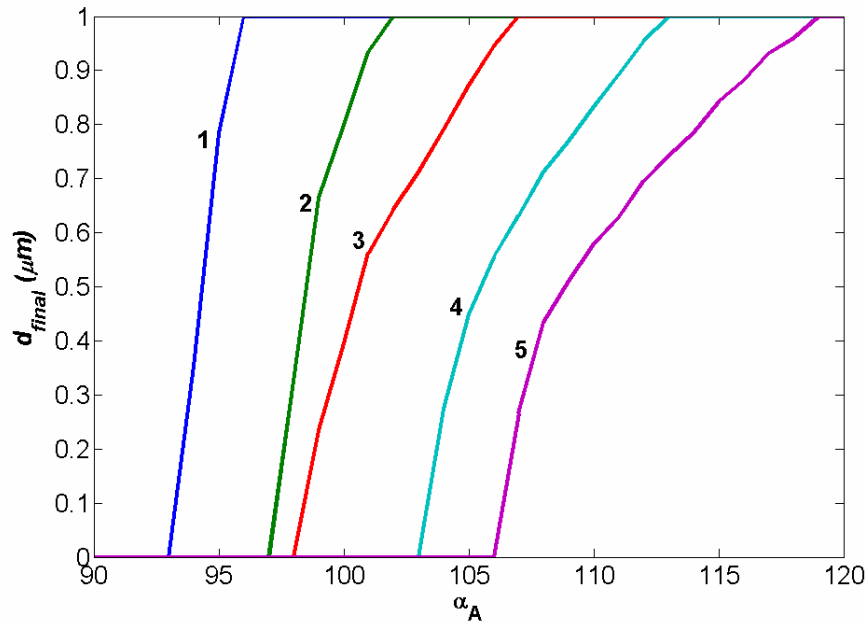
Figure 5-3: Final value of bubble size for a range of advancing contact angles and crevice half angles.

The strength of the surface tension is believed to have a significant effect on the stability of crevice bubbles under decompression and there is some uncertainty about what value would be expected for a physiological crevice bubble, Tikuisis (1986). The result of variations of the surface tension can be examined by variation of the non-dimensional surface tension parameter, σ'. The result of variations in this parameter, again for a range of advancing contact angle, is shown in Figure 5-4. If the surface tension is smaller, the crevice bubble can only support smaller compressions and hence a larger advancing contact angle is necessary. This is consistent with the Laplace equation which suggests that the smaller the value of the surface tension the smaller the pressure difference between the bubble and the ambient pressures that can be supported by the curvature of the interface.

The tissue half-time describes the rate of perfusion of gas in to or out of the tissue and is found to alter the rate of change of the interface angle, as illustrated in Figure 5-5 for the case where the advancing contact angle is not reached. Increasing the half-time results in a faster increase in the initial advancing contact angle variation; this is because the tissue takes longer to equilibrate with the atmosphere and hence there is a larger pressure difference allowing gas to be driven out of the bubble by diffusion. The main effect of variation in tissue half-time is the maximum value of contact angle that the interface makes with the crevice, Figure 5-5. Hence for a fast tissue (short

half-time) a smaller value of advancing contact angle would be needed if the bubble was to collapse, i.e. crevices embedded in fast tissue are more able to resist compression. The recovery of the interface angle back toward equilibrium is significantly slowed by an increase in tissue half time for the same reason: if the tissue takes longer to equilibrate with the atmosphere then it will similarly take longer for the pressure of the gas in the bubble to equal the atmospheric pressure.
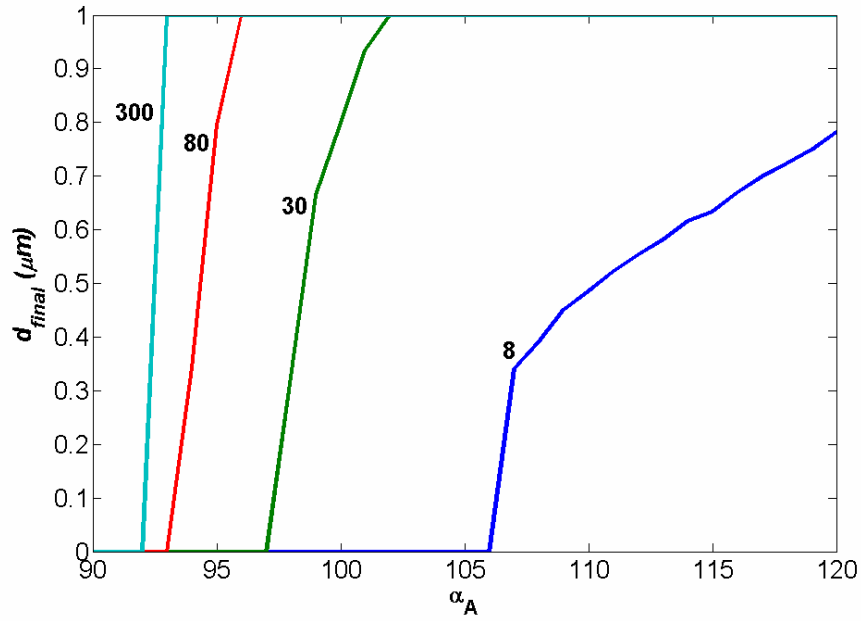

Figure 5-4: Final value of bubble size for a range of advancing contact angle and non-dimensional surface tension.
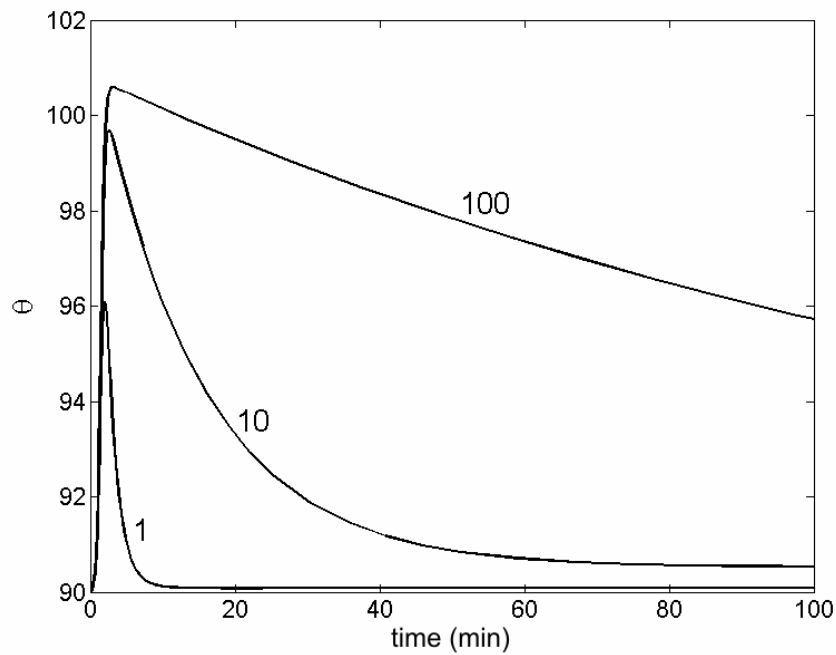

Figure 5-5: The effect on variation in interface angle of different tissue half times (minutes), with advancing contact angle > 101˚.

The diffusion time constant, τ_D, incorporates the gas diffusion constant, gas solubility in the tissue and the diffusion length for the gas, and governs the diffusion of gas between the bubble and the tissue across the crevice wall. Variations in this parameter, accounting for uncertainty in the underlying physiological parameters, are found to have negligible effect on the behaviour of the bubble. This is because the diffusion of gas between the bubble and the tissue is much faster than the perfusion dominated transfer of gas into the tissue from the blood. Hence for compression analysis of crevice bubble behaviour the precise value of diffusion time constant is unimportant; hence the uncertainty in the parameters that form this constant is not problematic.

Since compression only results in small changes in the volume of the bubble, gas transfer between tissue and bubble is not very significant. Hence the behaviour is not particularly dependent upon the gas diffusion time constant. The stability of the crevice bubble under compression is thus primarily controlled by the values of advancing contact angle, surface tension and crevice half angle. These all contribute to the bubble's ability to resist compression through the surface tension term in the Laplace equation.

5.3 Decompression behaviour

The behaviour of a crevice bubble under decompression is now also examined, again only considering a single inert gas, neglecting the metabolic gases and water vapour. A simple saturation decompression will be considered: the profile starts at 4 bar and consists of a decompression at a rate of $0.01 \ \mathrm{bar \ s^{-1}}$ ($0.6 \ \mathrm{bar \ min^{-1}}$) to 1 bar; essentially the reverse of the compression considered above. Using the default model parameters the simulation results for this decompression show that only θ varies, the bubble 'swelling' upward temporarily before returning to a flat interface.

The value of surface tension has already been shown to have a significant effect on the behaviour of a crevice bubble under compression and it is believed also to be significant in decompression, Tikuisis *et al.* (1983a). Surface tension is also known to be related to the number of vascular bubbles generated experimentally in pigs, Hjelde *et al.* (2000). Although values for surface tension of the order of $0.03 \ \mathrm{Nm^{-1}}$ may be expected in the body, it is thought that values of the order of $0.005 \ \mathrm{Nm^{-1}}$ may be observed, Tikuisis *et al.* (1983a). With this lower value of surface tension,

significantly different behaviour is observed, Figure 5-6. Initially the crevice wall surface angle reduces, the bubble interface 'swelling' upward until the receding contact angle is reached; whereupon the bubble starts to grow in length up the crevice; when it reaches the mouth the interface continues to become more convex, i.e. to 'bulge' out of the crevice. The interface curvature is now measured in terms of the vessel wall contact angle, γ, for illustrative purposes the value plotted in the figure is $\gamma - \pi/2$ so that the transition from variation in θ to γ is smooth. Once the limiting value of γ_s is reached a bubble detaches from the crevice (shown in the figure by '**o**') and the crevice is left 'full' of gas at the advancing contact angle, i.e. the interface is concave. The bubble continues to grow, 'swelling' out of the crevice, until it reaches γ_s again and another free bubble is released. This process continues until a total of 482 bubbles have been released, the rapid production of bubbles on the timescale of Figure 5-6 making it difficult to identify the production of individual bubbles. In the final stage, after approximately 800 seconds, no further free bubbles are released, although the bubble's interface does initially curve upwards out of the crevice. At the end, the gas pressure in the bubble is larger than the final value of tissue gas tension so gas diffuses back out of the bubble until the interface is flat, where bubble pressure is equal to ambient pressure which for a single inert gas is the final value of tissue gas tension.
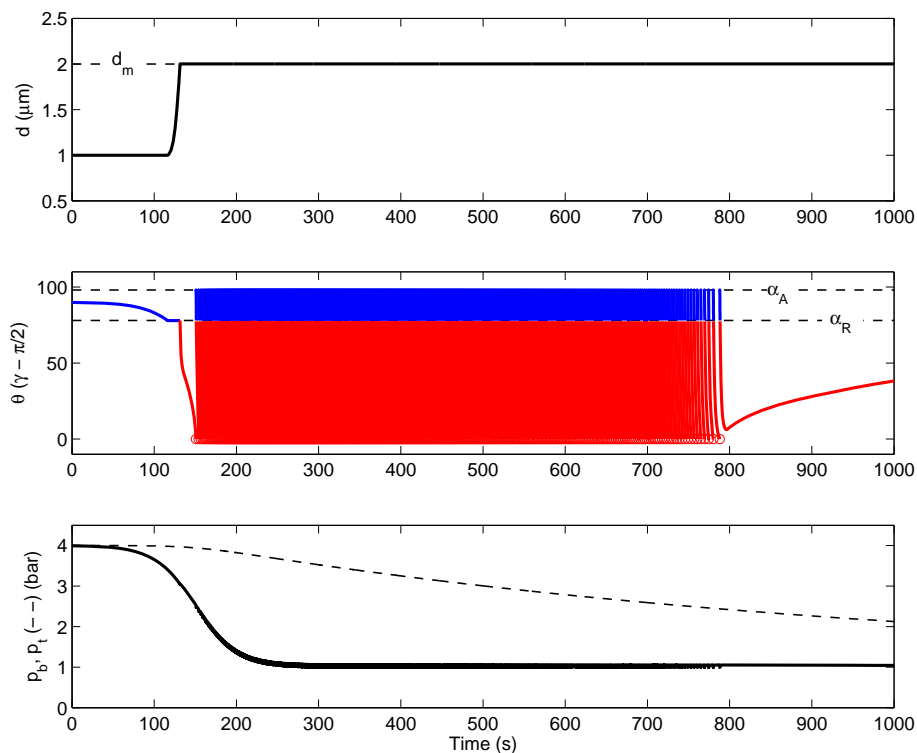

Figure 5-6: The growth of the crevice bubble and production of free bubbles under a 4 bar decompression from saturation.

The effect of variation in the surface tension value on the number of bubbles produced is shown in Figure 5-7. There is a limit at a surface tension value of approximately 0.09 Nm^{-1}, where higher surface tensions result in no bubbles being released. This occurs because with surface tensions greater than 0.09 Nm^{-1} the contact angle never reaches the critical value for the release of the bubble outside the crevice. This situation arises because as the bubble grows the tissue gas tension is also falling; bubble growth only proceeds as long as there is a pressure difference between bubble and tissue, driving gas into the bubble. As observed above, if the surface tension is high enough the bubble doesn't grow out of the crevice at all, this limit occurs around 0.22 Nm^{-1}. Therefore, one effect of lowering the surface tension is also to bring down the threshold for the bubble both to grow up the crevice and for the detachment of the bubble once it is outside the crevice. This appears to be the dominant effect of variations in surface tension, although a lower surface tension also increases the rate of gas influx into the bubble, because the average pressure difference between the bubble and the tissue is larger. For example, the rate of bubble production rises from 0.0119 bubbles s^{-1} with a surface tension of 0.005 Nm^{-1} to 0.0139 bubbles s^{-1} at 0.001 Nm^{-1}. However, this effect is much less marked for the total number of bubbles produced than that resulting from the change in threshold observed above.
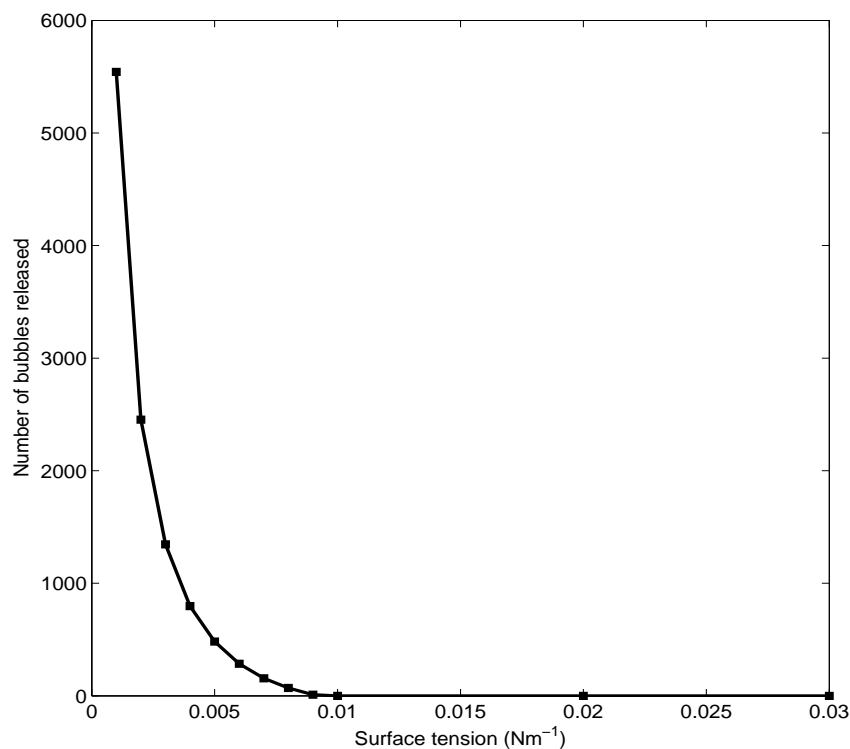

Figure 5-7: Variation in the number of bubbles produced from the crevice with changes in surface tension of the interface under a 4 bar decompression.

The parameter γ_s defines the size that the crevice bubble reaches as it emerges outside the crevice before a bubble is released. Figure 5-8 shows the variations with γ_s in the number of bubbles released and the total volume of gas liberated from the crevice. As might be expected, large values of γ_s, which result in a small quantities of gas being released in each free bubble, result in more bubbles being released. It might be expected that the total quantity of gas liberated would be approximately invariant with γ_s, i.e. few large bubbles or many small bubbles. However, this is only the case above $\gamma_s \simeq 90°$. Below this value there is a marked increase in the volume of gas liberated from the crevice as γ_s reduces. Similarly to variations in surface tension, the surface tension pressure term in the Laplace equation is important here. For smaller values of γ_s the surface tension pressure term is smaller at bubble release and hence the bubble pressure at detachment is smaller. Thus there will continue to be a pressure difference between bubble and tissue for longer; hence more bubbles will be released. Additionally this lower pressure will lead to a larger magnitude of gas flux and hence a faster rate of bubble release, although once again this effect is secondary.

Figure 5-9 shows the number of bubbles generated for variations in the crevice half angle, ϕ; again using a surface tension of 0.05 Nm^{-1}. For the conditions considered here the optimum crevice half-angle for maximum bubble production is about 5°. Increasing the crevice half-angle results in an increase in the width of the crevice mouth, which makes bubble growth outside the crevice easier, because the radius of curvature of the emerging bubble will be lower and hence the pressure due to surface tension will be smaller. However, the number of bubbles does not continue to increase with half-angle beyond 5°, although the total volume of gas liberated in bubbles does continue to increase, and does so in an almost linear fashion. Thus it is easier to liberate gas as the crevice gets wider, but because of the non-linear relationship between crevice half-angle and volume of gas liberated in each bubble the number of individual bubbles released falls.
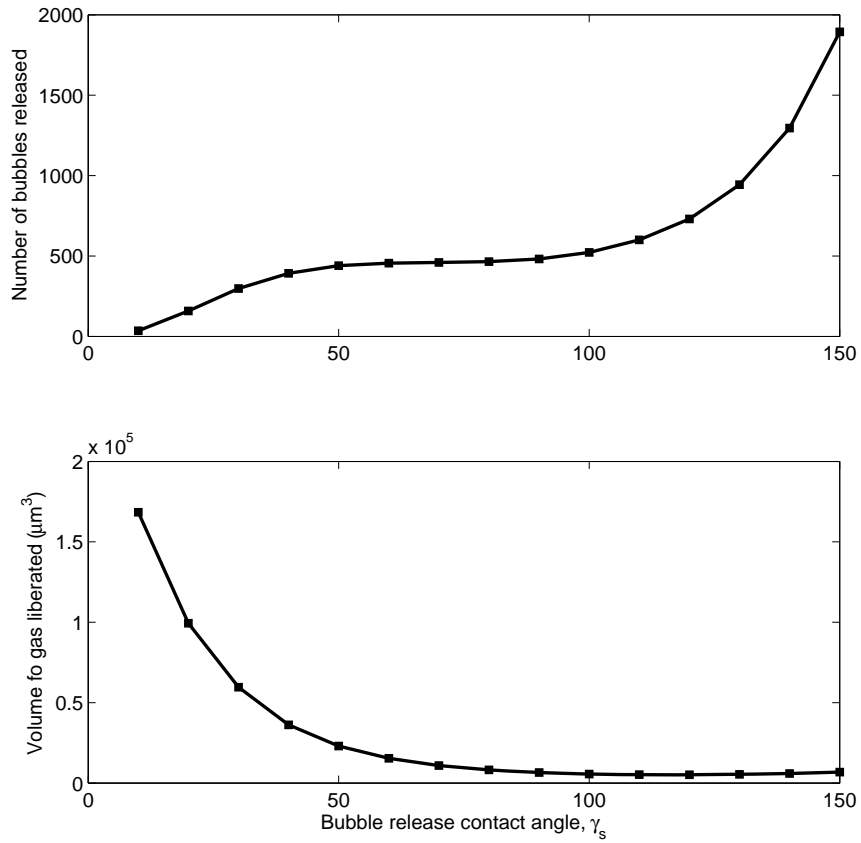
Figure 5-8: The effect on the number of bubbles produced and the total volume of gas liberated from a crevice with variation in γ_s, the bubble release contact angle.
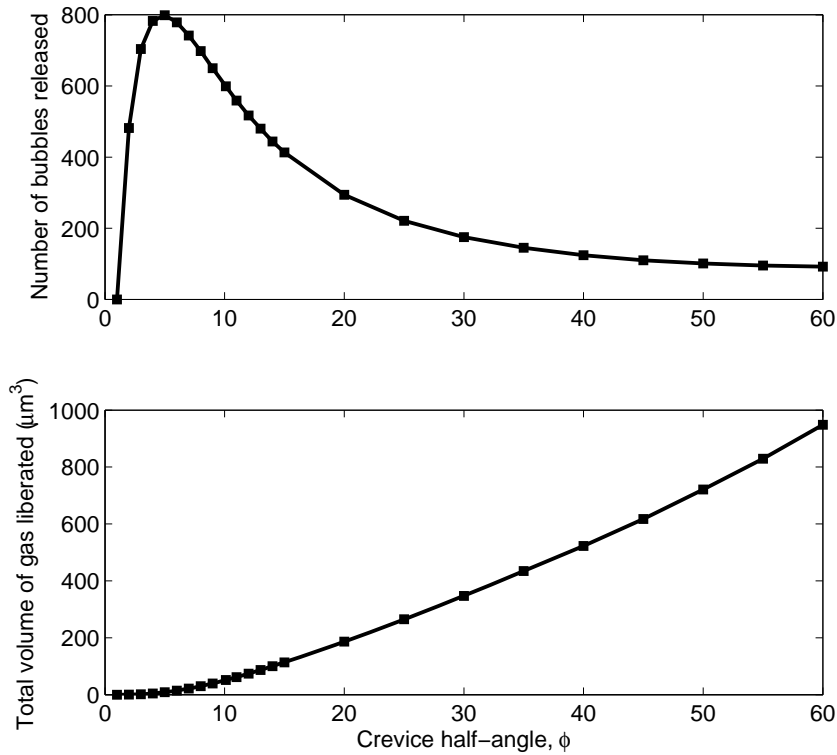

Figure 5-9: The effect on the number of bubbles produced and the total volume of gas liberated from a crevice with variation in crevice half-angle.

The value of the receding contact angle affects how easy it is for a crevice bubble to reach the crevice mouth: the smaller the value the more the bubble interface must change before the receding contact angle is reached and the bubble will grow in length up the crevice. It is possible for a bubble to resist decompression by variation of the bubble interface alone, if the receding contact angle is not reached. Hence the smaller the angle the more resistant the bubble will be to expansive growth. The receding contact angle could thus be regarded as a threshold that must be reached for any pressure profile before significant bubble growth can occur, this limit also being dependent upon the value of the surface tension. For example, with the baseline values of parameters from Table 4-2 the contact angle needs to be increased to 84° before the bubble will grow up the crevice under decompression, although the bubble then only briefly emerges outside the crevice, before settling back toward a flat interface at the crevice mouth. However, the dependence upon the value of surface tension appears to be more significant than on the receding contact angle.

The advancing contact angle has no obvious implication in bubble growth, since it is associated with the shrinkage of the bubble under compression. However, in the model derived here the advancing contact angle has been used as the value of interface curvature to which the crevice bubble returns after a free bubble has been released. Hence it will affect the size, and consequently the number, of bubbles released. However, variations in the value of the advancing contact angle are found to have a relatively small effect overall, for example with a surface tension of 0.005 Nm^{-1}, varying the advancing contact angle from 100˚ to 120˚ only reduces the number of bubbles produced from 482 to 426.

The effect of the length of the crevice, d_m on the number of bubbles produced and the total volume of gas liberated from one crevice is shown in Figure 5-10. The peak bubble production occurs around $d_m = 9 \ \mu m$, but the volume of gas liberated continues to increase, despite a reduction in number of bubbles released, as d_m increases. The effect of increasing d_m is similar to that of increasing the crevice-half angle, as both increase the width of the crevice mouth opening. Hence the results presented in Figure 5-10 are similar to Figure 5-9, although the shape of the number of bubbles released curve differs for each case, because the relationship between d_m and crevice mouth radius differs from that between crevice half-angle and mouth radius.

The gas diffusion time constant, τ_D, governs the rate at which gas enters the crevice from the tissue. Hence it has a significant effect on the rate of bubble production and the total number of bubbles produced. Figure 5-11 shows how the number of bubbles produced varies with τ_D, where a surface tension of 0.009 $\mathrm{Nm^{-1}}$ has been used to reduce the number of bubbles produced and hence the computation time. The results suggest a power law relationship between the number of bubbles, N_b, and the diffusion time constant:

$$N_b \simeq 5.89/\tau_D .$$

(5.1)

The tissue half-time also has an effect on the release of bubbles from the crevices. Unlike the gas diffusion time constant it does not affect the rate of production of bubbles, but it does determine the duration over which bubbles are released. Bubbles can only be released as long as there is a sufficient positive difference in gas tensions between the tissue and the bubble to drive gas into the bubble. Figure 5-12 shows that there is a linear relationship between tissue half-time and the number of bubbles produced (again using a surface tension of 0.009 $\mathrm{Nm^{-1}}$), except at very small values. Below approximately an 8 minute half-time no bubbles are produced. For smaller tissue half-times, by the time the bubble has grown to the bubble release contact angle the tension in the tissue has fallen sufficiently for there to be no gas transfer into the bubble because there is no pressure difference between tissue and bubble. For these conditions the threshold in tissue gas tension below which bubbles are no longer produced appears to be approximately 3.58 bar.

The decompression behaviour of the crevice bubble is more complex than under compression, because of the behaviour of the interface when it emerges outside the crevice. Similarly to compression behaviour the surface tension term in the Laplace equation play a very important role, thus the value of the surface tension, the crevice half angle and the crevice length affect the bubble behaviour, along with the receding contact angle, although to a lesser extent. However, unlike the compression behaviour, gas transfer is very significant for the bubble expansion under decompression. Thus the gas diffusion time constant is critical because it determines the rate of gas transfer and the tissue gas tension is important because it is the difference between this and the bubble pressure that drives gas into the bubble.
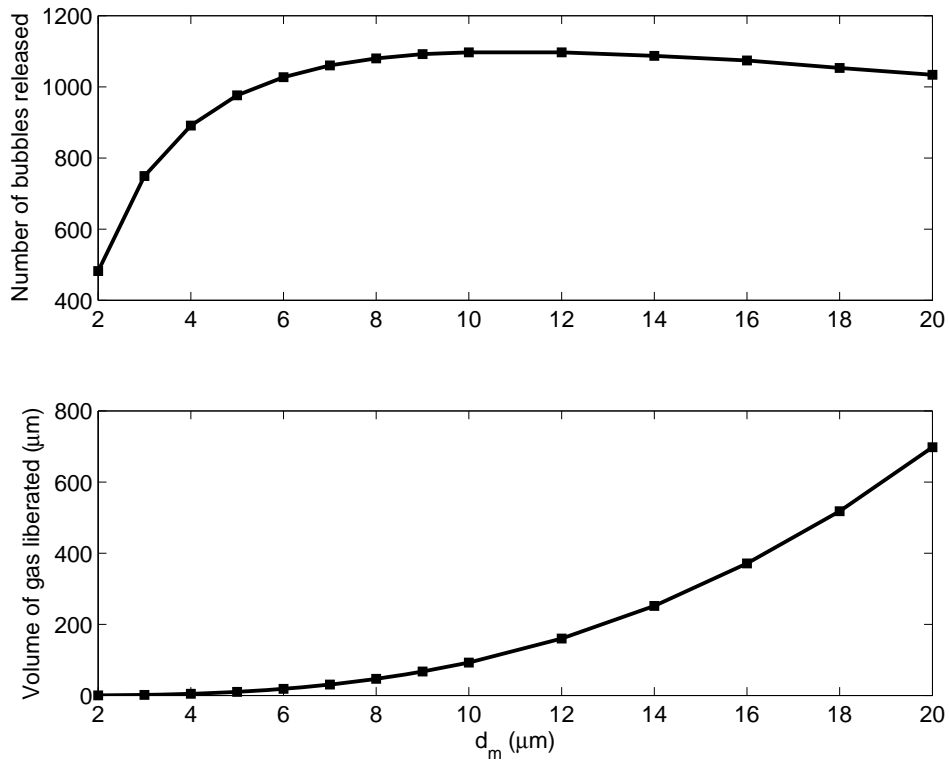
Figure 5-10: The effect on the number of bubbles produced and the total volume of gas liberated from a crevice with variation in crevice length.
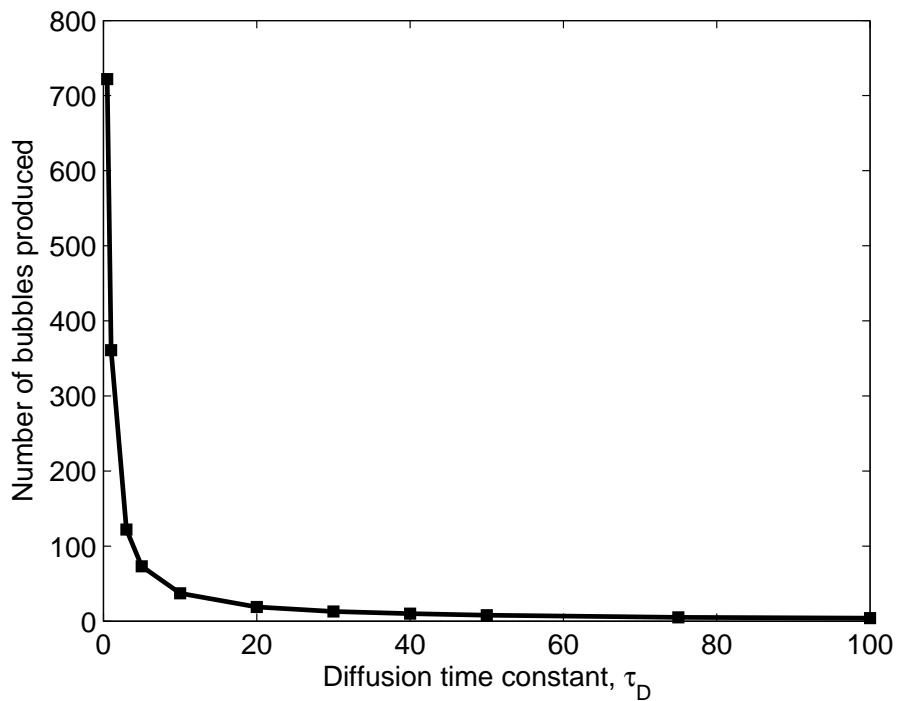
Figure 5-11: The effect of variation in the diffusion time constant (seconds) on the number of bubbles produced from the crevice.
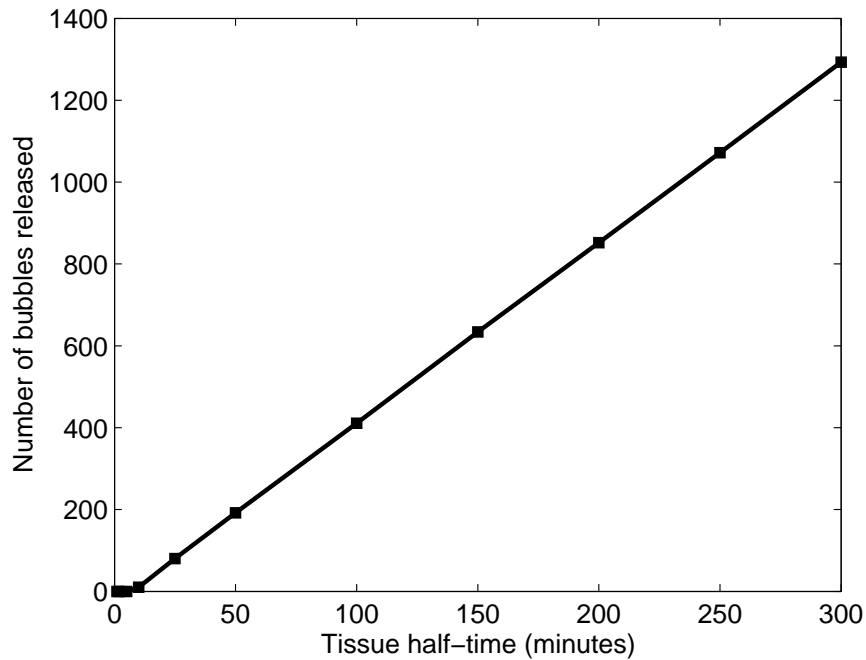
Figure 5-12: The effect on the number of bubbles produced from a crevice with variation in tissue half-time.

5.4 Discussion

5.4.1 Decompression behaviour

The number of bubbles released from the crevice under decompression is governed by two factors: pressure thresholds associated with the growth of the bubble and the rate of gas transfer into the bubble during growth. The existence of pressure thresholds for growth is very similar to the work of Atchley *et al.* (1989). In that work threshold values for the reduction in ambient pressure were determined for the unstable growth of a conical bubble nucleus neglecting gas transfer. It was the difference between bubble pressure and the ambient pressure which determined to what extent the bubble grew and whether this growth became unstable. Bubble growth was due to expansion of the gas, where a bubble would be expected to continue expanding until the internal pressure was the same as atmospheric pressure post-decompression.

However, in the dynamic model, gas transfer dominates, hence it is the difference between the bubble pressure and tissue gas tension which is critical, as the resulting gas transfer is what drives the large bubble growth observed here. Neglecting the expansion of the initial volume of gas in the bubble, which is small in comparison with the gas transfer volume, the bubble will grow only if the

tissue gas tension is greater than the bubble pressure, i.e. whilst gas transfers into the bubble. For this process two threshold values occur, both where the pressure in the bubble reaches a maximum:

- The interface reaches the receding contact angle inside the crevice. This corresponds closely with the first cavitation threshold identified by Atchley *et al.* (1989). According to that work this threshold may not necessarily occur when the interface first reaches the receding contact angle, but may occur later during the growth of the bubble up the crevice, as discussed further in chapter 6. However, for a narrow crevice, such as those primarily considered here, the first cavitation threshold and the pressure at the receding contact angle coincides. From the Laplace equation this threshold occurs at a pressure of:

$$p_i^1 = p_{amb} + \frac{2\sigma \cos \alpha_r}{d_0 \sin \phi}.$$

(5.2)

- The interface reaches a contact angle of γ_s with the external surface. This is a similar concept to the second cavitation threshold identified by Atchley *et al.* (1989). However their threshold was associated with the lateral growth of the bubble along the external surface, rather than detachment of the bubble interface. Again the pressure threshold can be calculated from the Laplace equation:

$$p_i^2 = p_{amb} + \frac{2\sigma \sin \gamma_s}{d_m \sin \phi}.$$

(5.3)

If the tissue pressure has fallen below the first threshold before the interface reaches the receding contact angle then the bubble will not grow up the crevice, i.e. there will be no nucleation at all. Likewise bubble detachment will not occur if the tissue gas tension is below the second threshold once the bubble has emerged outside the crevice. Additionally, this threshold sets the point at which bubbles stop being released; when the tissue gas tension drops below the second threshold, no more bubbles will be released, hence the value of this threshold and the tissue half-time are critical in determining the number of bubbles released. For example with the baseline parameters used in this chapter, but a surface tension of 0.009 Nm^{-1}, the second pressure threshold occurs at $p_i^2 = 3.58$ bar. This result was observed above when the effects of tissue half-time were explored, where it was found that bubble production ceased once the tissue gas tension fell to 3.58 bar.

Both thresholds are dependent upon the surface tension, which explains why this parameter is important in determining whether the bubble grows in the first place, as well as how many bubbles are released in total. Since both thresholds are also determined by the crevice half-angle, this is also an important parameter in determining the nucleus' behaviour. The value of crevice half-angle acts in conjunction with the 'vertical' position of the interface in the crevice, by setting the width of the crevice, which in turn relates to the radius of curvature. Thus both the initial value of d and the final length of the crevice are also found to have an impact on the behaviour. The first threshold is dependent upon the receding contact angle, thus, as observed above, this value can be seen in itself as a threshold for the initial growth of the bubble. The second threshold, however, is dependent upon the detachment threshold for the external contact angle.

Alongside the dependence of the bubble behaviour on the physiological parameters through the thresholds outlined above, the behaviour is also dependent upon the rate of gas transfer. This is determined by the diffusivity of the gas through the crevice wall, which is described in the model by the diffusion gas constant, as well as the gas concentration difference between the bubble and the tissue. The latter will vary during the course of the bubble growth, as the pressure in the bubble changes, with variation in the radius of curvature, and as the tissue gas tension falls due to perfusion. The average rate of bubble growth would be expected to be higher in short half-time tissues, although in such a case the tissue gas tension would fall more rapidly below the second pressure threshold and overall fewer bubbles would be produced than in a tissue with a longer half-time. Given that the pressure in the bubble is determined by the Laplace equation, in a similar manner to the pressure thresholds described above, it would be expected that the lower the values of the threshold, the lower (on average) the pressure would be in the bubble during growth, and thus the rate of gas transfer would likewise be larger. The result is higher bubble production rates, which was observed for variations in the surface tension in the results above. However, this effect is much smaller on the total number of bubbles produced than on altering the second pressure threshold.

5.4.2   Metabolic gases and water vapour

The results presented thus far have been related to the behaviour of a bubble for a single inert gas. In this section the effect of the inclusion of metabolic gases and water vapour is considered, using

the modification to the basic Laplace equation discussed in section 2.3.2.2, where the metabolic gases and water vapour are considered to contribute a fixed component to the bubble pressure, $p_{i,N}$, with a constant value of approximately 0.17 bar:

$$p_i = p_{amb} + \frac{2\sigma}{R} - p_{i,N} . \qquad (5.4)$$

The effect of the metabolic gases is such that when the gases in the crevice bubble are in equilibrium with the tissue, the total bubble pressure will be less than the atmospheric pressure. Hence in equilibrium the bubble interface would be expected to curve inward toward the root of the crevice. However, the offset between the equilibrium bubble pressure and atmospheric pressure only requires a relatively small increase in the interface angle of 0.3˚. For crevice bubbles the oxygen window increases the equilibrium value of the interface angle. It would be expected to make the bubble more susceptible to collapse under compression. This is found to be the case, as illustrated for variation in the magnitude of the applied compression in Figure 5-13. From comparison of this figure with Figure 5-2 it can be seen that larger advancing contact angles are required to prevent bubble collapse with the inclusion of metabolic gases, hence the bubble is less able to resist collapse. Additionally the 'oxygen window' will mean that if the bubble is in equilibrium with the tissue it will be under-saturated as compared to the blood, hence gas transfer would be expected across the bubble interface. As already noted this component is likely to be small and so can be neglected in consideration of the dynamic behaviour of the bubble. However, this may influence the steady state position of the bubble interface.

The alteration in the decompression behaviour of the bubble once the metabolic gases and water vapour have been included can be understood in terms of a change in the pressure threshold described above, along with a secondary alteration in the magnitude of gas transfer. The transfer of gas into the bubble is now determined by the difference between the total bubble pressure and the tissue's gas tension, i.e. $p_t > p_i + p_{i,N}$. Hence the effect is to shift upward the critical value of tissue gas tension which prevents bubble growth, in this case by 0.17 bar. Hence it will be more difficult, i.e. it will require a larger decompression, a lower surface tension or a smaller advancing contact angle, for the bubble to reach the receding contact angle and to grow. The result of raising the second pressure threshold will cause the production of bubbles to cease after a shorter duration;

hence fewer bubbles would be released. Additionally, the rate of gas transfer during the growth of the bubbles will also be reduced, because the difference between the pressure in the bubble and the tissue gas tension is smaller. Thus the rate of bubble production is reduced and fewer bubbles are produced, although this effect will be much smaller than that caused by the alteration of the pressure threshold.
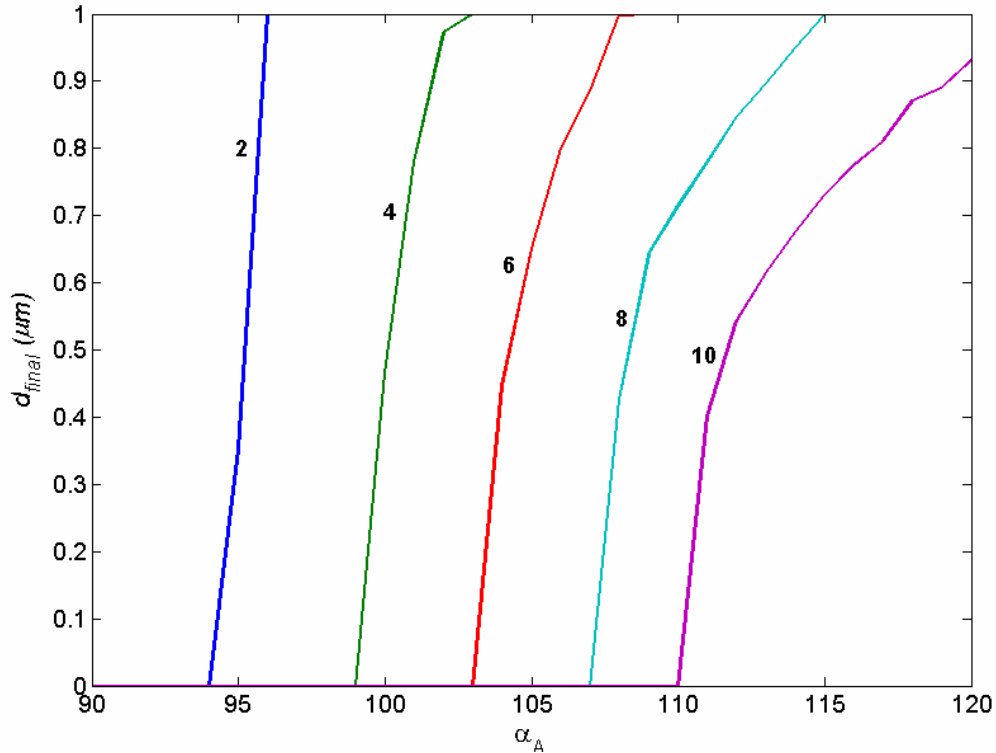
Figure 5-13: Final value of bubble size for a range of advancing contact angle and compression pressures (bar), when the metabolic gases have been included as infinitely diffusible gases.

The dynamic model can be modified to include the metabolic gases and water vapour. This is done firstly by inclusion of the $p_{i,N}$ term in the Laplace equation. Additionally, p_a, the arterial gas tension, is no longer equal to the ambient pressure but to the partial pressure of inert gas in the inspired gas mixture, i.e. $0.79 \times p_{amb}$ for air. Using this modified model the results as are expected; for example using the parameters in Table 4-2, except for a surface tension of 0.005 Nm^{-1}, the total number of bubbles produced is 482 which drops to 208 bubbles when the metabolic gases and water vapour is included. The mean rate of bubble production also falls, although this is only a small drop from 0.0119 to 0.0116 bubbles s^{-1}, confirming that it is the alteration of the pressure threshold that is the most significant.

5.4.3   Gas transfer across gas-blood interface

The model presented here has considered a crevice bubble connected via the crevice surface area to a reservoir of dissolved gas in a tissue. For crevices that might be found in a physiological environment, especially for the nucleation of bubbles in the blood, the assumption that gas cannot permeate across the bubble surface is potentially limiting. Given that the solubility and diffusivity of inert gases in the blood is a similar order of magnitude to that in tissues the relative importance of gas diffusion across the bubble's interface as compared to that through the crevice wall is governed by the relative surface areas and the pressure gradient.

The interface surface area is likely to be much smaller than the crevice surface area for bubbles of small crevice half angle, for example with a crevice half angle of 2° the surface area of the crevice wall within the bubble is almost 30 times as large as the bubble interface area. In general the partial pressure gradient of the gas for both diffusion routes will be similar unless the tissues have a very slow half time, when the gas tension in the tissue will significantly lag the value in the blood. Under these circumstances the transfer of gas across the interface may become more significant, especially if the crevice half angle takes a larger value.

Gas transfer through the bubble interface may also become more significant when the interface emerges outside the crevice: however, since the behaviour of the bubble in this region is less well understood, this assumption has been retained to keep the model as simple as possible. In particular the gas concentrations in the blood flowing past the crevice have not been considered directly, which prevents simple inclusion of the diffusion term across the blood-bubble interface. It would appear that in general the gas transfer across in the interface can be reasonably neglected in the generation of a simple model. However, its effects deserve further investigation, especially when the metabolic gases are included.

5.4.4   Gas diffusion time constant

In calculating the gas diffusion time constant the values for the solubility and the diffusivity of nitrogen have been taken from Srinivasan *et al.* (1999). In all four applications of their model, Srinivasan *et al.* (1999), Srinivasan *et al.* (2000), Srinivasan *et al.* (2002), (2003), a solubility of

0.0125 ml gas/ ml tissue was used and it is reasonable to assume a correspondence of their solubility to the Ostwald co-efficient employed here. Their chosen value for diffusivity ranged between 1.7×10^{-12} and 2.2×10^{-12} $m^2 s^{-1}$. Although the value for solubility is similar to those used in various other tissue bubble models, there is a discrepancy of three orders of magnitude between the value for diffusivity used by Srinivasan and colleagues and a number of other authors, Van Liew *et al.* (1993a), Burkard *et al.* (1994), Himm *et al.* (1999), Foster *et al.* (2000), Gürmen *et al.* (2001).

It is not clear what the source of discrepancy is, or from where Srinivasan and colleagues source their value. Lango *et al.* (1996) appears to be the most recent comprehensive review of the values of solubility and diffusivity of various gases in biological fluids, especially of those of relevance to the diving gases. This work illustrated the scarcity of experimental data for the solubility and diffusivity of nitrogen in biological tissues. For the Ostwald co-efficient of solubility the reported values in aqueous tissues is similar to that adopted here, possibly taking a slightly higher value near 0.015 ml gas/ ml tissue, nearer to the value in water. Values of the diffusion co-efficient in biological media are particularly scarce, but appear to take a value in the region of 1×10^{-9} $m^2 s^{-1}$, possibly slightly lower than that observed in water, which in again three orders of magnitude larger than that adopted by Srinivasan and colleagues. The gas diffusion time constant has been found to have a significant effect on the number of bubble produced by the crevice under decompression, because it determines the rate of gas influx into the bubble. The effect of this alternative value for the diffusivity of gas can be estimated from equation (5.1), which implies that the number of bubbles produced from the crevice would likewise increase by three orders of magnitude. This would imply a number of bubbles produced from one crevice that seems somewhat unrealistic. Although this effect might be rectified to some extent by a larger surface tension, if surface tension is too large bubbles are not released at all. Additionally the gas diffusion time constant also incorporates the characteristic length for diffusion, the value for which is not known; it is feasible that this value should also be larger than that used here, although as this increases there is greater probability that the diffusion region would incorporate blood vessels which complicates the diffusion field. Gas diffusion is a critical process for the growth and dissolution of decompression bubbles and would benefit from further investigation. It is possible that experiments performed in

the dissolution of cerebral gas emboli (e.g. Branger *et al.* (1999)) could provide further measurements to establish more reliable estimates for the gas diffusion time constant.

5.4.5   Surface tension

The strength of the surface tension is known to affect the rate of bubble production, Brubakk (2004), and has been confirmed here, Figure 5-7. It has previously been concluded that low values of surface tension would be required for the growth of crevice bubbles containing a single gas under decompression, Tikuisis *et al.* (1983a), which has also been confirmed here. However, very low surface tensions seem to be incompatible with stability of the bubble under compression. One way around this problem is the elliptical crevice geometry proposed by Tikuisis (1986), where the effective crevice half angle is smaller at the root of the crevice than at the mouth. This has the equivalent effect of having high surface tension at the root and low near the mouth. This geometry is also appropriate for the release of bubbles under decompression, since it is easier for bubbles to emerge from the crevice mouth when the mouth is wide, Tikuisis (1986). It is likely that the physiological crevices under consideration will not resemble geometrically the ideal conical pit considered here; it may be that an elliptical crevice is closer in form to the crevices found in the body, as it has a smoother transition in angle near the mouth. The effects of different crevice geometries are thus explored further in chapter 6.

5.4.6   Contact angles

In the examination of crevice bubbles in water, Crum (1979) has quoted values of advancing contact angle of the order of 106˚ for non-polar solids. Non-polar substances are known to have low interfacial energy and hence higher advancing contact angles. This value would translate to a crevice bubble that could resist compressions of over 6 bar, assuming the other physiological parameters used here. However, it is unclear how this advancing angle for non-polar surfaces could translate to physiological substances. Boyce *et al.* (1983) has reported an advancing contact angle of 86 ± 1˚ for a blood substitute on the endothelium of a rabbit's thoracic aorta.

It is possible that the advancing contact angle is itself dependent upon the surface tension, Crum (1979): the advancing contact angle can be written in terms of the equilibrium contact angle and a

hysterisis angle as: $\alpha_A = \alpha_E + \alpha_H$. It has been found that α_E can be expressed, for non-polar solids, by Crum (1979):

$$\alpha_E = -1 + \frac{C}{\sigma},$$
(5.5)

where C is a constant that depends upon the surface properties of the solid. Thus a crevice system with lower surface tension would have a larger advancing contact angle and hence the crevice bubble may be suitably resistant to collapse under applied pressure. The receding contact angle can be defined in a similar manner as: $\alpha_R = \alpha_E - \alpha_H$. Hence, a reduction in surface tension would result in a larger receding contact angle that may, by analogy to the compression behaviour, lead to greater bubble growth under decompression. It is far from clear, however, to what extent equation (5.5) can be applied in the physiological environment. The analysis presented here tends to suggest that the precise values of both contact angle limits are not vital as long as they fall within the expected hydrophobic range, as they have only limited effect on the behaviour of the bubble. Further experimental values of contact angles on physiological media would be valuable to establish in what range they lie, and thus the suitability of various surfaces to house nuclei.

5.4.7 Nucleation sites *in vivo*

In the derivation of the crevice bubble model a simple conical crevice has been used. However, as was noted in section 2.3.6 it is not clear what form nucleation sites in the vasculature may take. One candidate is intercellular clefts between the endothelial cells that line the blood vessels. Such clefts would have a similar geometry to a conical crevice across its width, although they may be closer in reality to the elliptical crevice geometry of Tikuisis *et al.* (2003). Intercellular clefts on the endothelium with half angles of approximately 1.6° have been reported in frogs, Clough *et al.* (1988), with depths of the order of 0.4 μm, which is shorter than the length used here. It is expected that the surfaces of the endothelium would be hydrophilic and present unsuitable contact angle limits for bubble nucleation. However, it is feasible that the surface properties of the intercellular clefts differ from that of the cell surfaces because contaminants collect within them. Alternatively, the vascular surface may be hydrophilic due to the collections of surfactants; muscular contractions may squeeze the inter-cellular clefts, clearing them of these surfactants to leave a hydrophobic surface.

Alternatively, more recently, Brubakk (2004) has proposed that blood bubbles may arise from caveolae. These are known to be flask shaped, or spherical, invaginations into the endothelial cells that line most blood vessels. The geometry of the opening of caveolae onto the blood would be similar to that of the conical crevice, although the internal geometry may produce different behaviour for the bubble when the interface inside the cavity, as explored in chapter 6. Since caveolae contain lipids it is likely that their surfaces would be hydrophobic as required for decompression bubble nucleation. Measurements of caveolae geometry are scarce, although Thorn *et al.* (2003) has reported caveolae with sizes in the range 25 to 150 nm, openings to the outside of the cell (for the larger caveolae) of the order of 20 nm for adipocytes. The sizes of these openings reported by Thorn *et al.* (2003) are smaller than those of the conical crevices modelled here.

5.5   Summary and conclusions

The crevice bubble model permits the nucleation of bubbles from crevices in the walls of the vasculature to be simulated. The results of the model under a simple compression suggest, as has been predicted, that the crevice bubble can resist compression by inversion of the interface radius of curvature. The model demonstrates that stability of the bubble occurs even when gas is free to enter or leave the bubble and the conditions for this are not greatly altered from those that could be predicted from considering the bubble closed using the Laplace equation alone.

Under decompression the dynamic model permits the simulation of the formation of a sequence of bubbles from the crevice. This is in contrast to previous stability analysis, which only determines the condition for unstable growth; the subsequent behaviour not being described. The decompression behaviour, in a similar manner to the results of stability analysis, is governed by thresholds associated with the movement of the interface up the crevice and the detachment of a bubble from the crevice. However, the amount of gas released from the crevice is primarily determined by the gas transfer into the bubble. Importantly, bubble production can only proceed whilst there is a driving pressure difference between the tissue gas tension and bubble pressure. Under this criterion the pressure threshold for bubble detachment and the tissue gas tension as determined by the tissue half-time interact. The model exhibits regions (or parameter values) where no bubbles are released from a crevice, this being mainly set by the pressure thresholds. Once

bubble production is feasible, large quantities of bubbles are produced from a single crevice. Thus the crevice bubble behaviour under decompression appears as very much an on/off process, i.e. either no or many bubbles are produced. This may imply that in the body many nucleation sites exist, but only a few have the correct conditions to produce bubbles under decompression or many nucleation sites are involved, but the physiological parameters fit within a relatively narrow range of values associated with low number of bubble produced per crevice.

Since accurate values for practically all the physiological parameters required in the model are not well established, various values have been explored here. This has allowed the general behaviour to be characterised although predictions for bubble production in the body due to decompression cannot be made at this stage. A critical piece of information needed for the simulation of nucleation in the body is details of the nuclei themselves. Although a conical crevice has been used here to facilitate the analysis, it is likely that real nucleation sites will have a more complex geometry. The added complexity of such geometry makes a full dynamic model infeasible for a generic cavity shape. However, it is important to establish what effect the nuclei geometry has on the nucleation behaviour and to what extent the results arrived at here may apply to a cavity of more generic geometry. Hence the subject of nuclei geometry will be addressed in the next chapter, returning to a stability approach to permit comparisons to be drawn.

6.   Analysis of the effects of cavity geometry*

6.1   Introduction

In chapter 4 a dynamic model was derived for a bubble nucleus in a conical crevice, allowing its behaviour under compression and decompression to be analysed. The conical crevice was intended to represent a nucleation site that may be found in the endothelium of a blood vessel and hence be the source of inter-vascular bubbles. Although very few sites have been proposed and the experimental evidence for any particular nucleation site geometry is very scarce, it is likely that the biological nucleation sites are not conical crevices. One of the primary advantages of analysing a conical crevice, however, was the simplicity of its geometry, which allowed the dynamic model to be derived. In this chapter the effects of varying the geometry of the nucleation sites will be examined. Since the derivation of a dynamic model rapidly becomes very complex as the geometry moves away from that of a simple conical crevice, the method adopted by Atchley *et al.* (1989) to analyse nucleation from a crevice will be adopted. Although this method is limited to a nucleus of constant mass content, i.e. no gas transfer, it will allow the effect of variation of cavity geometry on

---

* The work presented in this chapter appears as:
Chappell, M. A. and S. J. Payne (2007). "The Effects of Cavity Geometry on the Nucleation of Bubbles." The Journal of the Acoustical Society of America **121**: 853-862.

the nucleation process to be exploration. A modification to the method will also be proposed that permits gas transfer to be included.

6.2   Geometry

The cavity is defined with axial symmetry and a half-width, w, which is a function of the height above the base of the cavity, x, as shown in Figure 6-1. The contact angle between the interface and the cavity wall is composed of two angles:

$$\alpha = \theta + \phi, \tag{6.1}$$

where θ is the angle between the interface and the vertical and ϕ is the angle of the cavity wall to the vertical which is given by the slope of the cavity wall:

$$\phi = \arctan\left(\frac{\mathrm{d}w(x)}{\mathrm{d}x}\right), \tag{6.2}$$

hence:

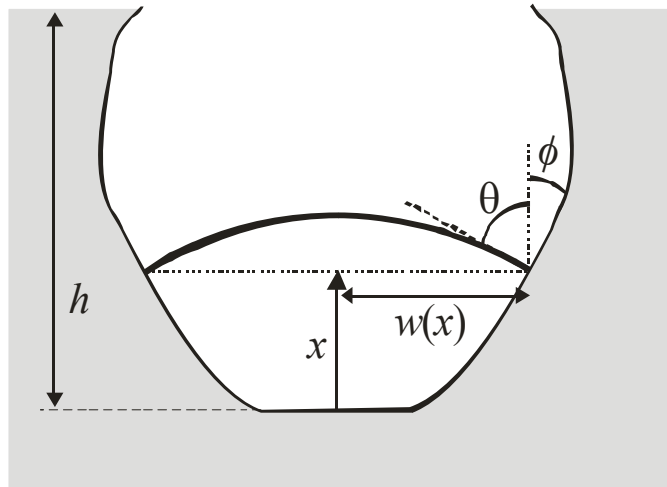$$\theta(x,\alpha) = \alpha - \arctan\left(\frac{\mathrm{d}w(x)}{\mathrm{d}x}\right). \tag{6.3}$$

Figure 6-1: Definition of parameters in a generic cavity.

6.2.1   Inside the cavity

The radius of curvature of the interface when it is inside the cavity can be found by treating the interface as the spherical cap of a sphere with radius:

$$R_{int}(x,\alpha) = \frac{w(x)}{\cos\theta(x,\alpha)}. \tag{6.4}$$

Likewise the volume can be found from the volume of the spherical cap described by the interface plus the volume of the cavity below the three-phase contact line:

$$V_{int}(x,\alpha) = \frac{1}{3}\pi R_{int}^3 \left[2 - \left(2 + \cos^2\theta(x,\alpha)\right)\sin\theta(x,\alpha)\right] + \pi \int_{\lambda=0}^{x} w^2(\lambda)\,\mathrm{d}\lambda. \qquad (6.5)$$

6.2.2 Emergence outside the cavity

Once the interface emerges outside the cavity the radius of curvature is given by the contact angle between the interface and the external surface, γ:

$$R_{ext}(\gamma) = \frac{w|_{x=h}}{\sin\gamma}. \qquad (6.6)$$

The volume of the gas pocket can also be defined, until γ equals the receding contact angle and the interface starts to grow along the external surface:

$$V_{ext}(\gamma) = \frac{1}{3}\pi R_{ext}^3 \left[2 + \left(2 + \sin^2\gamma\right)\cos\gamma\right] + \pi \int_{\lambda=0}^{h} w^2(\lambda)\,\mathrm{d}\lambda. \qquad (6.7)$$

6.2.3 Lateral growth

The lateral growth of the gas pocket along the external surface can be defined in terms of a variable half-width, w', which starts at the half-width of the cavity at its mouth. Hence the radius of curvature can be written as:

$$R_{ext}(w') = \frac{w'}{\sin\alpha_r}, \qquad (6.8)$$

with the volume being given by equation (6.7).

6.3   Analysis

Initially it will be assumed that there is no transfer of gas into or out of the bubble during expansion so that the gas content of the bubble remains constant. For simplicity only a single gas dissolved in the tissue is considered and hence:

$$p_i V_i = V_0 p_0, \qquad (6.9)$$

where V_0 and p_0 are the initial volume and bubble pressure respectively. Because the bubble is initially in equilibrium with the tissue $p_0 = p_t$. Hence the Laplace equation can be written as:

$$\frac{V_0 p_t}{V_i} + p_v = p_{amb} + \frac{2\sigma}{R}. \qquad (6.10)$$

From this equation it is possible to determine the liquid pressure and saturation values required for the interface to be stable at any position within the cavity. For nucleation due to super-saturation the condition $p_{amb} < p_t$ is of interest, i.e. the condition post-decompression.

Of particular interest are the critical values of p_{amb} which present a threshold to the growth of the gas pocket, hence a threshold to nucleation. This will analysed following the procedure set down by Atchley *et al.* (1989). It is assumed that the gas pocket is stable before the liquid pressure is reduced, hence initially the interface is close to flat with a large radius of curvature (this may be either positive for marginally super-saturated solution or negative for an under-saturated solution).

6.3.1   First nucleation threshold

As has already been noted, the first phase of expansion of the gas pocket proceeds by a reduction of the interface contact angle with the cavity wall. This will result in a reduction in the radius of curvature[*]. The reduction in radius of curvature leads to an increase in the pressure due to surface tension until the receding contact angle is reached. Hence the receding contact angle can be regarded as a threshold to nucleation, as given by:

$$p_{amb}^{A} = p_v - \frac{2\sigma}{R_{int}\left(x_0, \alpha_r\right)} + \frac{V_0 p_t}{V_{int}\left(x_0, \alpha_r\right)}. \tag{6.11}$$

However, as noted by Atchley *et al.* (1989), this will not represent an unstable threshold for growth of the gas pocket up the crevice unless the radius of curvature exceeds the critical radius. If it is not a unstable threshold, then further reduction in the liquid pressure, beyond p_{amb}^{A}, will be required for the gas pocket to continue to grow.

The critical radius can be determined by considering the stability of the collapsing and expanding forces as described by the Laplace equation. The left-hand side of the Laplace equation gives the expanding forces, the right-hand side the collapsing: when they are equal there is equilibrium. The equilibrium is only stable if the (negative) rate of change of the collapsing forces is larger than that of the expanding forces:

---

[*] Note that if the interface initially starts concave toward the base of the cavity, then the initial radius of curvature will be negative and growth will proceed by increases in the negative magnitude of R until it passes through infinity.

$$\frac{\mathrm{d}}{\mathrm{d}R}\left(\frac{V_0 p_t}{V_i} + p_v\right) < \frac{\mathrm{d}}{\mathrm{d}R}\left(p_{amb} + \frac{2\sigma}{R}\right). \tag{6.12}$$

The transition between stable and unstable behaviour is represented when equation (6.12) holds with an equality sign, giving the critical radius, beyond which the growth of the gas pocket becomes unstable. Performing the required differentiation gives the critical radius as a solution of:

$$\frac{p_t V_0 \dfrac{\mathrm{d}V_{int}\left(R,\alpha_r\right)}{\mathrm{d}R}}{V_{int}\left(R,\alpha_r\right)^2} = \frac{2\sigma}{R^2}. \tag{6.13}$$

Substituting back into the Laplace equation gives the corresponding pressure threshold:

$$p_{amb}^{B} = p_v - \frac{2\sigma}{R_c}\left(1 - \frac{V_{int}\left(R_c,\alpha_r\right)}{R_c \left.\dfrac{\mathrm{d}V_{int}\left(R,\alpha_r\right)}{\mathrm{d}R}\right|_{R=R_c}}\right). \tag{6.14}$$

Note that the value of contact angle for this analysis is the receding value, making the assumption that is only necessary to calculate this threshold during the second phase of growth, i.e. either the critical radius has already been exceeded by the time the receding contact angle has been reached at the end of the first phase, or it represents a further threshold to growth during the second phase. This assumption is discussed further later. For a conical crevice, as considered by Atchley *et al.* (1989), V_{int} can be written as a simple function of R^3 and thus equation (6.13) can be solved for the critical radius. However, for a more general cavity shape an explicit analytical solution is not guaranteed.

The next phase of growth of the gas pocket is movement of the interface up the cavity. If the critical radius has already been exceeded then unstable growth will proceed. Otherwise growth will remain stable, i.e. it will only continue as long as the liquid pressure is sufficiently low. The smaller of the two of these pressure values is thus the threshold for unstable growth within the cavity and is defined by Atchley *et al.* (1989) as the first threshold for cavitation, which here shall be called the first nucleation threshold.

6.3.2 Second nucleation threshold

Once the interface has reached the cavity mouth there is a sharp change in the slope of the wall from the inside of the cavity to the external surface. The interface now has a 'new' contact angle between itself and the external surface. As the value of this contact angle will be greater than the receding contact angle, growth of the gas pocket will proceed by the reduction in this external contact angle, γ. Thus a further threshold is expected at the point where $\gamma = \alpha_R$:

$$p_{amb}^{C} = p_v - \frac{2\sigma}{R_{ext}(\alpha_r)} + \frac{V_0 p_t}{V_{ext}(\alpha_r)}. \tag{6.15}$$

Again this only represents a threshold to unstable growth if the radius of curvature is greater than the critical radius. Since the interface has emerged outside of the cavity there may be a smaller critical radius, and hence threshold on pressure, than that found above for inside the crevice. Once again the critical radius can be found by considering the transition from stable to unstable at the equilibrium point:

$$\frac{p_t V_0 \dfrac{dV_{ext}(R_{ext}, \alpha_r)}{dR_{ext}}}{V_{ext}(R_{ext}, \alpha_r)^2} = \frac{2\sigma}{R_{ext}^2}. \tag{6.16}$$

Unlike the volume of the gas pocket when inside the cavity, the volume of the pocket once it has emerged can be given as a simple function of the radius of curvature from equation (6.7):

$$V_{ext}(\gamma) = g(\gamma) R_{ext}^3 + V_v, \tag{6.17}$$

where:

$$g(\gamma) = \frac{1}{3}\pi\left[2 + (2 + \sin^2 \gamma)\cos\gamma\right], \tag{6.18}$$

$$V_v = \pi \int_{\lambda=0}^{h} w^2(\lambda)\,d\lambda. \tag{6.19}$$

The critical radius is then a root of:

$$2g(\alpha_r)^2 \sigma R_{ext}^6 - 3g(\alpha_r) p_t V_0 R_{ext}^4 + 4g(\alpha_r) V_v \sigma R_{ext}^3 + 2V_v^2 \sigma = 0. \tag{6.20}$$

Two approximate cases may be considered. In the first, $V_c \ll g(\gamma) R^3$, i.e. the volume of the spherical segment outside the cavity is much larger than the total volume of the cavity. The radius of curvature, and hence the corresponding pressure threshold, can then be found explicitly, Atchley *et al.* (1989):

$$p_{amb}^{D} \approx p_v - \frac{4\sigma}{3} \sqrt{\frac{2\sigma\gamma(\alpha_r)}{3V_0 p_t}} \,. \tag{6.21}$$

In the second case $V_v \gg g(\gamma)R^3$, the volume of the cavity exceeds that of the spherical segment outside the cavity. Under these conditions the Laplace equation simplifies to:

$$\left(\frac{V_0}{V_v}\right)p_t + p_v = p_{amb} + \frac{2\sigma}{R}, \tag{6.22}$$

which, once the stability of the equilibrium point is considered, gives an infinite critical radius, i.e. at a flat interface curvature. Hence, the growth would be unstable once the receding contact angle with the external surface is exceeded.

6.3.3 Critical radii

As has already been noted in calculating the critical radius within the crevice, it has been assumed that either it has been exceeded during the first phase of growth or it occurs during the second phase, where the contact angle equals the receding value. This is also true for the critical radius for growth outside the cavity in relation to the third and fourth phases. However, it is possible for the critical radius to occur during the first phase and to require a liquid pressure that is smaller than the value to reach the receding contact angle. According to the analysis presented so far, under these conditions no valid value of p_{amb}^{B} would be found (the critical radius does not occur during the second phase) and so the value of p_{amb}^{A} would be taken as critical, but it would be larger than the true threshold. Strictly, therefore, it should be determined whether during the first phase there is a 'critical contact angle' (with x fixed at the initial value) and during the second phase a 'critical length' (with α fixed at the receding value). The 'critical contact angle', α_c, is the solution of:

$$\frac{\mathrm{d}}{\mathrm{d}\alpha}\left(\frac{V_0 p_t}{V_{int}(x_0,\alpha)} + p_v\right) = \frac{\mathrm{d}}{\mathrm{d}\alpha}\left(p_{amb} + \frac{2\sigma}{R_{int}(x_0,\alpha)}\right). \tag{6.23}$$

A physically relevant solution only exists if $\alpha_0 \geq \alpha_c \geq \alpha_r$. Similarly the 'critical length', x_c, can be determined from:

$$\frac{\mathrm{d}}{\mathrm{d}x}\left(\frac{V_0 p_t}{V_{int}(x,\alpha_r)} + p_v\right) = \frac{\mathrm{d}}{\mathrm{d}x}\left(p_{amb} + \frac{2\sigma}{R_{int}(x,\alpha_r)}\right). \tag{6.24}$$

Again a physically relevant solution only exists for $x_0 \le x_c \le h$. If the solution to equation (6.24) is given by $x > h$, then the critical value lies beyond the height of the cavity, so under these conditions the critical length would correspond to the interface reaching the crevice mouth i.e. $x_c = h$. The appropriate pressure thresholds can be determined by substitution back into the Laplace equation:

$$p_{amb}^{B'} = p_v - \frac{2\sigma}{R_{int}(x_0, \alpha_c)} \left(1 - \frac{V_{int}(x_0, \alpha_c)}{R_{int}(x_0, \alpha_c) \left. \frac{dV_{int}(x_0, \alpha)}{d\alpha}\right|_{\alpha=\alpha_c}} \right), \qquad (6.25)$$

$$p_{amb}^{B} = p_v - \frac{2\sigma}{R_{int}(x_c, \alpha_R)} \left(1 - \frac{V_{int}(x_c, \alpha_R)}{R_{int}(x_c, \alpha_R) \left. \frac{dV_{int}(x, \alpha_R)}{dx}\right|_{x=x_c}} \right). \qquad (6.26)$$

Note that p_{amb}^{B} as determined by x_c in equation (6.26) will be the same as that defined in equation (6.14) when the critical radius, as defined earlier, exists. Likewise the same should be done for the third and fourth phases to determine the critical values outside the cavity. Thus:

$$p_{amb}^{D} = p_v - \frac{2\sigma}{R_{ext}(w'_c)} \left(1 - \frac{V_{ext}(\alpha_r, w'_c)}{R_{ext}(w'_c) \left. \frac{dV_{ext}(\alpha_r, w')}{dw'}\right|_{w'=w'_c}} \right), \qquad (6.27)$$

where w'_c is the solution of:

$$\frac{d}{dw'}\left(\frac{V_0 p_t}{V_{ext}(\alpha_R, w')} + p_v \right) = \frac{d}{dw'}\left(p_{amb} + \frac{2\sigma}{R_{ext}(w')} \right), \qquad (6.28)$$

the definition of R_{ext} in equation (6.8) being used and $w'_c > w|_{x=h}$. Additionally, a critical radius may be found before the receding contact angle with the external surface is reached at a liquid pressure of:

$$p_{amb}^{D'} = p_v - \frac{2\sigma}{R_{ext}(\gamma_c)} \left(1 - \frac{V_{ext}(\gamma_c)}{R_{ext}(\gamma_c) \left. \frac{dV_{ext}(\gamma)}{d\gamma} \right|_{\gamma=\gamma_c}} \right), \qquad (6.29)$$

where γ_c is the solution of:

$$\frac{d}{d\gamma}\left(\frac{V_0 p_t}{V_{ext}(\gamma)} + p_v \right) = \frac{d}{d\gamma}\left(p_{amb} + \frac{2\sigma}{R_{ext}(\gamma)} \right), \qquad (6.30)$$

with R_{ext} as defined in equation (6.6) and $(\alpha_r - \beta + \pi/2) > \gamma_c > \alpha_r$.

Atchley *et al.* (1989) do not make the distinction that has been made here; however, this may not be particularly significant given the conditions which they considered. The critical radius is determined both by the extent to which the volume has increased and the change in the pressure due to surface tension. During the first phase of expansion the change in volume is typically relatively small; hence the required liquid pressure is dominated by variations in the surface tension term. This term gets smaller as the radius of curvature increases with reduction in contact angle. Hence the critical value of pressure will occur at the limit of contact angle variation: the receding value. This is less likely to be the case once the interface has emerged outside the cavity, as, during the third phase of growth, variations in contact angle (now with the external surface) can lead to more significant variations in volume. However, if the volume of the cavity is much greater than that of the spherical segment, once again the significance of this volume change is small and it would be expected that if the critical radius occurred before the receding contact angle, it would be exceeded with a higher liquid pressure than that needed for reach the receding contact angle.

6.4 Numerical results

Atchley *et al.* (1989) noted that the picture that emerged from the analysis of nucleation in the conical crevice was very complex and this is no less the case for the analysis of more generalised crevice geometries presented above. To establish the threshold for nucleation it is strictly necessary to test all four of the thresholds considered above to determine the limiting case. For the general case, this is complicated further because in two cases an analytic expression may not be available. Hence, like Atchley *et al.* (1989), the behaviour of different types of cavity will be examined using

numerical solutions. The numerical results will be presented as plots of volume occupied by the gas against the pressure in the liquid, showing the evolution of the gas pocket as the liquid pressure falls until the interface on the external surface has reached the receding contact angle and it has grown along the external surface up to twice the width of the cavity mouth. For comparison with previous work we will plot the quantity $p_v - p_{amb}$ as the x-ordinate and volume of the gas pocket as the y-ordinate.

Four types of cavity are considered:

1. Conical crevice, Figure 6-2a:

$$w(x) = x \tan(\beta).$$
(6.31)

 Since this is used in the model derived in chapter 4, this is the basis for comparison with other cavities.

2. Cylindrical cavity, Figure 6-2b:

$$w(x) = c.$$
(6.32)

 This geometry is even simpler than that of the conical crevice, although it seems less likely that biological nuclei would take this form. However, this form of cavity has been used to model the formation of bubbles in carbonated beverages, Liger-Belair *et al.* (2005), Uzel *et al.* (2006), as it has been found that nucleation occurs in hollow cylindrical fibres trapped on the walls of the glass, Liger-Belair *et al.* (2002).

3. Elliptical crevice, Figure 6-2c:

$$w(x) = b\left(1 - \sqrt{1 - \frac{x^2}{h^2}}\right).$$
(6.33)

 This is a variation on the conical crevice proposed by Tikuisis (1986), where in principle it is easier for the gas pocket to emerge from this form of cavity and the smooth transition between the inside of the cavity and outside surface may be a more realistic model of true nucleation sites.

4. Spherical cavity, Figure 6-2d:

$$w(x) = \sqrt{r^2 - (x-1)^2},$$
(6.34)

with a penetration, fraction of the diameter of the sphere within the surface, given by $z = h/2r$. This is a simple model for caveolae as the source of bubbles in the blood as proposed by Brubakk (2004). Caveolae are spherical invaginations into endothelial cells found on the lining of blood vessels, Rothberg *et al.* (1992). This cavity shape is also similar to the reservoir type of nucleation site, for example Sluyter *et al.* (1991).
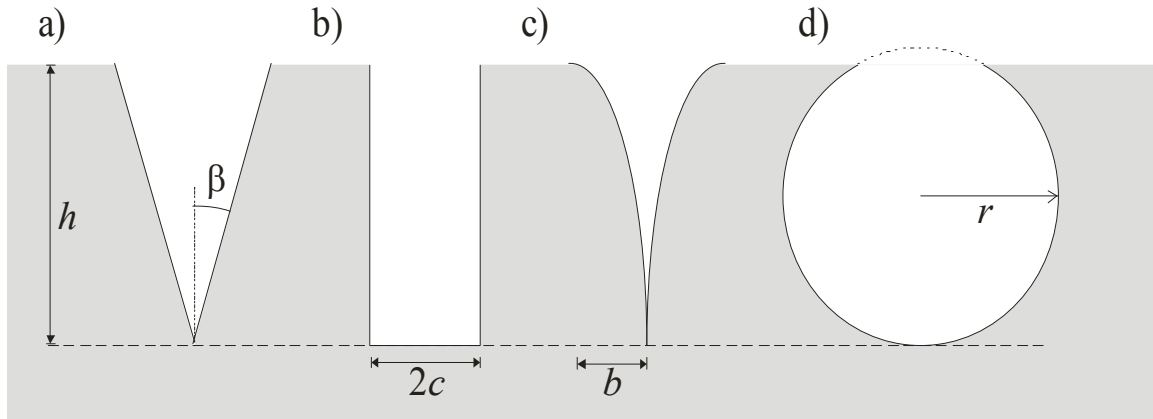

Figure 6-2: Geometry of the four cavities.

To compare these four cavity types, the dimensions are chosen so that they are all compatible: the height and size of opening onto the external surface of each is set equal to that of the conical crevice. The parameters used for the cavities are shown in Table 6-1, a receding contact angle of 80° being used to make the cavity hydrophobic, and the interface starting one quarter of the way up the crevice, $x_0 = h/4$. Surface tension is taken to have a value of 0.03 Nm^{-1} as originally used in chapter 4.

Figure 6-3 shows the evolution of the gas pocket for decompression from atmospheric pressure (p_t = 1 bar). Unlike the other three cavities, the elliptical cavity (c) does not have a threshold for the receding contact angle with the external surface, because the smooth transition at the mouth of the elliptical crevice means that at the surface the interface is already at the receding contact angle. In most cases there is no p_{amb}^{B}, as for both the conical and elliptical crevice it has already been exceeded by the interface reaching the receding contact angle, growth of the interface after this point resulting in a reduction in the required pressure. The cylindrical cavity, however, never reaches the critical radius: once the internal receding contact angle threshold is reached, the pressure continues to fall as the interface moves up the crevice, but no maximum is ever reached.

The spherical cavity does have a p_{amb}^{B} threshold, which occurs at the maximum pressure during the second phase of growth. For the conical and elliptic crevices and the spherical cavity there is also a p_{amb}^{D} threshold at a smaller volume than the p_{amb}^{C} value, i.e. the critical radius outside the cavity occurs during the third phase.

Table 6-1: Geometric parameters used for the four different cavity types.

Geometric parameter	Value
Conical crevice	
h	2 μm
β	15°
Cylindrical cavity	
h	2 μm
c	0.536 μm
Elliptical crevice	
h	2 μm
b	0.536 μm
Spherical cavity	
r	1.071 μm
z	0.933

It is the elliptical cavity which has the lowest threshold value of liquid pressure for nucleation; hence it is the hardest in which to promote nucleation. The other three have relatively similar minimum values for p_{amb} (in all three cases being associated with $p_{amb}^{D'}$), which is not surprising since once the interface has emerged outside the cavity the behaviour is primarily dominated by the surface tension term in the Laplace equation, the volume ratio term becoming small as the total volume of the gas pocket increases. This means the behaviour is dominated by the radius of curvature which will be the same for all these three cavities as they have been chosen to have the same radius of opening onto the external surface.
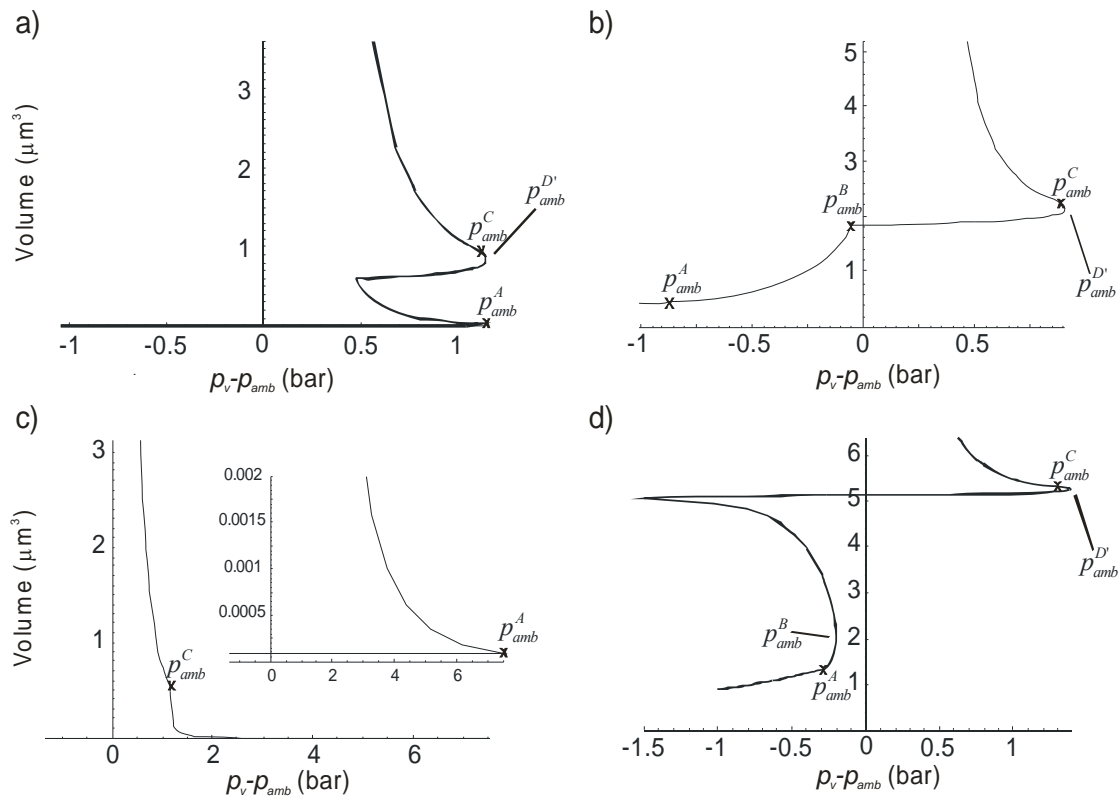
Figure 6-3: The evolution of the gas pocket in the four different cavity types: a) conical crevice, b) cylindrical cavity, c) elliptical crevice, d) spherical cavity.

In all cases the value of liquid pressure that would be required for nucleation is negative, hence in all cases it would be impossible, under these conditions, to cause the gas pocket interface to reach the stage where it spreads outwards along the external surface. However, this may not be the most appropriate definition for nucleation in many circumstances. The behaviour of the gas pocket once it has emerged is also determined by the conditions in the liquid, for example the presence of a flow. These conditions will dictate the nucleation behaviour of the interface outside the cavity, and hence the threshold for the emergence of the interface may be most important. Under the conditions assumed here the interface cannot emerge from either the conical or the elliptical crevice; in both cases it is p_{amb}^{A} that is critical. For the cylindrical cavity the critical radius inside the cavity is never reached, as the minimum value of p_{amb} occurs once the interface reached the cavity mouth. This is unlike the spherical cavity which reaches the critical radius relatively early within the growth of the gas pocket and hence is relatively easy to promote to emergence out of the cavity.

Figure 6-4 shows the evolution of the gas pocket in the four cavities if the interface starts half-way up the inside of the cavity, $x_0 = h/2$. The cylindrical and spherical cavities are largely unaffected

by this change. However, the threshold for nucleation, which is also the threshold for emergence, for the elliptical crevice is now substantially higher, hence it is easier to promote nucleation. The threshold for nucleation for the conical crevice is unaltered, although the behaviour within the crevice has changed and it is now easier for it to emerge than previously. As with the examples in Figure 6-3, for the elliptical crevice, cylindrical and spherical cavities the critical pressure for the second nucleation threshold is given by $p_{amb}^{D'}$, although in this case this threshold is practically indistinguishable from p_{amb}^{C}.
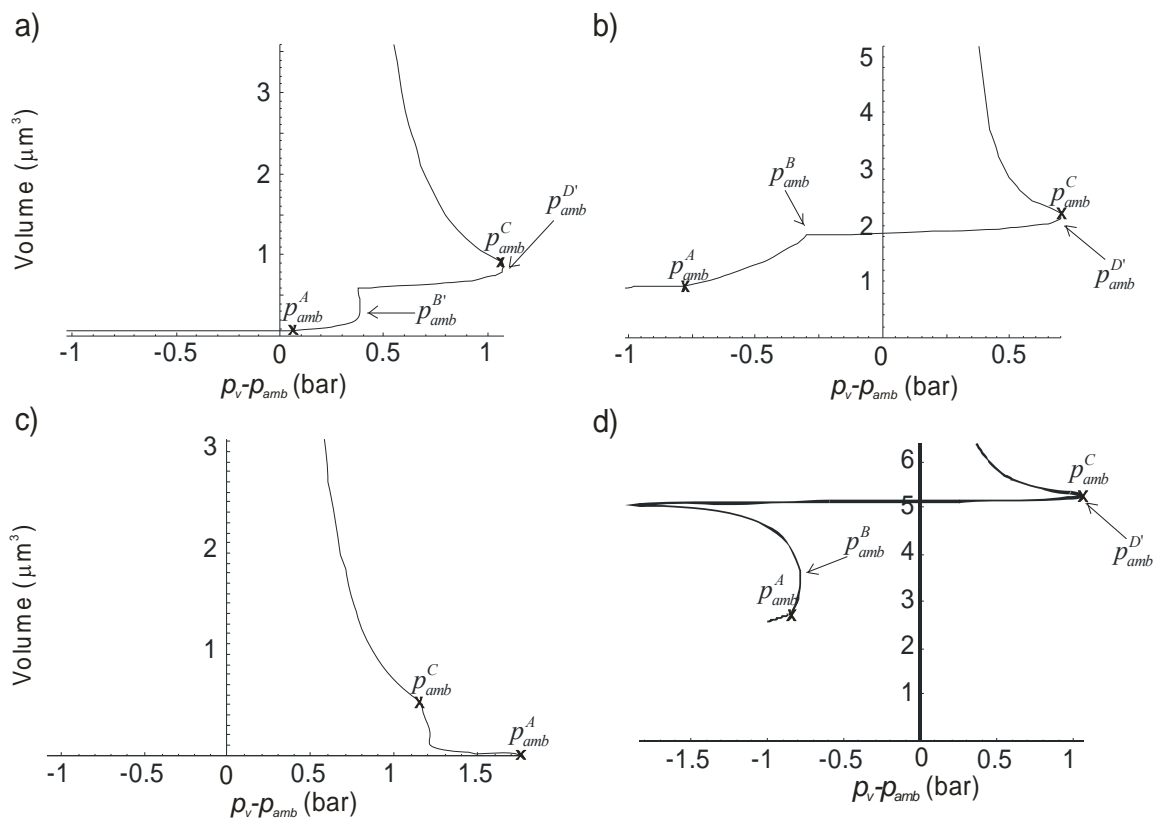
Figure 6-4: Evolution for the gas pocket in the four different types of cavity, when the interface initially starts half-way up the cavity: a) conical crevice, b) cylindrical cavity, c) elliptical crevice, d) spherical cavity.

6.4.1 Effect of surface tension

The effect of surface tension is introduced by the Laplace equation, where it contributes a pressure in the bubble that scales with the inverse of the interface radius of curvature. Thus it appears in the equations that define the pressure thresholds for growth of the bubble. From the threshold equations it can be seen that the surface tension scales the magnitude of the pressure threshold. Thus if surface tension is increased the pressure thresholds on Figure 6-3 and Figure 6-4 would

move closer to the y-axis. Hence it requires a larger reduction in liquid pressure to reach those thresholds that lie to the left of the y-axis, implying that nucleation is more difficult. Although the thresholds to the right of the y-axis move toward lower pressures, these are not attainable by decompression, because these require a negative liquid pressure. Additionally, it is impossible to make these un-attainable pressure thresholds possible by surface tension, as it cannot change the sign only the magnitude of the threshold. Thus increasing surface tension increase the magnitude of decompression required for nucleation to occur and vice-versa. This could be predicted, as surface tension resists an increase size of the bubble.

6.4.2   Effect of gas transfer

In the analysis above it has been assumed that there is no gas transfer in or out of the gas pocket during growth. Gas transfer is primarily a time dependent process and not readily amenable to the stability analysis used here. However it is possible to propose a simple modification to the constant volume analysis used thus far which allows the change of behaviour with gas transfer to be considered. The constant mass assumption embodied in equation (6.9) is replaced with:

$$p_i V_i = k V_0 p_t ,$$
(6.35)

where the total mass in the gas pocket is permitted to increase to a multiple, k, of the original value. Strictly gas transfer will be a gradual process over time and equation (6.35) cannot apply at the start of the evolution of the gas pocket. Hence the approximation will be taken that the increase in mass occurs during the first phase of growth, and there is no further transfer during the latter phases. The result of this for a range of values of k is shown in Figure 6-5. The lines in Figure 6-5 can be treated as iso-k-contours, hence it is possible to consider gas transfer during the second phase by movement from smaller to larger k-contours as time progresses. The effect of gas transfer is to reduce significantly the first nucleation threshold, for the interface to exit the cavity. Thus, if the decompression is insufficient for the first nucleation threshold to be reached, the effect of gas transfer will mean that interface will only become unstable once sufficient time has passed for an increase in k to occur. The behaviour outside the cavity is largely unaltered by gas transfer. Once again this can be understood by the reducing significance of the volume term in the Laplace equation once the gas pocket has grown outside the cavity.

a)

b)
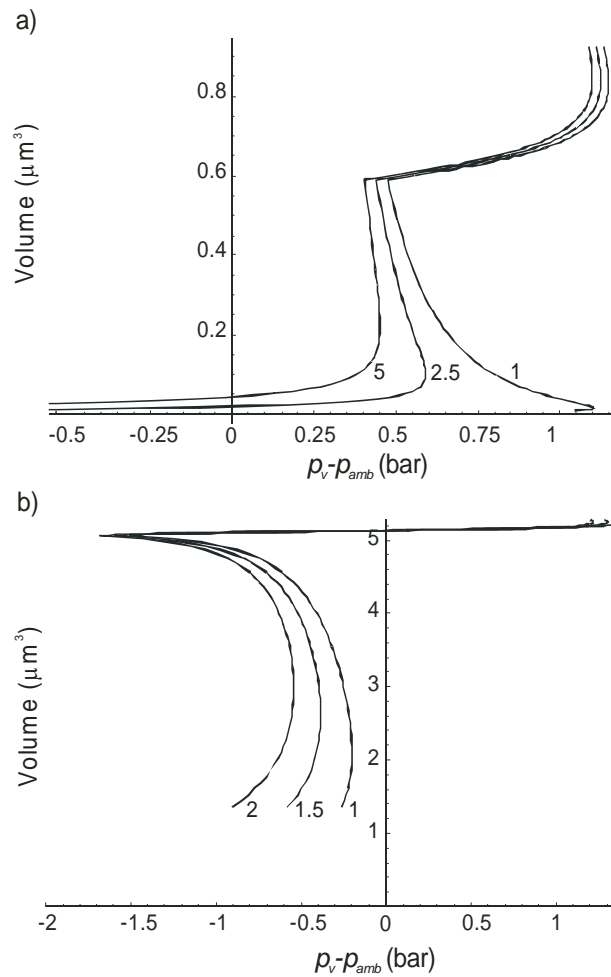
Figure 6-5: Evolution of a gas pocket during the second and third phases, where the mass of gas in the pocket at the start of the second phase is a proportion *k* of the original mass, for a) conical crevice, b) spherical cavity.

6.5   Summary & Conclusions

The constant mass method for the analysis of nucleation of a bubble from conical crevices of Atchley *et al.* (1989) has been modified for use with an axially symmetric cavity of arbitrary geometry. This has been used, in place of the derivation of a full dynamic model, to examine the effects of cavity geometry on nucleation.

The first nucleation threshold sets the decompression required to cause the interface to emerge outside the cavity. The results indicate that this aspect of behaviour is very dependent upon geometry, a higher-pressure threshold being required for emergence from the spherical cavity than non re-entrant cavities such as crevices. Once the nucleus interface has emerged outside of the cavity the behaviour of the nucleus is largely independent of the cavity geometry, as long as the interface initially starts deep within the cavity. The second nucleation threshold, as considered here,

may not be important in many nucleation scenarios, particularly that of bubbles emerging into the blood, where the flow conditions are likely to dictate when a bubble detaches from the nucleation site. This indicates that the behaviour of a gas pocket outside the cavity can be analysed by considering the interface at a circular opening, it being unnecessary to specify the cavity geometry precisely.

The original constant mass method presented by Atchley *et al.* (1989) did not allow for transfer of gas into the nucleus during growth. A simple modification to the method has been applied here to examine the effect of diffusion: as might be expected, this reduces the first nucleation threshold. If the time for the growth of the nucleus inside the cavity is sufficiently small then the effect of gas transfer will be negligible and hence the first nucleation threshold could be predicted using the method presented here. For the analysis of decompression bubbles it is likely that gas transfer is significant and hence a dynamic model would be necessary. However, given that the behaviour of the nucleus once it has emerged outside the cavity can be modelled by the interface at a circular opening, a simple dynamic model can be build of the nucleus behaviour. The geometry of the cavity is now only required to specify the surface area for diffusion across the cavity wall. This result will be used in the next chapter to examine in greater detail the detachment of a free bubble from a crevice due to the passing blood flow.

7. A model for the detachment of bubble from vasculature nuclei*

7.1   Introduction

This chapter addresses the detachment of a free bubble from the growing crevice bubble as it emerges into the blood flow. In chapter 4 the detachment process was modelled by setting a threshold value on the contact angle between the interface and the blood vessel wall at which a section of the bubble detaches. Here the effects of the blood flow on the emerging bubble will be considered to investigate the size of bubble at detachment more accurately. Additionally, the behaviour of the bubble as it is swept along a capillary vessel will also be explored. The behaviour of the detached bubble as it passes around the circulation is important in its role in DCS. In this chapter the first stage in this process, the growth of the bubble during transit in the capillaries, is examined to determine whether the bubble might block the vessel. In keeping with the results of chapter 6 the detachment behaviour of the crevice bubble interface will be explored by modelling the bubble interface at a circular opening in the vessel surface. The restriction to gas transfer through the cavity surface alone will be relaxed to include an estimate of the gas transfer across the

---

* Preliminary work for this chapter was completed by Sebastien Uzel. The work in this chapter appears as: Chappell, M. A., S. Uzel and S. J. Payne (2007). "Modelling the Detachment and Transport of Bubbles from Nucleation Sites in Small Vessels." IEEE Transactions on Biomedical Engineering: in press.

bubble surface, since this surface area is significant for the emerged bubble. As in the previous models only a single inert gas resembling nitrogen will be considered.

7.2 Model

The process of bubble detachment is assumed to be divided into two phases:

- Deformation: the bubble is deflected sideways slightly, but is still attached to the cavity mouth.

- Detachment: the bubble slides sideways along the vessel wall, initially still attached to the cavity by a narrow neck, before becoming completely detached from the crevice and lifting off into the bloodstream.

Clearly this is an approximation to the actual processes, which will be highly complex: however, the intention here is to develop a simple mathematical model of the bubble detachment that can be used to examine the characteristic behaviour of the bubble. This approach follows that of Bai *et al.* (2001), where bubbles emerging from a semi-infinite plane into a wide flow were considered.

7.2.1 Initial deflection of the bubble

As the bubble grows outside the crevice, a number of different forces act upon it, resulting in its deformation and ultimately detachment. In this section, these forces will be considered and the limiting condition for the bubble to remain positioned above the crevice will be derived. It will be assumed that the deformation of the bubble is small and thus it can be treated as approximately spherical for the analysis of the forces on it. In the following analysis the bubble has a radius of curvature, *r*, and the vessel has a radius, *R*.

7.2.1.1 Drag force

As soon as the bubble emerges outside the crevice it experiences a drag force, due to the flow of blood in the vessel. For simplicity, the velocity of the bloodstream is assumed to be plug flow with velocity $\bar{u}$. The drag force is related to the drag coefficient by:

$$F_D = C_D \frac{1}{2} \rho_l \bar{u}^2 \pi r^2 ,$$ (7.1)

where ρ_l is the liquid density and C_D the drag coefficient. Since the Reynolds number, Re , is very small (of order 0.001), C_D is approximated by $24/\mathrm{Re}$, the laminar solution for flow round a

sphere. A full three-dimensional flow model would have to be solved to calculate the exact value of the drag force and to take into account the variation in flow caused by the bubble partially blocking the vessel. However, as a first approximation a simple approach to explore the characteristic behaviour of the bubble detachment is being taken here. From the definition of Reynolds number, the drag force is thus:

$$F_D = 6\mu \bar{u} \pi r,$$

(7.2)

where μ is the viscosity of the liquid.

7.2.1.2 Capillary force

In order to counterbalance the drag force, the bubble will deform slightly to introduce a component of the capillary force that is parallel to the flow: otherwise the axial component of the capillary force would be zero. Thus the downstream contact angle decreases while the upstream one increases, as shown in Figure 7-1. The axial component of the capillary force is, Winterton (1971):

$$F_C = \frac{\pi}{2}\sigma a(\cos\theta_d - \cos\theta_u),$$

(7.3)

where σ is the surface tension, a the radius of the crevice mouth and θ_d and θ_u the downstream and upstream contact angles respectively.
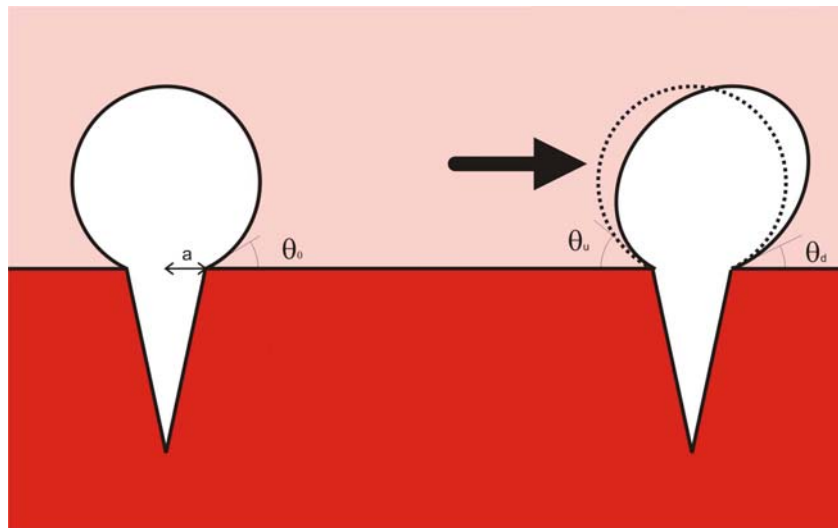

Figure 7-1: Schematic of sideways movement

For simplicity it is assumed that the variation of contact angles is approximately symmetrical. θ_d and θ_u are thus equal to $\theta_0 - \psi$ and $\theta_0 + \psi$ respectively, where θ_0 is the static contact angle and

ψ is the change in contact angle. In addition, since it is shown later that the deformations are small, equation (7.3) reduces to approximately:

$$F_C = \pi a^2 \frac{\sigma}{r} \psi .$$ (7.4)

7.2.1.3 Buoyancy force

The blood vessels in the human body will be orientated over the complete range of angles. Thus in some vessels, there will be a component of the buoyancy force in the axial direction:

$$F_B \approx k \frac{4}{3} \pi r^3 \rho_l g ,$$ (7.5)

where the constant k represents the component of the buoyancy force in the axial direction and can vary between -1 and 1. There will also be a component of buoyancy perpendicular which acts to pull the bubble out of the cavity, which again is dependant upon the vessel orientation. Likewise this effect of this force in the bubble will be small and is neglected here. However, in the absence of any flow this term is likely to be responsible for bubble detachment, with analogy of bubble detachment in carbonated drinks Liger-Belair (2005).

7.2.1.4 Force balance

Whilst the bubble remains attached to the crevice mouth, the forces balance:

$$F_D = F_C + F_B .$$ (7.6)

The ratio of the magnitude of the maximum buoyancy force and the drag force is of order:

$$\frac{F_B}{F_D} \approx \frac{\rho g R^2}{\bar{u} \mu} .$$ (7.7)

For typical values of blood viscosity flow speed and vessel diameter, given later, this is of order 0.01. The buoyancy force can thus be neglected in analysing the detachment of the bubble from the crevice. Thus the deformation introduced into the bubble by the blood flow can be calculated from:

$$\psi = \frac{6 \mu \bar{u}}{\sigma} \left(\frac{r}{a} \right)^2 .$$ (7.8)

Bai *et al.* (2001) found experimentally that bubble deformation continues until a limiting value of deformation angle was reached, at which point the bubble detached. Thus the size of the bubble at the end of this first phase, r_1, can be calculated if the limiting value of deformation angle, ψ_{crit}, is known:

$$\frac{r_1}{R} = \frac{a}{R} \sqrt{\frac{\psi_{crit}}{6} \frac{\sigma}{\mu \overline{u}}} \; , \tag{7.9}$$

where the equation has been re-cast into non-dimensional form: lengths having been normalised by the vessel radius. The end of this phase corresponds with the limit of detachment used in the crevice bubble model in chapter 4, i.e. r_1 corresponds to the radius of curvature at detachment used there. Hence this radius can be used to set the limiting value γ_s for that model.

7.2.2 Detachment of the bubble

When the drag force exceeds the capillary force, it is assumed that the bubble starts sliding along the vessel wall. At this stage a free bubble does not detach entirely from the cavity, instead it remains attached by a narrow neck. This was shown to be the case in both numerical simulations and experiments by Bai *et al.* (2001) for bubbles emerging from crevices in semi-infinite planes. Eventually the neck breaks between the cavity and the free bubble is carried away in the blood. During these phases diffusion still occurs, increasing the volume of the bubble. Once the neck has broken, gas transfer occurs purely through the bubble interface with the bloodstream. During the sliding phase gas transfer would be expected from both the blood surrounding the detaching bubble and from the tissue via the cavity surface. However, as the duration of this phase is likely to be short, it will be assumed that during the sliding phase the detaching bubble and the gas pocket that remains in the cavity can be treated as independent.

Bai *et al.* (2001) assumed that complete bubble detachment would occur when the most upstream point of the bubble has the same abscissa as the most downstream point of the crevice mouth. Thus the bubble size at full detachment could be estimated. However, for decompression bubbles this value is not particularly important and the bubble can effectively be considered to be detached at the point it starts to slide, because at this stage the bubble acts essentially as an independent spherical bubble. What is of interest is the growth of the bubble during the detachment phase, specifically whether the bubble grows to a size such that it may block the vessel before it is ejected from the capillary vessel into the larger diameter venous circulation.

It is will be assumed that the detaching bubble moves at the same speed as the blood flow velocity, $\bar{u}$. Thus the distance the bubble travels from when it begins to slide, t_1, until the time it has a radius equal to the vessel radius, t_2, is given by :

$$l = \int_{t_1}^{t_2} \bar{u}\, dt \,.$$

(7.10)

During this phase the bubble is a complete sphere, or initially approximately a sphere with a small neck connection it to the site where it formed. Gas transfer into the bubble occurs primarily from the blood and this can be determined by solving the diffusion equation in spherical co-ordinates. As in chapter 4 a 'three-region' model will be adopted, where the concentration in the blood is assumed to vary over a boundary layer of thickness, λ. The equation for gas transfer is thus, Srinivasan *et al.* (1999):

$$\frac{d\left(p_i V_i\right)}{dt} = L_t D_t A_i (p_t - p_i)(\frac{1}{\lambda} + \frac{1}{r}) \,,$$

(7.11)

where the surface area and volume of the bubble are $4\pi r^2$ and $4\pi r^3/3$ respectively. The diffusion of gas between the blood and bubble has been modelled using a simple characteristic diffusion length; this neglects the more complex effect of the mixing of the blood around the interface. Such mixing might be expected to replenish the concentration of gas around the bubble more rapidly than would occur by diffusion alone. Hence it could be modelled, as a first approximation, by a smaller value for λ than used in chapter 5, where diffusion through stationary tissue was considered.

The chain rule can be used to give:

$$\frac{d\left(p_i V_i\right)}{dt} = \left(4\pi p_{amb} r^2 + \frac{16}{3}\pi\sigma r \right)\frac{dr}{dt} \,.$$

(7.12)

where it is assumed that the bubble deformation is small and thus is approximately spherical and p_i can be calculated using the Laplace equation (2.6). Additionally, it has been assumed that the ambient pressure does not vary during the bubble detachment. Thus the model describes the bubble growth after the end of decompression, which appears to be reasonable, as chapter 5 shows that most bubble growth occurs after decompression has been completed. Since tissue gas tension is determined by the relatively slow tissue time constant, it will also be assumed that the tissue gas

tension is approximately constant during the bubble detachment phase. Hence the difference between ambient pressure and tissue gas tension, $\Delta p = p_t - p_{amb}$, remains constant. This pressure difference will vary on a slower time scale after decompression; hence large Δp is associated with the conditions soon after the end of a large decompression.

Combination of equations (7.10), (7.11) and (7.12) then gives, where the radius at time t_2 is equal to the vessel radius, R:

$$l = \frac{\overline{u}\lambda}{L_t D_t} \int_{r_1}^{R} \frac{\left(p_{amb}r + \frac{16}{3}\pi\sigma\right)}{(\Delta p r - 2\sigma)(r+\lambda)} dr,\tag{7.13}$$

The solution to equation (7.13) is:

$$\frac{l}{R} = \frac{\overline{u}R}{L_t D_t} \frac{\lambda'}{(\lambda'\Delta p' + 2\sigma')} \left\{ \frac{\left(2\sigma' + \frac{16}{3}\pi\sigma'\Delta p'\right)}{\Delta p'^2} \left[\Delta p'\left(1-r_1'\right) + 2\sigma'\ln\left(\frac{\Delta p' - 2\sigma'}{\Delta p'r_1' - 2\sigma'}\right) \right] + \right.$$
$$\left. \left(\lambda' - \frac{16}{3}\pi\sigma'\right)\left[1 - r_1' - \lambda'\ln\left(\frac{1+\lambda'}{r_1'+\lambda'}\right)\right] \right\},\tag{7.14}$$

where pressures are normalised according to the ambient pressure, p_{amb}, lengths are normalised according to the vessel radius, R, so that $\lambda' = \lambda/R$, $\Delta p' = \Delta p/p_{amb}$ and $\sigma' = \sigma/p_{amb}R$. If the length in equation (7.14) is shorter than the length of the blood vessel, then bubbles forming under these conditions may be capable of completely occluding the flow. The occlusion by a bubble will not be modelled further, as this is a complicated process, particularly since the vessel walls have a certain amount of compliance. However, it is quite possible that, since the bubble continues to increase in volume by diffusion, some form of occlusion will occur if the bubble radius becomes similar to that of the vessel.

7.3   Results

Table 7-1 gives the governing non-dimensional parameters in the model. For the deformation phase the size of the bubble at the point of detachment is governed by three parameters. However, neither the cavity mouth radius nor the critical value of contact angle deformation is known and hence variation in these will be explored here. For the detachment phase the bubble is governed by a

further four parameters. Although the properties of the blood and the geometry of the vessel are reasonably well defined, the size of the bubble at the start of this phase is not known. Given the crevice explored in chapter 5 a cavity mouth radius of the order of 70 nm would be expected, but variation in this parameter will be explored. Since the driving pressure, Δp, is dependent upon the magnitude of the decompression and the time after decompression, a range of values will be explored up to 5 bar, which would approximately correspond to a saturation dive to 40 m. The value for the characteristic diffusion length is not well established and so effects of its variation will also be examined. Additionally, the effects of variation in surface tension will be explored, as this is known to have a critical effect on bubble behaviour as noted in chapter 5.

Table 7-1: Governing non-dimensional parameters.

Governing Parameter	Description
Deformation	
$a' = a/R$	Non-dimensional cavity opening radius.
$\sigma/\bar{u}\mu$	
ψ_{crit}	Critical deformation angle
Detachment	
$\sigma' = \dfrac{\sigma}{p_{amb}R}$	Non-dimensional surface tension.
$\lambda' = \lambda/R$	Non-dimensional characteristic diffusion length.
$\Delta p' = \Delta p/p_{amb}$	Non-dimensional pressure difference between gas tension and ambient pressure.
$\bar{u}R/L_t D_t$	

Table 7-2 gives the baseline values of the physiological parameters that will be used here. For the calculation for the non-dimensional parameters an ambient pressure of 1 bar was used and a vessel radius of 3 μm, which is representative of capillaries found in the body, Schneck (2000). Capillaries are known to have lengths in the range 100-300 μm, Schneck (2000), which represents the limit for *l*, the length the bubble travels before reaching vessel blocking dimensions, the corresponding limit for l/R being 66.7-100 in a vessel of radius 3 μm.

7.3.1 Initial deflection of the bubble

The first part of the proposed model predicts the deformation of the bubble whilst growing out of the mouth into the bloodstream. The relationship between the angle, ψ, and the non-dimensional bubble radius at the end of the first stage of detachment, r_1/R, is shown in Figure 7-2 for a range of values of a/R from 0.005 to 0.1, which corresponds to a range for a of 0.0017 to 0.333 μm in a vessel of radius 3 μm. The radius of the cavity openings in the body is not well known, although the crevice used in chapter 4 has a value for a of 0.07 μm, whereas the radii of opening associated with caveolae is of the order of 0.02 μm, Rothberg $et\ al.$ (1992). These values in a capillary of radius of 3 μm gives a/R values of 0.023 and 0.0066 respectively.

Table 7-2: Physiological parameters used in the model.

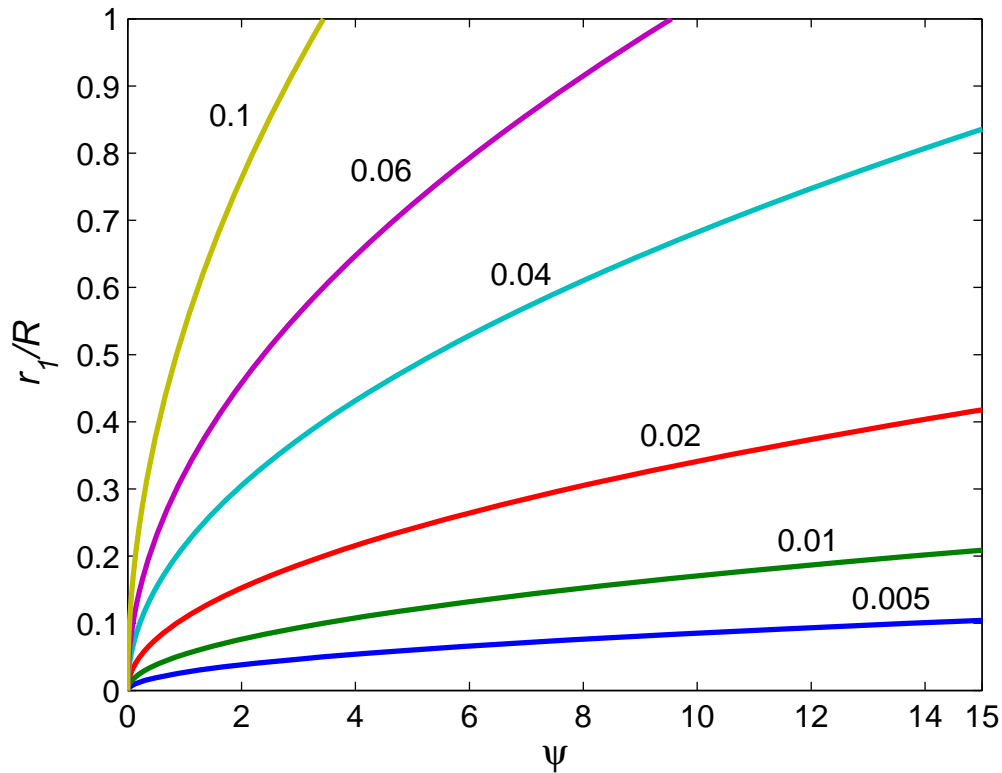| Parameter	Value	Reference
μ	0.003 Nm^{2}s^{-1}	Mohrman $et\ al.$ (2003)
σ	0.03 N m^{-1}	Srinivasan $et\ al.$ (1999)
L_t	0.0125 ml gas/ml blood	Srinivasan $et\ al.$ (1999)
D_t	2.2×10^{-9} m^{2}s^{-1}	Lango $et\ al.$ (1996)
$\bar{u}$	1 mm s^{-1}	Mohrman $et\ al.$ (2003)
Non-dimensional parameters:		
a'	0.0666	
$\sigma/\bar{u}\mu$	10^4	
σ'	0.1	
λ'	0.3333	
$\bar{u}R/L_t D_t$	109	

Figure 7-2: Relationship between deformation angle and non-dimensional bubble radius at end of first stage of detachment for varying values of non-dimensional cavity opening radius.

Figure 7-2 illustrates that the assumption of small deformation is true for almost all the likely cases of bubble size at detachment, although this may not be so reasonable for bubbles emerging from cavity mouths corresponding to caveolae. Moreover, as expected, large deformation is associated with large bubbles and small openings. The critical deformation angle is likely to be a constant value for a particular flow condition, Bai *et al.* (2001). However, values of deformation angle are not available for the flow conditions under consideration here, although at the low flow speeds considered it is likely that this value would be much smaller than those measured by Bai *et al.* (2001). For a particular value of ψ smaller crevices can be seen to result in smaller values of r_1/R, i.e. the bubble is smaller at detachment. Blood vessels with smaller radii but the same size of openings would be expected to produce bubbles that are a larger fraction of the size of the blood vessel. It might even be possible that, for small ψ, the bubble grows to similar dimensions as the vessel, risking some form of blockage before it comes away from the opening. However, as the bubble fills a larger proportion of the vessel cross-sectional area the assumption that the bubble does not significantly alter the blood flow conditions would no longer be valid. It is possible that

the alteration to the blood flow would result in a greater force upon the bubble, leading to greater deformation and earlier detachment than might be predicted here.

7.3.2   Bubble detachment

Since the critical value of deformation angle is unknown for bubbles growing in vessels, the value of the bubble's radius of curvature at the end of the first phase cannot be specified accurately. Hence a range of values will be used to examine the behaviour of the detaching bubble. The influx of gas into the bubble, causing its growth as it travels down the vessel, is driven by the difference between the pressure of gas in the bubble and the gas tension in the blood, which is a function of Δp and the pressure due to surface tension, $2\sigma/R$.

Figure 7-3 shows the effect of initial bubble size and driving pressure difference on the length that the bubble travels before reaching vessel-blocking dimensions. As might be expected, smaller pressure differences result in the bubble travelling a greater distance before its size is comparable to that of the vessel, because a greater time is needed for a comparable transfer of gas into the bubble. Additionally the larger the bubble is at the end of the deformation phase the sooner it reaches vessel size dimensions, because a smaller quantity of gas transfer is required. For each value of Δp there are values of r_1/R for which there are no valid solutions for l/R. These represent initial bubble sizes for which the pressure in the bubble, from the Laplace equation, is greater than the gas tension in the blood, hence the gas flux is out of the bubble and so it shrinks rather than grows, i.e. $\Delta p < 2\sigma/r_1$. Thus for larger values of Δp, e.g. with a higher blood gas tension, there is a greater range of r_1/R for which the bubble can potentially reach vessel blocking dimensions rather than collapsing. It is likely that bubbles will detach at small bubble sizes relative to the vessel diameter because the critical deformation angle will be reached. Thus it appears unlikely that a bubble would reach vessel-blocking dimensions with the conditions considered here unless the difference between ambient pressure and tissue gas tension is 2 bar or greater, as only with that pressure difference is l/R less than 100. For high-pressure differences the possibility of vessel blockage is much higher as l/R is below the lower limit for vessel length of 66.7 for most bubble detachment sizes.
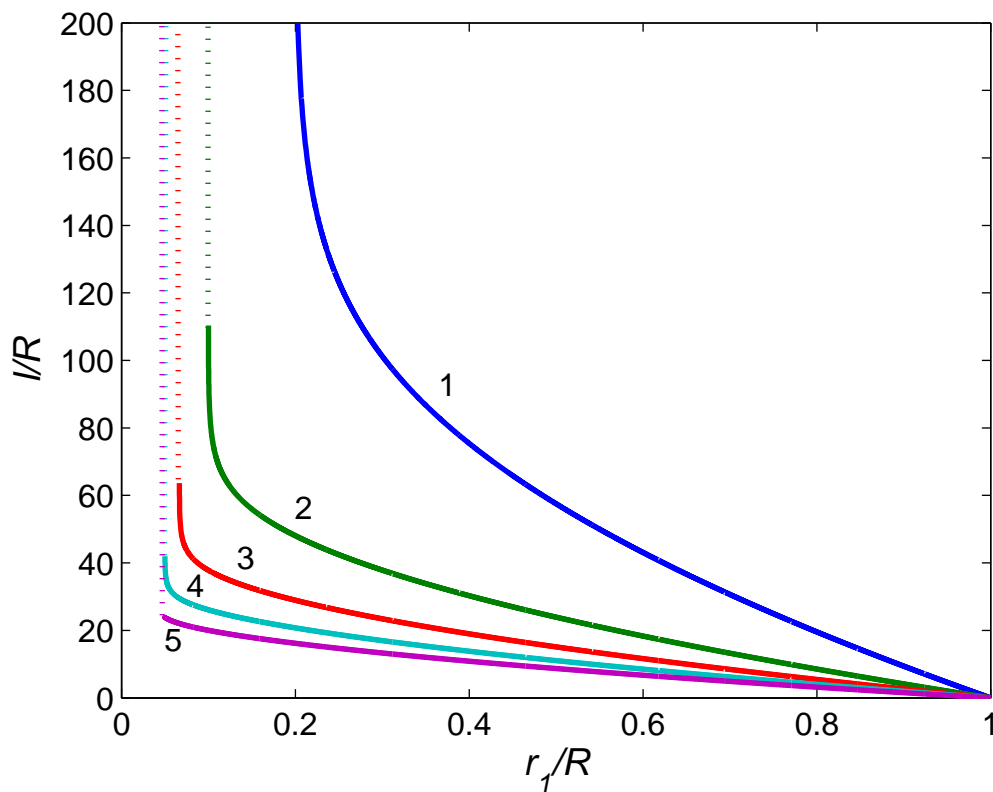
Figure 7-3: Effect of driving pressure difference on the length the bubble travels before it reaches vessel-blocking size, for a range of initial bubble size.

The characteristic diffusion length also affects the rate of gas transfer into the bubble, a smaller value corresponding to higher rates. The value for this parameter is not well known and may itself be a more general representation of more complex processes of gas transfer. Hence the effect of variation in this parameter on the bubble growth behaviour has been examined, Figure 7-4. Here a Δp of 5 bar has been used, which results in the bubble reaching vessel blocking dimensions within the length of a capillary for practically all initial bubble sizes. Unlike variation in the pressure difference, variation in λ' has no effect on the limiting value of r_1/R below which bubbles do not grow. The relationship between r_1/R and l/R is approximately linear, except at small values of r_1/R below approximately 0.1. The most marked effect of varying λ' occurs around the value adopted here; significantly larger or smaller values converge upon a fixed solution. As has already been noted, it is likely that the equivalent value for λ' in the blood might be lower than that assumed for body tissues, as a result of mixing in the blood: this would tend to encourage bubble growth and increase the risk of blockage.

Figure 7-4: Effect of variation in the characteristic diffusion length on the distance travelled by the bubble until it reaches vessel blocking dimensions for a range of initial bubble size.

The strength of the surface tension, whilst affecting the size of bubble at detachment at the end of the previous phase, also determines how rapidly the bubble grows through variation in the pressure in the bubble via the Laplace equation and altering the rate of gas transfer into the bubbles. Thus, as illustrated in Figure 7-5, higher surface tensions result in greater values of l/R, and a smaller range of r_1/R for which there is a valid solution. The surface tension of blood plasma is well established, although it is unclear to what extent adherence of surfactants to the surface of the bubble might have an impact. However, it is generally observed that surfactants reduce the surface tension, which would permit more rapid growth of the bubble.
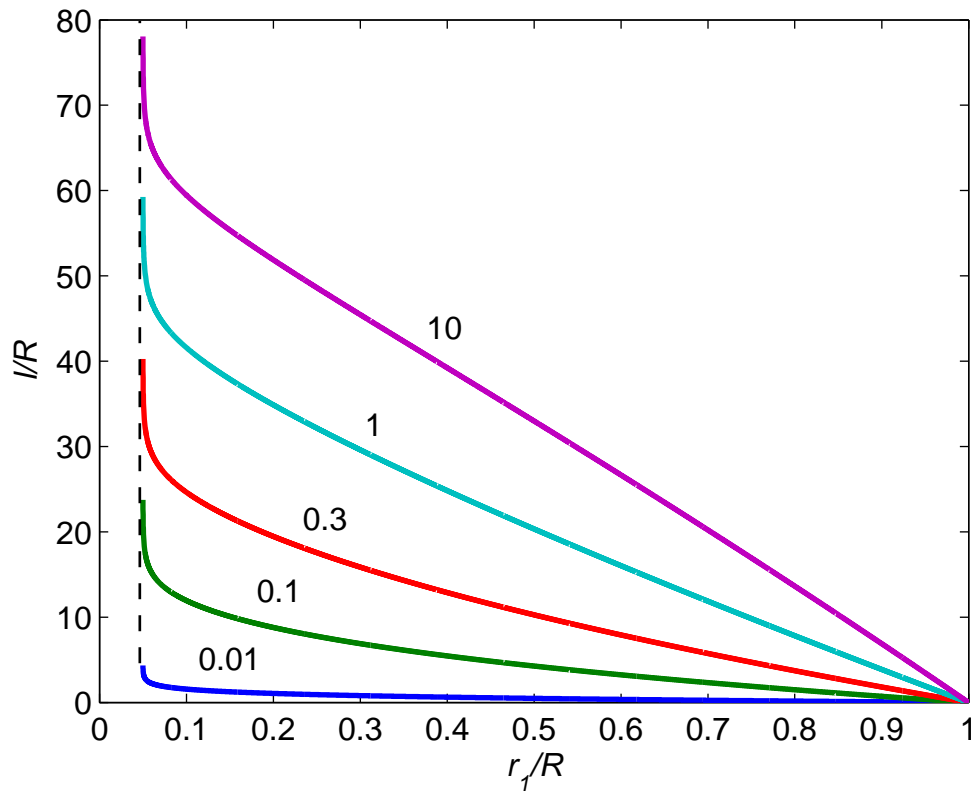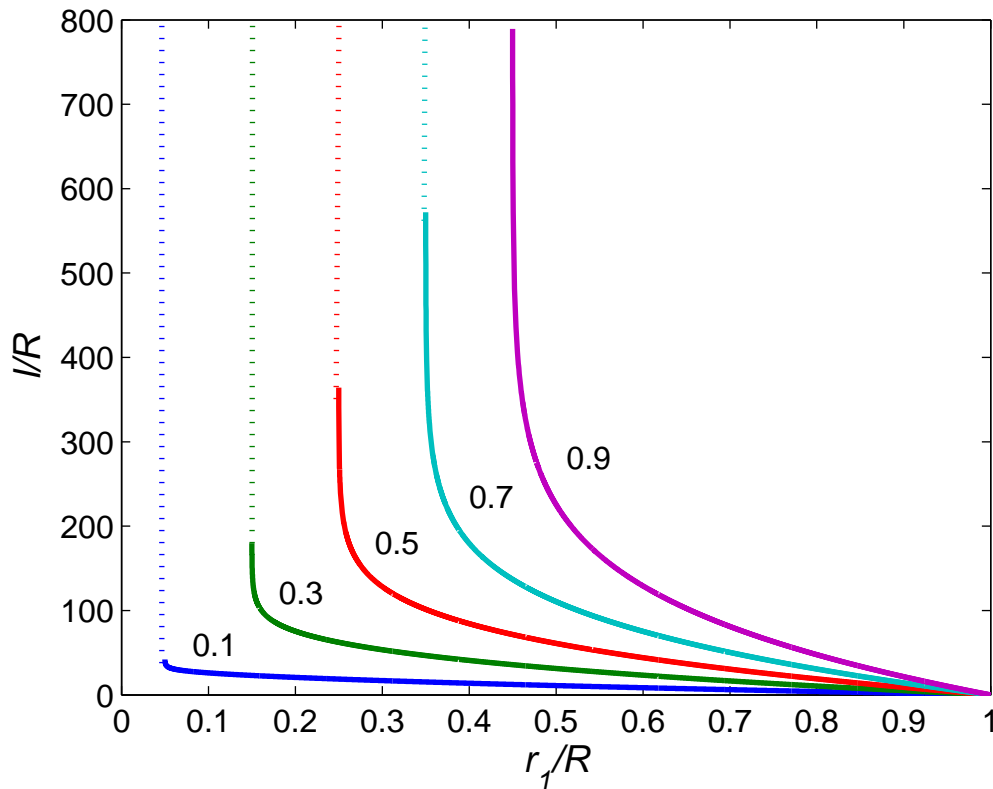
Figure 7-5: Effect of variation in surface tension on the distance travelled by the bubble until it reaches vessel blocking dimensions for a range of initial bubble size.

7.4   Discussion

7.4.1   Bubble detachment mode

It has been assumed here that the bubble detachment occurs by the sliding of the bubble along the vessel wall, whilst initially remaining attached at the cavity mouth; this process was termed Mode I by Bai *et al.* (2001). It is possible, especially as the bubble shape is deformed by the flow, that the contact angle on the sheltered side of the bubble may reach the value of receding contact angle. In this case the bubble may be expected to spread along the vessel wall, with accompanying movement of the line of contact of the bubble. This process is highly dependent upon the value of receding contact angle and hence the surface properties of a blood vessel, which is assumed to have a hydrophilic surface. The receding value of contact angle is likely to be small and may not easily be reached. Additionally, this spreading process would be complicated by the non-symmetric bubble shape: the receding contact angle would only be reached by the section of the interface downstream, and hence the bubble could only spread by further deviation from a spherical shape. Thus in preference it may be expected to pull away from the cavity mouth i.e. the bubble to slide

144

and detach. Bai *et al.* (2001) only observed such spreading of bubbles emerging into a flow at very high flow velocities, which may be associated with the high forces required to cause appropriate bubble deformation.

7.4.2 Vessel blockage

In this work we have only calculated at what point a bubble would have a size comparable to that of the vessel. Attainment of such size may imply that the bubble would block the vessel, although this process has not been considered in any detail. To do so it would be necessary to specify more completely how the presence of the bubble affects the blood flow in the vessel, as well as the effects of compliance of the vessel wall as the bubble grows.

Since capillary vessels have lengths in the range 100-300 μm, the model predicts that vessel blockage by bubbles nucleated in the capillaries is feasible for all but the smallest driving pressure differences. The likelihood is also determined by how near the end of the capillary is to the bubble formation site. It is also likely that the pressure difference between bubble and blood will vary along the length of the capillary, as the blood on entrance to the tissue will not have had time to become saturated with gas from the tissue.

The model used here has greatly simplified the interaction of the bubble and blood flow. This permits some predictions to be made about the behaviour of bubbles forming on the walls of blood vessels. However, more comprehensive 2D or 3D models are required to examine the behaviour more accurately. Previously Halpern and colleagues have examined in 2D, using the Boundary Element Method, the growth of a bubble in a blood vessel up to vessel blocking size, Halpern *et al.* (1994), Halpern *et al.* (1999). This permitted the effects of the bubble on the flow to be included. This model did not include the emergence and detachment of a bubble from a formation site, which is important here. However, it is likely that this method could be employed to examine the blockage of the vessel by a bubble of comparable size to the vessel diameter. It is also likely that this method could be employed to investigate the behaviour of two bubbles travelling down the same vessel, for example if bubbles detached from neighbouring formation sites. Strictly the detachment of a bubble due to the blood flow requires a full 3D model, which may be amenable to Computational Fluid Dynamics analysis.

7.4.3 Behaviour of bubbles in the circulation

The very early stages of the behaviour of bubbles forming on blood vessel walls as they are swept into the circulation have been considered here. The model results imply that it is feasible for a bubble forming in the capillaries to reach vessel-blocking size before it leaves the capillary. Under such circumstances it might be expected that a 'gas plug' would form, i.e. the bubble would continue to grow by elongation down the vessel. Such 'gas plugs' are associated with injury and potentially with DCS like symptoms. The behaviour of such gas plugs has previously been analysed by Eckmann and colleagues in relation to cerebral gas embolism arising from operative procedures or decompression, Branger *et al.* (1999), Branger *et al.* (2001), Sta Maria *et al.* (2003). Both Lever *et al.* (1966) and Buckles (1968) have observed bubbles in the venous and arterial circulations in animal experiments of a size where they formed significant elongated 'gas plugs'. These bubbles do not necessarily remain fixed in place, but may move under the influence of the blood pressure, this raises the possibility that 'gas plugs' emerging into venous vessel from capillaries may break up into further bubbles. The behaviour of such large moving 'gas plugs' has previously been examined by Bull and colleagues, Calderon *et al.* (2005), Eshpuniyani *et al.* (2005). However, they were interested in the splitting of a 'gas plug' at a bifurcation, which would be a condition more likely to be associated with progression of the bubble in the arterial circulation where vessels progressively narrow and split in the direction of movement. For this reason most work on 'gas plugs' appears to apply to arterial bubbles, where these bubbles are assumed to have been introduced through some artificial opening, e.g. operative procedure or damage to the lungs during decompression. The risk from venous 'gas plugs' due to decompression bubbles seems generally to have been ignored; it appears to be assumed that they do not form. The results presented here imply that 'gas plugs' can form before a bubble reaches the wider venous circulation and, therefore, may be associated with DCS injury. However, further work is required to examine the behaviour of such gas plugs as they pass toward the venous vessels.

7.4.4 Blood cells

For the model presented here the blood has been assumed to be a simple homogenous liquid, i.e. the presence of blood cells has been ignored. However such cells are of a similar size to the bubble being considered and hence their passing could significantly interfere with bubble detachment. The

number density of red blood cells is approximately $5 \times 10^6 \, \text{mm}^{-3}$, Mohrman *et al.* (2003), which for the typical vessel considered above, would predict that blood cells pass down the blood vessel at intervals of approximately 10µm. Thus a passing bubble might cause premature bubble detachment; alternatively its motion may be blocked by a bubble whilst still attached to its formation site further interfering with blood flow. This topic is beyond the scope of the model presented here, but is worthy of further investigation.

7.5 Conclusions

A simple model has been presented to examine the behaviour of a bubble forming on the wall of a blood vessel detaches due to the forces on it from the blood flow and its subsequent growth as it passes down the vessel. This model presented has thus enabled the question of whether the bubbles formed from cavities under decompression can impede the blood flow in the microvasculature to be answered. It is clear, even from the relatively simple models presented here, that the bubbles formed do interact with the flow field and can easily lead to blockage of flow under certain, physiologically reasonable, conditions. What happens to the bubbles once they become of comparable size to the blood vessel is not at all clear, however. Given that there is still a pressure difference driving diffusion of gas into the bubble from the bloodstream, the bubble will continue to expand, although at a smaller rate, since the area in contact with the bloodstream diminishes. Whether the blood vessel wall expands, due to its distensible nature, to help to let the bubble pass downstream is not known and this will need to be examined in future. It is likely that any trapped bubbles will continue to move downstream, due to the pressure difference driving the flow: however, this movement would be expected to be much slower than when moving in the free stream of the flow.

Finally, it should be noted that only a single bubble emerging from a single cavity has been considered. It is likely that there will be many cavities per vessel each of which will produced bubbles. There is thus likely to be significant interaction between bubbles in the blood vessel and determining how they interact, particularly whether they pile up or join together, will be important in assessing the role of bubbles in decompression sickness. Neither has the presence of blood cells travelling down the capillaries been considered: again this is likely to play an important role in the model behaviour.

8. The interaction between the growth of tissue and blood bubbles[*]

8.1   Introduction

The growth of bubbles in the blood, as simulated using the crevice model presented in chapter 4, cannot be considered independently of the growth of bubbles in the tissues, as both rely on the same source of dissolved gas. For example, if more gas passes into the tissue bubbles, then less gas will diffuse into the crevice bubbles and vice versa. In this chapter a joint model based on the crevice bubble model and an existing model for the formation of tissue bubbles is presented and used to examine the interaction between the two modes of bubble formation. Since it is much easier to measure the presence of moving bubbles in the body, which themselves are only a fraction of those found in the vasculature, than the stationary tissue bubbles, the interaction between the two can only easily be explored using models. It is thus the aim that this joint model will add to the understanding of what information can be extracted from measurements of moving bubbles about the presence of both blood borne and tissue bubbles throughout the body and hence the relationship of these measurements to the risk of DCS.

---

[*] The work in this chapter appears as:
Chappell, M. A. and S. J. Payne (2006c). "A Physiological Model of the Interaction between Tissue Bubbles and the Formation of Blood-Borne Bubbles under Decompression." Physics in Medicine and Biology **51**: 2321-2338.

8.2   Methods

The model is based on the crevice bubble model of chapter 4 and the tissue bubble model of Srinivasan *et al.* (1999). For simplicity the model will be derived for a single inert gas, so that the interaction of the two types of bubble can be explored easily. It would be possible to derive a multiple inert gas joint bubble model using the full crevice bubble model presented in Appendix A and the tissue model proposed by Srinivasan *et al.* (1999).

The partial pressure of the inert gas in a tissue ($p_{i,t}$) or crevice ($p_{i,c}$) bubble is given by the Laplace equation for each bubble type:

$$p_{i,t} = p_{amb} - p_{i,N} + \frac{2\sigma_t}{r} + \frac{4\pi}{3}Mr^3, \tag{8.1}$$

$$p_{i,c} = p_{amb} - p_{i,N} + \frac{2\sigma_c}{R}, \tag{8.2}$$

where σ_t and σ_c are the gas-liquid surface tension for tissue bubble and for the crevice bubbles respectively, and *M* is the bulk tissue modulus of elasticity, Srinivasan *et al.* (1999), which for the crevice bubble is zero. It is assumed that tissue bubbles grow from pre-existing spherical gas nuclei, of radius r_0, and that they remain spherical during growth. The geometrical parameters for the model are illustrated in Figure 8-1 and the equation for growth is, Srinivasan *et al.* (1999):

$$\frac{dr}{dt} = \frac{L_t D_t \left(p_t - p_{i,t}\right)\left(\frac{1}{\lambda} + \frac{1}{r}\right) - \frac{r}{3}\frac{dp_{amb}}{dt}}{p_{amb} + \frac{4\sigma_t}{3r} + \frac{8\pi}{3}Mr^3}, \tag{8.3}$$

where for simple spherical diffusion λ is the thickness of the diffusion region which surrounds the bubble. The pressure in the bubble is calculated directly from the Laplace equation (8.1).
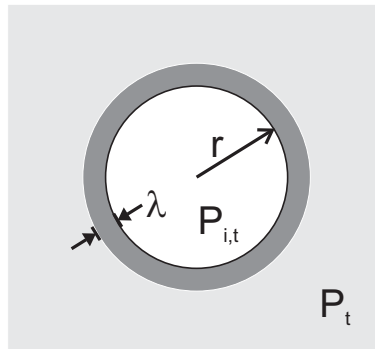

Figure 8-1. Geometry of the tissue bubble model, where *r* is the radius of the bubble and λ is the thickness of the diffusion region.

To describe the growth of bubbles in the blood the equations from chapter 4 are used:

$$\frac{d\theta}{dt} = \frac{\frac{3L_t D_t}{\lambda}\left(p_{i,c} - p_{t,c}\right) + d\varepsilon\frac{dp_{amb}}{dt}\sin^2\phi}{\frac{3}{4}dp_{amb}\sin^2\phi + 2\sigma_c\left\{\varepsilon\sin\theta + \frac{3}{4}\cos\theta\right\}\sin\phi}, \qquad \alpha_r < \phi + \theta < \alpha_a, \qquad (8.4)$$

$$\frac{dd}{dt} = -\frac{\frac{3L_t D_t}{\lambda}\left(p_{i,c} - p_{t,c}\right) + d^2\varepsilon\frac{dp_{amb}}{dt}\sin^2\phi}{\left(4\sigma_c\cos\theta + 3dp_{amb}\sin\phi\right)\varepsilon\sin\phi}, \qquad \begin{cases}\phi + \theta = \alpha_a \\ \phi + \theta = \alpha_r\end{cases} \qquad (8.5)$$

$$\frac{d\gamma}{dt} = \frac{\frac{3L_t D_t}{\lambda}\left(p_{i,c} - p_{t,c}\right)\sin^3\left(\frac{\gamma}{2}\right) + d_m\sin\phi\frac{dp_{amb}}{dt}\xi_2}{3d_m p_{amb}\sin^2\phi\,\text{cosec}\left(\frac{\gamma}{2}\right) + 2\sigma_c\xi_3}, \qquad d = d_m, \qquad (8.6)$$

where:

$$\begin{aligned}
\varepsilon &= \cot\phi - \tfrac{3}{4}\left(\theta - \tfrac{\pi}{2}\right), \\
\xi_1 &= \cos\phi + \left(2\text{cosec}^3\gamma + \cot\gamma\left(1 + 2\text{cosec}^2\gamma\right)\sin\phi\right), \\
\xi_2 &= 3\sin\left(\phi + \gamma/2\right) - \sin\left(\phi + 3\gamma/2\right), \\
\xi_3 &= 6\sin\phi\cos\left(\gamma/2\right) - \xi_2\cos\gamma.
\end{aligned} \qquad (8.7)$$

For simplicity the diffusion region thickness, λ, for both the spherical tissue bubble and conical crevice bubble are assumed identical here.

In a similar manner to the crevice model it is assumed that the transfer of inert gas between the tissue and blood is perfusion dominated. However, it is now necessary to include the effects of transfer of gas into both types of bubbles, as for high bubble densities this may have a significant effect on the tissue gas tension. The rate of change of tissue gas tension is thus determined by mass balance, including the flux of gas into the two types of bubble:

$$\frac{dP_t}{dt} = \frac{p_a - p_t}{\tau} - \frac{1}{L_t V_t}\left(N_{i,t}\frac{d(pV)_{i,t}}{dt} + N_{i,c}\frac{d(pV)_{i,c}}{dt}\right), \qquad (8.8)$$

where V_t is the tissue volume, and $N_{i,t}$ and $N_{i,c}$ are the number of tissue and crevice bubble nuclei respectively. It is via the gas flux terms in equation (8.8) that the two modes of bubble formation may interact, by competition for the dissolved gas in the tissue. Local effects of diffusion directly between tissue and crevice bubbles in close proximity are neglected, as this would be is highly dependent upon the precise geometric arrangement of bubble sites.

The baseline values of parameters used in the model are given in Table 8-1. These are mostly reproduced from chapter 4, with values for the tissue model chosen from previous applications, Srinivasan *et al.* (1999), (2003). The tissue parameters assume that the inert gas under consideration is nitrogen and that the tissue has a half-time of 10 minutes, although the effects of a longer tissue half-time on the joint bubble behaviour will be explored below. The value of *M,* the bulk tissue modulus of elasticity, is initially set to zero for simplicity. A lower value of crevice bubble surface tension was chosen that originally proposed in chapter 4 given its effects on crevice bubble behaviour observed in chapter 5.

Table 8-1. Model parameters for the three aspects of the model; tissue, tissue bubbles and crevice bubbles.

Parameter	Value
Tissue	
τ	2000 s
L_t	0.0125 ml-gas/ml-tissue
D_t	2.2×10^{-12} m^{2}s^{-1}
Tissue bubble	
r_0	10 μm
λ	1 μm
σ_t	0.05 Nm^{-1}
M	0 Pa m^{-3}
Crevice bubble	
θ_0	90°
d_0	1 μm
ϕ	2°
d_m	5 μm
α_a	100°
α_r	80°
γ_s	90°
σ_c	0.01 Nm^{-1}

Tissue bubbles are assumed to grow from nuclei with a radius of 10 μm, which is the upper end of the size that has previously been used, Srinivasan *et al.* (1999), Srinivasan *et al.* (2000), Srinivasan

et al. (2002), (2003). Crevice bubbles are assumed to grow from an initial size of $1 \ \mu m$. In the body it would be expected that there would be variation across the population of tissue bubble nuclei and crevice nucleation sites. However, for simplicity only a single type of each was simulated to reduce the complexity of the model; although this will affect the precise predictions from the model it will still allow the joint behaviour of tissue and crevice bubbles to be examined, which is the primary aim of this chapter.

Initially tissue bubble and crevice densities of $1 \ ml^{-1}$, a negligible density, were used in simulations so that variations in the values of each could be explored independently. It is difficult to estimate the density of tissue bubble nuclei and crevice nucleation sites on blood vessel walls that may be present in the body; hence the effects of variations in the number of nucleation sites were explored. Similarly to chapter 4 the joint bubble model was parameterised into a pseudo non-dimensional form, where only the time dimension was retained.

8.3   Results

The behaviour of the joint bubble model will be considered under a simple saturation decompression from 4 bar to 1 bar at a rate of $0.01 \ bar \, s^{-1}$ ($0.6 \ bar \, min^{-1}$). An example of the evolution of the crevice and tissue bubbles for the parameters in Table 8-1 is shown in Figure 8-2. The evolution of the crevice bubble is similar to Figure 5-6, but only 117 bubbles are released in this case, the bubble release process finishing 10 minutes after the start of decompression. Finally, as the tissue bubble collapses the crevice bubble interface recedes back into the crevice until stability is reached.

The behaviour of the bubbles will be examined by recording the number of bubbles produced from the crevices and the maximum size to which the tissue bubbles grow. Figure 8-3 shows how the density of crevice bubble sites affects the growth behaviour of both types of bubble. No effect is seen until the crevice density equals $10^7 \ sites \, ml^{-1}$. The number of bubbles produced from a crevice and the maximum size reached by the tissue bubbles show similar behaviour because they are both dependent upon the same source of dissolved gas. The production of crevice bubbles tends to reduce the tissue gas tension, as this process removes gas from the tissue into bubbles in the

blood. The number of bubbles released drops as the crevice density increases, hence large numbers of crevice sites drain the tissue more rapidly, leading to a reduction in maximum tissue bubble size.
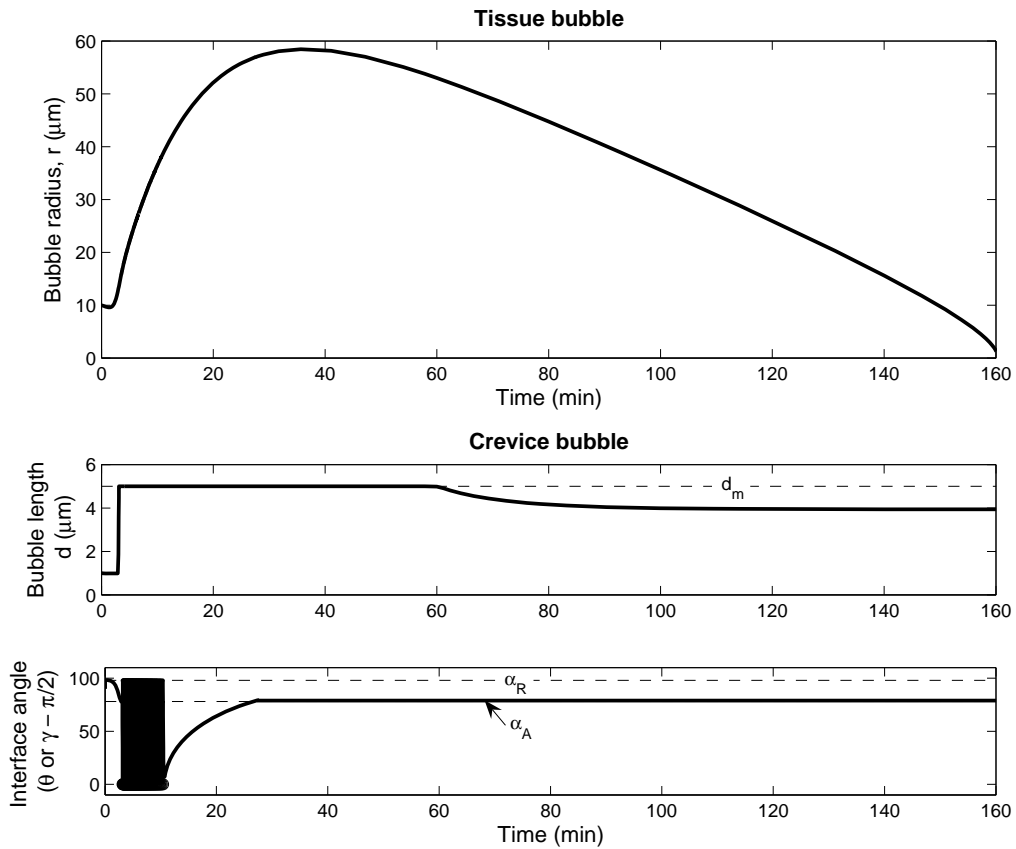

Figure 8-2. The evolution of the joint crevice bubble model using the parameters in Table 8-1. The release of bubbles from the crevice nuclei is relatively rapid and is shown by the solid section on the interface angle plot.

Unlike bubble production from crevices, which carries gas away from the tissue, the growth of tissue bubbles stores gas within the tissue. This storage could, in principle, be highly efficient as the total gas content of one ml of tissue could be contained in about a 100th of the volume in gas phase. For the values of parameters considered here, an increase in tissue bubble density beyond 10^3 ml^{-1} results in a reduction in the maximum size of the tissue bubbles and likewise a reduction in the number of bubbles produced from the crevices, Figure 8-3. This is to be expected as the tissue bubbles are in competition with each other and with the crevice bubbles for the gas held in solution in the tissue. In this case the storage of gas by the tissue bubbles is seen to reduce the impact of the decompression in terms of the production of blood bubbles. Although, as the density of tissue bubbles increases the maximum size of the tissue bubbles decreases, the volume of gas

contained in the bubble sites increases, so the tissue bubbles are acting to store significant quantities of gas at high bubble densities.

Figure 8-3. Variation in the number of bubbles produced from the crevice nuclei (top) and the maximum radius of the tissue bubbles (bottom) with variation in nuclei density.

A longer tissue half-time inevitably leads to a greater production of crevice bubbles and larger increases in tissue bubble size, because the tissue gas tension remains above ambient for longer, driving gas into the bubbles. Consequently lower densities of crevice sites and tissue bubble nuclei are needed, as compared to a tissue with a shorter half-time, before an impact on the bubble

behaviour is seen. For example, with a tissue half time of 100 minutes the effects of competition between tissue bubbles can be seen in densities as low as 10 ml^{-1}, as shown in Figure 8-4, whereas densities of 10^7 ml^{-1} were needed for a 10 minute half-time. The impact of the crevice bubbles is not seen until their density reaches 10^6 ml^{-1}.
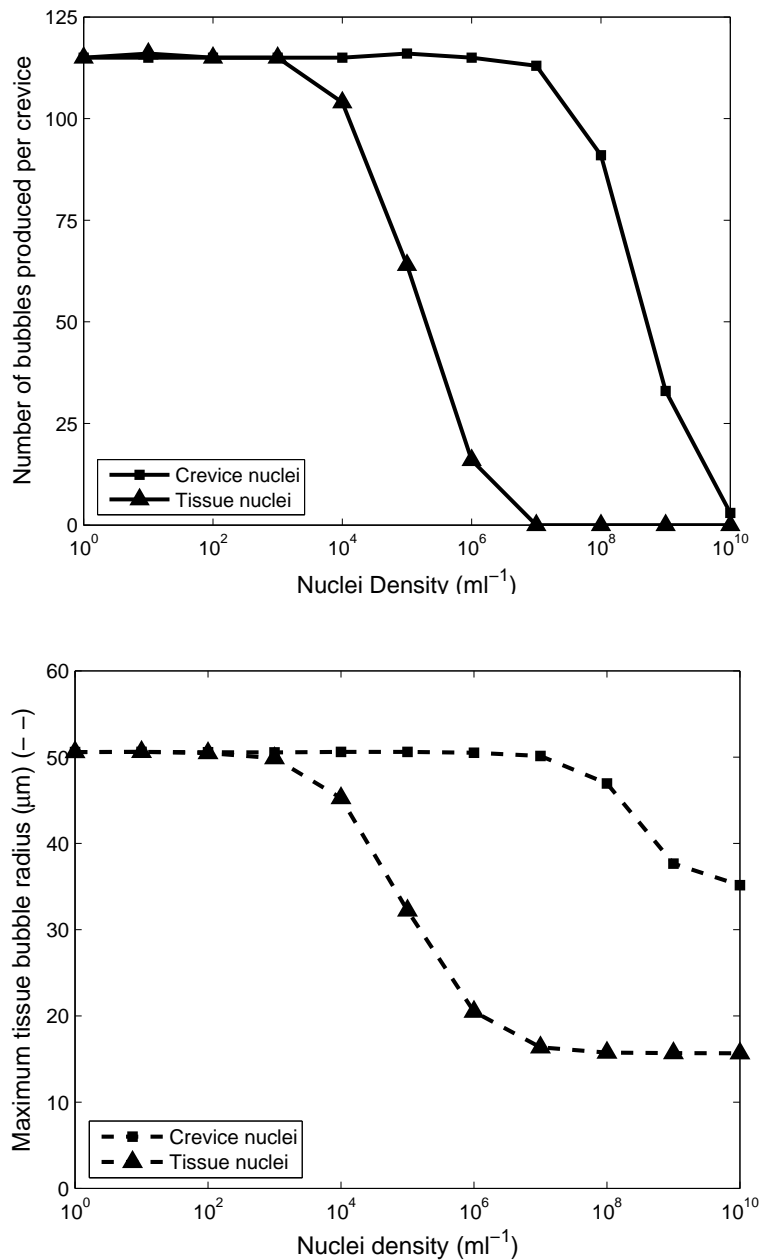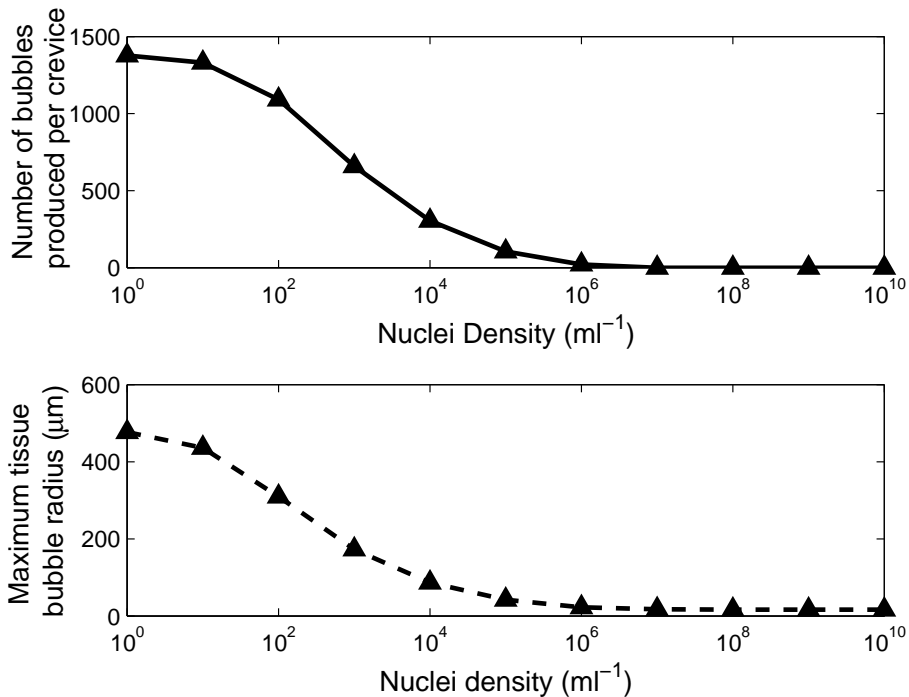

Figure 8-4. Variation in the number of bubbles produced from the crevice nuclei (top) and the maximum radius of the tissue bubbles (bottom) with variation in tissue nuclei density for a 100 minute half-time tissue.

Figure 8-5a shows how the rate of bubble production from the crevices over time varies with the density of tissue bubbles for a half-time of 10 minutes. The initial rate of bubble production is not affected by the tissue bubble density, except at very high densities. However, as the density increases, the time over which bubble production occurs reduces; hence fewer bubbles are ultimately released. This result is consistent with the tissue bubbles serving as gas storage: the greater the density of tissue bubbles, the more of the dissolved gas transfers into them and hence the more rapid is the reduction of the tissue gas tension which drives the production of bubbles from the crevices.
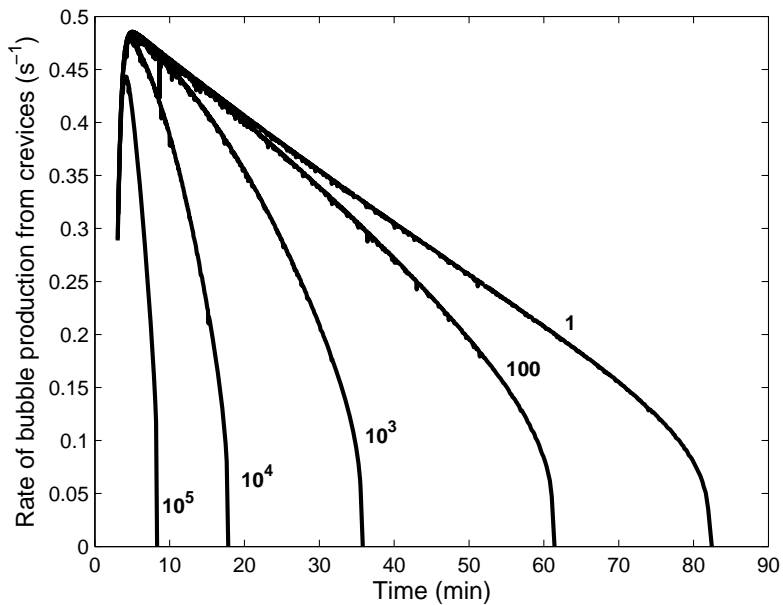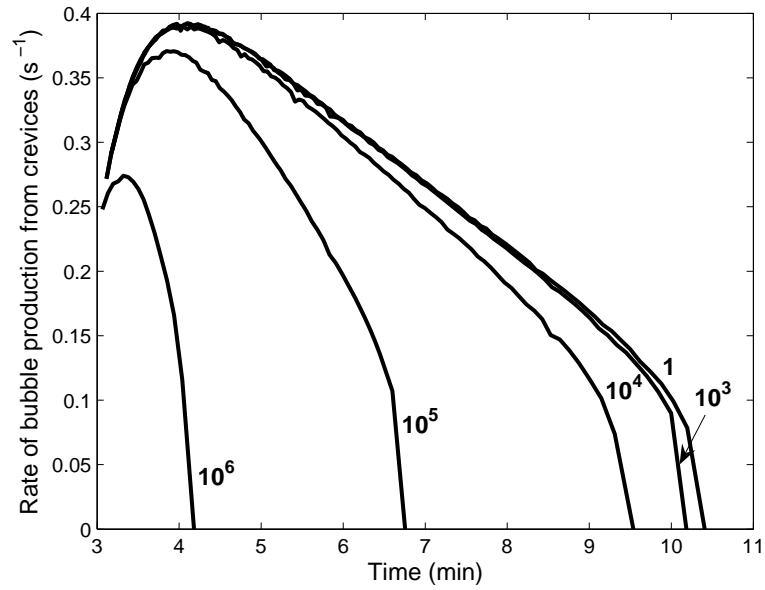
Figure 8-5. Variation in the rate of bubble production from crevices with variation in crevice nuclei density, for both a 10 minute (top) and 100 minute (bottom) tissue half-time.

The effect of increasing the tissue half-time is illustrated by comparison with Figure 8-5b, where a half-time of 100 minutes has been used. Similar to variations in tissue bubble density the tissue half-time has little effect on the initial peak rate of bubble production, although the duration of bubble production is almost an order of magnitude longer for a 100 minute half-time compared to a tissue with a 10 minute half-time. With the longer tissue half-time, the reduction in tissue gas tension by perfusion is smaller; hence there is a much longer period of time over which bubbles will be produced from the crevices. However, again, as the tissue bubble density increases, the

duration of bubble production reduces, because the reduction in tissue tension is more rapid due to storage in the tissue bubbles. Neither of the effects of tissue bubble density and half-time are significant early in the post-decompression period, as neither has had time to cause a significant reduction to the tissue gas tension; hence the initial and peak rates of bubble production are primarily determined by the initial tissue gas tension and the decompression.

As has been illustrated above, one of the effects of storage of gas in bubbles is a more rapid reduction of the tissue gas tension than that which occurs by perfusion alone. However, unlike perfusion, which removes gas from the tissues, the transfer of gas into tissue bubbles is only temporary and ultimately has to be released back into the tissue to be removed by perfusion, albeit at a later stage. With a short tissue half-time, such as 10 minutes, as considered above, the release of the gas stored in the tissue bubbles occurs slowly as they collapse over a time scale of the order of 3 hours. This release of gas is sufficiently gradual, compared with the time constant for removal by perfusion, that there is no appreciable increase in the tissue gas tension during this time. However, this is not the case with a longer tissue half-time, for example 100 minutes as illustrated in Figure 8-6.

With a low tissue bubble density, 1 ml^{-1}, the reduction in tissue gas tension is primarily by perfusion and so approximately follows an exponential decay with a time constant of τ. With a tissue bubble density of 1000 ml^{-1} the initial rate of growth of the bubble is approximately the same as with a lower tissue bubble density, but because the density is now higher the rate of gas transfer into the tissue bubbles becomes significant. Hence the transfer of gas into the tissue bubbles can be seen to increase the rate of reduction of the tissue gas tension. However, unlike the low tissue bubble density case the tissue gas tension does not tend (during the lifetime of the tissue bubbles) toward equilibrium with the partial pressure of inert gas in the breathing mixture, taken here to be 0.79 bar. Instead it settles around 1 bar, because of the release of gas that was stored in the tissue bubbles as they collapse. In this case it appears that the rate of release of gas from storage in the tissue bubbles is almost as fast as the removal via perfusion, as the rate of reduction of tissue gas tension during bubble collapse is almost zero.
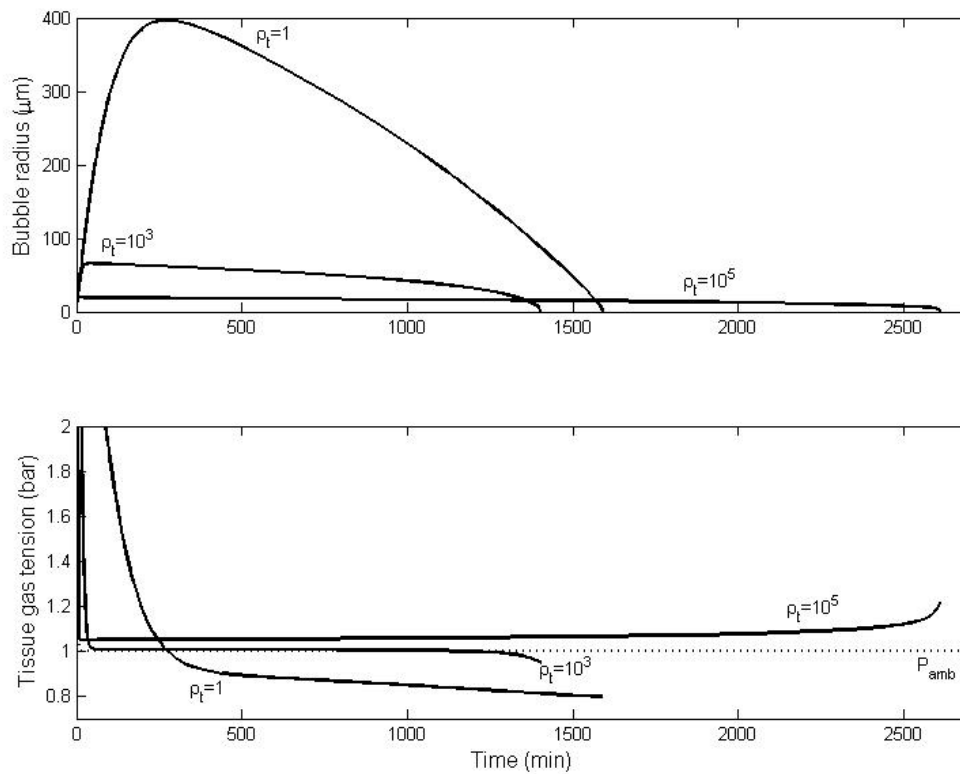
Figure 8-6. The effect of bubble storage on tissue gas tension (tissue half-time of 100 minutes): with as increase in tissue nuclei density (ρ_t) a greater volume of gas is stored in tissue bubbles, when they collapse this release of gas causes the tissue gas tension to be held near or above ambient pressure for an extended duration.

This behaviour is not seen in simulations of a 10 minute tissue because in this case the rate of removal of inert gas by perfusion is sufficiently fast that, during tissue bubble collapse, it exceeds the rate of release of gas from the tissue bubbles. For an even higher density of 10^5 ml^{-1} the initial reduction of tissue gas tension as the bubbles grow is again even more rapid then the lower density case. With this density, during bubble collapse the rate of transfer of gas into the tissue from storage exceeds the removal via perfusion, hence during bubble collapse the tissue gas tension increases slowly. The rate of release of gas from tissue bubbles accelerates towards the end of the tissue bubbles' lifetime; this can be attributed to the increase in the pressure within the bubble due to the surface tension as the bubble gets smaller. As the pressure inside the bubble increases so the pressure difference between the bubble and the tissue that drives gas out of the bubble increases resulting in a greater flux of gas.

Such results have been observed previously in an application of the tissue bubble model incorporated here into the joint bubble model, Srinivasan *et al.* (1999), and it has been noted that the tissue gas tension essentially becomes 'clamped' to the pressure of gas in the bubble, Tikuisis *et al.* (2003). That the storage of gas in bubbles slows the removal of gas from the tissues has previously been noted by Thalmann and formed the basis of the Exponential-Linear gas exchange model, Tikuisis *et al.* (2003).

The above results show that the tissue gas tension can be maintained above equilibrium with the partial pressure of inert gas in the breathing mixture due to the release of gas stored in tissue bubbles. In principle this could lead to a further production of bubbles in the blood from the crevices. The growth of crevice bubbles is driven by the transfer of gas from the tissue into the crevice bubble which will occur if the total pressure of dissolved gases (the tension of the inert gases plus the metabolic gases and water vapour pressure) in the tissue exceeds the pressure in the crevice bubble, as given by the Laplace equation. For example with a density of 10^5 ml^{-1} in Figure 8-6 the inert gas tension in the tissue stabilises at approximately 1.2 bar, hence the total tissue gas tension is 1.37 bar (including $P_{i,N}$ from the metabolic gases and water vapour). For this to cause a bubble to be seeded from a crevice this pressure must be greater than that in the bubble when the interface angle of the crevice bubble, when it is at the mouth of the crevice, with the blood vessel wall equals γ_s. This requires a bubble radius of curvature of 0.17 μm resulting in a pressure due to surface tension of 1.17 bar, hence a total pressure inside the crevice bubble of 2.17 bar. Thus under these conditions bubble production from the crevices would not continue during the collapse of the tissue bubbles.

However, as has already been noted, with high tissue bubble densities the tissue gas tension increases during the final stages of bubble collapse, thus it is feasible that the production of bubbles in the blood from crevices might resume some time after decompression. The evolution of both types of bubbles with a tissue half-time of 360 min, a tissue bubble density of 10^5 ml^{-1} and surface tensions of 0.3 Nm^{-1} and 0.003 Nm^{-1} in the tissue and at crevice respectively is shown in Figure 8-7. Bubbles are produced from the crevice from 3 minutes after the start of the profile until 18

minutes and resumes once the tissue gas bubbles have collapsed to 15 μm approximately 39 hours after the start of the decompression.
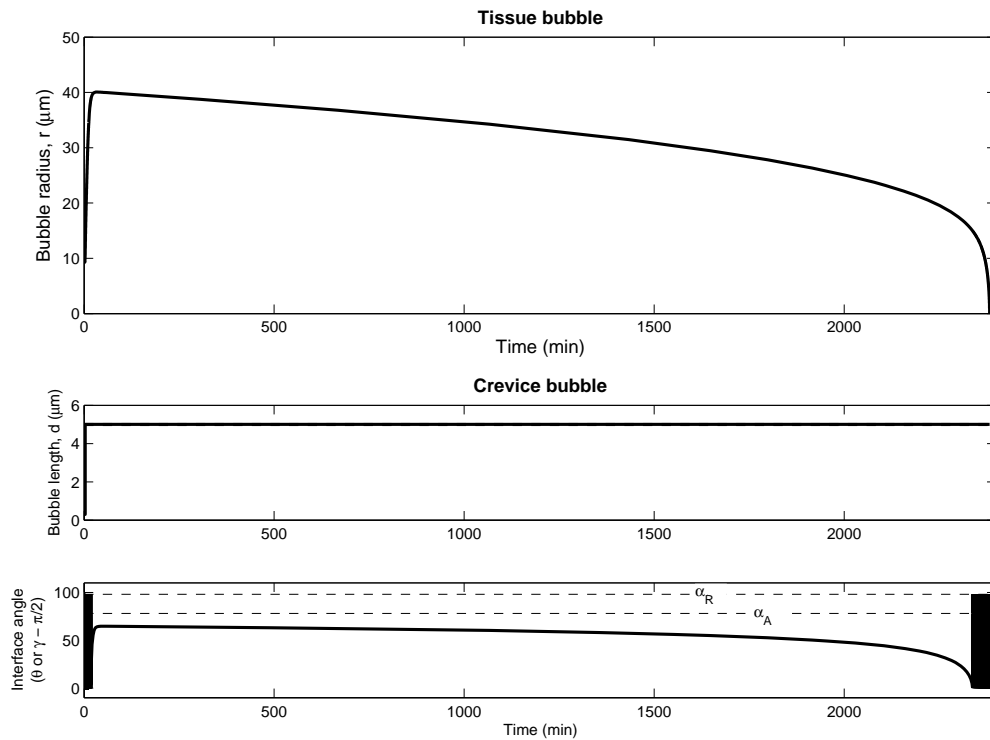
Figure 8-7. An example of 'secondary seeding', where the crevices resume the seeding of bubbles into the blood due to the release of gas from the collapsing tissue bubbles.

In this case a large tissue surface tension is required to increase the rate at which gas is driven out of the bubble during the final stages of collapse, when the pressure due to the surface tension becomes large. A small surface tension for the crevice bubbles is also required to reduce the threshold needed for the crevice bubble to grow to a size where a bubble is released into the blood. The 'secondary seeding' of bubbles occurs at a much slower rate than the initial seeding, reaching a maximum of 0.2 s^{-1} as compared to 1.9 s^{-1}, because the pressure difference between the tissue gas tension and the bubble pressure is only just above the threshold for bubble production. However, bubble production occurs for over 40 minutes, finishing only once the tissue bubbles finally collapse.

For gas storage the value of the tissue bubble surface tension is important, as this raises the pressure inside the bubble, as shown by its appearance in the Laplace equation (8.1). An increased surface tension will result in a smaller growth of the tissue bubbles as the pressure gradient (between tissue tension and bubble partial pressure) driving gas into the bubble is smaller, because

the pressure due to the surface tension is larger making the pressure inside the bubble higher. However, an increased surface tension also acts to drive gas out of the tissue bubbles more rapidly once the tissue gas tension has fallen. Hence, although large surface tensions act to reduce the quantity of gas stored in the tissue bubbles, a raised surface tension, as used in the previous simulation, results in the tissue gas tension being held at a larger raised pressure during tissue bubble collapse, which led to the resumption of bubble production from the crevices. Since the pressure due to surface tension is inversely proportional to the radius, as the bubbles collapse this pressure, which drives gas out of the bubbles, rises. Hence for a tissue bubble density of 10^5 ml^{-1} the tissue gas tension rises during bubble collapse.

The bulk tissue elasticity has a similar influence on the tissue bubbles as the surface tension, because it increases the internal pressure of the tissue bubbles. This pressure is a cubic function of the radius, hence it is most significant for large bubbles. This would imply that it should resist large bubble growth and in turn increase the pressure driving gas out of large bubbles, where the pressure due to surface tension is small. However, a value for M of 14.5×10^{14} Pa m^{-3}, Srinivasan et $al.$ (2003) was found here to have no significant effect on the joint bubble behaviour. Simple analysis of the Laplace equation suggests that the bulk tissue elasticity would only become significant for bubbles with radii approaching 1000 μm. Since such tissue bubbles sizes have not been observed using the parameter values considered here, the bulk tissue elasticity can safely be ignored.

8.4   Discussion

8.4.1   Tissue bubble model assumptions

The simplest interpretation of the tissue bubble model used here is to assume that the bubble grows in a region of tissue that is homogeneous and that the bubbles are located away from blood vessels which would act as sources or sinks of gas. Under these assumptions the length parameter, λ, can be regarded as the thickness of the diffusion region that surrounds the bubble, Srinivasan et $al.$ (1999). Strictly the diffusion region thickness should vary with the radius of the bubble; otherwise the content of the diffusion region would remain constant which would violate Henry's law, Srinivasan et $al.$ (2000).

In a recent work Srinivasan *et al.* (2003) extended the tissue bubble model to include the presence of sources and sinks within the tissue. Under these conditions the model structure remains the same but the length parameter no longer has such a simple physical interpretation, as the effects of blood vessel proximity to the bubbles are incorporated into λ. Thus it is no longer possible to estimate a priori what value the parameter should take. Typically the inter-capillary distance is of the order of 10 μm. Hence with the tissue bubble sizes considered here the assumption that the bubbles may be far from sources and sinks of gas bubbles is unrealistic and λ cannot be treated as having an exact physical representation in the body. It might be expected that the presence of sources or sinks of gas in the diffusion region of the bubble would increase the rate of gas transfer in or out of the bubble which would be equivalent to a reduction in λ. Thus the bubble would be expected to grow larger, but also collapse sooner. This is consistent with the results of Srinivasan *et al.* (2003) using a 180 minute tissue half time.

For shorter tissue half times the variation in λ appears only directly to affect bubble size and not its lifetime, because the removal of gas from the tissue by diffusion is rapid. Thus it would be expected that the bubble sizes in the joint model presented here may be an underestimate and that the storage of gas in tissue bubbles for a given bubble density would be larger than predicted, with resultant implications on the time taken for the removal of gas from the tissue and the production of crevice bubbles.

8.4.2 Tissue bubble density

Typically tissue bubbles are assumed to grow from pre-existing spherical micro bubbles which are stabilised against collapse due to the presence of certain surface active materials, Fox *et al.* (1954), Yount (1979), Van Liew *et al.* (1997). Their presence in the gas-liquid interface is assumed to support the bubble against dissolution at very small sizes by resisting a reduction in the bubble's surface area. Such nuclei have been confirmed *in vitro*, for example in gelatine and water, Herman (1974), Johnson *et al.* (1981), Yount *et al.* (1984). However, the precise source of tissue bubbles is still unknown; hence it is difficult to estimate tissue bubble densities for real body tissues from these proposed mechanisms.

Experimental data for the growth of populations of bubbles in body tissues is also rare. Bubbles may be detected *in vivo* using ultrasound whereby tissue bubbles can be detected as highly reflective stationary targets in 2-dimensional scans, Rubissow *et al.* (1971). It is possible using, for example, the work of Daniels *et al.* (1980) to establish some very simple estimates for the density of bubble production under simple decompressions. This work involved the assessment of bubble production in the hind legs of guinea-pigs after a rapid (60 s) decompression from saturation on air. The thickness of the collection region of their scanning system was approximately 2 mm, Daniels *et al.* (1979), hence the collection volume was of the order of 0.1 ml. In these experiments persistent echoes (those that lasted for more than one frame) were observed these might have correlated with tissue or stationary vascular bubbles. In the examples given, with decompressions of 0.69 MPa (0.115 bar s^{-1}) and 0.83 MPa (0.134 bar s^{-1}), persistent event numbers of 16 and 60 were observed respectively, although it is possible that each echo may have represented more than a single bubble in close proximity due to the resolution of the system. This implies tissue bubble densities up to 100-1000 ml^{-1}, this being an upper bound because some persistent events may have corresponded with stationary intravascular bubbles, for example due to the coalescence of bubbles causing them to block small vessels. Although the decompressions considered in these experiments were more provocative than those considered theoretically here, these estimates imply that such densities of tissue bubble nuclei may be feasible in the body. However, it would seem unlikely that densities larger than this would be expected under normal decompression profiles. It is likely that less severe decompressions would recruit fewer nuclei, because fewer of the nuclei would be above the critical size for growth for the given decompression magnitude.

8.4.3 Crevice model assumptions

It has been assumed in the crevice model that there is no diffusion of gas across the gas-blood interface. Under decompression it would be expected that gas would also diffuse into the bubble from the blood as well as the tissue, increasing its growth rate as discussed in section 5.4.3. Thus the rate of bubble production would be increased. However, this effect is unlikely significantly to lower the high crevice density required to have an effect on the growth of tissue bubbles.

8.4.4 Crevice site density

As has already been noted in section 2.3.6, a number of different sites for bubble nucleation in the vasculature have been proposed: the intercellular clefts between endothelial cells or the invaginations found on the surface of endothelial cells called caveolae. As has been noted the geometry of both proposed nucleation sites is broadly represented by the conical crevice considered here, although specific details of the geometry do differ.

For the intercellular clefts of endothelial cells, Clough *et al.* (1988), have reported a cleft length density of 2064 cm per cm^2 from observations of the surfaces of capillaries and venules of frog mesentery. Capillaries typically vary in diameter from 3.5-10 μm, Schneck (2000), with an average density of 600 mm^{-3}, resulting in an surface area of capillaries of the order of 0.01-0.1 m^2 ml^{-1}. An upper bound for an estimate for the number of nuclei would be to assume that a length of cleft is equivalent to a series of conical crevices: as the width of a typical cleft was found to be 0.02 μm, this results in 50 nuclei per 1 μm of cleft length. Hence the upper bound on the number of nuclei is of the order of 10^{10} ml^{-1}, although the true value would be expected to be orders of magnitude smaller than this.

The density of caveolae in endothelial cells, however, is not apparent from the literature. Measurements have been made of orifices associated with caveolae in adipocytes of approximately 20 openings per mm^2, Thorn *et al.* (2003). Using the surface area of endothelium per ml calculated above gives an estimated caveolae density of the order of 10^5 ml^{-1}. This is significantly lower than the estimate based on cleft length and from the results of the simulations presented here this density would imply that the seeding of bubbles from nucleation sites in the blood vessels would not have a significant impact on the reduction of the tissue gas tension post-decompression and hence no significant effect on the joint bubble model behaviour.

It is difficult to compare predictions from this model for the number of bubbles produced from crevices in the blood and observations of moving bubbles in the body. Daniels *et al.* (1980) observed transient echoes in the 2-dimensional ultrasound scans in the experiments described

above. During the 60 s of decompression and a further 60 s post-decompression, 77 and 195 transient events (appearing in only 1 frame) were found for the 0.69 MPa and 0.83 MPa decompressions respectively. Transient events were assumed to correspond to bubbles in the blood passing through the collection volume. Since scanning was performed at a rate of 1 Hz, Daniels *et al.* (1980) estimated that the total number of blood borne bubbles might be up to a factor of 100 greater than those observed, accepting that the upper end of this range is probably an over estimate. These values lead to estimated bubble production rates of up to approximately 10 s^{-1}. It is impossible to tell from where these bubbles originated, although it is reasonable to assume they come from sites within the hind leg of the animal and hence from a volume of approximately 1 ml. Peak bubble production rates from the decompression considered here are 0.4 s^{-1} from each crevice, hence for even relatively low crevice density the bubble production estimate of Daniels *et al.* (1980) is exceeded. Again the profile used in these experiments was far more provocative than that modelled here.

However, a critical difficulty in comparing bubble production from crevices and their detection using ultrasound in experiments is bubble size. Daniels *et al.* (1980) estimated that they would be unable to detect bubbles smaller than 10 μm, Daniels *et al.* (1979). Thus the bubbles produced from the crevices in this model would be undetectable using the techniques described here. However, the bubbles produced from the crevices would be expected to grow during their transit in blood vessels and bubbles might coalesce resulting in sizes above the detection threshold, thus a large density of crevices could result in a much smaller density of bubbles observed in the blood using ultrasound.

In their experiments, Daniels *et al.* (1980) estimated the amount of gas present in the transient events they observed based on estimates of the bubble sizes. Having applied corrections for movement and subjectivity the estimated gas volume that passed through the plane during the observation period was 4.87×10^{-11} m^3 and 4.05×10^{-10} m^3 for the 0.69 MPa and 0.83 MPa decompressions respectively. Since these estimates only take into account transient events, and not stationary intra-vascular bubbles, this figure may be an underestimate. Again these figures could be multiplied by 100 to account for the scanning rate of the ultrasonic equipment used. The volume of

each bubble that is released from a crevice for the parameters used here is approximately 10^{-20} m^3. If it is assumed that these observed transient bubbles are purely due to the coalescence of smaller bubbles that come from nucleation sites in the hind-leg alone, i.e. these bubbles have not grown during their time in the vasculature, these estimates would imply nucleation densities of the order of $10^8 - 10^{12}$ ml^{-1}. This estimated value is very large and seems somewhat unlikely. The assumption that bubbles don't grow in the vasculature is the main limitation of these estimates of crevice nuclei density, as it is highly likely that bubbles would grow from the dissolved gas in the blood. It is also unclear as to what extent bubbles might have the opportunity to coalesce whilst in the vasculature. This phenomenon has been observed experimentally, Lever *et al.* (1966), but appropriate theory does not exist to predict it. It is probable that the theory of bubble coalescence in chemical processes, for example Wang *et al.* (2005), can be adopted. However, this is beyond the scope of the work presented here.

Measurements of bubbles moving in the blood are routinely made using Doppler ultrasound. This is most commonly done in the precordial area so that the production of bubbles in the whole vasculature can be estimated. However, not all bubbles that form in the vasculature are necessarily observed in the predordium. For example bubbles might grow sufficiently large by diffusion or coalescence to block smaller vessels and hence be held stationary. Additionally such measurements are typically provided on a standard semi-quantitative scale. Thus although measurements for human subjects, over a wide range of pressure profiles, are available in the literature, comparison with the results presented here are very difficult. Although more quantitative measurements of bubbles in the precordial area have been provided by Eftedal *et al.* (1997), it is still difficult to draw comparisons between measured bubbles in the blood and the results of the joint bubble model.

Using the methods described, the peak in bubble occurrence in the blood is typically an hour after decompression and often some delay is seen before bubbles are observed: in some cases delays of up to an hour have been reported, Nishi *et al.* (2003). The joint bubble model predicts peak bubble production rate at around 5 minutes after the start of the decompression irrespective of the tissue half-time. Although some variation may be expected with the exact form of the decompression, the joint bubble model does not appear to predict the observed peak in blood bubble production or

large delays in bubble detection. However, as has been noted, the joint bubble model does not describe the behaviour of the bubbles once they leave the crevice as they transit in the bloodstream. It is likely that the interaction between bubbles and the vasculature and other bubbles may introduce further time delays for the arrival of bubbles at the observation sites.

8.5   Conclusions

The joint bubble model presented here allows the interaction between the growth of tissue bubbles and the production of bubbles from crevices in the blood to be investigated. The influence of tissue bubbles is found to occur at relatively low densities, especially for long tissue half-times. Although it is very difficult to estimate the density of tissue bubble nucleation sites in the body, it seems likely that they would be sufficiently large for tissue bubble growth that would have an impact both on the maximum size reached by tissue bubbles and the number of bubbles that are released from crevices in the blood vessels.

The main effect of high tissue bubble densities is that the reduction in the tissue gas tension is more rapid than by perfusion alone. This will result in fewer bubbles produced from the crevices as the pressure difference driving this growth is reduced more rapidly. Significantly, gas which transfers into tissue bubbles is not removed from the tissue but held in storage; thus the time taken fully to remove the gas from the tissue is substantially extended because the release of gas from the tissue bubbles via the tissue is much slower than the perfusion process alone.

The release of the gas from storage in the tissue bubbles can occur at a greater rate than removal by perfusion when the tissue half-time is large. The result is that the tissue gas tension is held at a raised level whilst the bubbles collapse and even may increase sometime after decompression. It is possible with a long half-time and a relatively high surface tension for the tissue gas tension to increase to a value such that bubble production from crevices restarts. However, the parameters required to achieve this effect in simulation are at the limits of those that might realistically be expected in the body. This effect has not been reported using ultrasonic observation of blood borne bubbles post-decompression, although there are few observations which are of sufficient length or detail to confirm this.

The effect of crevice density is found to occur at much higher nuclei density than that of the tissue bubbles, the effect of high crevice bubble density being to remove gas from the tissue, thus speeding the rate of reduction of tissue gas tension, without the storage effects of the tissue bubbles. Since the size of the bubbles produced by the crevices is small, the resultant removal of gas is also relatively small compared to the storage in tissue bubbles, hence high densities are required. Given the simple estimates of crevice site density that may be observed in the body and comparisons with experimental results it seems unlikely that crevice site densities in the body would be sufficiently large to have a significant impact on the joint bubble behaviour.

9. Conclusions
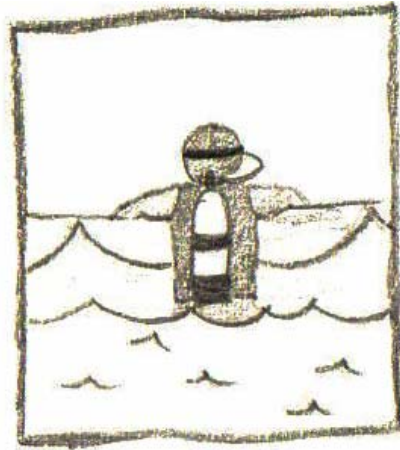
The role of bubbles in DCS is complex and not well understood. A major obstacle is presented by the difficulties associated with experimental investigation: large number of variables, rarity of DCS in practice, large range of disparate symptoms. Additionally visualisation of bubbles as they form and are transported around the body is virtually impossible, especially as numerous tissues and blood vessels need to be considered. The most effective methods for making measurements of bubbles *in vivo* are ultrasonic techniques. However these are all limited by the information they can provide. 2D ultrasound can potentially give detailed picture of bubble formation and transport, but within a much-localised area of investigation and it remains difficult to interpret such scans from tissue areas. Doppler ultrasound has been widely adopted for the simplicity of data collection. However it is limited to the detection of circulating bubbles, i.e. only the bubbles emerging in blood vessels from limbs or even the whole body can be assessed.

Previously the information available has been further limited by the subjectivity and semi-quantitative nature of the Doppler grading methods. However, for the first time non-stationary signal processing techniques, such as those applied to Doppler signals in chapter 3, offer the opportunity to extract fully quantitative bubble occurrence measurements from Doppler ultrasound data. Since the technique is automated, continuous measurement of bubbles produced in the body is feasible, allowing the time course of bubbles to be tracked and, for example, related to DCS risk.

However, the system as proposed in chapter 3 is still in its early stages of development and needs full-scale validation before it can be applied as a Doppler data bubble evaluation tool. Validation is particularly difficult given the limitations of the existing 'gold standard' labelling method, although with the large quantities of data available it is feasible.

The utility of Doppler ultrasound is still severely limited by the lack of a clear correlation between observable bubbles and the symptoms of DCS. Although more information about bubbles will be available if the time course of bubble production is continuously monitored, it is still unlikely that a simple correlation will be evident. Fundamentally, Doppler or any other method of bubble evaluation can only provide limited information and to be able to make use of it the relationship between such measurements and the complete bubble production and transport in the whole body needs to be described. This has been the aim of chapters 4 through 8 in which mathematical models have been used to describe the formation of bubbles in the vasculature and to determine under what conditions these bubbles detach from their sites of formation and are swept around the circulation, whereupon they can be detected using Doppler. Principally this work has concentrated on the formation of bubbles at nucleation sites, in the form of crevices, in the surfaces of the blood vessels. The simulations in chapter 5 demonstrate that under physiologically realistic conditions such a form of crevice is a feasible form of nucleation site for blood borne bubbles.

A limitation of the modelling in chapter 4 is that the geometry of nucleation sites in the body has yet to be verified experimentally. This issue was considered in chapter 6 where it was shown that, although the precise geometry does have an impact on the initial bubble behaviour, the general behaviour is described well by the simple conical crevice, especially once the bubble has emerged from inside the cavity and the production of blood-borne bubbles begins. The bubble production process determining the number of bubbles launched into the circulation, which can be observed by the Doppler ultrasonic detector. This process, as a result of the flow of blood past and over the bubble was considered simply in chapters 4 and 5 and in more detail in chapter 7. The general behaviour tends to result, dependent upon the physiological conditions, in a single crevice either remaining dormant under decompression and releasing no bubbles or rapidly releasing a large quantity of bubbles into the blood. This distinctly on/off behaviour is surprising as large number of nucleation sites may be expected in the body, but the rate of bubbles passing through the

pulmonary artery are not commonly that high. It may be that there are many nucleation sites in the body, but only a few at any one time which have the suitable conditions to release bubbles. Additionally, bubbles observed at the pulmonary artery have passed through the circulation, during which time various processes, such as bubble coalescence, may have occurred.

One process that could substantially affect the number and timing of bubbles observed in the pulmonary artery is the sticking of bubbles in capillaries. Chapter 7 has addressed to what extent bubbles forming in capillaries might grow to a size where they are able to lodge in the capillary before reaching the wider venous circulation. This simple analysis starts to address the issues of bubble transport in the circulation: however, there has not been scope in this project to undertake the modelling of bubble transport further to describe what happens to the bubbles between their formation and the Doppler monitoring site. Hence, although the theory seeks to address how the Doppler measurements can be interpreted, the issue of bubble transport still needs to be addressed. Alongside exploring the link between the formation of blood-borne bubbles and those measured by Doppler, the link between these moving bubbles and those that form within the tissues is also important. Both bubbles forming in the blood and those in the tissues are implicated in the various symptoms of DCS and it is feasible that different occurrences of symptoms under different conditions may be accounted for by differences in which types of bubbles form where in the body. Chapter 8 addresses this relationship between the formation of blood and tissue bubbles. It demonstrates that the growth of tissue bubbles can have a significant impact of the number of duration of bubble production in the vasculature. However, the effects of vascular bubble formation on tissue bubbles are minimal.

The validation of the theoretical model itself is an important issue, which has not been addressed here. Although built on existing models, themselves describing aspects of bubble behaviour which have been verified elsewhere, the model for the formation of bubbles in the blood, in particular, needs physiological validation. However, there is no clear and easy method for doing this, primarily because the close observance of bubbles in the body is infeasible. The use of quantitative Doppler measurements, however, does offer a certain capability for validation. This is feasible because the pressure profile from which that data has arisen is known in most cases and large quantities of data already exist which would permit statistically significant validation to be

performed. However, this process will also require a model of bubble transport around the vasculature, which it has not been possible to consider here.

Ultimately the model and bubble detection algorithm are complementary: the model permitting bubble measurements to be interpreted in terms of the bubble production in the whole body and in turn the measurements giving some form of validation for the model. The intent is to make the most of the limited information available from measurements of bubbles in the body. As such, however, the model only extends as far as bubbles in the body and not through to the symptoms of DCS. It is feasible that with a more comprehensive bubble model which incorporates bubble transport and multiple tissues that some correlation can be found with the pattern of bubble formation and commonly observed symptoms, i.e. bubbles forming preferentially in one region of the body under a certain profile may correspond to a specific type of symptom. Ideally the model should also incorporate the passage of bubbles into the lungs and their subsequent dissolution. Additionally the potential for bubbles to pass through into the arterial circulation, e.g. via a Patent Foramen Ovalae or through the lungs also needs to be explored. It may also be possible to model the formation of gas plugs forming in capillary vessels, especially important if bubbles pass into the arterial circulation, using existing modelling work on gas embolism, for example Branger *et al.* (1999), Branger *et al.* (2001). This would move the model closer to exploring the relationships between bubbles and symptoms, as gas plugs may be directly responsible for some symptoms by impeding blood flow to sensitive organs.

Physiological models offer an opportunity for a better understanding of the role of bubbles in DCS. For example, many variables can easily be explored within a model. A model for bubbles in the body inevitably needs to be relatively complex; hence validation of such a model against real physiology is important. An advantage of a model, however, is that it can be used to focus experiments on particular areas. Since experimental investigation of bubbles in the body is difficult, time consuming and expensive, a combination of theoretical modelling and appropriate experimentation is likely to be much more efficient.

A significant opportunity from the combination of physiological modelling along with measurements of bubbles in the body may be the provision of personalised decompression

schedules. An ideal would be the creation of a decompression monitor based on a Doppler device worn during the dive that can assess the risk of DCS in real-time. However, it is far from clear that sufficient information would be available during decompression to make this a reality, given that bubbles are known not to appear in a measurable form until some time after decompression. However, the longer-term monitoring of individual physiology may be a more realistic goal. For example, it may be possible to learn from an individual's physiology their personal susceptibility to DCS, something which, without a good method for interpreting Doppler data, is not possible, and thus derive decompression schedules accordingly.

10. References

Atchley, A. A. and A. Prosperetti (1989). "The Crevice Model of Bubble Nucleation." Journal of the Acoustical Society of America **86**(3): 1065-1084.

Bai, H. and B. G. Thomas (2001). "Bubble Formation During Horizontal Gas Injection into a Downward Flowing Liquid." Metallurgical and Materials Transactions B **32**(6): 1143-1159.

Belcher, E. O. (1980). "Quantification of Bubbles Formed in Animals and Man During Decompression." IEEE Transactions on Biomedical Engineering **27**(6): 330-338.

Benkhe, A. R. (1951). "Decompression Sickness Following Exposure to High Pressures." Decompression Sickness, Caisson Sickness, Diver's and Flier's Bends and Related Syndromes. J. F. Fulton, Ed. Philadelphia, WB Saunders: 53-89.

Boyce, J. F., P. C. Wong, S. Schurch and M. R. Roach (1983). "Rabbit Arterial Endothelium and Subendothelium. A Change in Interfacial Free Energy That May Promote Initial Platelet Adhesion." Circulation Research **53**(3): 372-377.

Boycott, A. E., G. C. C. Damant and J. S. Haldane (1908). "The Prevention of Compressed Air Illness." Journal of Hygiene **8**: 342-443.

Boyle, R. (1670). "New Pneumatical Experiments About Respiration. Continued." Philosophical Transactions **63**: 2035-2056.

Branger, A. B. and D. M. Eckmann (1999). "Theoretical and Experimental Intravascular Gas Embolism Absorption Dynamics." J Appl Physiol **87**(4): 1287-1295.

Branger, A. B., C. J. Lambertsen and D. M. Eckmann (2001). "Cerebral Gas Embolism Absorption During Hyperbaric Therapy: Theory." J Appl Physiol **90**(2): 593-600.

Brubakk, A. O. (2004). "Endothelium and Bubble Injury: The Role of Endothelium in Decompression Illness." 30th Annual Scientific Meeting of the European Underwater Baromedical Society, Ajaccio, Corsica, France, EUBS.

Buckles, R. G. (1968). "The Physics of Bubble Formation and Growth." Aerospace Medicine **39**: 1062-1068.

Bühlmann, A. A. (1984). Decompression: Decompression Sickness, Springer-Verlag.

Burkard, M. E. and H. D. Van Liew (1994). "Simulation of Exchanges of Multiple Gases in the Body." Respiration Physiology **95**(2): 131-145.

Butler, B. D. and B. A. Hills (1979). "The Lung as a Filter for Microbubbles." Journal of Applied Physiology **47**: 537-543.

Calderon, A. J., J. B. Fowlkes and J. L. Bull (2005). "Bubble Splitting in Bifurcating Tubes: A Model Study of Cardiovascular Gas Emboli Transport." J Appl Physiol **99**(2): 479-487.

Chan, B. C. B., F. H. Y. Chan, F. K. Lam, P. Lui and P. W. F. Poon (1997). "Fast Detection of Venous Air Embolism in Doppler Heart Sounds Using the Wavelet Transform." IEEE Transactions on Biomedical Engineering **44**(4): 237-246.

Clifford, G. D. (2002). Signal Processing Methods for Heart Rate Variability. Department of Engineering Science. Oxford, University of Oxford.

Clough, G. and C. C. Michel (1988). "Quantitative Comparisons of Hydraulic Permeability and Endothelial Intercellular Cleft Dimensions in Single Frog Capillaries." Journal of Physiology (London) **405**(1): 563-576.

Conkin, J., P. P. Foster, M. R. Powell and J. M. Waligora (1996). "Relationship of the Time Course of Venous Gas Bubbles to Altitude Decompression Illness." Undersea and Hyperbaric Medicine **23**: 141-149.

Crum, L. A. (1979). "Tensile Strength of Water." Nature **278**: 148-149.

Daniels, S. (1984). "Ultrasonic Monitoring of Decompression Procedures." Philosophical Transactions of the Royal Society of London B Biological Sciences **304**: 153-175.

Daniels, S., J. M. Davies, W. D. Paton and E. B. Smith (1980). "The Detection of Gas Bubbles in Guinea-Pigs after Decompression from Air Saturation Dives Using Ultrasonic Imaging." Journal of Physiology (London) **308**(1): 369-383.

Daniels, S., W. D. M. Paton and E. B. Smith (1979). "Ultrasonic Imaging System for the Study of Decompression-Induced Gas Bubbles." Undersea Biomedical Research **6**(2): 197-207.

Didenkulov, I. N., S. W. Yoon, A. M. Sutin and E. J. Kim (1999). "Nonlinear Doppler Effect and Its Use for Bubble Flow Velocity Measurement." Journal of the acoustical society of America **106**(5): 2431.

Doolette, D. J., R. N. Upton and C. Grant (1998). "Diffusion Limited, but Not Perfusion Limited, Compartmental Models Describe Cerebral Nitrous Oxide Kinetics at Both High and Low Cerebral Blood Flows." Journal of Pharmacokinetics and Biopharmaceutics **26**: 649-672.

Doolette, D. J., R. N. Upton and C. Grant (2005a). "Countercurrent Compartmental Models Describe Hind Limb Skeletal Muscle Helium Kinetics at Resting and Low Blood Flows in Sheep." Acta Physiologica Scandinavica **185**(2): 109-121.

Doolette, D. J., R. N. Upton and C. Grant (2005b). "Isobaric Exchange of Helium and Nitrogen in Skeletal Muscle at Resting and Low Blood Flow (Abstract)." Undersea & Hyperbaric Medicine **32**(4): 307.

Dujić, Ž., D. Duplančic, I. Marinovic-Terzić, D. Baković, V. Ivančev, Z. Valic, D. Eterović, N. M. Petri, U. Wisløff and A. O. Brubakk (2004). "Aerobic Exercise before Diving Reduced Venous Gas Bubble Formation in Humans." Journal of Physiology **555**(3): 637-642.

Eftedal, O. S. and A. O. Brubakk (1993). "Detecting Intravascular Gas Bubbles in Ultrasonic Images." Medical & Biological Engineering & Computation **31**: 627-633.

Eftedal, O. S. and A. O. Brubakk (1997). "Agreement between Trained and Untrained Observers in Grading Intravascular Bubble Signals in Ultrasonic Images." Undersea and Hyperbaric Medicine **24**: 293.

El-Brawany, M. A. and D. K. Nassiri (2002). "Microemboli Detection Using Ultrasound Backscatter." Ultrasound in Medicine & Biology **28**(11-12): 1439-1446.

Elliott, D. H. and J. Vorosmarti (2003). "An Outline History of Diving Physiology and Medicine." Bennett and Elliott's Physiology and Medicine of Diving, 5th edition. A. O. Brubakk and T. S. Neuman, Eds., Saunders: 4-16.

Epstein, P. S. and M. S. Plesset (1950). "On the Stability of Gas Bubbles in Liquid-Gas Solutions." The Journal of Chemical Physics **18**(11): 1505-1509.

Eshpuniyani, B., J. B. Fowlkes and J. L. Bull (2005). "A Bench Top Experimental Model of Bubble Transport in Multiple Arteriole Bifurcations." International Journal of Heat and Fluid Flow **26**(6): 865-872.

Evans, A., V. L. Babikian and L. R. Wechsler (1999). "Detection of Microemboli." Transcranial Doppler Ultrasonography, 2nd edition Boston, Butterworth-Heinemann: 141.

Evans, D. H. and W. N. McDicken (2000). Doppler Ultrasound Physics, Instrumentation and Signal Processing. Chichester, Wiley.

Fan, L., D. H. Evans and A. R. Naylor (2001). "Automated Embolus Identification Using a Rule-Based Expert System." Ultrasound in Medicine and Biology **27**(8): 1065-1077.

Flandrin, P., G. Rilling and P. Gonçalvés (2004). "Empirical Mode Decomposition as a Filter Bank." IEEE Signal Processing Letters **11**(2): 112-114.

Forest, T. W. (1982). "The Stability of Gaseous Nuclei at Liquid-Solid Interfaces." Journal of Applied Physiology **53**(9): 6191-6201.

Foster, P. P., A. H. Feiveson, R. Glowinski, M. Izygon and A. M. Boriek (2000). "A Model for Influence of Exercise on Formation and Growth of Tissue Bubbles During Altitude Decompression." American Journal of Physiology - regulatory integrative and comparative physiology **279**(6): 2304-2316.

Fox, F. E. and K. F. Herzfeld (1954). "Gas Bubbles with Organic Skin as Cavitation Nuclei." Journal of the Acoustical Society of America **26**: 984-989.

Francis, T. J. R. and S. J. Mitchell (2003). "Pathophysiology of Decompression Sickness." Bennett and Elliott's Physiology and Medicine of Diving, 5th edition. A. O. Brubakk and T. S. Neuman, Eds., Saunders: 530-556.

Gibby, G. L. (1993). "Real-Time Automated Computerized Detection of Venous Air Emboli in Dogs." Journal of Clinical Monitoring **9**(5): 354-363.

Gibby, G. L. and M. D. Ghani (1988). "Computer-Assisted Doppler Monitoring to Enhance Detection of Air Emboli." Journal of Clinical Monitoring **4**(1): 64-73.

Gürmen, N. M., A. J. Llewellyn, R. A. Gilbert and S. M. Egi (2001). "Simulation of Dynamic Bubble Spectra in Tissues." IEEE Transactions on Biomedical Engineering **48**(2): 185-193.

Halpern, D. and I. D. P. Gaver (1994). "Boundary Element Analysis of the Time-Dependent Motion of a Semi-Infinite Bubble in a Channel." Journal of Computational Physics **115**(2): 366-375.

Halpern, D., Y. Jiang and J. F. Himm (1999). "Mathematical Model of Gas Bubble Evolution in a Straight Tube." Journal of Biomechanical Engineering **121**: 505-513.

Hamilton, P. and W. Tompkins (1986). "Quantitative Investigation of Qrs Detection Rules Using the Mit/Bih Arrythmia Database." IEEE Transactions on Biomedical Engineering **33**(12): 1157-1165.

Harvey, E. N. (1951). "Physical Factors in Bubble Formation." Decompression Sickness. J. F. Fulton, Ed. Philadelphia, WB Saunders: 90-114.

Harvey, E. N., D. K. Barnes, W. D. McElroy, A. H. Whiteley, D. C. Pease and K. W. Cooper (1944). "Bubble Formation in Animals. I. Physical Factors." Journal of Cellular and Comparative Physiology **24**(1): 1-22.

Hemmingsen, E. A. (1989). "Nucleation of Bubbles *in Vitro* and *in Vivo*." Supersasturation and Bubble Formation in Fluids and Organisms. A. O. Brubakk, B. B. Hemmingsen and G. Sundnes, Eds. Trondheim, Norway, Tapir: 43-59.

Herman, M. (1974). "Acoustic Fluctuations Due to Microbubbles in the near-Surface Ocean." Journal of the Acoustical Society of America **56**(4): 1100-1104.

Hills, B. A. (1977). Decompression Sickness, Wiley.

Himm, J. F. and L. D. Homer (1999). "A Model of Extravascular Bubble Evolution: Effect of Changes in Breathing Gas Composition." Journal of Applied Physiology **87**(4): 1521-1531.

Hjelde, A., S. Koteng, O. S. Eftedal and A. O. Brubakk (2000). "Surface Tension and Bubble Formation after Decompression in the Pig." Applied Cardiopulmonary Pathophysiology **9**: 47-52.

Hlastala, M. P. and H. D. Van Liew (1975). "Absorption of *in Vivo* Inert Gas Bubbles." Respiration Physiology **24**: 148-158.

Homer, L. D., P. K. Weathersby and S. Survanashi (1990). "How Contercurrent Blood Flow and Uneven Perfusion Affect the Motion of Inert Gas." Journal of Applied Physiology **69**(1): 162-170.

Huang, N. E., C. W. Man-Li, S. R. Long, S. P. Shen, Q. Wendong, P. Gloersen and K. L. Fan (2003). "A Confidence Limit for the Empirical Mode Decomposition and Hilbert Spectral Analysis." Proceedings of the Royal Society of London. Series A: Mathematical, Physical and Engineering Sciences **459**: 2317-2345.

Huang, N. E., Z. Shen, S. R. Long, M. C. Wu, H. H. Shih, Q. Zheng, N. Yen, C. C. Tung and H. H. Liu (1998). "The Empirical Mode Decomposition and the Hilbert Spectrum for Nonlinear Time Series Analysis." Proceedings of the Royal Society of London. Series A **454**: 903-995.

Jankowski, L. W., R. Y. Nishi, D. J. Eaton and A. P. Griffin (1997). "Exercise During Decompression Reduces the Ammount of Venous Gas Emboli." Undersea and Hyperbaric Medicine **42**(2): 59-65.

Johnson, B. D. and R. C. Cooke (1981). "Generation of Stabilized Microbubbles in Seawater." Science **213**(4504): 209-211.

Jones, S. F., G. M. Evans and K. P. Galvin (1999). "Bubble Nucleation from Gas Cavities - a Review." Advances in Colloid and Interface Science **80**: 27-50.

Kislyakov, Y. Y. and A. V. Kopyltsov (1988). "The Rate of Gas-Bubble Growth in Tissue under Decompression. Mathematical Modeling." Respiration Physiology **71**: 299-306.

Kisman, K. E. (1977). "Spectral Analysis of Doppler Ultrasonic Decompression Data." Ultrasonics **15**(3): 105-110.

Krongold, B. S., A. M. Sayeed, M. A. Moehring, J. A. Ritcey, M. P. Spencer and D. L. Jones (1999). "Time-Scale Detection of Microemboli in Flowing Blood with Doppler Ultrasound." IEEE Transactions on Biomedical Engineering **46**(9): 1081-1089.

Kumar, V. K., R. D. Billica and J. M. Waligora (1997). "Utility of Doppler-Detectable Microbubbles in the Diagnosis and Treatment of Decompression Sickness." Aviation, Space and Environmental Medicine **68**(2): 151-158.

Kunkle, T. D. and E. L. Beckman (1983). "Bubble Dissolution Physics and the Treatment of Decompression Sickness." Medical Physics **10**: 184-190.

Lango, T., T. Morland and A. O. Brubakk (1996). "Diffusion Coefficients and Solubility Coefficients for Gases in Biological Fluids and Tissues: A Review." Undersea & Hyperbaric Medicine **23**: 247-272.

Lee, Y. C., Y.-C. Wu, W. A. Gerth and R. D. Vann (1993). "Absence of Intravascular Bubble Nucleation in Dead Rats." Undersea & Hyperbaric Medicine **20**(4): 289-296.

Lever, M. J., K. W. Miller, W. D. Paton and E. B. Smith (1966). "Experiments on the Genesis of Bubbles as a Result of Rapid Decompression." Journal of Physiology **184**: 964-969.

Liger-Belair, G. (2005). "The Physics and Chemistry Behind the Bubbling Properties of Champagne and Sparkling Wines: A State-of-the-Art Review." Journal of Agricultural and Food Chemistry **53**(8): 2788-2802.

Liger-Belair, G., M. Vignes-Alder, C. Voisin, B. Robillard and P. Jeandet (2002). "Kinetics of Gas Discharging in a Glass of Champagne: The Role of Nucleation Sites." Langmuir **18**: 1294-1301.

Liger-Belair, G., C. Voisin and P. Jeandet (2005). "Modeling Nonclassical Heterogeneous Bubble Nucleation from Cellulose Fibers: Application to Bubbling in Carbonated Beverages." Journal of Physical Chemistry B **109**: 14573-14580.

Lightfoot, E. N., A. Baz, E. H. Lanphier, E. P. Kindwall and A. Seireg (1978). "Role of Bubble Growth Kinetics in Decompression." Underwater Physiology, volume VI. C. W. Shilling and M. W. Beckett, Eds. Bethesda, FASEB: 449-457.

Markus, H., M. Cullinane and G. Reid (1999). "Improved Automated Detection of Embolic Signals Using a Novel Frequency Filtering Approach." Stroke **30**(8): 1610-1615.

Markus, H., A. Loh and M. M. Brown (1993). "Computerized Detection of Cerebral Emboli and Discrimination from Artifact Using Doppler Ultrasound." Stroke **24**(11): 1667.

Marroni, A., P. B. Bennett, F. J. Cronje, R. Cali-Corleo, P. Germonpre, M. Pieri, C. Bonuccelli and C. Balestra (2004). "A Deep Stop During Decompression from 82 Fsw (25 M) Significantly Reduces Bubbles and Fast Tissue Gas Tensions." Undersea & Hyperbaric Medicine **31**(2): 233-243.

Marroni, A. and R. Cali Corleo (1995). "Project Safe Dive - a Preliminary Report." XXI Annual Meeting of the European Underwater and Barometric Society, EUBS.

Marroni, A., R. Cali Corleo, C. Balestra, P. Longobardi, P. Germonpre, E. Voellm, M. Pieri and R. Pepoli (2001). "Incidence of Asymptomatic Circuating Venous Gas Emboli in Unrestricted, Uneventful Recreational Diving. Skin Cooling Appears to Be Related to Post-Dive Doppler Detectable Bubble Production. An Unexpected Finding. Dsl Special Project 03/2001." 27th Annual Meeting of the European Underwater and Barometric Society, Hamburg, EUBS.

Mohrman, D. E. and L. J. Heller (2003). Cardiovascular Physiology, McGraw Hill.

Nikolaev, V. P. (2000). "Effects of Heterogeneous Structure and Diffusion Permeability of Body Tissues on Decompression Gas Bubble Dynamics." Aviation, Space and Environmental Medicine **71**(7): 723-729.

Nishi, R. Y. (1975). "The Scattering and Absorption of Sound Waves by a Gas Bubble in a Viscous Liquid." Acoustica **33**(2): 173-179.

Nishi, R. Y., A. O. Brubakk and O. S. Eftedal (2003). "Bubble Detection." Bennett and Elliott's Physiology and Medicine of Diving, 5th edition. A. O. Brubakk and T. S. Neuman, Eds. London, Saunders: 501-529.

Nishi, R. Y. and B. C. Eatock (1989). "The Role of Ultrasonic Bubble Detection in Table Validation." Validation of Decompression Tables. H. R. Schreiner and R. W. Hamilton, Eds. Bethesda, Undersea and Hyperbaric Medical Society: 133-137.

Palanchon, P., A. Bouakaz, J. Klein and N. de Jong (2003). "Subharmonic and Ultraharmonic Emissions for Emboli Detection and Characterization." Ultrasound in Medicine and Biology **29**(3): 417-425.

Palanchon, P., A. Bouakaz, J. H. van Blankenstein, J. Klein, N. Bom and N. de Jong (2001). "New Technique for Emboli Detection and Discrimination Based on Nonlinear Characteristics of Gas Bubbles." Ultrasound in Medicine and Biology **27**(6): 801-808.

Rothberg, K. G., J. E. Heuser, W. C. Donzell, Y. S. Ying, J. R. Glenney and R. G. W. Anderson (1992). "Caveolin, a Protein-Component of Caveolae Membrane Coats." Cell **68**(4): 673-682.

Roy, E., P. Abraham, S. Montresor and J.-L. Saumet (2000). "Comparison of Time-Frequency Estimators for Peripheral Embolus Detection." Ultrasound in Medicine & Biology **26**(3): 419-423.

Rubissow, G. J. and R. S. MacKay (1971). " Ultrasonic Imaging of in Vivo Bubbles in Decompression Sickness " Ultrasonics **9**: 225.

Ruterbusch, V. L., W. A. Gerth and E. T. Long (2004). "Diver Thermal Status as a Risk Factor for Decompression Sickness (Dcs)." Undersea and Hyperbaric Medical Society Annual Scientific Meeting, Sydney, Australia, UHMS.

Sawatzky, K. D. and R. Y. Nishi (1991). "Assessment of Inter-Rater Agreement on the Grading of Intravascular Bubble Signals." Undersea Biomedical Research **18**(5-6): 373-396.

Schneck, D. J. (2000). "An Outline of Cardiovascular Structure and Function." The Biomedical Engineering Handbook, Second edition. J. D. Bronzino, Ed., CRC press & IEEE Press: **1**:1-12.

Shankar, P. M., P. D. Krishna and V. L. Newhouse (1999). "Subharmonic Backscattering from Ultrasound Contrast Agents." Journal of the acoustical society of America **106**(4): 2104.

Siebler, M., G. Rose, M. Sitzer, A. Bender and H. Steinmetz (1994). "Real-Time Identification of Cerebral Microemboli with Us Feature Detection by a Neural Network." Radiology **192**(3): 739.

Sluyter, W. M., P. C. Slooten, C. A. Copraij and A. K. Chesters (1991). "The Departure Size of Pool-Boiling Bubbles from Artificial Cavities at Moderate and High Pressures." International Journal of Multiphase Flow **17**(1): 153-158.

Smith, J. L., D. H. Evans, F. L. Thrush and A. R. Naylor (1994). "Processing Doppler Ultrasound Signals from Blood-Borne Emboli." Ultrasound in Medicine and Biology **20**(5): 455.

Srinivasan, R. S., W. A. Gerth and M. R. Powell (1999). "Mathematical Models of Diffusion-Limited Gas Bubble Dynamics in Tissue." Journal of Applied Physiology **86**(2): 732-741.

Srinivasan, R. S., W. A. Gerth and M. R. Powell (2002). "Mathematical Model of Diffusion-Limited Gas Bubble Dynamics in Unstirred Tissue with Finite Volume." Annals of Biomedical Engineering **30**(2): 232-246.

Srinivasan, R. S., W. A. Gerth and M. R. Powell (2003). "Mathematical Model of Diffusion-Limited Evolution of Multiple Gas Bubbles in Tissue." Annals of Biomedical Engineering **31**(4): 471-481.

Srinivasan, R. S. a. G. W. A. and M. R. Powell (2000). "A Mathematical Model of Diffusion-Limited Gas Bubble Dynamics in Tissue with Varying Diffusion Region Thickness." Respiration Physiology **123**(1-2): 153-164.

Sta Maria, N. and D. M. Eckmann (2003). "Model Predictions of Gas Embolism Growth and Reabsorption During Xenon Anesthesia." Anesthesiology **99**: 638-645.

Strong, K., D. W. Westenskow, P. G. Fine and J. A. Orr (1997). "A Preliminary Laboratory Investigation of Air Embolus Detection and Grading Using an Artificial Neural Network." International Journal of Clinical Monitoring and Computing **14**(2): 103-107.

Subramanian, R. S. and C. W. Michael (1980). "The Role of Convective Transport in the Dissolution or Growth of a Gas Bubble." The Journal of Chemical Physics **72**(12): 6811-6813.

Sutherland, J. (1999). "Automated Cardiac Monitoring Using Holographic/Quantum Neural Technology." PC AI **13**(5): 20-22.

Tao, L. N. (1978). "Dynamics of Growth or Dissolution of a Gas Bubble." Journal of Chemical Physics **69**(9): 4189-4194.

Thorn, H., K. G. Stenkula, M. Karlsson, U. O?rtegren, F. H. Nystrom, J. Gustavsson and P. Strålfors (2003). "Cell Surface Orifices of Caveolae and Localization of Caveolin to the Necks of Caveolae in Adipocytes." Molecular Biology of the Cell **14**(10): 3967-3976.

Tikuisis, P. (1982). "The Stability and Evolution of a Gas Bubble in a Finite Volume of Stirred Liquid (Thesis)." Report No. 82-R-17. Toronto, Canada: Defense and Civil Institute of Environmental Medicine.

Tikuisis, P. (1986). "Modeling the Observations of in Vivo Bubble Formation with Hydrophobic Crevices." Undersea Biomedical Research **13**(2): 165-180.

Tikuisis, P. and W. A. Gerth (2003). "Decompression Theory." Bennett and Elliott's Physiology and Medicine of Diving, 5th edition. A. O. Brubakk and T. S. Neuman, Eds., Saunders: 419-454.

Tikuisis, P. and W. R. Johnson (1983a). "Conditions for the Heterogeneous Nucleation in the Physiological Environment." Underwater Physiology volume VIII. A. J. Bachrach and M. M. Matzen, Eds. Bethesda, Undersea and Hyperbaric Medical Society: 107-118.

Tikuisis, P., C. A. Ward and R. D. Venter (1983b). "Bubble Evolution in a Stirred Volume of Liquid Closed to Mass-Transport." Journal of Applied Physics **54**(1): 1-9.

Uzel, S., M. A. Chappell and S. J. Payne (2006). "Modelling the Cycles of Growth and Detachment of Bubbles in Carbonated Beverages." Journal of Physical Chemistry B **110**: 7579-7586.

Van Liew, H. D. and M. E. Burkard (1993a). "Density of Decompression Bubbles and Competition for Gas among Bubbles, Tissue, and Blood." Journal of Applied Physiology **75**(5): 2293-2301.

Van Liew, H. D. and M. E. Burkard (1995). "Bubbles in Circulating Blood: Stabilization and Simulations of Cyclic Changes of Size and Content." Journal of Applied Physiology **79**: 1379-1385.

Van Liew, H. D., J. Conkin and M. E. Burkard (1993b). "The Oxygen Window and Decompression Bubbles - Estimates and Significance." Aviation, Space and Environmental Medicine **64**(9): 859-865.

Van Liew, H. D. and M. P. Hlastala (1969). "Influence of Bubble Size and Blood Perfusion on Absorption of Gas Bubbles in Tissues." Respiration Physiology **7**: 111-121.

Van Liew, H. D. and S. Raychaudhuri (1997). "Stabilized Bubbles in the Body: Pressure-Radius Relationships and the Limits to Stabilization." Journal of Applied Physiology **82**: 2045-2053.

Van Zuilen, E. V., W. H. Mess, C. Jansen, I. Van Der Tweel, J. Van Gijn and R. G. A. Ackerstaff (1996). "Automatic Embolus Detection Compared with Human Experts: A Doppler Ultrasound Study." Stroke **27**(10): 1840.

Vann, R. D., J. Grimstad and C. H. Nielsen (1980). "Evidence for Gas Nuclei in Decompressed Rats." Undersea Biomedical Research **7**(2): 107-112.

Walder, D. N. (1991). "The Pain and Mechanism of Bends." Forty-Third Undersea and Hyperbaric Medical Society Workshop: What is bends?, Shimizu, Japan, UHMS.

Wang, T., J. Wang and Y. Jin (2005). "Population Balance Model for Gas-Liquid Flows: Influence of Bubble Coalescence and Breakup Models." Industrial & Engineering Chemistry Research **44**(19): 7540-7549.

Ward, C. A. (1977). "The Rate of Gas Absorption at a Liquid Interface." The Journal of Chemical Physics **67**(1): 229-235.

Ward, C. A., W. R. Johnson, R. D. Venter, S. Ho, T. W. Forest and W. D. Fraser (1983). "Heterogeneous Bubble Nucleation and Conditions for Growth in a Liquid-Gas System of Constant Mass and Volume." Journal of Applied Physics **54**(4): 1833-1843.

Ward, C. A., M. Rizk and A. S. Tucker (1982a). "Statistical Rate Theory of Interfacial Transport. Ii. Rate of Isothermal Bubble Evolution in a Liquid-Gas Solution." The Journal of Chemical Physics **76**(11): 5606-5614.

Ward, C. A., P. Tikuisis and R. D. Venter (1982b). "Stability of Bubbles in a Closed Volume of Liquid-Gas Solution." Journal of Applied Physics **53**(9): 6076-6084.

Wienke, B. R. (1989). "Tissue Gas-Exchange Models and Decompression Computations - a Review." Undersea Biomedical research **16**(1): 53-89.

Winterton, R. H. S. (1971). "Sizes of Bubbles Produced by Dissolved Gas Coming out of Solution on the Walls of Pipes in Flowing Systems." Chemical Engineering Science **27**: 1223-1230.

Wisløff, U. and A. O. Brubakk (2001). "Aerobic Endurance Training Reduces Bubble Formation and Increases Survival in Rats Exposed to Hyperbaric Pressure." Journal of Applied Physiology **537**(2): 607-611.

Wisløff, U., R. S. Richardson and A. O. Brubakk (2003). "Nos Inhibition Increases Bubble Formation and Reduces Survival in Sedentary but Not Exercised Rats." Journal of Physiology **546**(2): 577-582.

Wisløff, U., R. S. Richardson and A. O. Brubakk (2004). "Exercise and Nitric Oxide Prevent Bubble Formation: A Novel Approach to the Prevention of Decompression Sickness?" Journal of Physiology **555**(3): 825-829.

Wu, Z. and N. E. Huang (2004). "A Study of the Characteristics of White Noise Using the Empirical Mode Decomposition Method." Proceedings of the Royal Society of London. Series A: Mathematical, Physical and Engineering Sciences **460**(2046): 1597-1611.

Yount, D. E. (1979). "Skins of Varying Permeability: A Stabiliziation Mechanism for Gas Cavitation Nuclei." Journal of the Acoustical Society of America **65**: 1429-1439.

Yount, D. E., E. W. Gillary and D. C. Hoffman (1984). "A Microscopic Investigation of Bubble Formation Nuclei." The Journal of the Acoustical Society of America **76**(5): 1511-1521.

Appendix A Multiple inert gas crevice bubble model[*]

A.1   Gas transfer

A.1.1   Between the bubble and the tissue

For each individual gas the diffusion equation is solved as in chapter 4 and incorporated with the Fick equation to give multi-gas versions of equations (4.14) and (4.15):

$$\frac{\mathrm{d}}{\mathrm{d}t}\left(p_{i,m}V_i\right) = L_{t,m}D_{t,m}\pi d^2 \sin\phi \frac{p_{t,m} - p_{i,m}}{\lambda_m}, \tag{A.1}$$

$$\frac{\mathrm{d}}{\mathrm{d}t}\left(p_{i,m}V_i\right) = L_{t,m}D_{t,m}\pi d_m^{\,2} \sin\phi \frac{p_{t,m} - p_{i,m}}{\lambda_m}, \tag{A.2}$$

where $p_{i,m}$, $p_{t,m}$, $L_{t,m}$, $D_{t,m}$ and λ_m are the pressure in the bubble and tissue, Ostwald co-efficient of solubility and diffusivity in the tissue and characteristic length for diffusion of the mth inert gas.

A.1.2   Between the tissue and the blood

Each inert gas is governed by the perfusion-limited assumption with its own tissue time constant, τ_m:

$$\frac{\mathrm{d}p_{t,m}}{\mathrm{d}t} = \frac{p_{a,m} - p_{t,m}}{\tau_m}. \tag{A.3}$$

Unlike a single inert gas the arterial pressure in the blood, $p_{a,m}$, is not equal to the ambient pressure, p_{amb}, but equal to the partial pressure of that gas in the atmosphere, i.e. $p_{a,m} = f_m p_{amb}$, where f_m is the fraction of the mth gas in the breathing gas mixture.

A.2   Crevice model

---

[*] This appendix expands upon the theory which appears as:
Chappell, M. A. and S. J. Payne (2006b). "A Physiological Model of the Release of Gas Bubbles from Crevices under Decompression." Respiration Physiology & Neurobiology **153**: 166-180.

For a single diffusible gas it was possible to solve equation (4.14) or (4.15) for the rate of change of θ, d or γ as appropriate, with p_i being given by the Laplace equation. However, for multiple gases the Laplace equation gives only the sum of the inert gases in the bubble:

$$p_{i,M} = \sum_{m=1}^{M} p_{i,m} = p_{amb} - p_{i,N} + \frac{2\sigma}{R}, \tag{A.4}$$

where this is equation (2.8) with $p_{i,M}$ as the sum of the inert gases in the bubble and $p_{i,N}$ as the sum of the infinitely diffusible gases (metabolic gases) and water vapour. Thus with multiple gases there is no explicit expression for the pressure of each gas in the bubble. Now, for each gas, equation (4.14) or (4.15), dependent upon whether the interface is inside or outside the crevice, is solved for the rate of change of $p_{i,m}$. The total influx of gas into the bubble can be found from a summation of that of the individual gases as given by equations (4.14) or (4.15), i.e. when the interface is inside the crevice:

$$\frac{d}{dt}\left(p_{i,M}V_i\right) = \sum_{m=1}^{M}\frac{d}{dt}\left(p_{i,m}V_i\right) = \sum_{m=1}^{M}\left(L_{t,m}D_{t,m}\pi d^2 \sin\phi \frac{p_{t,m}-p_{i,m}}{\lambda_m}\right), \tag{A.5}$$

or when the interface is outside the crevice:

$$\frac{d}{dt}\left(p_{i,M}V_i\right) = \sum_{m=1}^{M}\frac{d}{dt}\left(p_{i,m}V_i\right) = \sum_{m=1}^{M}\left(L_{t,m}D_{t,m}\pi d_m^{\ 2} \sin\phi \frac{p_{t,m}-p_{i,m}}{\lambda_m}\right). \tag{A.6}$$

The appropriate one of equations (A.5) and (A.6) is then solved, using the version of the Laplace equation given in equation (A.4), for the required geometric parameter, as described below.

A.2.1 Phase one

$$\alpha_r < \phi + \theta < \alpha_a \tag{A.7}$$

Equation (4.14) is solved for $p_{i,m}$ for each individual gas with $dd/dt = 0$ to give:

$$\frac{dp_{i,m}}{dt} = \frac{-\dfrac{3L_{t,m}D_{t,m}}{\lambda}\left(p_{i,m}-p_{t,m}\right)+\dfrac{3}{4}dp_{i,m}\dfrac{d\theta}{dt}\sin^2\phi}{d\varepsilon\sin^2\phi}, \tag{A.8}$$

and equation (A.5) is solved for θ using equation (A.4), with R for the interface inside the crevice and $dd/dt = 0$ to give:

$$\frac{\mathrm{d}\theta}{\mathrm{d}t}=\frac{\sum_{m=1}^{M}\left\{\frac{3L_{t,m}D_{t,m}}{\lambda}\left(p_{i,m}-p_{t,m}\right)\right\}+d\varepsilon\frac{\mathrm{d}p_{amb}}{\mathrm{d}t}\sin^{2}\phi}{\frac{3}{4}dp_{amb}\sin^{2}\phi+2\sigma\left\{\varepsilon\sin\theta+\frac{3}{4}\cos\theta\right\}\sin\phi},$$

(A.9)

where:

$$\varepsilon=\cot\phi-\tfrac{3}{4}\left(\theta-\tfrac{\pi}{2}\right).$$

(A.10)

A.2.2 Phase two

$$\begin{aligned}\text{growing:}\phi+\theta&=\alpha_{r}\\\text{collapsing:}\phi+\theta&=\alpha_{a}\end{aligned}$$

(A.11)

Equation (4.14) is now solved for $p_{i,m}$ with $\mathrm{d}\theta/\mathrm{d}t=0$ to give:

$$\frac{\mathrm{d}p_{i,m}}{\mathrm{d}t}=-\frac{3}{d}\left\{\frac{L_{t,m}D_{t,m}}{\lambda\varepsilon\sin^{2}\phi}\left(p_{i,m}-p_{t,m}\right)+p_{i,m}\frac{\mathrm{d}d}{\mathrm{d}t}\right\},$$

(A.12)

and equation (A.5) is solved for d using equation (A.4), with $\mathrm{d}\theta/\mathrm{d}t=0$:

$$\frac{\mathrm{d}d}{\mathrm{d}t}=-\frac{\sum_{m=1}^{M}\left\{\frac{3L_{t,m}D_{t,m}}{\lambda}\left(p_{i,m}-p_{t,m}\right)\right\}+d^{2}\varepsilon\frac{\mathrm{d}p_{amb}}{\mathrm{d}t}\sin^{2}\phi}{\left(4\sigma\cos\theta+3dp_{amb}\sin\phi\right)\varepsilon\sin\phi}.$$

(A.13)

A.2.3 Phase three

$$d=d_{m}$$

(A.14)

As the interface is now outside the crevice equation (A.6) is solved for $p_{i,m}$:

$$\frac{\mathrm{d}p_{i,m}}{\mathrm{d}t}=\frac{-\frac{3L_{t,m}D_{t.m}}{\lambda}\left(p_{i,m}-p_{t,m}\right)+\frac{1}{4}d_{m}p_{i,m}\frac{\mathrm{d}\gamma}{\mathrm{d}t}\sin^{2}\phi\mathrm{cosec}^{4}\left(\frac{\gamma}{2}\right)}{16d_{m}\sin\phi\xi_{3}},$$

(A.15)

where

$$\xi_{3}=\cos\phi+\left(2\mathrm{cosec}^{3}\gamma+\cot\gamma\left(1+2\mathrm{cosec}^{2}\gamma\right)\sin\phi\right).$$

(A.16)

To calculate γ equation (A.6) is now solved using Laplace equation in equation (A.4), with R for the interface outside the crevice:

$$\frac{\mathrm{d}\gamma}{\mathrm{d}t}=\frac{\sum_{m=1}^{M}\left\{\frac{3L_{t,m}D_{t,m}}{\lambda}\left(p_{i,m}-p_{t,m}\right)\right\}\sin^{3}\left(\frac{\gamma}{2}\right)+d_{m}\sin\phi\frac{\mathrm{d}p_{amb}}{\mathrm{d}t}\xi_{1}}{3d_{m}p_{amb}\sin^{2}\phi\mathrm{cosec}\left(\frac{\gamma}{2}\right)+2\sigma\xi_{2}},$$

(A.17)

where:

$$\xi_1 = 3\sin\left(\phi + \gamma/2\right) - \sin\left(\phi + 3\gamma/2\right), \tag{A.18}$$

and:

$$\xi_2 = 6\sin\phi\cos\left(\gamma/2\right) - \xi_1\cos\gamma. \tag{A.19}$$

A.3   Bubble release

For solution purposes, unlike the single gas version of the model presented in chapter 4, it is necessary to correct the pressure of the individual gases in the crevice every time a bubble is released. Otherwise the total pressure in the bubble no longer follows the Laplace equation, the result being that the model predicts that fewer bubbles are released. This arises because in the multiple gas model presented here the Laplace equation is not used explicitly in the model to calculate the bubble pressure, instead the individual gas pressure in the bubble are calculated from differential equations. Consequently the discontinuity in the bubble pressure that occurs at bubble release is not correctly calculated using the standard numerical differential equation solvers. The answer is to solve the model equations up to the point of release and stop. The solver can then be restarted using the final conditions from the previous solution as the initial conditions, except for the pressure of gases in the bubble and the contact angle. The latter is set to a pre-determined value, i.e. in chapter 4 the advancing contact angle was used, and the former calculated using the Laplace equation for the total pressure in the bubble and using the proportions of the different gases from before bubble release. This process is repeated as long as the bubble grows up to the critical contact angle for bubble release. It is assumed that the time taken for the bubble to release is negligible compared to the time for bubble growth.

Appendix B   Non-dimensional version of crevice model equations

In this appendix the pseudo non-dimensional version of the equations that compose the crevice bubble model presented in chapter 4 are given. The parameters $\bar{p}$ (1 bar) and $\bar{r}$ (1 μm) are introduced, only the time dimension is retained. Pressures are now defined in non-dimensional form, $p' = p/\bar{p}$, and likewise for lengths, $d' = d/\bar{r}$.

B.1   Phase one

$$\alpha_r < \phi + \theta < \alpha_a \tag{B.1}$$

Equation (4.18) becomes:

$$\frac{\mathrm{d}\theta}{\mathrm{d}t} = \frac{\dfrac{3}{\tau_D}\left(p_i' - p_t'\right) + d'\varepsilon\dfrac{\mathrm{d}p_{amb}'}{\mathrm{d}t}\sin^2\phi}{\frac{3}{4}d'p_{amb}'\sin^2\phi + 2\sigma'\left\{\varepsilon\sin\theta + \frac{3}{4}\cos\theta\right\}\sin\phi}, \tag{B.2}$$

where:

$$\varepsilon = \cot\phi - \tfrac{3}{4}\left(\theta - \tfrac{\pi}{2}\right). \tag{B.3}$$

and p_i' is given the pseudo non-dimensional version of equation (4.20):

$$p_i' = p_{amb}' + \frac{2\sigma'\cos\theta}{d'\sin\phi}. \tag{B.4}$$

B.2   Phase two

$$\begin{aligned} \text{growing:} & \phi + \theta = \alpha_r \\ \text{collapsing:} & \phi + \theta = \alpha_a \end{aligned} \tag{B.5}$$

Equation (4.22) becomes:

$$\frac{\mathrm{d}d'}{\mathrm{d}t} = -\frac{\dfrac{3}{\tau_D}\left(p_i' - p_t'\right) + d'^2\varepsilon\dfrac{\mathrm{d}p_{amb}'}{\mathrm{d}t}\sin^2\phi}{\left(4\sigma'\cos\theta + 3d'p_{amb}'\sin\phi\right)\varepsilon\sin\phi}, \tag{B.6}$$

and p_i' is given by equation (4.20).

B.3 Phase three

$$d' = d'_m \tag{B.7}$$

Equation (4.24) becomes:

$$\frac{\mathrm{d}\gamma}{\mathrm{d}t} = \frac{\dfrac{3}{\tau_D}\left(p'_i - p'_t\right)\sin^3\left(\dfrac{\gamma}{2}\right) + d'_m \sin\phi \dfrac{\mathrm{d}p'_{amb}}{\mathrm{d}t}\xi_1}{3d'_m p'_{amb}\sin^2\phi\operatorname{cosec}\left(\dfrac{\gamma}{2}\right) + 2\sigma'\xi_2}, \tag{B.8}$$

where:

$$\xi_1 = 3\sin\left(\phi + \gamma/2\right) - \sin\left(\phi + 3\gamma/2\right), \tag{B.9}$$

$$\xi_2 = 6\sin\phi\cos\left(\gamma/2\right) - \xi_1\cos\gamma, \tag{B.10}$$

and p'_i is given by:

$$p'_i = p'_{amb} + \frac{2\sigma'\sin\gamma}{d'_m\sin\phi}. \tag{B.11}$$